# Studies of Non-LTE Processes Relating to Atmospheric IR Backgrounds and Clutter

W. Pendleton
J. Dodd
M. Taylor
U. Makhlouf

Stewart Radiance Laboratory, Utah State University
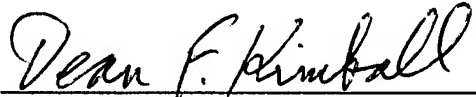139 The Great Road
Bedford, MA 01730

30 Dec 1997

**AIR FORCE RESEARCH LABORATORY**
Space Vehicles Directorate
29 Randolph Rd
**AIR FORCE MATERIEL COMMAND**
Hanscom AFB, MA 01731-3010

20020415 028
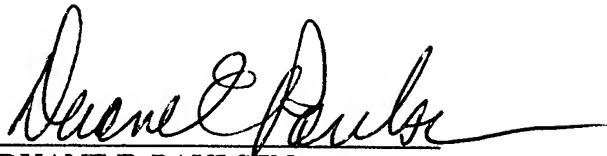
This technical report has been reviewed and is approved for publication.

_DEAN F. KIMBALL_
DEAN F. KIMBALL
Contract Manager

_DUANE E. PAULSEN_
DUANE E. PAULSEN
Deputy Chief, AFRL/VSSS

# REPORT DOCUMENTATION PAGE

Public reporting burden for this collection of information is estimated to average 1 hour per response, including the time for reviewing instructions, searching existing data sources, gathering and maintaining the data needed, and completing and reviewing the collection of information. Send comments regarding this burden estimate or any other aspect of this collection of information, including suggestions for reducing this burden, to Washington Headquarters Services, Directorate for Information Operations and Reports, 1215 Jefferson Davis Highway, Suite 1204, Arlington, VA 22202-4302, and to the Office of Management and Budget, Paperwork Reduction Project (0704-0188), Washington, DC 20503.

| 1. AGENCY USE ONLY *(Leave blank)* | 2. REPORT DATE 30 December 1997 | 3. REPORT TYPE AND DATES COVERED Scientific Report # 20 |
|---|---|---|

**4. TITLE AND SUBTITLE**
STUDIES OF NON-LTE PROCESSES RELATING TO IR BACKGROUNDS AND CLUTTER

**5. FUNDING NUMBERS**
PE: 61102F
PR: 2310
TA: GD
WU: AK

Contract: F19628-93-C-0165

**6. AUTHOR(S)**
W. Pendleton, J. Dodd*, M. Taylor, U. Makhlouf*

**7. PERFORMING ORGANIZATION NAME(S) AND ADDRESS(ES)**
UTAH STATE UNIVERSITY FOUNDATION
dba Space Dynamics Laboratory (Science Division)
1747 North Research Parkway
Logan, UT 84322

**8. PERFORMING ORGANIZATION REPORT NUMBER**

SDL/97-101

**9. SPONSORING/MONITORING AGENCY NAME(S) AND ADDRESS(ES)**
Air Force Research Laboratory
29 Randolph Road
Hanscom AFB MA 01731-3010

Contract Manager: Dean Kimball/VSSS

**10. SPONSORING/MONITORING AGENCY REPORT NUMBER**

AFRL-VS-HA-TR-98-0125

**11. SUPPLEMENTARY NOTES**
*Stewart Radiance Laboratory
139 The Great Road
Bedford, MA 01730

**12a. DISTRIBUTION AVAILABILITY STATEMENT**
Approved for Public Release; Distribution Unlimited

**12b. DISTRIBUTION CODE**

**13. ABSTRACT** *(Maximum 200 words)*

This collection of reprints describes work performed under the three basic work elements of the contract during the period 10/01/96-09/30/97. The work elements are: (1) laboratory studies of key production and loss processes for IR-active species of special interest to upper atmospheric non-LTE IR emissions; (2) ground-based field measurements of selected IR airglow and auroral emissions, with emphasis on sources of background and clutter; (3) atmospheric modeling of the dynamics of the non-LTE processes relating to the laboratory and field measurements. Results from the laboratory studies include rate constants for the collisional relaxation of $OH(X^2\Pi, v, N)$ [$v=1$ ($N = 8-25$), $v=2$ ($N = 8-22$), $v=3$ ($N = 9-17$)] by $O_2$ and fractional populations of $NO(v-1)$ resulting from collision-induced vibrational relaxation of $NO(v=3)$ by O atoms and NO ($v=2,3$) by NO. Results from the field measurements include a statistical study of the characteristics of >50 wave events which were identified in airglow images obtained at equatorial latitudes, documentation of a technique for two-dimensional spectral analyses of mesospheric airglow image data, and the presentation of evidence for ducting and evanescence in selected wave events observed in the airglow over the Hawaiian islands. Results from the modeling effort include the use of ground-based image data for the [OI] 557.7-nm airglow emission for benchmarks to deduce the presence (and key properties) of wave activity near the base of the thermosphere, followed by use of the dynamical model to estimate the enhanced vertical diffusion resulting from the wave activity.

**14. SUBJECT TERMS**
Airglow, Aurora, Infrared radiation, Vibrational relaxation, Rotational relaxation, Atmospheric code, Dynamical simulation, Vertical eddy diffusivity

**15. NUMBER OF PAGES**

**16. PRICE CODE**

| 17. SECURITY CLASSIFICATION OF REPORT | 18. SECURITY CLASSIFICATION OF THIS PAGE | 19. SECURITY CLASSIFICATION OF ABSTRACT | 20. LIMITATION OF ABSTRACT |
|---|---|---|---|
| UNCLASSIFIED | UNCLASSIFIED | UNCLASSIFIED | SAR |

# Fractional population of NO($v − 1$) from vibrational relaxation of NO($v = 2, 3$) by O and NO

**James A. Dodd,[a]\* Ronald B. Lockwood,[b] Steven M. Miller[b] and William A. M. Blumberg[b]**

[a] *Stewart Radiance Laboratory, 139 Great Road, Bedford, Massachusetts 01730 USA*
[b] *Phillips Laboratory/GPOC, Hanscom Air Force Base, Massachusetts 01731 USA*

Significant populations of NO in excited vibrational levels $v \geqslant 2$ have recently been observed in the lower thermosphere, for which the relaxation rates and pathways are largely governed by collisions with O atoms. Laboratory experiments can provide accurate kinetic parameters for modelling and interpreting such steady-state $v$-dependent population distributions. In this study, a two-laser, pump–probe arrangement has been used to measure the fractional population of NO($v − 1$) arising from the collision-induced relaxation of NO($v = 3$) by O atoms and, in an ancillary experiment, NO($v = 2, 3$) by NO. The branching fraction $\chi_O(v = 3 \rightarrow 2) = 0.35 \pm 0.12$ for O-atom collisions. The $\chi_O$ value is consistent with a long-lived NO$_2^*$ collision complex, in which the total energy is randomly distributed among the internal degrees of freedom prior to dissociation, and agrees with a recent quasiclassical trajectory calculation. For collisions with NO, $\chi_{NO}(v = 3 \rightarrow 2) = 0.73 \pm 0.19$, indicating a significant multi-quantum component. The branching fraction $\chi_{NO}(v = 2 \rightarrow 1) = 1.19 \pm 0.31$ can be considered an effective value only, since its interpretation relies on an assumption regarding the relaxation mechanism. The rate constants $k_O(v = 3) = (3.0 \pm 0.6) \times 10^{-11}$ cm$^3$ s$^{-1}$ for the vibrational relaxation of NO($v = 3$) by O atoms, and $k_{NO}(v = 2) = (2.7 \pm 0.5) \times 10^{-12}$ cm$^3$ s$^{-1}$ and $k_{NO}(v = 3) = (3.4 \pm 0.7) \times 10^{-12}$ cm$^3$ s$^{-1}$ for the relaxation of NO($v = 2, 3$) by NO have also been obtained, and are in good agreement with previous results from this laboratory.

## 1 Introduction

A great deal of attention has recently been focused on the chemical sources and sinks of NO in the lower thermosphere. Reactions (1) and (2) constitute the dominant NO production mechanisms:[1–4]

$$N(^4S) + O_2 \rightarrow NO(v \leqslant 7) + O \qquad (1)$$

$$N(^2D) + O_2 \rightarrow NO(v \leqslant 18) + O \qquad (2)$$
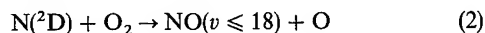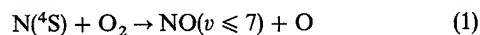
Reactions (1) and (2), in conjunction with other NO formation reactions, can clearly give rise to a large degree of vibrational excitation in the NO product, consistent with laboratory measurements.[5] Evidence that excited $v$-level populations of NO are present in the thermosphere is exemplified by recent observations of NO($v \geqslant 2$) fundamental band radiance in high-resolution earthlimb emission data from the CIRRIS 1A mission.[6,7] Excited NO($v$) populations are especially prevalent in auroras, for which the NO production rate can be vastly increased. NO populations up to $v = 5$ were detected in CIRRIS 1A measurements of naturally occurring auroras,[6] and up to $v = 12$ in the EXCEDE III space-based artificial aurora experiment.[8] The decay pathways of the vibrationally excited NO populations will partially govern the resultant infrared background radiance and the extent to which the initial chemical energy is converted into thermal heating. Kinetic models for the production and decay of NO vibrational levels have been developed,[9,10] but need to be updated and enhanced with more accurate input parameters.

Vibrational energy transfer in thermospheric NO is dominated by collisions with oxygen atoms, since both $N_2$ and $O_2$ are inefficient relaxers.[11–13] However, relatively little is known concerning the rates and pathways of NO($v$)/O vibrational excitation or relaxation. In 1979 Fernando and Smith[14] performed a landmark measurement of the room-temperature rate constant $k_O(v = 1)$ for NO($v = 1$) vibrational relaxation by oxygen atoms. Their measurement is particularly important, since it is related through detailed balance to the vibra-

tional uppumping reaction

$$NO(v = 0) + O \rightarrow NO(v = 1) + O \qquad (3)$$
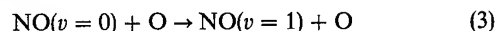
Reaction (3) is a primary mechanism for lower thermospheric cooling through the conversion of kinetic energy into NO($v = 1 \rightarrow 0$) fundamental band emission, which largely escapes into space. The temperature dependence of $k_O(v = 1)$ in the 500–1200 K range has not been empirically determined, increasing the uncertainty with which the Fernando and Smith measurement can be applied to models of the lower thermosphere.

Our group has recently examined the analogous process for NO($v = 2, 3$),[15] providing the only determination of the O-atom-induced quenching rates for NO($v \geqslant 2$), aside from a shock-tube measurement of NO($v = 2$) relaxation at 2700 K.[16] The determination of additional $v$-dependent relaxation rate constants and single/multiquantum relaxation pathways would be of great use in modelling the dynamics of nascently-formed high-$v$ NO in the thermosphere. The problem is potentially very similar to that of OH($v \leqslant 9$) collisional quenching at the mesopause,[17] in which the question of collision-induced single- vs. multi-quantum decay remains largely unanswered.

In this paper we extend our earlier work on the relaxation of NO($v = 2, 3$) by O and NO, and report measurements of the branching fractions of initially populated NO($v = 2, 3$) into the lower $v − 1$ level. In the case of O-atom relaxation, this represents the first measurement of a detailed vibrational relaxation pathway. The results can be compared with the statistical models of Quack and Troe,[18,19] who calculated pathways based on the presence of a long-lived NO$_2^*$ intermediate, *viz.*

$$NO(v_i) + O \rightarrow NO_2^* \rightarrow NO(v_f) + O \qquad (4)$$
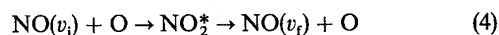
The measurements can also be compared with the more recent semiclassical trajectory calculations of Duff and Sharma[20] on the same system. All of these studies are in general agreement that the final vibrational state populations are approximately equal, *i.e.* independent of $v_f$.

## 2 Experimental

The experimental apparatus and methodology were very similar to that used in our previous study of NO($v = 2, 3$) vibrational relaxation[15] (see Fig. 1). The primary apparatus consisted of a 2 in (in = 2.54 cm) internal diameter glass flow tube, coated on its internal surfaces with halocarbon wax in order to minimize oxygen-atom recombination. Clamped to the flow tube was the detection cell, which consisted of a stainless-steel cube bored through to give the same 2 in internal diameter, and Teflon-coated on its internal surfaces. Two 10 cm long side-arms containing a series of black anodized aluminium light baffles were attached at right angles to the flow tube axis, in order to pass laser light through Brewster-angle windows. The cell provided the capability for multi-photon ionization (MPI) and laser-induced fluorescence (LIF) detection of trace species in the gas flow. Vibrational level populations of NO were probed in the previous study using 1 + 1 resonance-enhanced MPI; in this study we used the LIF technique as described in the following.

Fig. 2 shows an example schematic of the IR pump–UV probe methodology for initial excitation of NO($v = 2$). NO($v = 2, 3$) rotational levels were populated using tunable IR laser pulses, generated by mixing visible dye laser output with the 1.06 μm Nd : YAG fundamental in a LiNbO$_3$ crystal. Residual visible and 1.06 μm radiation was eliminated by passing the mixed output through a silicon window at Brewsters angle (for 1.8 μm), and additionally through a germanium window, also at Brewsters angle (for 2.7 μm). Laser pulse energies in the 2.7 μm region with frequencies corresponding to several of the $v = 0 \rightarrow 2$, $J'' \rightarrow J'' + 1$ $R$-branch transitions were found to vary by a factor of three owing to varying absorption by water vapour in room air. The 2–0 $R(J'' = 6.5)$ and 3–0 $R(J'' = 7.5)$ transitions were used in the two cases, with a fractional excitation of ca. $10^{-5}$–$10^{-4}$ of the total NO population (vide infra). The IR pulse was weakly focused using a 500 mm CaF$_2$ lens positioned 370 mm before the cell, giving a $1/e^2$ Gaussian beam diameter of ca. 3 mm.

NO($v = 1$–3) time-dependent populations were detected using LIF and various bands in the A–X $\gamma$-band system. To generate the detection laser wavelengths, an Inrad Autotracker II was used to frequency-double laser light from a Nd : YAG-pumped dye laser. The detection beam was shaped
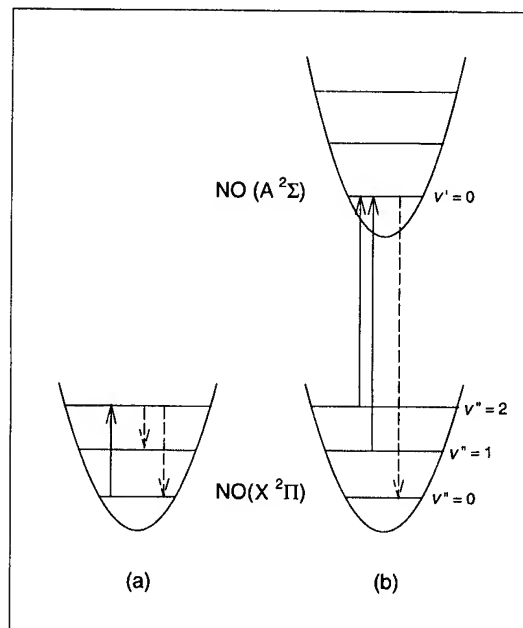


**Fig. 2** Schematic of laser excitation/detection methodology. In (a), a tunable IR laser excites a small fraction of the NO $v = 0$ population to $v = 2$. Collisions with relaxer species then transfer the initially excited population to lower $v$ levels on a timescale of tens of μs. In (b), a UV laser is used to probe either the initially excited $v = 2$ level, or the $v = 1$ level which is populated by collisional relaxation. Detection is accomplished using the $\gamma$(0–0) band, which occurs at a shorter wavelength. Detection via the $\gamma$(2 − $v''$) bands is performed in a similar manner. Note that the separation between the A and X levels is not drawn to scale.

into a circular cross-section using a pair of cylindrical lenses, then sent through a pair of 1 mm diameter irises prior to entry into the cell in order to precisely maintain its position relative to the larger IR beam. UV pulse fluences were kept very low (1–10 μJ) to avoid saturation of the strong $\gamma$-band transitions. A Burleigh WA-5500 pulsed wavemeter was used to monitor both the IR and UV dye laser frequencies to be certain they were not drifting off resonance. While we did observe inaccuracies in these measurements consistent with the instrument
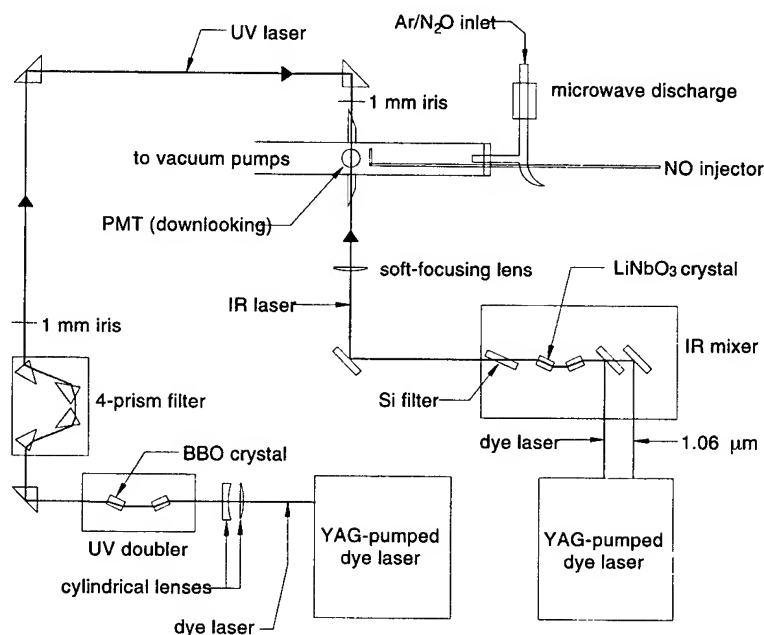


**Fig. 1** Experimental apparatus. See text for discussion.

specification (*e.g.* $\pm 0.1$ cm$^{-1}$ at 600 nm, $\pm 0.2$ cm$^{-1}$ at 300 nm), the reading remained stable over the course of several days in the absence of optics readjustment.

The NO $\gamma$-band fluorescence was detected at a shorter wavelength than the pump wavelength, largely eliminating background arising from laser light scatter off the windows, the microwave discharge, and from NO$_2^*$ fluorescence, which extends from 400 nm into the near-IR. In many cases it was easy to detect the NO($v$) under photon-counting conditions, although the fluorescence signals were typically much stronger. Two $\gamma$-band series were used, the $\gamma(2-v'')$ series, in which the $\gamma(2-2)$ and $\gamma(2-3)$ bands at 222 and 231 nm were pumped, and the $\gamma(2-0)$ band at 205 nm detected, and the $\gamma(0-v'')$ series, in which the $\gamma(0-1)$ and $\gamma(0-2)$ bands at 237 and 247 nm were pumped, and the $\gamma(0-0)$ band at 227 nm detected. The $\gamma(2-0)$ detection method gave rise to about a factor-of-two better S/N, owing to more favourable A–X Franck–Condon factors. Fluorescence was detected by a Hamamatsu R166 solar-blind PMT, in conjunction with 10 nm FWHM bandpass filters (Corion Corp., Andover Corp.) centred at 206.5 and 224.4 nm, respectively. In each case the use of the same upper state allowed relative $v''$ population measurements to be accomplished without needing to account for such factors as detector wavelength response and NO($A$, $v$) fluorescence lifetime.

Between 8 and 32 laser shots were averaged for each time element, resulting in typical run times of between 3 and 13 min for 250 time values. At each time delay the integrated LIF signal and the UV and IR laser fluences were separately averaged on digital oscilloscopes, and the averaged values stored on a laboratory computer. In the data workup the LIF signals were ratioed by 50 point running averages of the IR and UV laser fluences to account for long-term drift, which was generally <10%. These ratioed signals were then converted to relative populations of the NO($v$) populations by dividing by the product of the appropriate Boltzmann population factor and linestrength[22] of the rotational level probed, and by the $v'' \rightarrow v'$ Franck–Condon factor.[23] In each case a rotational transition was chosen that was separated from its nearest neighbours by more than the FWHM bandwidth (0.7 cm$^{-1}$) of the UV laser.

A mixture of *ca.* 25 sccm N$_2$O in 1100 sccm Ar was flowed through a McCarroll cavity microwave discharge in order to form O atoms. A 0.5 in od. Pyrex tube was used instead of the magnesium oxide tube used previously. The discharge region was followed by a Woods horn and a right angle in order to minimize stray light in the fluorescence detection region. An additional 425 sccm Ar was introduced through a loop injector just upstream of the discharge effluent in order to minimize turbulence. One sccm NO was introduced a few mm upstream of the detection region, through an injector formed from a 1 in long, 0.125 in od Teflon tube aligned along the laser axis, with about ten small holes pointing downstream. This arrangement was found to minimize mixing of the injected NO with oxygen atoms prior to the laser pump–probe sequence. Reactions (5) and (6) reduce the O-atom concentration, and give rise to NO($v$) background through the sequence

$$NO + O + M \rightarrow NO_2^* + M \qquad (5)$$

$$NO_2 + O \rightarrow NO(v \leqslant 9) + O_2 \qquad (6)$$
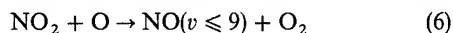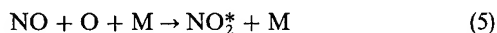
with rate constants $k_5 = 2.4 \times 10^{-14}$ cm$^3$ s$^{-1}$ (at 8.5 Torr) and $k_6 = 9.7 \times 10^{-12}$ cm$^3$ s$^{-1}$.[21] The observed NO LIF background was linear in laser power, consistent with the presence of a small amount of NO($v$) created through reactions (5) and (6). Conceivably, photolysis of NO$_2$ followed by detection of product NO($v$) in the same laser pulse could also give rise to a background signal, though such a process would have a quadratic laser power dependence at the low probe fluences used. In our previous study we found that reactions (5) and (6)

reduced the O-atom density by about 5% upon the addition of NO. The chemiluminescent NO$_2^*$ formed in reaction (5) was used to advantage in adjusting the various flow rates to minimize the turbulence in the cell region. The microwave discharge was operated at *ca.* 110 W. The O-atom density was measured to be $1.8 \times 10^{15}$ cm$^{-3}$ through NO$_2$ titrations,[24] about a factor of three higher than densities achieved in our previous study employing the magnesium oxide discharge tube.[15]

For the NO($v$ = 2, 3)–NO self-relaxation studies, the microwave discharge and the N$_2$O flow were turned off, and mixtures of either 50 sccm NO–1525 sccm Ar or 10 sccm NO–215 sccm Ar were used, corresponding to NO number densities of $8.6 \times 10^{15}$ cm$^{-3}$ and $1.2 \times 10^{16}$ cm$^{-3}$, respectively. For both flow rates the total pressure was set to *ca.* 8.5 Torr by throttling the downstream vacuum pump, giving rise to linear flow velocities of 120 and 17 cm s$^{-1}$, respectively. The measured branching fractions did not depend on the flow speed. In general, the observed NO($v$) decay rates were dominated by O-atom- and NO-induced collisional relaxation, respectively. The collision-induced decay rates of NO($v$ = 2, 3) by Ar and N$_2$O were <100 s$^{-1}$, and the NO($v$ = 2, 3) radiative decay rates are *ca.* 30 s$^{-1}$. The transport loss rate of NO($v$) from the laser field of view is accounted for in the kinetic equations outlined below.

## 3 Data interpretation and reduction

Rotational energy transfer in NO in general occurs at or near gas kinetic rates,[25–27] with little dependence on the initially excited $J$ level. The 8.5 Torr Ar bath gas gives rise to an NO rotational energy transfer timescale of *ca.* 10–20 ns, based on the NO($v$ = 2, 3; $J$) removal rate constants of *ca.* 2–3 $\times 10^{-10}$ cm$^3$ s$^{-1}$ measured by Islam *et al.*[25] In addition, Islam *et al.*[27] have recently measured a large number of state-to-state rovibronic rate coefficients for collisions of initially created NO($v$ = 2, $\Omega$, $J$) with NO, He and Ar. It was found the $\Omega$-changing collisions of NO with Ar occur at no greater than 10% of the rate for $\Omega$-preserving collisions,[27] which places a lower limit of 100 ns on the timescale for $\Omega$-changing collisions. However, these rotational and spin–orbit equilibration time scales are still about a factor of 100–1000 times smaller than the timescale for NO vibrational decay in our experiment.

Fig. 3 shows a series of NO($v$ = 3) LIF spectra, obtained at various times following IR excitation, along with a synthetic spectrum calculated assuming a room-temperature distribution of rotational populations. The $v = 0 \rightarrow 3$, $R(J'' = 7.5)$ F$_1$ and F$_2$ vibrational overtone transitions are separated by only 0.07 cm$^{-1}$, far less than the IR laser bandwidth of 1.1 cm$^{-1}$, and both the F$_1$ and F$_2$ $J' = 8.5$ levels are initially populated in the upper vibrational state. Each of the two excited rotational populations gives rise to four resolved emission lines shortly after the IR pump pulse (Fig. 3). The entire $v = 3$ manifold is seen to fill in and approximate the predicted room-temperature spectrum after <100 ns, consistent with the rotational energy transfer timescales estimated above. Thus, since the rotational level populations reequilibrate on a timescale short compared to vibrational relaxation, the vibrational populations can be probed using any one of a number of $\gamma$-band rotation-vibration transitions.

Too high a concentration of vibrationally excited NO can lead to 'ladder-climbing' effects, in which the excited species exchange energy in an efficient, near-resonant process[28]

$$NO(v') + NO(v'') \rightarrow NO(v' - 1) + NO(v'' + 1) \qquad (7)$$
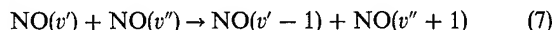
Wysong,[11,29] in previous measurements of NO($v$ = 2, 3) self-quenching rates, found that NO($v$) fractions > *ca.* 10$^{-3}$ of the total NO concentration led to discernible second-order effects in model calculations of NO($v$) vibrational relaxation. It is
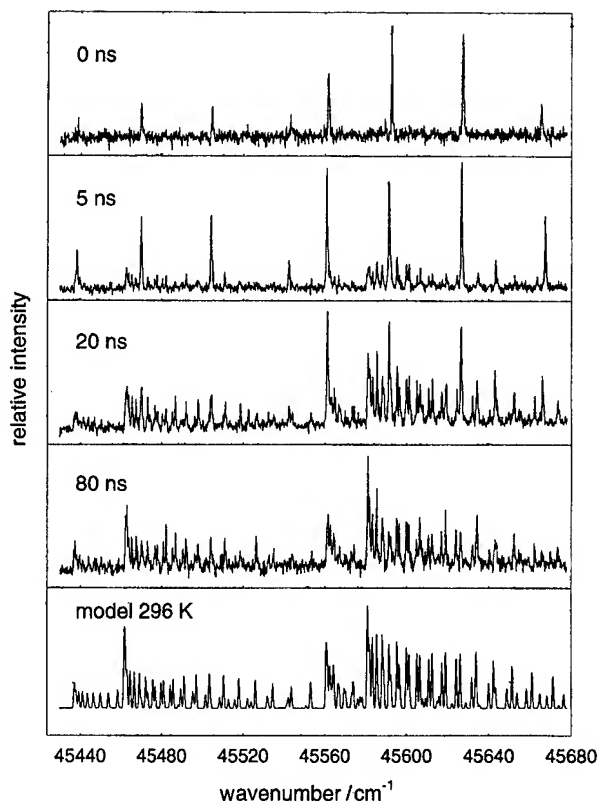
**Fig. 3** Time series of NO $\gamma$(3, 3) laser-induced fluorescence spectra following IR excitation of NO($v = 3$) at $t = 0$ ns. Collisions with Ar bath gas molecules efficiently transfer the initially formed $F_1$ and $F_2$ $v = 3$, $J' = 8.5$ populations to other rotational levels. After *ca.* 100 ns the rotational level populations are equilibrated at ambient temperature.
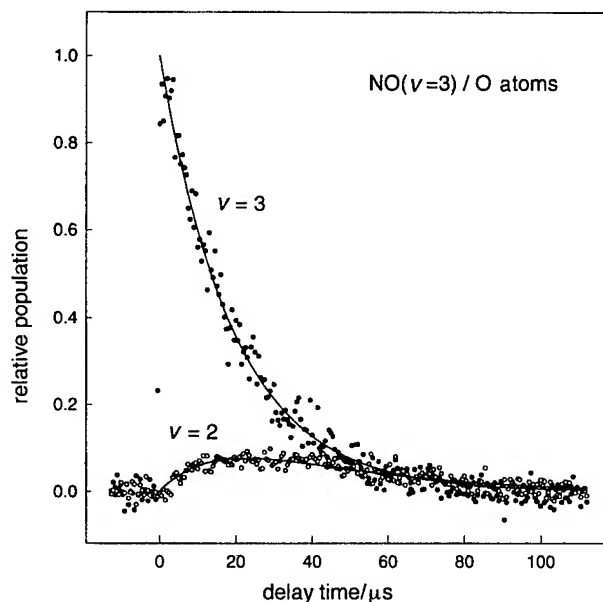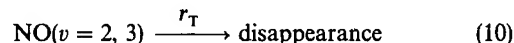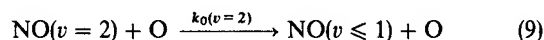


**Fig. 4** Quenching of NO($v = 3$) by O atoms. The IR laser fires at $t = 0$, which populates the $v = 3$ level. NO($v = 3$) decays exponentially, while NO($v = 2$) grows in over time according to the branching fraction $\chi_O(v = 3 \rightarrow 2)$ and the relaxation rate constants $k_O(v)$. The NO($v = 2$) population builds up only modestly because $\chi_O(v = 3 \rightarrow 2)$ is relatively small, and $k_O(v = 2) \approx k_O(v = 3)$. The NO($v = 2$, 3) background LIF signals have been subtracted; the background signals are about $6 \times (v = 2)$ and $0.5 \times (v = 3)$ the magnitude of the transient signals.

straightforward to estimate the excited fraction by comparing the maximum NO($v = 2$) population to the background NO($v = 1$) population, where both are obtained from normalized LIF signals. The Boltzmann equilibrium $v = 1$ background population is equal to a $1.1 \times 10^{-4}$ fraction of the $v = 0$ population at 295K. From observations of several data sets, the initially pumped NO($v = 2$) population was found to equal about one-half of the ambient $v = 1$ population, a $5 \times 10^{-5}$ fraction of the total NO. The maximum NO($v = 3$) population is estimated to be about one-half that of NO($v = 2$), based on relative IR laser fluences and bandwidths, and absorption coefficients and Doppler linewidths of the NO(X) 3–0 and 2–0 overtone bands.

In a typical experiment the UV laser was first tuned to detect the initially populated NO($v$) level, and several NO($v$) time series obtained. The UV laser frequency was then adjusted to detect NO($v − 1$), and again several time series accumulated. Data on several different days were obtained in this manner for each different excited species–quencher pair. For $v = 3 \rightarrow 2$ relaxation this was relatively straightforward, owing to negligible population of the lower $v$ level in room-temperature NO. For $v = 2 \rightarrow 1$ relaxation, however, the *ca.* $10^{-4}$ fraction of the total NO concentration in $v = 1$ resulted in a large background signal in the absence of IR excitation. This background signal dominated the noise observed on the $v = 1$ signals. For NO($v = 2$) self-relaxation the noise could be sufficiently reduced through signal averaging to obtain a branching fraction $\chi_{NO}(v = 2 \rightarrow 1)$. For NO($v = 2$, 3)–O relaxation the combination of reactions (5) and (6) gave rise to an additional source of background signal for NO($v = 1$), and to a lesser extent for NO($v = 2$).[30] These complications obviated an acceptable measurement of $\chi_O(v = 2 \rightarrow 1)$.

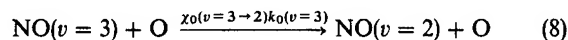Fig. 4 shows time-dependent NO($v$) populations and a model fit for a sample NO($v = 3$)–O-atom run. The rate pro-

cesses governing the relaxation of initially excited NO($v = 3$) are written

$$NO(v = 3) + O \xrightarrow{\chi_O(v = 3 \rightarrow 2)k_O(v = 3)} NO(v = 2) + O \quad (8)$$

$$NO(v = 2) + O \xrightarrow{k_O(v = 2)} NO(v \leqslant 1) + O \quad (9)$$

$$NO(v = 2, 3) \xrightarrow{r_T} \text{disappearance} \quad (10)$$

In eqn. (8)–(10), $k_O(v)$ is the rate constant for O-atom-induced relaxation of NO($v$), $\chi_O(v = 3 \rightarrow 2)$ is the branching fraction for single-quantum decay, and $r_T$ is the transport loss rate out of the UV laser field of view. The transport loss rate has both convective and diffusive components under the present conditions, and can be estimated as $5 \times 10^3$ s$^{-1}$ based on the observed decay rate of NO($v = 1$) (*vide infra*), i.e. *ca.* 10% of the O-atom-induced decay rate. Reactions (8)–(10) were modelled using the coupled differential equations

$$\frac{d[NO(v = 3)]}{dt} = -[NO(v = 3)]\{r_T + k_M(v = 3)[M]\} \quad (I)$$

$$\frac{d[NO(v = 2)]}{dt} = -[NO(v = 2)]\{r_T + k_M(v = 2)[M]\} + [NO(v = 3)]\{\chi_M(v = 3 \rightarrow 2)k_M(v = 3)[M]\} \quad (II)$$

In eqn. (I) and (II) [NO($v$)] and [M] refer to time-dependent species concentrations, with M being the identity of the chief quencher species, i.e. O atoms or NO as appropriate. Trial integrations performed on a PC showed second-order reactions such as eqn. (7) to be unimportant owing to the very small amount of excited level populations present.

Fig. 5 and 6 show time-dependent NO($v$) populations and model fits for sample NO($v = 3$)–NO and NO($v = 2$)–NO runs, respectively. The NO($v = 3$)–NO kinetics are governed
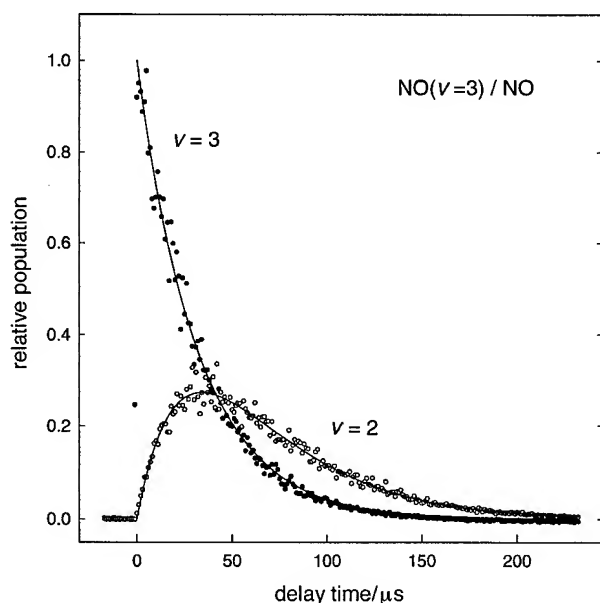
**Fig. 5** Quenching of NO($v = 3$) by NO. The larger build-up of NO($v = 2$) relative to the NO($v = 3$)–O system shown in Fig. 4 is due mostly to the larger branching coefficient $\chi_{NO}(v = 3 \rightarrow 2)$.

by a set of equations very similar to those given in eqn. (I) and (II), except for the identity of the relaxing species. The NO($v = 2$)–NO system, however, follows a somewhat different scheme. Two relaxation pathways are possible, depending on whether the relaxation of an initially excited NO($v = 2$) molecule gives rise to a pair of NO($v = 1$) molecules through the efficient near-resonant vibration-to-vibration (V–V) energy-transfer process[31]

$$NO(v = 2) + NO(v = 0) \rightarrow NO(v = 1) + NO(v = 1) \quad (11a)$$

or to a single NO($v = 1$) molecule through a vibration-to-translation (V–T) process, generally assumed to be much
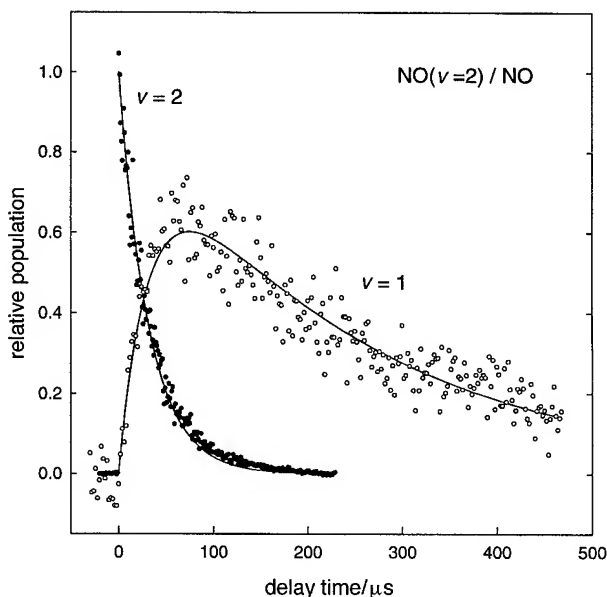


**Fig. 6** Quenching of NO($v = 2$) by NO. The NO($v = 1$) population build-up is substantial due to the large branching fraction $\chi_{NO}(v = 2 \rightarrow 1)$ (see text), and to the slow decay of NO($v = 1$), which is governed by the transport loss rate $r_T$ out of the detection laser field of view. The NO($v = 1$) background LIF signal is about twice that of the transient signal, and has been subtracted.

slower due to the large energy defect:

$$NO(v = 2) + NO(v = 0) \rightarrow NO(v = 1) + NO(v = 0) \quad (11b)$$

Either reaction would be followed by the slow quenching of NO($v = 1$),

$$NO(v = 1) + NO \rightarrow NO(v = 0) + NO \quad (12)$$
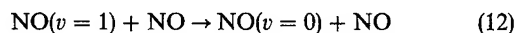
with $k_{NO}(v = 1) = 7 \times 10^{-14}$ cm$^3$ s$^{-1}$, or *ca.* 700 s$^{-1}$ under the present conditions. Reactions (11) and (12) were modelled *viz.*

$$\frac{d[NO(v = 2)]}{dt} = -[NO(v = 2)]\{r_T + k_{NO}(v = 2)[NO]\} \quad (III)$$

$$\frac{d[NO(v = 1)]}{dt} = -[NO(v = 1)]\{r_T + k_{NO}(v = 1)[NO]\}$$
$$+ [NO(v = 2)]\{\chi_{NO}(v = 2 \rightarrow 1)k_{NO}(v = 2)[NO]\} \quad (IV)$$

In eqn. (III) and (IV), $k_{NO}(v = 1, 2)$ are the appropriate disappearance rate constants, and $\chi_{NO}(v = 2 \rightarrow 1)$ is the observed fractional population of NO($v = 1$) upon decay of NO($v = 2$). Since the observed decay rate of product NO($v = 1$) is dominated by transport loss, $r_T$ can be determined directly through least-squares fitting. In this case accounting for transport loss increased the best-fit $\chi_{NO}$ value by *ca.* 40%.

Eqn. (I) and (II) were used to model the population time evolution in the NO($v = 3$)–O and NO($v = 3$)–NO systems, and eqn. (III) and (IV) in the NO($v = 2$)–NO system. In each case the appropriate differential equations were numerically integrated using trial kinetic parameters to generate a solution against which the data could be compared. A non-linear least-squares fitting routine was used to determine the best fit through the automatic adjustment of the kinetic parameters. In general, a total of four parameters was allowed to vary in the fits: the decay rates $k_M(v)[M]$ for the upper and lower $v$ level populations, the branching coefficient $\chi_M(v \rightarrow v - 1)$, and an arbitrary scaling parameter. While not the object of this study, the best-fit NO($v$) decay rates were found to be consistent with previous measurements[11,15,25,29] and are reported below. For O-atom quenching the decay constant $k_O(v = 2)[O]$ could not be accurately determined due to poor S/N. Instead, $k_O(v = 2)$ was held equal to $k_O(v = 3)$, consistent with the published values in Dodd *et al.*[15] Also, for NO($v = 2$) relaxation the decay of NO($v = 1$) is dominated by transport loss, as described above.

## 4 Results and Discussion

The least-squares fitting results were averaged to yield the branching fractions $\chi$ shown in Tables 1 and 2. The scatter in the best-fit $\chi$ values gave rise to standard deviations of 5–10% for relaxation by NO, and *ca.* 20% for relaxation by O atoms. The error bars quoted in Tables 1 and 2 include these errors, with an additional 25% of the best-fit result added in quadrature to account for the estimated systematic error in the

**Table 1** Branching fractions $\chi_O(v \rightarrow v - 1)$ for relaxation of NO($v$) by O[a]

| $v = 2 \rightarrow 1$ | $v = 3 \rightarrow 2$ | ref. |
|---|---|---|
| | $0.35 \pm 0.12$ | present work, decay rates varied |
| | $0.35 \pm 0.12$ | present work, decay rates fixed |
| 0.37 | | Quack and Troe[18] |
| 0.43 | 0.29 | Duff and Sharma[20] |

[a] Values of $\chi_O$ from the present work were obtained either by allowing the NO($v$) decay rates to vary in the fit, or by fixing them using known parameters. See text for discussion.

**Table 2** Branching fractions $\chi_{NO}(v \to v - 1)$ for relaxation of NO($v$) by NO[a]

| $v = 2 \to 1$ | $v = 3 \to 2$ | ref. |
|---|---|---|
| $1.19 \pm 0.31$[b] | $0.73 \pm 0.19$ | present work, decay rates varied |
| $1.11 \pm 0.30$[b] | $0.74 \pm 0.19$ | present work, decay rates fixed |

[a] Values of $\chi_{NO}$ from the present work were obtained either by allowing the NO($v$) decay rates to vary in the fit, or by fixing them using known parameters. See text for discussion. [b] Observed fractional population of $v = 1$, for which the interpretation depends on an assumption regarding the reaction mechanism. See text for discussion.

experiment. The non-linear least-squares fits used to determine the branching fractions $\chi$ were also performed by fixing the NO($v = 2, 3$) decay rates using the known O and NO number densities and the rate constants measured by Dodd *et al.*[15] The resultant branching fractions are also given in Tables 1 and 2, and are seen to be in excellent agreement with the $\chi$ values obtained when the rates are adjusted in the fit. This agreement is consistent with the good agreement between the best-fit rate constants $k_M(v = 2, 3)$ obtained in the present work and those obtained previously.[15] The rate constant results are discussed below, with the best-fit $k_{NO}(v = 2, 3)$ from the present work given in Table 3.

### NO($v = 3$)–O

In Table 1, the measured branching fraction $\chi_O(v = 3 \to 2) = 0.35 \pm 0.12$ is seen to be in good agreement with the prediction of 0.29 made by the recent quasiclassical trajectory calculation of Duff and Sharma[20] (DS). A second calculation highlighted in Table 1 is taken from the statistical adiabatic channel model of Quack and Troe[18] (QT), which was originally developed to model the rates of unimolecular dissociation. The latter model calculates the rate of dissociation of a strongly bound 'activated complex', taking into account the coupling of initial and final state angular momenta. It is ideally suited for the NO($v$)–O system, given the 3 eV binding energy available to an $NO_2^*$ intermediate.

The QT and DS calculations both predict NO final vibrational state $v_f$ population distributions that are approximately independent of $v_f$. For the initially populated level $v_i = 2$, both models predict final state populations that are weighted slightly toward $v_f = 0$ (Table 1). The DS study predicts that for higher $v_i$ levels this proclivity toward low-$v$ final states disappears, and that the final state populations are divided equally among the levels $v_f < v_i$. This distribution is consistent with a long-lived $NO_2^*$ intermediate [reaction (4)], as are the large relaxation rate coefficients.[11]

QT predict from first principles a room-temperature $k_O(v = 2)$ value which is in good agreement with that recently measured by Dodd *et al.*[15] It is likely, however, that the QT calculation underestimates the actual rate constant, since it considers only one of the two attractive potential-energy surfaces that arise in the interaction of ground-state NO and O. The DS trajectory calculation uses both attractive $(1\,^2A' + 1\,^2A'')$ surfaces, resulting in a $k_O(v = 2)$ value which is *ca.* 50% higher than the QT result, and *ca.* 30–40% higher

**Table 3** Rate constants $k_{NO}(v)$ for the relaxation of NO($v = 2, 3$) by NO at *ca.* 295 K (units of $10^{-12}$ cm$^3$ s$^{-1}$)[a]

| $v = 2$ | $v = 3$ | ref. |
|---|---|---|
| $2.7 \pm 0.5$ | $3.4 \pm 0.7$ | present work |
| $3.2 \pm 0.3$ | $4.0 \pm 0.3$ | Dodd *et al.*[15] |
| $2.72 \pm 0.15$[a] | $3.26 \pm 0.24$ | Wysong[11,29] |
| $2.44 \pm 0.3$ | $2.22 \pm 0.2$ | Islam *et al.*[25] |

[a] The measured value of $k_{NO}(v = 2)$ (ref. 11) was listed incorrectly in Table 2 of ref. 15, and is given correctly here.

than the empirical result.[15] However, the DS paper points out the complexity inherent in a system with a total of 18 adiabatic doubly degenerate electronic states. The only existing *ab initio* calculation of the O($^3P$) + NO(X $^2\Pi$) potential-energy surfaces does not include the effects of non-adiabatic coupling.[32] Clearly more effort is needed in both the experimental and theoretical areas in order to resolve the discrepancies and further understanding of the NO($v$)–O system.

There exist at least two worthwhile extensions to the experiments described herein. First, it would be useful to measure the temperature dependence of the branching fractions in the 500–1200 K range, *i.e.* for thermospheric temperatures, albeit these measurements may be difficult using the present apparatus due to the increased ambient population of excited $v$ levels and the resultant LIF background. Alternatively, a photolytic source of NO($v$) such as $NO_2$[30] could be employed in order to mitigate the background NO signal. Some temperature-dependent rate coefficients for NO($v = 2, 3$) relaxation by NO and other stable species have been measured,[11,25] though it is difficult to predict the effect of temperature on the NO($v_i \to v_f$) branching fractions in the absence of detailed experimental or theoretical information. The NO($v$)–O system in particular is lacking in information.

A second extension is suggested by the observations of Lipson *et al.*[33] and Sharma *et al.*,[34] who independently derived steady-state NO($v = 1$) spin–orbit populations from high-resolution earthlimb IR emission data. The spin–orbit populations were found to depart strongly from local thermodynamic equilibrium, favouring the lower $F_1$ component. Effective spin–orbit temperatures of *ca.* 200 K at higher altitudes were derived,[33,34] in contrast to the kinetic temperature of *ca.* 900 K inferred from the NO($v = 1$) rotational distribution observed simultaneously. It has been proposed[33] that the subthermal spin–orbit distribution results from selective formation of the $v = 1$ $F_1$ spin–orbit level in uppumping collisions of NO($v = 0$) with O. Thus, measurements of the spin–orbit dependence of NO($v$) relaxation rate constants would be valuable, as well as measurements of NO($v = 1$, $\Omega$) final state propensities in the uppumping of NO($v = 0$) by O. These experiments may require a molecular beam apparatus instead of the cell arrangement used here, due to the efficiency with which collider species (*e.g.* He and Ar) interconvert the NO spin–orbit components.[27]

### NO($v = 3$)–NO

The branching fraction $\chi_{NO}(v = 3 \to 2) = 0.73 \pm 0.19$ listed in Table 2 is significantly lower than the value of unity predicted assuming a single-quantum relaxation mechanism, but instead indicates some degree of multiquantum behaviour. It is generally accepted that NO vibrational self-relaxation proceeds *via* the resonant V–V transfer mechanism (13) for the lower $v$ levels:[25,35,36]

$$NO(v) + NO(0) \to NO(v - 1) + NO(1) \qquad (13)$$
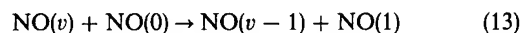
As $v$ increases reaction (13) gradually becomes more endothermic owing to a small degree of vibrational anharmonicity, *ca.* 28 cm$^{-1}$ per $v$ level, which slows the reaction. The reaction endothermicity exceeds the room-temperature $kT$ value at $v = 9$, and Yang *et al.*[36] have suggested that the V–V mechanism (13) is unimportant for $v \geqslant 8$. For $v \geqslant 13$ the $k_{NO}(v)$ values increase rapidly, which the authors attribute at least partially to the onset of multiquantum relaxation pathways. In one experiment, Yang *et al.* populated NO($v = 19$), then monitored NO($v = 17–19$) populations as a function of delay time in a manner very similar to the present work. They determined $\chi_{NO}(v = 19 \to 18) = 0.47$, $\chi_{NO}(19 \to 17) = 0.33$, and $\chi_{NO}(18 \to 17) = 0.48$,[36] consistent with a high degree of multiquantum behaviour.

## NO($v = 2$)–NO

The measured branching fraction $\chi_{NO}(v = 2 \to 1) = 1.19 \pm 0.31$ is also listed in Table 2. Unfortunately, the NO($v = 2$)–NO measurement performed here does not unambiguously identify the reaction mechanism. Such an identification requires determining (1) the relative contributions of single- and double-quantum relaxation, and (2) for the single-quantum component, the relative contributions of the V–V process (11a) and the V–T process (11b). Thus, the measured $\chi_{NO}(v = 2 \to 1)$ value is consistent with an effective single-quantum branching fraction of 0.5–1.0, depending on the contributions of (11a) and (11b) to the single-quantum component. We note, however, that all interpretations of $\chi_{NO}(v = 2 \to 1)$ are in disagreement with the expectation of a negligible V–T contribution to the overall disappearance rate.[36] Clearly a more definitive experiment could be used to determine the precise mechanism of the NO($v = 2$)–NO relaxation process. For instance, a small amount of admixed isotopically labelled NO* in unlabelled NO could be excited to $v = 2$, followed by observing the population time evolution of both NO*($v = 1$) and NO($v = 1$).

Wysong[11,29] performed semiquantitative measurements of the extent of single-quantum behaviour in NO($v = 2$) self-relaxation. The NO($v = 2$) population was excited *via* tunable IR laser excitation of ambient NO, using an apparatus very similar to that of the present work. Transient population of NO($v = 1$) was measured to be 'about twice' that of initially excited NO($v = 2$), consistent with the single-quantum V–V transfer mechanism governed by eqn. (13).

Stephenson[31] performed a landmark measurement of the rate constant for reaction (14a) by measuring the rate of appearance of NO($v = 2$):

$$NO(v = 1) + NO(v = 1) \to NO(v = 2) + NO(v = 0) \quad (14a)$$

$$NO(v = 2) + NO(v = 0) \to NO(v = 1) + NO(v = 1) \quad (14b)$$

As pointed out by Hopkins and Chen,[37] who pioneered the measurement technique and data interpretation in the analogous process in HCl($v$), the necessary simplification of the kinetic equations can lead to an overestimate of $k_{14a}$ by as much as 25%. The rate constant $k_{14a}$ can be related to $k_{14b}$ through detailed balance; at room temperature, $k_{18b} = 0.87k_{14a}$. Thus, assuming that reaction (14b) proceeds wholly as shown, measurements of the vibrational relaxation of $v = 2$ can be related to Stephenson's measurement. Subsequent determinations of the rate constant for reaction (14b) are lower than that derived from Stephenson's work by factors ranging from 1.3 to 2.4,[11,15,35,38,39] with the later, more reliable measurements[11,15,35] in good agreement with each other and with the Stephenson value, albeit just within the combined error bars.

It is important to note that despite the degree of effort in measuring the disappearance rates of NO($v$) in collisions with itself and with other species, we are unaware of any explicit measurements of the relaxation pathways aside from the NO($v = 19$) study of Yang *et al.*[36] The $v = 4$–8 region is particularly open to investigation at this juncture, although it is not easily accessible using either the stimulated emission pumping technique of Yang *et al.*, nor the IR pumping technique owing to rapidly decreasing $0$–$v'$ absorption coefficients. Yang *et al.*[36] predict that the relaxation proceeds *via* a single-quantum mechanism for $v$ levels as high as $v = 14$; this has not been experimentally verified.

### NO($v = 2, 3$) Disappearance rate constants

The best-fit NO($v = 2, 3$) decay rates can be combined with the known quencher species concentrations to determine relaxation rate constants. The rate constants result essentially from one- or two-point Stern–Volmer plots, and thus have

lower precision than the values measured previously in this laboratory;[15] here we quote *ca.* 20% error bars. Using the measured O-atom density of $1.8 \times 10^{15}$ cm$^{-3}$, the rate coefficient $k_O(v = 3)$ was determined to be $(3.0 \pm 0.6) \times 10^{-11}$ cm$^3$ s$^{-1}$. This result agrees well with the value of $(2.5 \pm 0.3) \times 10^{-11}$ cm$^3$ s$^{-1}$ reported by Dodd *et al.*,[15] in which NO($v = 2, 3$) time-dependent populations were detected using MPI, and the maximum O-atom density was much lower, *ca.* $0.5 \times 10^{15}$ cm$^{-3}$. Thus the current measurement provides a valuable corroboration of the previously measured $k_O(v = 2, 3)$.

For NO self-quenching, the relaxation rate constants were determined to be $k_{NO}(v = 2) = (2.7 \pm 0.5) \times 10^{-12}$ and $k_{NO}(v = 3) = (3.4 \pm 0.7) \times 10^{-12}$ cm$^3$ s$^{-1}$. The $k_{NO}(v = 2)$ value is average of $2.5 \times 10^{-12}$ and $2.9 \times 10^{-12}$ cm$^3$ s$^{-1}$ obtained from analyzing the decay of initially excited NO($v = 3$) and NO($v = 2$), respectively. The rate constants $k_{NO}(v = 2, 3)$ are compared in Table 3 with values measured using similar laser IR pump–UV probe experiments. The two sets of values are seen to be in general agreement with the exception of the Islam *et al.*[25] measurement of $k_{NO}(v = 3)$, which is about 40% lower than the mean of the other three values and outside the error bars of any of them. While the Islam *et al.* $k_{NO}(v = 2)$ measurement is also lower than the others, it is in good agreement with two of them and just outside the error bars of the third.

## 5 Summary

We have measured the fractional population of NO($v - 1$) arising from the collision-induced relaxation of NO($v = 3$) by O atoms and NO($v = 2, 3$) by NO. The branching fraction $\chi_O(v = 3 \to 2)$ is consistent with the existence of a long-lived NO$_2^*$ collision complex, and agrees well with the results of a recent quasiclassical trajectory study[20] of NO($v = 3$)–O-atom collisions on a calculated potential-energy surface. The $\chi_{NO}(v = 3 \to 2)$ value is significantly lower than the value of unity arising from a V–V, single-quantum relaxation mechanism, and suggests a multiquantum component. For NO($v = 2$) self-relaxation the $\chi_{NO}(v = 2 \to 1)$ value cannot be used to unambiguously assign the mechanism, owing to the possible, unknown contribution of resonant uppumping of NO($v = 0$) to NO($v = 1$) in the relaxation process. Both NO self-relaxation results imply a significant V–T component to the quenching process, contrary to the relatively low rate for NO($v = 1$) self-relaxation. Rate constants for the vibrational relaxation of NO($v = 3$) by O and NO($v = 2, 3$) by NO were obtained in the course of fitting for the branching fractions, and are consistent with previous results from this laboratory.

This work has the strongest application in improving the accuracy of auroral models, in which the NO production rate is greatly enhanced over the quiescent atmosphere. Auroral energy deposition is typically a maximum in an altitude region where the O-atom density is also high, *i.e.* in the lower thermosphere near 100 km. Thus, O atoms play a key role in determining the NO($v$) population distribution.[9] The recent measurements of NO($v \geqslant 2$) fundamental band radiance in the quiescent atmosphere[6,7] also point up the need for more accurate energy-transfer parameters for the NO($v$)–O system. Finally, the observation of subthermal NO spin–orbit distributions in the lower thermosphere[33,34] suggests the need for additional measurements and theory concerning final state propensities in NO($v, J, \Omega$) collisions with O atoms.

## References

1 C. A. Barth, *Planet. Space Sci.*, 1992, **40**, 315.

2 D. W. Rusch, J-C. Gerard and C. G. Fesen, *J. Geophys. Res.*, 1991, **96**, 11331.

3 J-C. Gerard, D. V. Bisikalo, V. I. Shematovich and J. W. Duff, *J. Geophys. Res.*, 1997, **102**, 285.

4 R. D. Sharma, V. A. Kharchenko, Y. Sun and A. Dalgarno, *J. Geophys. Res.*, 1996, **101**, 275.

5 W. T. Rawlins, M. E. Fraser and S. M. Miller, *J. Phys. Chem.*, 1989, **93**, 1097.

6 P. S. Armstrong, S. J. Lipson, J. A. Dodd, J. R. Lowell, W. A. M. Blumberg and R. M. Nadile, *Geophys. Res. Lett.*, 1994, **21**, 2425.

7 R. D. Sharma, H. Dothe, F. von Esse, V. A. Kharchenko, Y. Sun and A. Dalgarno, *J. Geophys. Res.*, 1996, **101**, 19707.

8 P. S. Armstrong, J. A. Dodd, S. J. Lipson, W. A. M. Blumberg, R. B. Lockwood, J. R. Lowell, R. M. Nadile, D. E. Paulsen, R. E. Murphy, W. T. Rawlins, M. E. Fraser and B. D. Green, *Eos Trans. AGU*, 1995, **76**, F439.

9 G. E. Caledonia and J. P. Kennealy, *Planet. Space Sci.*, 1982, **30**, 1043.

10 T. C. Degges, *Appl. Opt.*, 1971, **10**, 1856.

11 I. J. Wysong, *J. Chem. Phys.*, 1994, **101**, 2800.

12 R. E. Murphy, E. T. P. Lee and A. M. Hart, *J. Chem. Phys.*, 1975, **63**, 2919.

13 B. D. Green, G. E. Caledonia, R. E. Murphy and F. X. Robert, *J. Chem. Phys.*, 1982, **76**, 2441.

14 R. P. Fernando and I. W. M. Smith, *Chem. Phys. Lett.*, 1979, **66**, 218.

15 J. A. Dodd, S. M. Singleton, S. M. Miller, P. S. Armstrong and W. A. M. Blumberg, *Chem. Phys. Lett.*, 1996, **260**, 103.

16 K. Glanzer and J. Troe, *J. Chem. Phys.*, 1975, **63**, 4352.

17 D. V. Shalashilin, A. V. Michtchenko, S. Ya. Umanskii and Yu. M. Gershenzon, *J. Phys. Chem.*, 1995, **99**, 11627.

18 M. Quack and J. Troe, *Ber. Bunsen-Ges. Phys. Chem.*, 1975, **79**, 170.

19 M. Quack and J. Troe, *Ber. Bunsen-Ges. Phys. Chem.*, 1977, **81**, 160.

20 J. W. Duff and R. D. Sharma, *J. Chem. Soc., Faraday Trans.*, 1997, **93**, 2645.

21 W. B. DeMore, S. P. Sander, C. J. Howard, A. R. Ravishankara, D. M. Golden, C. E. Kolb, R. F. Hampson, M. J. Kurylo and M. J. Molina, *Chemical Kinetics and Photochemical Data for Use in Stratospheric Modeling, Eval. No. 11*, 1994, JPL Publ. 94-26.

22 L. T. Earls, *Phys. Rev.*, 1935, **48**, 423.

23 R. W. Nicholls, *J. Res. Nat. Bur. Stand.*, 1964, **68A**, 535.

24 R. P. Fernando and I. W. M. Smith, *J. Chem. Soc., Faraday Trans. 2*, 1979, **75**, 1064.

25 M. Islam, I. W. M. Smith and J. W. Wiebrecht, *J. Phys. Chem.*, 1994, **98**, 9285.

26 Aa. S. Sudbo and M. M. Loy, *J. Chem. Phys.*, 1982, **76**, 3646.

27 M. Islam, I. W. M. Smith and J. W. Wiebrecht, *J. Phys. Chem.*, 1995, **103**, 9676.

28 S. Saupe, I. Adamovich, M. J. Grassi, J. W. Rich and R. C. Bergman, *Chem. Phys.*, 1993, **174**, 219.

29 I. J. Wysong, *Chem. Phys. Lett.*, 1994, **227**, 69.

30 I. W. M. Smith, R. P. Tuckett and C. J. Whitham, *Chem. Phys. Lett.*, 1992, **200**, 615.

31 J. C. Stephenson, *J. Chem. Phys.*, 1973, **59**, 1523.

32 H. Katagiri and S. Kato, *J. Chem. Phys.*, 1993, **99**, 8805.

33 S. J. Lipson, P. S. Armstrong, J. A. Dodd, J. R. Lowell, W. A. M. Blumberg and R. M. Nadile, *Geophys. Res. Lett.*, 1994, **21**, 2421.

34 R. D. Sharma, H. Dothe and F. von Esse, *J. Geophys. Res.*, 1996, **101**, 17129.

35 M. J. Frost, M. Islam and I. W. M. Smith, *Can. J. Chem.*, 1994, **72**, 606.

36 X. Yang, E. H. Kim and A. M. Wodtke, *J. Chem. Phys.*, 1992, **96**, 5111.

37 B. J. Hopkins and H-L. Chen, *J. Chem. Phys.*, 1972, **57**, 3816.

38 H. Horiguchi and S. Tsuchiya, *Jpn. J. Appl. Phys.*, 1979, **18**, 1207.

39 R. G. Macdonald and F. C. Sopchyshyn, *Chem. Phys.*, 1985, **94**, 455.

*Paper 7/01534H; Received 4th March, 1997*

# Rotational relaxation of high-N states of OH (X²Π, v=1-3) by O₂

K.W. Holtzclaw, B.L. Upschulte, G.E. Caledonia, J.F. Cronin, and B.D. Green

Physical Sciences Inc., Andover, Massachusetts

S.J. Lipson and W.A.M. Blumberg

Phillips Laboratory, Hanscom Air Force Base, Massachusetts

J.A. Dodd

Stewart Radiance Laboratory, Bedford, Massachusetts

**Abstract.** We have studied the relaxation of OH(X²Π, v, N) produced by the reaction O($^1D$) + H₂ → OH$^*$ + H. Infrared emission measurements of the fundamental vibration-rotation band of OH were acquired at a temperature of 100 K in a large cryogenic chamber. Trace amounts of ozone were added to mixtures of H₂, O₂, and Ar at low (≤38 mT) pressures. The ozone was photolyzed to produce O($^1D$). Rapid reaction with H₂ produced OH$^*$. Spectrally and temporally resolved emissions from levels up to the exothermic limit were observed with sufficient spectral resolution to permit kinetic analysis of individual level populations. The production rate was observed to scale as the rotational quantum number except at the highest levels populated. At early times we observed inverted rotational state distributions that subsequently relaxed to form thermal distributions in each vibrational level. Under these conditions, rotational relaxation was rapid in comparison with vibrational relaxation. Rotational relaxation within a given vibrational state could be represented by single quantum collisional exchange at near-gas-kinetic rates. The rotational level dependence of the deduced relaxation was determined.

## Introduction

Hydroxyl population distributions have been used to quantify mesospheric temperatures, reactive species concentrations [*Llewellyn et al.*, 1978], and the altitude dependence of OH concentrations [*McDade*, 1991]. The atmospheric kinetic temperatures are based on measurement of the OH rotational temperature inferred from OH rotational distributions. For lower rotational states, Boltzmann distributions at temperatures characteristic of the mesosphere [*Turnbull and Lowe*, 1983; *Sivgee and Hamwey*, 1987] have been observed. More recent observations, however, have demonstrated that higher rotational states are not in thermal equilibrium. *Pendleton et al.* [1989] observed rotational distributions in v' = 7 that were characterized by effective temperatures of 200 K for N = 2 to 5 but 1900 K for N ≥ 6.

Orbital observations of long-wavelength infrared radiances from the upper atmosphere nighttime airglow [*Smith et al.*, 1992; *Dodd et al.*, 1994] display pure rotational emission from high-lying rotational-vibrational states of OH. In the airglow, rotational levels up to N = 33 for vibrational levels v=0-3 were observed, suggesting that these levels are not easily relaxed at pressures characteristic of the airglow altitude. Knowledge of the nature and magnitude of collisional relaxation processes occurring in the mesopause region (85 to 95 km) is essential to relate the observed distributions to the aeronomic production process(es).

We have investigated the nature of the relaxation mechanisms operating in highly rotationally excited OH under controlled laboratory conditions at 100 K. Several groups have studied vibrational relaxation of OH (produced from the reaction of H + O₃) by atmospheric species [*Knutsen et al.*, 1996; *Dodd et al.*, 1991]. To understand OH produced with substantial rotational excitation, we chose to study rotational relaxation rates for high rotational states of OH produced in the reaction

$$O(^1D) + H_2 \rightarrow OH(v \leq 4) + H \qquad \Delta H = -188 \text{ kJ/mole.} \qquad (1)$$

This reaction has sufficient exothermicity to populate states up to (v,N) of (0,29), (1,26), (2,22), (3,17), and (4,10). Relaxation studies of similar molecules such as HF have provided evidence of slow relaxation rates for high rotational states of molecules with large rotational spacings. *Taatjes and Leone* [1988] measured rotational relaxation rate coefficients for HF(v = 0, J = 13) in the $10^{-12}$ cm³ molecule$^{-1}$ s$^{-1}$ range for room temperature quenching by rare gas species. Because the rotational spacings are significant (ΔE = 550 cm$^{-1}$), models for vibrational relaxation were successfully used to explain the results. We report here the observation of large rotational relaxation rates for the OH molecule with an O₂ collision partner.

## Experimental Method

The experiments were performed in the LABCEDE chamber at the Phillips Laboratory Geophysics Directorate. The apparatus is shown in Figure 1. Controlled gas mixtures were introduced through a porous array to produce a plug flow inside a temperature-controlled shroud 90 cm in diameter and 270 cm long. For these experiments the shroud walls were maintained near 100 K to reduce infrared backgrounds and slow diffusion out of the reaction volume. Optical ports viewing across the plug flow permitted optical access. Ozone was photolyzed to produce O($^1D$) using a KrF excimer laser at 248 nm. The OH chemiluminescence was observed by an InSb
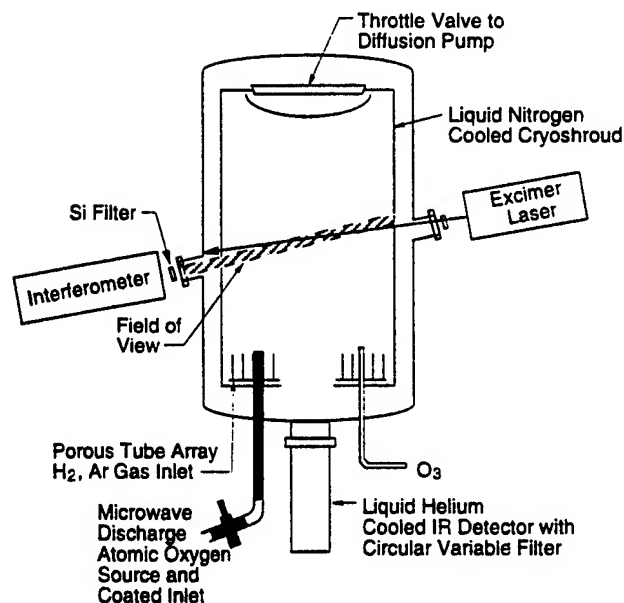
**Figure 1.** Cryogenic LABCEDE apparatus with excimer photolysis laser, gas inlets, ozone generator, and Michelson interferometer detection system.

detector viewing the photolysis region through a Michelson interferometer. The optical axis of the interferometer was aligned with the photolysis region to maximize signal collection. An antireflection coated Si blocking filter prevented the intense laser and plasma tube radiation from affecting the IR detector. Absorption of 248 nm radiation by $O_3$ was in the optically thin limit ($\sigma Nl < 0.1$); hence $O(^1D)$ was produced uniformly along the laser beam path.

Gas mixtures of Ar, $H_2$, and $O_2$ with a trace of $O_3$ were used for these experiments. All stable gases were ultrahigh-purity grade. Argon was the dominant gas (27 mT), with hydrogen added at 9 mT. The Ar buffer gas inhibits diffusion, confining the $O(^1D)$ reactant and OH product to the detector field of view but not contributing significantly to the OH rotational relaxation. This procedure simplifies the kinetic interpretation of the data while improving the signal-to-noise ratio. The $H_2$ density was chosen to complete OH production on a timescale much faster than its relaxation. Higher concentrations of $H_2$ were not used so as to prevent its contributing significantly to the observed total OH relaxation. The $O_2$ pressure was varied between 1.3 and 2.6 mT to isolate its contribution to the relaxation rate. Except for $O_3$, all gases were precooled to 100 K before entering the chamber through a porous tube array. Total pressures for these experiments were 38 mtorr with Ar the dominant gas.

Ozone was generated each day with a commercial ozonator and stored in a silica gel trap cooled to -78 C. Ozone was introduced directly into the chamber through a room temperature Teflon inlet tube. Its concentration was monitored by UV absorption prior to entering the chamber and held constant by adjusting the $O_3$ trap temperature. Sufficient molecular collisions occurred between the gas inlet and the reaction zone to thermally equilibrate the $O_3$ at 100 K. The $O_3$ partial pressure at the photolysis region, < 0.3 mtorr, was far below the limiting vapor pressure of $O_3$ at these temperatures.
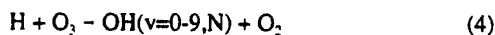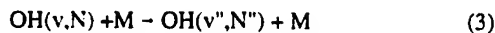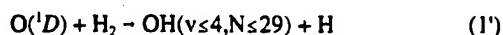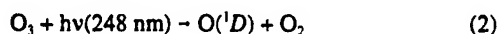
The principal reactions are

$$O_3 + h\nu(248\ nm) \rightarrow O(^1D) + O_2 \qquad (2)$$

$$O(^1D) + H_2 \rightarrow OH(v \leq 4, N \leq 29) + H \qquad (1')$$

$$OH(v,N) + M \rightarrow OH(v'',N'') + M \qquad (3)$$

$$H + O_3 \rightarrow OH(v=0-9,N) + O_2 \qquad (4)$$

The timescales for the experiment were as follows: a laser photolysis pulse of 20 ns initiated the experiment, the $O(^1D)$ reacted to form OH in 30 μs, and the OH relaxed rotationally over several hundred μs. The next laser pulse occurred 59 ms later, after diffusion had replaced the gas in the photolysis volume. Reaction (4), involving the interaction of two trace species in a relatively inefficient chemical process, does not significantly impact the experimental results.

The time dependent fluorescence signal on the InSb detector from each laser pulse was recorded at 5 μs intervals. The detection system response time was also about 5 μs. The interferometer was scanned at 1 s per HeNe reference laser fringe. The fluorescence signals from multiple (≈17) laser pulses occurred between adjacent fringes of the reference laser and could be averaged. An interferogram was accumulated from the time dependent fluorescence due to sequential sets of laser pulses at 3000 different mirror positions (path differences). Each experiment lasted nearly 1 hour and contained 50,000 laser pulses. The fluorescent signal typically remained constant to better than 3% over this period. The resulting time histories as a function of mirror position were sorted to generate interferograms as a function of time and then were transformed to produce complete spectra (1850 to 7900 cm$^{-1}$), monitoring the reaction progress at 5 μs intervals. This approach has been described previously for electron beam excitation [*Dodd et al.*, 1991; *Green et al.*, 1982]. For the current experiments the data acquisition is synchronized to the laser trigger pulse.

Although OH has widely separated rotational lines, many states are populated in the exothermic reaction, and the observed spectrum is quite complex. Thus the interferometer was carefully aligned prior to measurements to achieve close to its theoretical maximum spectral resolution of 6 cm$^{-1}$ (based on scan distance and detector size). This resolution was adequate to permit most OH(v,N) lines to be isolated and their time history to be measured. The data were transformed by using triangular apodization to minimize spectral ringing. At this resolution, individual P and R branch lines (as well as spin sublevels for $N \leq 6$) from each vibration and rotational level created could be resolved. Overlaps of the different transitions were significant, but the ability to use the pair of P,R branch intensity ratios dictated by Einstein coefficients [*Holtzclaw et al.*, 1993] permitted most level populations to be determined through spectral fitting.

Spectral data at several times after the laser photolysis that were acquired by this process are shown in Figures 2a-2c. In Figure 2a, taken at 30 μs after laser pulse, the OH(v,N) production by $O(^1D)$ is nearly complete. Little relaxation has occurred, and fluorescence from levels near the exothermic limit is observed. The prominent sharp features at 3760 and 3960 cm$^{-1}$ are the v = 2 and v = 1 R branch rovibrational bandheads composed of emission from levels N = 18 through 22. As production stops, the highest rotational level populations begin to relax rapidly. In Figure 2b the v = 2 bandhead has disappeared, and rotational distribution is relaxed to lower N (shifting of the intensity of the P and R branch lines toward band center). In Figure 2c the late time spectrum at 1000 μs is displayed. The spectrum is much simpler; only rotational levels up to N = 4 are observed.

To permit quantitative analysis, we employed a spectral fitting procedure. The relative population in each rovibrational level was determined by the linear solution vector that minimized the least squares difference between the computed and observed spectra. The rotational population in each vibrational level is determined by best matching its observed P and R branch intensities to the experimental
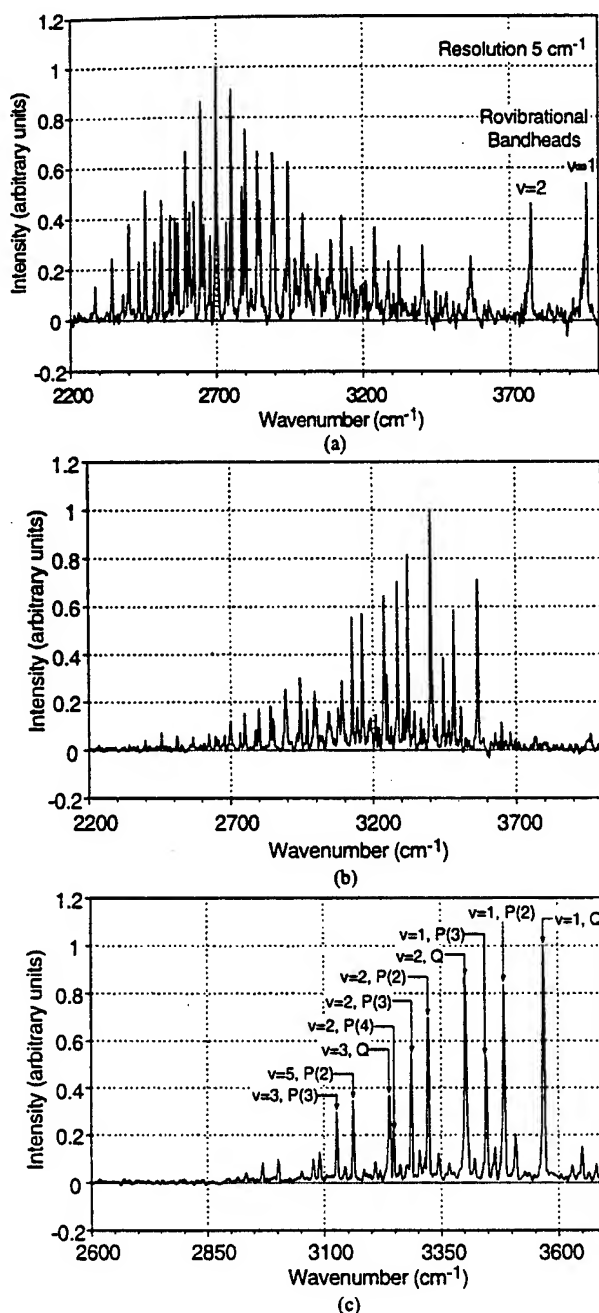
**Figure 2.** Spectrally resolved fluorescence from OH(v,N) transitions at various delays after the photolysis pulse (individual peaks are labeled by the upper state rotational and vibrational quantum number): (a) 30 μs after the pulse near the end of the production period, (b) at 110 μs while relaxation is cooling the distribution, and (c) at 1000 μs.



**Figure 3.** Comparison of observed fluorescence (solid line) with the synthetic spectral fit (dashed line).

coefficients [*Holtzclaw et al.*, 1993] and the detection system response function. The time dependence of these population histories deduced from these fits provides the basis for the kinetic analysis provided in the next section.

## Data Analysis

For purposes of discussion we will consider a data set taken at conditions of 38 mtorr and a nominal temperature of 100 K. The relative species concentrations were Ar, $2.5 \times 10^{15}$ cm⁻³; $H_2$, $8 \times 10^{14}$ cm⁻³; $O_2$, $2.5 \times 10^{14}$ cm⁻³; and $O_3$, $< 3 \times 10^{13}$ cm⁻³.

From the fitting procedure described in the previous section, rotational population relaxation histories for v = 1 to 4 were determined (the data are relatively noisy for v = 4). In other data sets the Ar concentration was reduced by a factor of 2 with no significant change in the relaxation behavior. Although the $H_2$ concentration was not changed, we found that the observed relaxation times increased by a factor of 2 when the $O_2$ concentration was reduced by a factor of 2. We concluded then that oxygen molecules provide the dominant source of collisional relaxation in this gas mix. On the basis of these observations we conclude that rotational relaxation by $H_2$ is at least an order of magnitude less efficient than that by $O_2$.

data at each time interval after the photolysis pulse. The 2600 to 3200 cm⁻¹ portion of an example fluorescence spectrum is shown in Figure 3 along with the synthetic spectral fit. The comparison is seen to be excellent, with the line positions accurately matching the observed features and the intensities agreeing to within a few percent. The high-N rotational P and R branch lines are widely separated; e.g., for v = 1, N = 25 the R branch transition occurs at 3937.9 cm⁻¹, while the corresponding P branch transition occurs at 2282.8 cm⁻¹, a 1655 cm⁻¹ separation. For isolated lines, good agreement is observed, indicating accurate knowledge of the Einstein



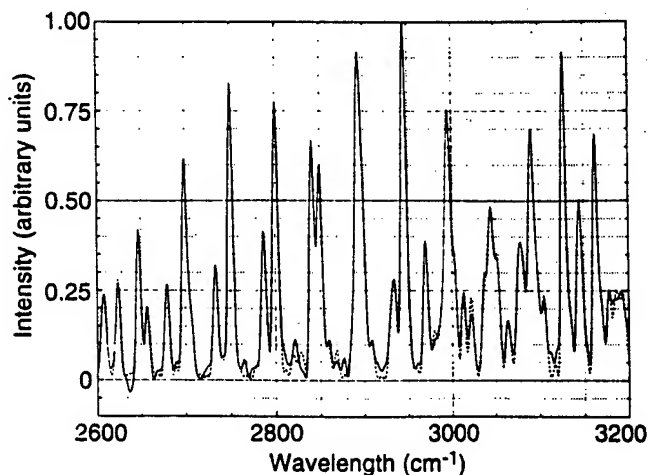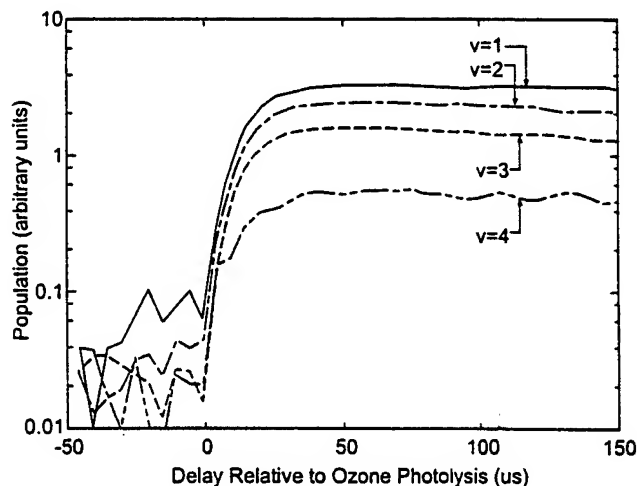**Figure 4.** Deduced OH vibrational populations versus time $N_{O_2} = 2.5 \times 10^{14}$ cm⁻³, $N_{H_2} = 8 \times 10^{14}$ cm⁻³, and $N_{AR} = 2.5 \times 10^{15}$ cm⁻³.

**Table 1.** Relative Populations of OH(v)

| Vibrational Level | Relative Population | | | | | |
|---|---|---|---|---|---|---|
| | Present Work | Butler et al. [1983] | Huang et al. [1986] | Aker and Sloan [1986] | Kuntz et al. [1991] | Berg et al. [1991] |
| 1 | 1 | 1 | 1 | 1 | 1 | 1 |
| 2 | 0.75 ± 0.04 | 1.11 ± 0.19 | 0.92 ± 0.06 | 1.10 ± 0.20 | 0.63 | 0.67 |
| 3 | 0.48 ± 0.03 | 1.08 ± 0.19 | 0.87 ± 0.14 | 0.86 ± 0.20 | 0.35 | 0.42 |
| 4 | 0.16 ± .01 | 0.62 ± 0.19 | < 0.77 | 0.45 ± 0.20 | 0.17 | 0.19 |

Argon-induced rotational relaxation is at least 2 orders of magnitude less efficient than relaxation by $O_2$.

The observed vibrational population history, i.e., summed over all rotational levels, is shown in Figure 4. As can be seen, the populations rise after $O_3$ photolysis, reflecting OH(v) production via reaction (1). The vibrational populations flatten out as the $O(^1D)$ is depleted through reaction (1). The characteristic e-fold rise time observed is ~12 μs, corresponding to a rate constant for reaction (1) of $1.1 \times 10^{-10}$ cm³ s⁻¹. This value is in reasonable agreement with the recommended value $1.2 \times 10^{-10}$ cm³ s⁻¹ from earlier measurements made at temperatures of 200 K and above; see the review of Atkinson et al. [1992].

Note from Figure 4 that no significant vibrational relaxation is observed in the first 150 μs after $O_3$ photolysis. As will be shown, rotational relaxation is largely complete on that timescale. Thus vibrational and rotational relaxation can be treated separately. Indeed, vibrational relaxation under these conditions is found to be quite slow with a characteristic time of ≥600 μs. This observation is not surprising given earlier measurements, e.g., those of Dodd et al. [1991] among others, of OH vibrational relaxation by $O_2$, which show that the characteristic relaxation time for vibrational levels of OH (v≤4) would exceed 1000 μs under our experimental conditions. Since excited state diffusion out of the field of view is also important on this timescale ($\tau_D$ is estimated to be 900 μs), we were not able to evaluate the vibrational level dependent relaxation rate constants.

One additional interesting feature in Figure 4 is the relative vibrational populations. Since vibrational relaxation is unimportant on this timescale, these populations directly reflect the relative production efficiencies of reaction (1) for OH formation in specific vibrational levels. These relative production efficiencies are listed in Table 1. The listed values are the average of four sets of measurements, all at 100 K (two sets for v=3,4), but with varying total pressures and mixture ratios. The standard deviations shown are statistical. We estimate that systematic errors should introduce an additional uncertainty of less than 15%.

The database on reaction efficiencies for reaction (1) was recently reviewed by Mikulecky and Gericke [1992]. Other infrared chemiluminescence measurements [Butler et al., 1983; Huang et al., 1986; Aker and Sloan, 1986] of the reaction efficiencies performed at room temperature are also shown in Table 1. Note that our measurements, which were performed at 100 K, exhibit noticeably less vibrational excitation than these earlier data. There is still some uncertainty in this database, since several laser-induced fluorescence studies on adjacent vibrational levels show population ratios different from those observed in these earlier infrared measurements reported above [see Mikulecky and Gericke, 1992]. Furthermore, recent theoretical evaluations for 300 K [Kuntz et al., 1991; Berg et al., 1991] shown in Table 1 are more in accord with our observations than with these earlier studies.

We now address the rotational relaxation of the OH(X²Π) state. An example set of rotational population histories for v = 1, N = 1 to 25, arbitrarily normalized, is shown in Figures 5 to 9. Data of similar quality pertain for v = 2,3. Only a few rotational levels are available at v = 4, and the signal to noise ratio of these data is too low to permit rotational relaxation analysis for this level.

It can be seen from the early time behavior of these data that the highest rotational levels are populated largely by reaction (1), reaching a peak density when the $O(^1D)$ state is consumed, and then relaxing thereafter. The lowest levels, on the other hand, reach peak concentrations at longer times and are populated dominantly by relaxation from the higher states. This observation is borne out in Figure 10, which contrasts the time history of the sum of the populations for N = 7 to 27 with that for the lower levels N = 1 to 6. An important point to note is that the total rotational population
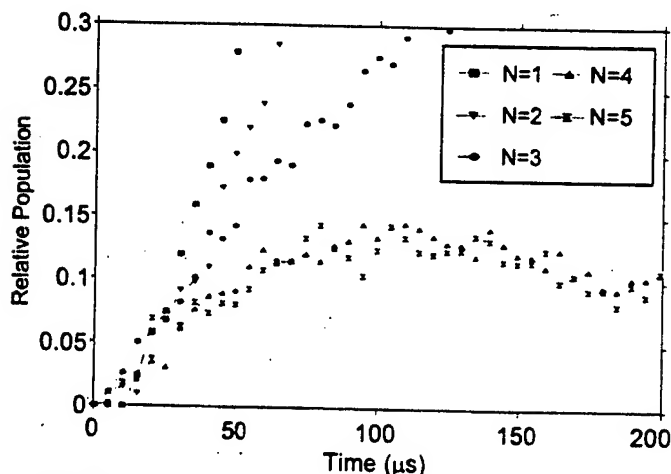


**Figure 5.** Deduced rotational population histories v = 1, N = 1-5.
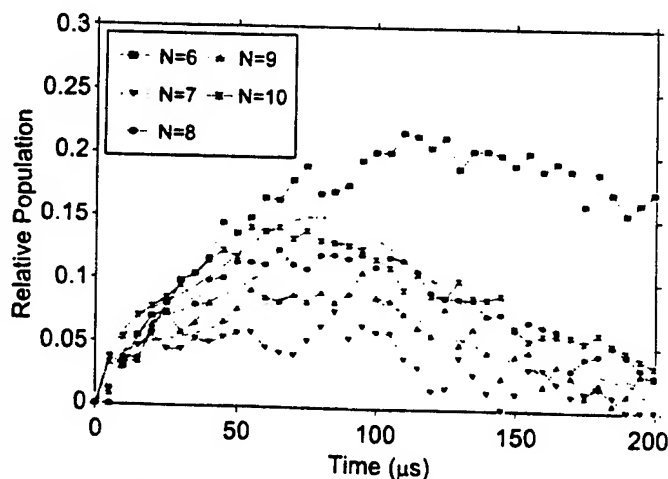


**Figure 6.** Deduced rotational population histories v = 1, N=6-10. Dashed lines are model comparisons for N=8-10.

**Figure 7.** Deduced rotational population histories v = 1, N=11-15. Dashed lines are model comparisons.
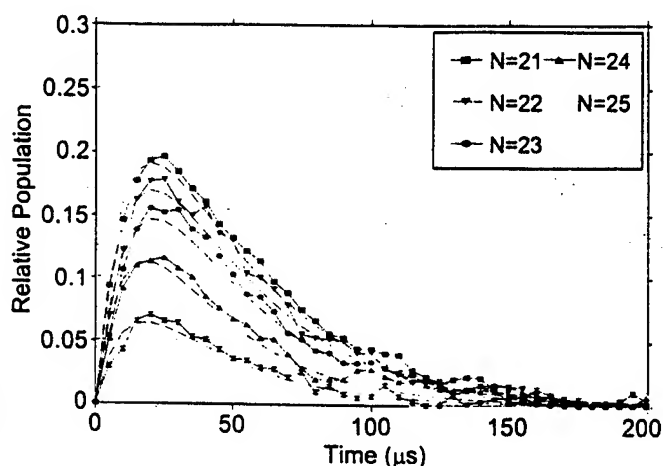


**Figure 9.** Deduced rotational population histories v = 1, N=21-25. Dashed lines are model comparisons.
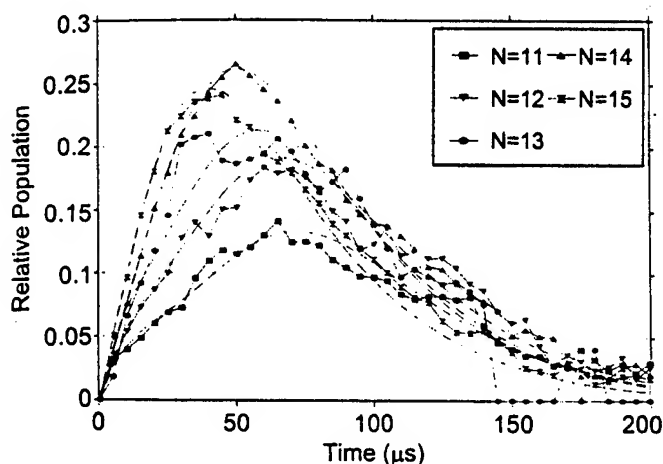
decreases by less than 10% as the distribution relaxes from high to low rotational levels; for example, in Figure 10 it can be seen that the sum of the populations at, say, a time of 50 μs is nearly the same as that at 150 μs. The same is true for all three vibrational levels analyzed, a strong suggestion that the observed rotational relaxation occurs in the absence of vibrational exchange.

Last, at longer times, we found that the population of the lowest levels corresponds to that of a Boltzmann distribution with a rotational temperature of 100 K, consistent with the translational temperature of the experiment. Thus we conclude that the observed rotational relaxation is consistent with a rotational cascade from high levels to low levels. We have analyzed the data assuming single-quantum transitions. The corresponding master equations are, for each vibrational level,

$$d[OH(N)]dt = k_p(N) [O(^1D)] [H_2] + k_r (N + 1)$$

$$\bullet [OH(N+1)] [O_2] - k_r(N) \bullet [OH(N)] [O_2]$$

$$+ k_r(N) [OH(N-1)] [O_2] e^{-\Delta E_{N,N-1}/kT}$$

$$- k_r(N+1) [OH(N)] [O_2] e^{-\Delta E_{N-1,N}/kT} \qquad (5)$$

where OH(N) is the population of rotational level N, $k_p(N)$ is
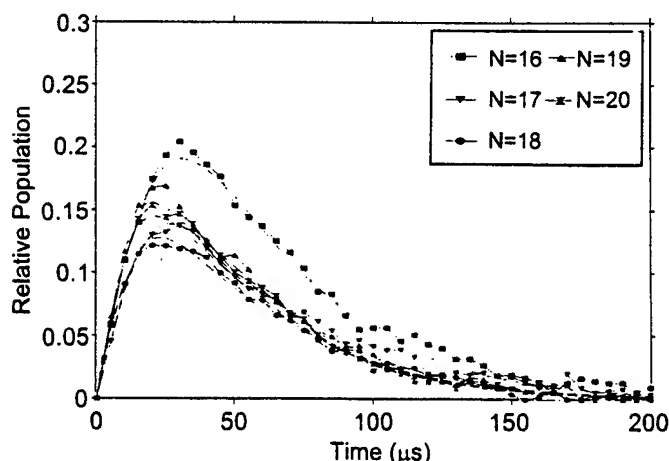


**Figure 8.** Deduced rotational population histories v = 1, N=16-20. Dashed lines are model comparisons.

the production rate constant for reaction (1) into level N, $k_r(N)$ is the rotational relaxation rate constant from level N to N-1, the bracketed quantities represent the densities of the respective chemical species, and $\Delta E_{N,N-1}$ represents the energy difference between states N and N-1. Note the rotational detailed balancing terms, e.g., N→N+1, have been included in (5), although these terms are only important at the lowest rotational levels considered.

$O(^1D)$ is being consumed in reaction (1) and is thus not constant in (5). The defining relationship for $O(^1D)$ is

$$d[O(^1D)]/dt = - k_1[O(^1D)] [(H_2)] \qquad (6)$$

which has the solution

$$[O(^1D)] = [O(^1D)_0] \, e^{-k_1H_2t} \qquad (7)$$

The quantity $k_1H_2$ is the inverse of the characteristic reaction time observed in the data, Figure 4, of 12 μs, thus $k_1H_2 = 8.3 \times 10^4 \, s^{-1}$. The expression for $O(^1D)$, equation (7), can be substituted into (5), which can be integrated, resulting in the relationship

$$[OH(N,t_f)] - [OH(N,t_i)] =$$

$$- b_N \left[ e^{-8.3 \times 10^4 t_f} - e^{-8.3 \times 10^4 t_i} \right]$$

$$+ k_r(N+1) \int_{t_i}^{t_f} [OH(N+1)] [O_2] \, dt$$

$$- k_r(N) \int_{t_i}^{t_f} [OH(N)] [O_2] \, dt$$

$$+ k_r(N) \int_{t_i}^{t_f} OH(N-1) [O_2]e^{-\Delta E_{N,N-1}/kT} \, dt$$

$$- k_r(N+1) \int_{t_i}^{t_f} [OH(N)] [O_2]e^{-\Delta E_{N,N-1}/kT} \, dt \qquad (8)$$

where

$$b_N = \frac{[O(^1D)] [H_2] k_p(N)}{8.3 \times 10^4} \qquad (9)$$
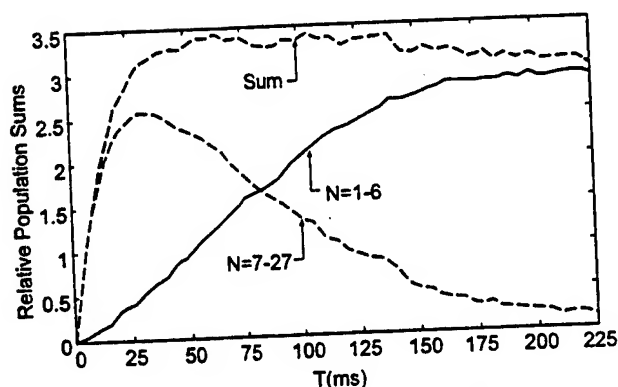
Figure 10. Relative partial rotational populations versus time for vibrational level 1. Conditions of Figure 4.

Figure 12. Relative excitation rates for reaction (1) conditions of Figure 4.

Now the individual relative rotational populations and their integrals are known from the data for all times $t_i$, $t_f$. The unknowns in (8) are the quantities $k_r(N)$, $b_N$. As will be shown below, these parameters can be evaluated directly from the data.

There are 2m unknowns with m defining equations, where m is the total number of rotational levels analyzed. Rather than employ a linear regression analysis, we have used a simple algorithm to interpret the data in terms of these unknown quantities. Specifically, the quantities $k_r(N)$, $b_N$ have different regions of dominance in the time domain. With the exception of the lowest levels the quantity $b_N$ dominates at early times, where chemical production is important. Therefore we evaluated (8) over the time domain t = 0 to 30 µs, about twice the reaction time for reaction (1), to develop a relationship between $b_N$ and $k_r(N)$. Equation (8) was then evaluated between approximately 30 and 150 µs, where relaxation dominates, with the former relationship substituted in to eliminate $b_N$. The resulting values of $k_r(N)$ were then substituted into the early time relationship to deduce $b_N$.

This algorithm obviously breaks down at the lowest levels whose whole time history is dominated by rotational relaxation. Given the accuracy of the data, it would be difficult to deduce values for $b_N$ at these levels in any case. Coincidentally, as we analyzed the data, we noted that the population of level N = 6 was anomalous. Although its temporal behavior is appropriate, its population is larger than that of both levels N = 7 and N = 5, a behavior difficult to rationalize in terms of our cascade relaxation assumption. The kinetic analysis breakdown at (v,N) levels (1,6) and (2,5) appears to be due to severe spectral overlaps. As a result we performed our analysis only for N = 7 and higher.

The same analytical procedure was applied to the data for levels v = 2,3, again excluding the lowest levels from the analysis. The deduced rotational relaxation rate constants for these three vibra-

tional levels are shown in Figure 11. The relative production efficiencies for reaction (1), e.g., the $b_N$, are shown in Figure 12. Before discussing these results we must test the validity of the single quantum cascade relaxation model. This is done by solving (5) from time zero, using the deduced values of $b_N$, $k_r(N)$. These solutions are shown in Figures 6 to 8, in comparison with the data. As can be seen, although there are some variations between data and model, the comparison is generally quite good, demonstrating that a single quantum relaxation model is sufficient to explain the temporal behavior of the observations.
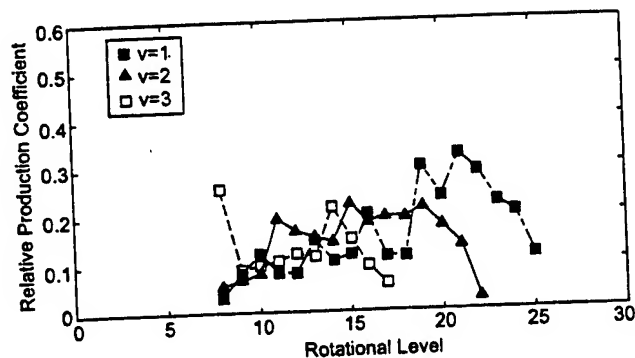
We have performed this analysis on four sets of data taken under similar conditions but on different days. The results of this analysis are also shown in Figure 13 for v = 1, and it can be seen that the data sets are in very good agreement. The average value and standard deviations of the deduced relaxation rate constants for v = 1 to 3 are summarized in Table 2.

The rate constants exhibit two interesting features. First, the relaxation rate constants are of gas kinetic order. Rotational relaxation from these vibrational levels is apparently very efficient. We know of no other measurements to directly compare these results to. An observation [Copeland and Crosley, 1984] at low N for other collision partners suggests that rotational relaxation is relatively efficient, however. Sears et al. [1989] did study OD (N=40) relaxation in a mix of $H_2$ and $O_3$ and deduced an efficient relaxation rate constant of 7 x $10^{-11}$ cm³ s⁻¹.

More interesting is the rotational level dependence observed in the rate constants. These rate constants initially decrease with increasing N, not unexpectedly, given the increasing amount of rotational energy involved in the deactivation process. However, an unexpected change in the rate constant distribution appears around N = 14 (for v = 1), with a subsequent increase in rate constant peaking at about N = 18 before falling again. As can be seen in
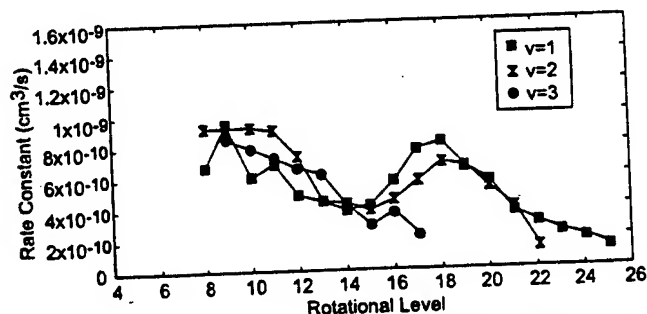
Figure 11. Deduced rate constants for rotational relaxation by oxygen molecules. Conditions of Figure 4.
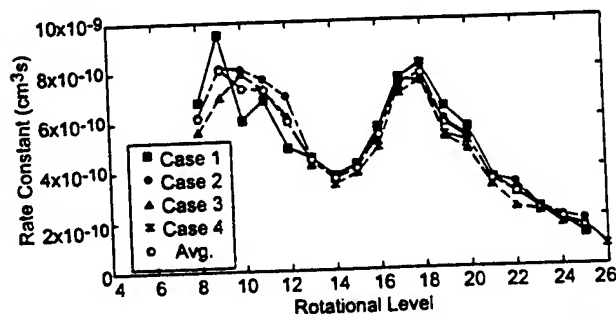
Figure 13. Deduced rate constants for rotational relaxation at oxygen molecules for OH vibrational level 1. Four data sets.

**Table 2.** Relaxation Rate Constants OH(v,N) + $O_2$ → OH(v,N-1) + $O_2$

| N | k(N,v=1) x $10^{10}$, cm$^3$ s$^{-1}$ | k(N,v=2) x $10^{10}$, cm$^3$ s$^{-1}$ | k(N,v=3) x $10^{10}$, cm$^3$ s$^{-1}$ |
|---|---|---|---|
| 8 | 6.2 +/- 0.6 | 7.2 +/- 1.6 | |
| 9 | 8.2 +/- 1.3 | 7.5 +/- 1.4 | 7.6 +/- 1.1 |
| 10 | 7.4 +/- 1.1 | 7.9 +/- 1.2 | 7.2 +/- 0.8 |
| 11 | 7.3 +/- 0.4 | 8.3 +/- 1.0 | 6.8 +/- 0.4 |
| 12 | 6.0 +/- 1.0 | 6.5 +/- 0.7 | 6.3 +/- 0.4 |
| 13 | 4.4 +/- 0.2 | 4.3 +/- 0.5 | 5.1 +/- 0.8 |
| 14 | 3.7 +/- 0.2 | 4.0 +/- 0.4 | 3.5 +/- 0.6 |
| 15 | 4.1 +/- 0.2 | 3.5 +/- 0.3 | 2.7 +/- 0.3 |
| 16 | 5.4 +/- 0.4 | 4.1 +/- 0.3 | 3.2 +/- 0.5 |
| 17 | 7.5 +/- 0.3 | 5.1 +/- 0.5 | 2.0 +/- 0.3 |
| 18 | 7.9 +/- 0.4 | 6.1 +/- 0.6 | |
| 19 | 5.8 +/- 0.6 | 5.8 +/- 0.6 | |
| 20 | 5.2 +/- 0.4 | 4.8 +/- 0.3 | |
| 21 | 3.5 +/- 0.1 | 3.7 +/- 0.8 | |
| 22 | 3.0 +/- 0.4 | 1.9 +/- 1.6 | |
| 23 | 2.3 +/- 0.1 | | |
| 24 | 1.9 +/- 0.2 | | |
| 25 | 1.6 +/- 0.3 | | |

Figure 11, vibrational levels v = 2 and possibly 3 exhibit a similar behavior.

The "bottleneck" in the relaxation of the rotational distribution is shown in Figure 14, which presents snapshots of the rotational population at five times. Note the buildup in the population around N = 14 with increasing time, even after OH(v,N) production by reaction (1) ceases. (The previously mentioned anomaly in the population of N=6 can also be seen in this figure.)

A single bottleneck in the relaxation of a rotational distribution has been observed previously, for example, in CN created highly excited through chemical reaction [*Hay et al.*, 1985]. Here an initially highly excited rotational distribution is observed to relax via a bimodal distribution of high and low rotational states. Presumably, this relaxation reflects the slow relaxation of the higher levels (large energy gap) in contrast with the more rapid relaxation of the lowest rotational levels.

*Polanyi and Woodall* [1972] provided a detailed discussion of the systematics of rotational relaxation in their analysis of observed bimodal rotational distributions in HCl created highly excited through chemical production. In that work they explored the possibility of multiple quantum relaxation and discussed the relaxation of double-peaked nascent rotation distributions. In the present work, as seen in Figure 14, we observe that a single-peaked nascent distribution collisionally relaxes at intermediate times to a distribution characterized by a double peak at high N and a thermalized distribution.
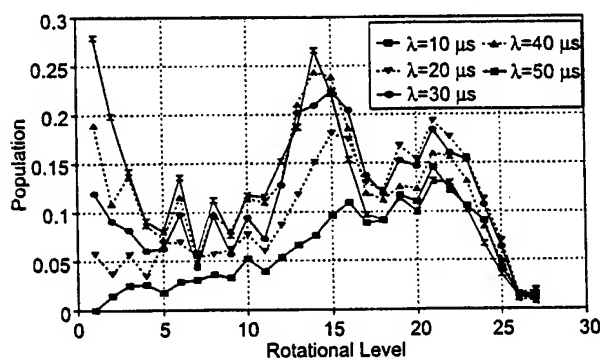
While we find that the single quantum relaxation model agrees very well with the data, we cannot exclude a possible contribution from multiple quantum transitions. Our procedure was to deduce the rate constants individually from the experimental data without assuming any form of N dependence. The introduction of multiple quantum transitions introduces too many unknowns to make this approach tenable.

It can be seen that the relative production efficiencies shown in Figure 12 for v = 1 to 3 of the data set quantity have greater scatter than the relaxation rate constants. This discrepancy is the result of at least two effects: (1) The data were taken in 5 µs intervals, and thus the data must be extrapolated to time zero. Any uncertainty here, while unimportant in evaluating rotational relaxation, can be critical in evaluating the excitation rate. (2) The lower rotational levels are increasingly dominated by feed from above, rather than direct excitation, thus making deduction of the excitation rate more difficult.

The general trend in the excitation data is similar to that reported by others [e.g., *Mikulecky and Gericke*, 1992; *Smith and Butler*, 1980; *Butler et al.*, 1986; *Cleveland et al.*, 1987] for this range of rotational levels. The excitation rate is found to increase approximately linearly with increasing rotational level and then fall off at total internal energies near the reaction exoergicity.

## Conclusions

Highly rotationally and vibrationally excited OH produced by the photolytically initiated O($^1D$) + $H_2$ reaction has been observed under low-pressure conditions with sufficient spectral and temporal resolution to permit relaxation processes to be observed. The dominant mechanism is consistent with pure single quantum rotational relaxation within each vibrational manifold. The rate constants for OH ($X^2\Pi$, v=1-3,N) rotational relaxation by $O_2$ are approximately gas kinetic. An unexpected bottleneck is observed in the rate constants around N=14. Similar relaxation by $H_2$ and Ar is at least an order of magnitude and 2 orders of magnitude less efficient, respectively.

These rate coefficients suggest that rotational relaxation of high rotational levels of OH produced in the airglow layer will compete with radiative decay of these levels. Assuming an oxygen density of 1.5 x $10^{13}$ cm$^{-3}$ at 90 km, we find rotational collisional quenching rates of about 4500 s$^{-1}$, an order of magnitude larger than the pure rotational radiative decay rates. In light of the recent observations



**Figure 14.** Deduced rotational population distribution for v=1 at five times.

of hot rotational distributions in the airglow layer, and the fast relaxation of these populations, the production rate for the rotationally excited component may be larger than was previously estimated. Future work will examine the relaxation of these populations by the other significant atmospheric quenchers $N_2$ and O.

# References

Aker, P.M., and J.J. Sloan, The initial product vibrational energy distribution in the reaction between O($^1$D) and H$_2$, *J. Chem. Phys.*, 85, 1412, 1986.

Atkinson, R., D.L. Baulch, R.F. Cox, J.R. Hampson, and J. Troe, Evaluated kinetic and photochemical data for atmospheric chemistry, *J. Phys. Chem. Ref. Data*, 21, supplo IV, 1125, 1992.

Berg, P.A., J.J. Sloan, and P.J. Kuntz, The effect of reagent excitation on the dynamics of the reaction O ($^1$D$_2$)+ H$_2$ → OH (x$^2$π) + H, *J. Chem. Phys.*, 95, 8038, 1991.

Butler, J.E., R.G. MacDonald, D.J. Donaldson, and J.J. Sloan, Vibrational excitation of OH (x$^2$π) produced in the reaction of O($^1$D) with H$_2$, *Chem. Phys. Lett.*, 95, 193, 1983.

Butler, J.E., G.M. Jursich, J.A. Watson, and J.R. Wiesenfeld, Reaction dynamics of O($^1$D$_2$)+ H$_2$, HD, D$_2$ : OH, OD(x$^2$π) product internal energy distributions, *J. Chem. Phys.*, 84, 5365, 1986.

Cleveland, C.B., C.M. Jursich, M. Trolier, and J.R. Wiesenfeld, Dynamics of the reaction O($^1$D$_2$)+ H$_2$ → OH(x$^2$π, v"=2,3) + H : Full characteristics of the product energetics, *J. Chem. Phys.*, 86, 3253, 1987.

Copeland, R.A., and D.R. Crosley, Λ - doublet transfer and propensities in collisions of OH(x$^2$π$_i$, v=2) with H$_2$O, *J. Chem. Phys.*, 81, 6400, 1984.

Dodd, J.A., S.J. Lipson, and W.A.M. Blumberg, Formation and vibrational relaxation of OH(X$^2$Π, v) by O$_2$ and CO$_2$, *J. Chem. Phys.*, 95, 5752, 1991.

Dodd, J.A., S.J Lipson, J.R. Lowell, P.S. Armstrong, W.A.M. Blumberg, R.M. Nadile, S.M. Adler-Golden, W.J. Marinelli, K.W. Holtzclaw, and B.D. Green, Analysis of hydroxyl earthlimb airglow emissions: Kinetic model for state-to-state dynamics of OH(v,N), *J. Geophys. Res.*, 99, 3559, 1994.

Green, B.D., G.E. Caledonia, R.E. Murphy, and F.X. Robert, The vibrational relaxation of NO(v=1-7) by O$_2$, *J. Chem. Phys.*, 76, 2441, 1982.

Hay, S., F. Shokoohi, S. Callister, and C. Wittig, Collisional metastability of high rotational states of CN(x$^2$Σ$^+$, v"=0), *Chem. Phys. Lett.*, 118, 6, 1985.

Holtzclaw, K.W., J.C. Person, and B.D. Green, Einstein coefficients for emission from high rotational states of the OH(X$^2$Π) radical, *J. Quant. Spectrosc. Radiat. Transfer*, 49, 223, 1993.

Huang, V., Y. Gu, C. Liu, X. Yang, and Y. Tao, The nascent product vibrational energy distribution of the reaction O($^1$D) + H$_2$ by the grating selection technique, *Chem. Phys. Lett.*, 127, 432, 1986.

Knutsen, K., M.J. Dyer, and R.A. Copeland, Collisional removal of OH(x$^2$π, v=7) by N$_2$, CO$_2$ and N$_2$O, *J. Chem. Phys.*, 104, 5798, 1996.

Kuntz, P.J., B.J. Niefer, and J.J. Sloan, A multisurface classical trajectory study of the dynamics of the reaction O($^1$D$_2$)+ H$_2$ → OH(v, J, T, θ) + H using the diatomics-in-molecules method, *Chem. Phys.*, 151, 77, 1991.

Llewellyn, E.J., B.H. Long, and B.H. Solheim, The quenching of OH* in the atmosphere, *Planet. Space Sci.*, 26, 525, 1978.

McDade, I.C., The altitude dependence of the OH(X$^2$Π) vibrational distribution in the nightglow: Some model expectations, *Planet. Space Sci.*, 39, 1049, 1991.

Mikulecky, K., and K.H. Gericke, The influence of vibrational and translational motion on the reaction dynamics of O($^1$D) +H$_2$($^1$Σ$^+_g$, v), *J. Chem. Phys.*, 96, 7490, 1992.

Pendleton, W., P. Espy, D. Baker, A. Steed, M. Fetrow, and K. Henricksen, Observation of OH Meinel (7,4) P(N"=13) transitions in the night airglow, *J. Geophys. Res.*, 94, 505, 1989.

Polanyi, J.C., and K.B. Woodall, Mechanism of rotational relaxation, *J. Chem. Phys.*, 56, 1563, 1972.

Sears, T.J., G.E. Hall, and J.J.F. McAndrew, Rotational populations in OD formed in the reaction O($^1$D) + D$_2$ investigated by infrared rotational absorption spectroscopy, *J. Chem. Phys.*, 91, 5201, 1989.

Sivjee, G.G., and R.M. Hamwey, Temperature and chemistry of the polar mesopause OH, *J. Geophys. Res.*, 92, 4663, 1987.

Smith, D.R., W.A.M. Blumberg, R.M. Nadile, S.J. Lipson, E.R. Huppi, N.B. Wheeler, and J.A. Dodd, Observation of high-N hydroxyl pure rotational lines in atmospheric emission spectra by the CIRRIS 1A space shuttle experiment, *Geophys. Res. Lett.*, 19, 593, 1992.

Smith, G.K., and J.E. Butler, OH(X$^2$Π$_i$) product internal energy distribution formed in the reaction of O($^1$D$_2$) with H$_2$, *J. Chem. Phys.*, 73, 2243, 1980.

Taatjes, C.A., and S.R. Leone, Laser double-resonance measurements of rotational relaxation rates of HF(J=13) with rare gases, H$_2$, and D$_2$, *J. Chem. Phys.*, 89, 302, 1988.

Turnbull, D.N., and R.P. Lowe, Vibrational population distribution in the hydroxyl night airglow, *Can. J. Phys.*, 61, 244, 1983.

W.A.M. Blumberg and S.J. Lipson, Phillips Laboratory, Hanscom Air Force Base, MA 01731. (e-mail: blumberg@plh.af.mil)

G.E. Caledonia (corresponding author), J.F. Cronin, B.D. Green, K.W. Holtzclaw, and B.L. Upschulte, Physical Sciences Inc., 20 New England Business Center, Andover, MA 01810. (e-mail: caledonia@psicorp.com)

J.A. Dodd, Stewart Radiance Laboratory, Bedford, MA 01730. (e-mail: dodd@plh.af.mil)

# Image measurements of short-period gravity waves at equatorial latitudes

M. J. Taylor, W. R. Pendleton Jr., and S. Clark

Space Dynamics Laboratory and Physics Department, Utah State University, Logan

H. Takahashi and D. Gobbi

Instituto Nacional de Pesquisas Espaciais (INPE), São Jose dos Campos, São Paulo, Brazil

R. A. Goldberg

Laboratory for Extraterrestrial Physics, NASA Goddard Space Flight Center, Maryland

**Abstract.** A high-performance, all-sky imaging system has been used to obtain novel data on the morphology and dynamics of short-period (<1 hour) gravity waves at equatorial latitudes. Gravity waves imaged in the upper mesosphere and lower thermosphere were recorded in three nightglow emissions, the near-infrared OH emission, and the visible wavelength OI (557.7 nm) and Na (589.2 nm) emissions spanning the altitude range ~80–100 km. The measurements were made from Alcantara, Brazil (2.3°S, 44.5°W), during the period August–October 1994 as part of the NASA/Instituto Nacional de Pesquisas Espaciais "Guara campaign". Over 50 wave events were imaged from which a statistical study of the characteristics of equatorial gravity waves has been performed. The data were found to divide naturally into two groups. The first group corresponded to extensive, freely propagating (or ducted) gravity waves with observed periods ranging from 3.7 to 36.6 min, while the second group consisted of waves of a much smaller scale and transient nature. The later group exhibited a bimodal distribution for the observed periods at $5.18 \pm 0.26$ min and $4.32 \pm 0.15$ min, close to the local Brunt-Vaisala period and the acoustic cutoff period, respectively. In comparison, the larger-scale waves exhibited a clear tendency for their horizontal wavelengths to increase almost linearly with observed period. This trend was particularly well defined around the equinox and can be represented by a power-law relationship of the form $\lambda_h = (3.1 \pm 0.5)\tau_{ob}^{1.06\pm0.10}$, where $\lambda_h$ is measured in kilometers and $\tau_{ob}$ in minutes. This result is in very good agreement with previous radar and passive optical measurements but differs significantly from the relationship $\lambda_h \propto \tau_{ob}^{1.5}$ inferred from recent lidar studies. The larger-scale waves were also found to exhibit strong anisotropy in their propagation headings with the dominant direction of motion toward the ~NE-ENE suggesting a preponderance for wave generation over the South American continent.

## 1. Introduction

Observations of gravity waves at equatorial latitudes are extremely rare. Gravity waves, particularly small-scale, short-period (<1 hour) waves, are known to be important drivers of the mean winds and thermal structure of the mesosphere and lower thermosphere via wave energy and momentum transport [e.g., *Fritts and Vincent*, 1987]. Variations in the seasonal flux of these waves are therefore expected to have marked effects on the dynamics of the upper middle atmosphere at equatorial, middle, and high latitudes. The statistical properties of small-scale gravity waves (at any latitude and season) are still uncertain, and measurements of their occurrence frequency, horizontal wavelengths, horizontal phase velocities (and hence their observed periods and dominant directions of motion) are of considerable importance for assessing their impact on the local atmospheric dynamics. In this paper we present image

measurements of an ensemble of 56 short-period wave events recorded in the visible and near-infrared (NIR) nightglow emissions. The measurements were made from Alcantara, Brazil (located on the magnetic equator at 2.3°S), as part of the NASA/Instituto Nacional de Pesquisas Espaciais (INPE) Guara campaign, and provide a rare opportunity to investigate the occurrence and dominant characteristics of short-period gravity waves in close proximity to the geographic equator.

To date, most nightglow imaging studies have utilized the bright NIR hydroxyl (OH) emission which originates from a well-defined layer (~8 km half width) centered at a mean altitude of ~87 km [*Baker and Stair*, 1988]. These observations have mainly been made from midlatitude mountain sites and have revealed a variety of wave motions. Classification of the waves into different groups has been attempted by several researchers [e.g., *Clairemidi et al.*, 1985; *Armstrong*, 1986; *Taylor*, 1986]. In most cases this classification has been based on a somewhat arbitrary division of the observed range of horizontal wavelengths ($\lambda_h$) which vary from typically $5 < \lambda_h < 100$ km. As a result of these studies, distinct spatial and temporal properties have emerged which suggest the existence of two

**Table 1.** Filter Details and Exposure Times for the Guara Campaign

| Filter/Emission, nm | Bandwidth, nm | Transmission, % | Exposure Time, s | Altitude, km |
|---|---|---|---|---|
| OI (557.7) | 2.67 | 81 | 90 | 96 |
| Na (589.2) | 2.37 | 81 | 120 | 90 |
| OH* (715–930) | 215 | 87 | 15 | 87 |
| Bg (572.5) | 2.65 | 83 | 90 | ⋯ |
| OI (630.0) | 2.33 | 83 | 180 | 280 |

*With a 20 nm notch at 865 nm to suppress the $O_2(0, 1)$ emission.

types (or groups) of short-period waves. The most prominent group, termed "bands," usually appears as an extensive series of quasi-monochromatic waves that exhibit horizontal wavelengths of a few to several tens of kilometers and phase speeds up to $\sim100$ ms$^{-1}$. Band displays are quite persistent, lasting for typically a few hours, but it is not uncommon for them to endure for over 8 hours [e.g., *Taylor and Hill*, 1991]. Occasional studies have shown that this type of wave pattern is associated with the passage of freely propagating (or ducted) gravity waves most probably of tropospheric origin [e.g., *Taylor and Hapgood*, 1988; *Taylor et al.*, 1995a]. Recent measurements indicate that gravity waves associated with band patterns are as prevalent over oceans as they are over continental mountainous regions, suggesting weather disturbances rather than orographic forcing as their most likely source [*Taylor and Hill*, 1991; *Swenson et al.*, 1995; *Taylor et al.*, 1995a]. The second type of wave motion, termed "ripples," is distinct from bands in that ripples extend over much smaller geographic areas (typically $<5 \times 10^3$ km$^2$) and usually exhibit considerably shorter lifetimes ($<45$ min) [*Peterson*, 1979]. Because of their transient nature, observations of ripples are comparatively few and have until now been restricted to measurements of their horizontal wavelengths which range from $\sim6$ to 16 km [*Peterson and Adams*, 1983]. To our knowledge, only three ripple velocity measurements have been reported, suggesting relatively high horizontal phase speeds of 71 and 91 ms$^{-1}$ [*Peterson*, 1979] and 46 ms$^{-1}$ [*Taylor and Hill*, 1991].

The apparent similarity in morphology and dynamics of ripple events to the "billow" waves seen in noctilucent clouds (NLC) [e.g., *World Meteorological Organization (WMO)*, 1970], suggests similar-type source mechanisms [*Taylor*, 1986; *Clairemidi et al.*, 1985]. A likely source for ripples and billows is thought to result from the chance combination of wind and wave motions (of tidal or other origin) creating localized regions of strong wind shear which in turn generate small-scale waves in situ through the Kelvin-Helmholtz instability [e.g., *Haurwitz and Fogle*, 1969; *Taylor and Hapgood*, 1990]. This is a dynamic-type instability and in the absence of strong winds, or if the winds are aligned parallel to the perturbing wave, then the ripple structures should appear "spanwise" (i.e., oriented approximately parallel to the perturbing wave front). However, *Fritts et al.* [1993] have recently suggested an alternative three-dimensional, convective-type instability as a potential source for the generation of some of the smaller-scale ($\sim5$ km), shorter-lived ($<$several minutes) wave events. In this case and under similar wind conditions the resultant ripple structures will be "streamwise" oriented and should appear approximately perpendicular to the primary wave front. In principle, measurements of small-scale waves in the presence (and/or absence) of

larger-scale motions can therefore be used to discriminate between these source mechanisms.

With the development of sensitive solid state (CCD) imaging systems, measurements of gravity waves in the faint visible wavelength OI(557.7 nm) nightglow emission (peak altitude $\sim96$ km) and the Na (589.2 nm) emission (peak altitude $\sim90$ km) are now practical even from low-altitude sites. As these emissions peak at heights above the OH layer (peak altitude $\sim87$ km), they enhance significantly the potential of image measurements for investigating the occurrence and properties of gravity waves that exist throughout the upper mesosphere and lower thermosphere (altitude range $\sim80$–100 km). For the Guara campaign a multiwavelength, all-sky imaging system was used to record gravity waves over a large geographic area ($>0.6 \times 10^6$ km$^2$) using sequential measurements of the NIR OH and visible wavelength OI and Na nightglow structure. Observations were made during two periods (6 August to 10 September and 1–16 October 1994) in conjunction with radar, photometer, and in situ rocket soundings.

In this study we present the results of the image analysis classifying the data into two categories using the "band" and "ripple" criteria defined earlier to determine the average properties of the quasi-monochromatic wave motions present at equatorial latitudes. The results have then been compared with previous gravity wave measurements at middle and low latitudes obtained by radar and lidar techniques [e.g., *Meek et al.*, 1985; *Reid*, 1986; *Gardner and Voelz*, 1987; *Manson*, 1990; *Beatty et al.*, 1992]. A clear tendency for the observed period of the bands to increase systematically with horizontal wavelength was found during the campaign. This trend was particularly well defined for the wave motions imaged around the equinox. Associated with this significant trend, a marked anisotropy in the distribution of wave azimuths was observed. The dominant direction of motion of the bands was found to be toward the equator from the SW–WSW suggesting frequent, recurring wave generation over the South American continent. In comparison, the ripple data exhibited an unusual bimodal distribution of horizontal wavelength with observed period.

## 2. Gravity Wave Imager

The image measurements were made using a large area (6.45 cm$^2$) solid state charged coupled device (CCD), consisting of 1024 $\times$ 1024 pixels, thermoelectrically cooled to $-40°$C. The high quantum efficiency ($\sim80\%$ at visible and 50% at NIR wavelengths) and low-noise characteristics of this device (dark current $<0.5$ e-/pixel/s) provide an exceptional capability for quantitative measurements of faint, low contrast ($>5\%$) gravity wave signatures in the nightglow emissions. The camera was fitted with a fast (f/4) telecentric lens system and a five-position, temperature stabilized, filter wheel providing all-sky (180°) coverage using narrowband interference filters. The format of the all-sky lens system was such that each pixel in the CCD array subtended an equal angle on the sky resulting in an almost linear relationship between zenith angle and distance as measured from the center of the image. Table 1 lists the characteristics of the filters used for these measurements. Exposure times ranged from 15 s for the bright OH emission to 90 s and 120 s, respectively, for the fainter OI(557.7 nm) and NaD lines. As part of the image sequence, two additional measurements were made, one at 572.5 nm to assess the background sky conditions and the other at 630 nm to investigate the high
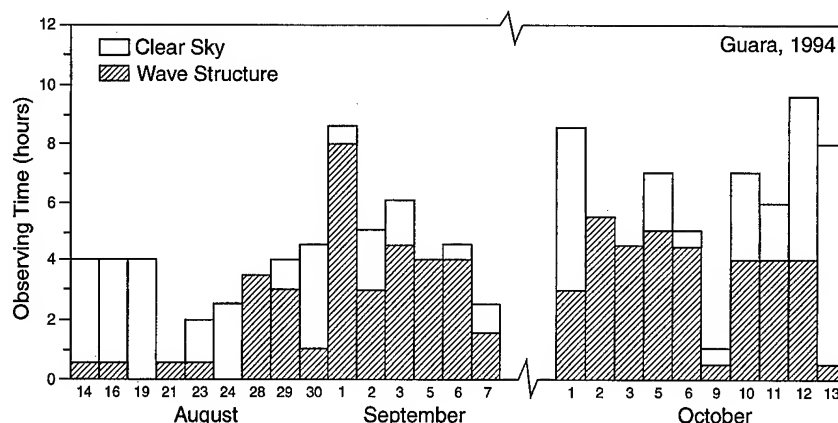
**Figure 1.** Frequency of occurrence of wave structure (bands and ripples) and "clear sky" observing hours for the Guara campaign. Approximately 120 hours of useable data were obtained during two periods: 6 August to 10 September and 1–16 October 1994.

altitude (~280 km) $F$-region OI(630.0 nm) emission (the results of which will be the subject of a separate report.

For this study the background images were used to help discriminate the presence of tropospheric cloud in the data. More detailed spectral analyses utilize the background images to subtract out the effects of scattered light (mainly from the city of Sao Luis ~40 km away) and airglow continuum emission from the data images prior to analysis. Observations of each nightglow emission were recorded once every ~9 min except for the OI(557.7 nm) emission which was sampled every 4–5 min. For a pure monochromatic wave motion this implies a limiting Nyquist period of 18 min for the OH and ~9–10 min for the OI(557.7 nm) emissions. However, spatial nonuniformities in the waveforms, such as "fronts" or "edges," often enable us to accurately track the motion of individual waveforms and hence to evaluate wave periods significantly less than the Nyquist limit.

## 3. Analysis and Results

### 3.1. Guara Image Measurements

The imaging system was located at the INPE Satellite Tracking Station, Centro de Lancamento de Alcantara, Brazil (2.3°S, 44.5°W). Measurements were made in conjunction with the NASA/INPE Guara campaign during two observing periods: 6 August to 10 September, as part of the "MALTED" program [Goldberg et al., 1995], and 1–16 October, as part of the "SPREAD F" program. Although the measurements were made from approximately sea level, a wealth of high contrast, short-period wave structure was recorded during both observing periods. This result is depicted in Figure 1 which plots the frequency of occurrence of wave structure at any position within the "all-sky field," for the OI(557.7 nm) image data. In practice, the useful field of view was found to extend down to zenith angles of ~80° (limited primarily by local horizon and tropospheric scattering and extinction effects). This corresponds to an effective ground range of ~480 km for the OI emission assuming a mean altitude of 96 km. Depending on the orientation of the waveforms, the cutoff for identifying periodic structure at this limiting range is ~20 km. Despite the sometimes severe restrictions imposed by meteorological cloud, approximately 120 hours of useable data were recorded on 23 out of 25 nights, of which ~70 hours contained distinct wave struc-

ture indicating a relatively high frequency of occurrence (~60%).

Figure 2 shows four examples of the gravity waves imaged during this campaign. In Figure 2a a well-developed extensive OI(557.7 nm) band display is evident. This wave pattern exhibited a horizontal wavelength $\lambda_h = 32.0 \pm 0.9$ km and a phase speed $v_h = 67 \pm 1$ ms$^{-1}$ indicating an observed period $\tau_{ob} = 8.0 \pm 0.3$ min. The waves were observed for more than 5 hours as they progressed toward the ~NE. Figure 2b illustrates a similar wave pattern recorded in the NIR OH emission approximately one month later. In this example over 11 near-linear wave crests of average $\lambda_h = 18.2 \pm 0.3$ km were
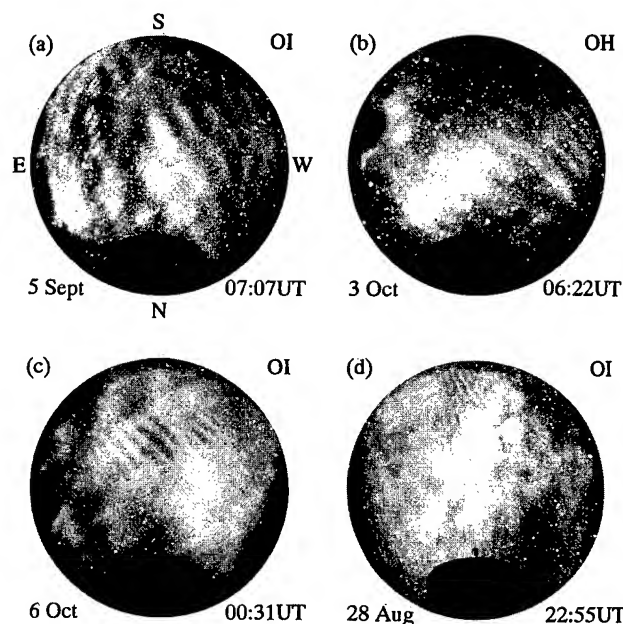


**Figure 2.** Four images showing examples of gravity wave structure recorded in the OI(557.7 nm) and near-infrared OH emissions during the campaign: (a, b) extensive bands; (c) example of transient ripples; (d) a complex mixture of band and ripple waves. Note that the oval silhouette at the bottom of each image is the Instituto Nacional de Pesquisas Espaciais satellite tracking antenna, while the dark patches at low elevations in Figures 2b and 2c are clouds.
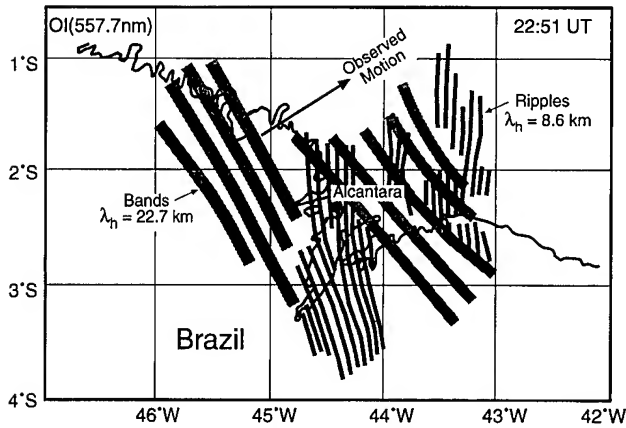
**Figure 3.** Map showing the geographic location and orientation of the complex OI(557.7 nm) band and ripple display shown in Figure 2d. The data are plotted for an assumed emission height of 96 km.

imaged as they progressed toward the ~NNE on a similar heading to the bands shown in Figure 2a.

Figure 2c shows an example of a ripple display. During the Guara campaign over 25 ripple events were recorded yielding

novel measurements of their velocities and observed periods. In this example the ripples were imaged in the OI(557.7 nm) emission and exhibited a mean $\lambda_h = 12.0 \pm 0.3$ km and an average $v_h = 35.4 \pm 1.4$ ms$^{-1}$, yielding a $\tau_{ob} = 5.6 \pm 0.3$ min. More complex wave patterns consisting of a mixture of two (or more) band patterns or band and ripple displays were observed on several occasions during this campaign. The OI (557.7 nm) image of Figure 2d shows an extensive set of N-S aligned ripples in the zenith and eastern sky ($\lambda_h = 8.6 \pm 0.1$ km) superposed on a faint band pattern ($\lambda_h = 22.7 \pm 0.6$ km) that was observed to progress from low elevations toward the equator, again on an ~ENE heading. The geographic location, orientation, and the relative scale sizes of these two wave displays are shown in the map of Figure 3 which also illustrates the observing geometry for these measurements.

### 3.2. Equatorial Wave Characteristics

Analysis of this data set has focused on identifying wave events, primarily in the OI(557.7 nm) emission (peak altitude ~96 km), with a subsequent investigation of the lower-altitude NaD (589.2 nm) and NIR OH emissions to determine additional events that were not evident in the OI data set. The images were calibrated first using the star background, and then prominent wave features were mapped onto the Earth's surface to form a series of maps (e.g., Figure 3), from which the

**Table 2.** Chronological List of Measured Wave Parameters ($\lambda_h$, $v_h$, $\tau_{ob}$) for Band Events and Calculated Values for $(\tau_i)_m$ and $(\lambda_z)_m$ Using Model Winds

| Band Event | Date | Layer | $\lambda_h$, km | $v_h$, ms$^{-1}$ | $\tau_{ob}$, min | Azimuth, °N | $\tau_b$, min | $(\tau_i)_m$, min | $(\lambda_z)_m$, km |
|---|---|---|---|---|---|---|---|---|---|
| 1 | 28 Aug. | OI | 22.7 | 36 | 10.4 | 60 | (5.10) | 15 | 8.0 |
| 2 | 29 Aug. | OH | 16.4 | 27 | 10.0 | 170 | (5.10) | 12 | 7.5 |
| 3 | 29 Aug. | OI | 25.4 | 49 | 8.6 | 160 | (5.10) | 9.3 | 17 |
| 4 | 30 Aug. | OH | 18.4 | 26 | 11.9 | 80 | 5.10 | 13 | 8.1 |
| 5 | 30 Aug. | OH | 17.6 | 20 | 14.9 | 50 | 5.10 | 14 | 6.9 |
| 6 | 30 Aug. | OI | 30.9 | 49 | 10.5 | 270 | 5.10 | 8.1 | 25 |
| 7 | 1 Sept. | OI | 15.7 | 38 | 6.9 | 210 | 5.14 | 6.0 | 26 |
| 8 | 1 Sept. | OI | 23.6 | 62 | 6.4 | 210 | 5.14 | 5.8 | 45 |
| 9 | 1 Sept. | OI | 27.5 | 33 | 13.7 | 140 | 5.14 | 20 | 7.3 |
| 10 | 1 Sept. | OI | 27.9 | 55 | 8.4 | 100 | 5.14 | 12 | 14 |
| 11 | 1 Sept. | OI | 20.6 | 33 | 10.3 | 110 | 5.14 | 18 | 6.1 |
| 12 | 1 Sept. | Na | 30.8 | 14 | 36.7 | 255 | 5.14 | 20 | 8.2 |
| 13 | 1 Sept. | OH | 18.2 | 27 | 11.1 | 335 | 5.14 | 8.8 | 13 |
| 14 | 2 Sept. | OH | 13.8 | 63 | 3.7 | 55 | 5.21 | 3.6 | ? |
| 15 | 2 Sept. | OH | 20.7 | 41 | 8.4 | 60 | 5.21 | 8.2 | 17 |
| 16 | 3 Sept. | OH | 13.9 | 57 | 4.1 | 80 | 5.03 | 4.2 | ? |
| 17 | 3 Sept. | OI | 39.4 | 71 | 9.3 | 65 | 5.03 | 11 | 19 |
| 18 | 5 Sept. | OI | 26.6 | 61 | 7.2 | 70 | 5.13 | 9.3 | 18 |
| 19 | 5 Sept. | OI | 32.0 | 67 | 8.0 | 95 | 5.13 | 10 | 18 |
| 20 | 5 Sept. | OH | 15.4 | 46 | 5.6 | 50 | 5.13 | 5.1 | ? |
| 21 | 5 Sept. | OI | 37.6 | 56 | 11.2 | 60 | 5.13 | 14 | 14 |
| 22 | 6 Sept. | OI | 15.6 | 54 | 4.8 | 50 | 5.24 | 6.0 | 28 |
| 23 | 7 Sept. | OI | 38.3 | 56 | 11.5 | 65 | 5.14 | 15 | 14 |
| 24 | 1 Oct. | OI | 17.5 | 68 | 4.3 | 355 | 5.02 | 4.3 | ? |
| 25 | 2 Oct. | OI | 41.7 | 59 | 11.8 | 60 | (5.02) | 16 | 13 |
| 26 | 3 Oct. | OH | 18.2 | ⋯ | ⋯ | ⋯ | ⋯ | ⋯ | ⋯ |
| 27 | 5 Oct. | OI | 31.0 | 62 | 8.3 | 310 | 5.15 | 7.0 | 34 |
| 28 | 5 Oct. | OI | 25.2 | 61 | 6.9 | 70 | 5.15 | 9.9 | 15 |
| 29 | 10 Oct. | OI | 20.3 | 42 | 8.2 | 160 | 5.26 | 8.6 | 16 |
| 30 | 11 Oct. | OI | 19.6 | 53 | 6.2 | 315 | 5.29 | 5.2 | ? |
| 31 | 11 Oct. | OI | 31.7 | 55 | 9.6 | 150 | 5.29 | 11 | 18 |

The date listed corresponds to the evening when the measurements were initiated. Values of $\tau_b$ were deduced from O$_2$ and OH temperature measurements using a tilting filter photometer; values in parentheses are estimated. The space between events 13 and 14 indicates the division into two sets corresponding to the onset of strong anisotropy in the wave headings (i.e., prior to and after 2 September). The question mark indicates situations where a value for $(\lambda_z)_m$ is indeterminate using equation (2) as the estimated intrinsic period was less than $\tau_b$.

**Table 3.**  Chronological List of Measured Wave Parameters ($\lambda_h$, $v_h$, $\tau_{ob}$) for Ripple Events

| Ripple Event | Date | Layer | $\lambda_h$, km | $v_h$, ms$^{-1}$ | $\tau_{ob}$, min | Azimuth, °N | $\tau_b$, min |
|---|---|---|---|---|---|---|---|
| 1 | 17 Aug. | OI | 16.1 | 41.5 | 6.5 | 130 | ... |
| 2 | 17 Aug. | OH | 16.0 | 51.4 | 5.2 | 135 | ... |
| 3 | 17 Aug. | OH | 9.8 | ... | ... | ... | ... |
| 4 | 17 Aug. | OH | 10.5 | ... | ... | ... | ... |
| 5 | 17 Aug. | OH | 9.5 | ... | ... | ... | ... |
| 6 | 22 Aug. | OI | 14.9 | 43.8 | 5.7 | 110 | ... |
| 7 | 28 Aug. | OI | 8.6 | ... | ... | ... | ... |
| 8 | 1 Sept. | OI | 10.3 | 62.0 | 2.8 | 210 | 5.14 |
| 9 | 1 Sept. | OI | 10.2 | 29.9 | 5.7 | 110 | 5.14 |
| 10 | 1 Sept. | OI | 12.8 | 38.9 | 5.5 | 75 | 5.14 |
| 11 | 1 Sept. | Na | 11.3 | 27.3 | 6.9 | 200 | 5.14 |
| 12 | 1 Sept. | OH | 7.5 | 29.7 | 4.2 | 180 | 5.14 |
| 13 | 1 Sept. | OH | 6.0 | 23.3 | 4.3 | 175 | 5.14 |
| 14 | 2 Sept. | OH | 8.2 | 24.9 | 5.5 | 80 | 5.21 |
| 15 | 5 Sept. | OH | 10.2 | 40.7 | 4.2 | 130 | 5.13 |
| 16 | 3 Oct. | OI | 11.4 | 25.4 | 7.5 | 20 | ... |
| 17 | 3 Oct. | OI | 17.8 | 69.6 | 4.3 | 40 | ... |
| 18 | 5 Oct. | OI | 14.1 | 85.9 | 2.7 | 180 | 5.15 |
| 19 | 6 Oct. | OI | 12.0 | 35.4 | 5.6 | 40 | 5.20 |
| 20 | 6 Oct. | OI | 12.3 | 48.6 | 4.2 | 30 | 5.20 |
| 21 | 10 Oct. | OI | 17.7 | 53.9 | 5.5 | 0 | 5.26 |
| 22 | 11 Oct. | OI | 12.8 | 47.7 | 4.5 | 170 | 5.29 |
| 23 | 11 Oct. | OI | 7.0 | ... | ... | ... | 5.29 |
| 24 | 12 Oct. | OI | 15.3 | 47.5 | 5.4 | 340 | 5.30 |
| 25 | 12 Oct. | OI | 10.0 | ... | ... | ... | ... |

Note that on six occasions it was not possible to determine the wave phase speed accurately. Values of $\tau_b$ are listed (where available) for comparison with the deduced $\tau_{ob}$ for the 19 events. As in Table 2, the space indicates the division into two groups.

horizontal parameters ($\lambda_h$, $v_h$, $\tau_{ob}$) and the wave propagation heading were determined for each identifiable event. (Note that very low contrast features that were not easily identifiable in the data have not been included in this analysis.) A full description of this spatial analysis procedure (as applied to narrow angle image data) has been given by *Hapgood and Taylor* [1982]. This method of analysis was determined to be the most practical, in this case, as attempts to perform two-dimensional spectral analysis of the wave motions (as described by *Taylor and Garcia* [1995] were often impeded by transient clouds. The results of the spatial analysis were then separated into two groups corresponding to bands and ripples using the differences in the geographical extent and the duration of each wave pattern as the primary dividing criteria. A total of 37 OI(557.7 nm) displays were analyzed in this manner, 21 of which consisted of extensive band motions (often, but not always, occupying the entire field of view), with 16 small-scale, short-duration ripple events. In addition, 17 OH displays (9 bands and 8 ripples) and 2 Na(589.2 nm) displays (1 band, 1 ripple) were observed totaling 56 wave events. Because of clouds the number of displays yielding accurate measurements of wave velocity was reduced to 49 events. For comparison, a summary of the measured band and ripple parameters is given in Tables 2 and 3, respectively. On some occasions the wave activity was very high, and several band and/or ripple events were imaged during a single night (e.g., September 1). However, bands and ripples were not always present on the same nights.
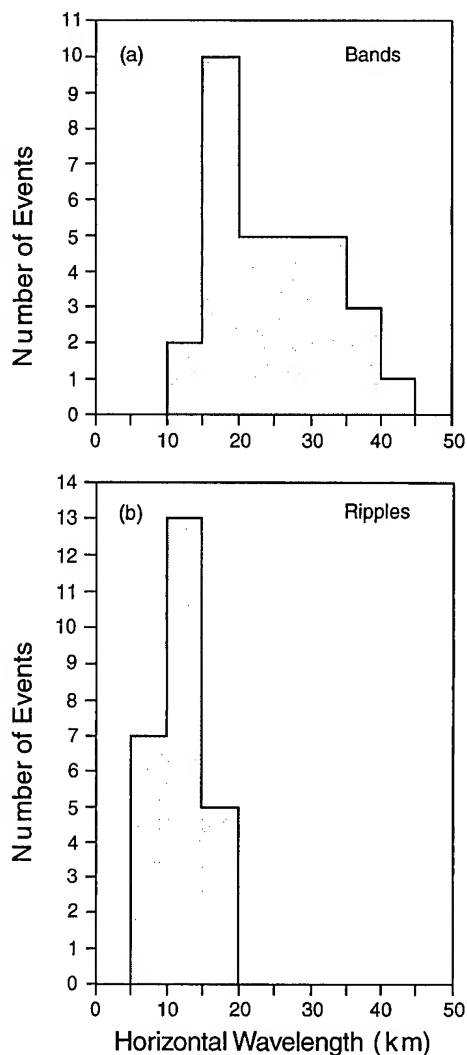
Figure 4 plots the distribution of horizontal wavelengths for the bands and ripples as a function of their occurrence frequency. The data have been binned into histograms of 5 km width (which is well within the typical measurement accuracy of ±3% corresponding to <±1 km) to determine the most frequently observed horizontal scale sizes. The strong tendency for ripples (Figure 4b) to occur over a very narrow wavelength range is immediately apparent with ~83% of all events having wavelengths in the 5–15 km range. In contrast, the band displays exhibited a significantly broader range of horizontal wavelengths extending from ~10–45 km (Figure 4a) and ~94% of all bands had wavelengths >15 km. The average band wavelength was 24.3 km, approximately twice that of the ripples at 11.7 km.

Figure 5 shows the corresponding distribution of wave speeds (for 49 events) plotted at 10 ms$^{-1}$ intervals (typical individual measurement error ±5% or <±3 ms$^{-1}$). The band measurements (Figure 5a) range from 14 to 71 ms$^{-1}$ and exhibit an average value of 48 ms$^{-1}$. However, there is a clear tendency for many of the waves in this data set to exhibit relatively high phase speeds, with the highest frequency of occurrence in the 50–60 ms$^{-1}$ range. Surprisingly, the ripples (Figure 5b) exhibited a similar distribution range to the bands (23–86 ms$^{-1}$) and an almost identical average speed of 44 ms$^{-1}$. No obvious tendency toward high phase speeds was found. The resulting distribution of observed wave periods (binned at 2 min intervals) is given in Figure 6. The ripples exhibit a remarkably sharp distribution centered on the 4–6 min bin (with ~74% of events occurring within this range) and an average wave period 5.1 min. In comparison, the distribution of band periodicities is considerably broader than for the ripples and shows a clear tendency toward longer wave periods (with 83% of bands exhibiting periods >6 min) and a significantly higher average value of 9.6 min (approximately twice that of the ripples).

### 3.3.  Distribution of Wave Headings

The propagation headings for both wave groups, summed over 15° intervals, are plotted in Figure 7. The distribution of
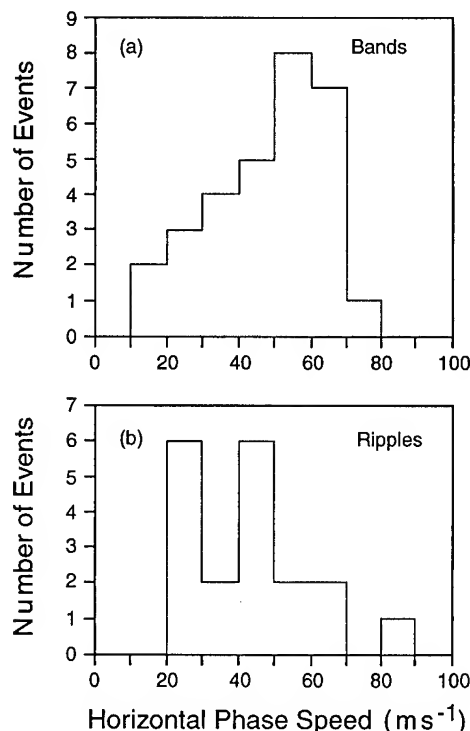
**Figure 4.** Histogram plots showing the distribution of horizontal wavelengths for (a) bands and (b) ripples as a function of number of wave events. Note the strong tendency for short horizontal wavelengths for the ripples.

bands (Figure 7a) is highly anisotropic, exhibiting a strong preference (12 events) for wave progression toward the ~NE-ENE (azimuth range ~45°–75°). In contrast, the ripples (Figure 7b) indicate a much broader range of propagation azimuths with an underlying tendency for eastward phase progression (with 13 out of 19 events exhibiting an eastward component of motion). Figure 8 depicts the velocity distribution of the two wave groups. Although the phase speeds of the bands and ripples varied considerably (from ~10 to ~90 ms$^{-1}$), there is no obvious evidence of an azimuthal bias for faster or slower wave motions. For reasons that are discussed later (section 4), each plot has been divided into two parts: the dashed arrows indicate the velocity vectors for all wave events observed prior to 2 September, while the solid arrows represent wave vectors recorded on and after this night. The band azimuths (Figure 8a) appear to be randomly distributed prior to 2 September. However, measurements on subsequent nights indicate a major change in their azimuthal distribution with a large number of displays (>65%) exhibiting motion toward the ~NE-ENE. The majority of the wave events responsible for the strong anisotropy in the band headings (Figure 7a) there-

fore occurred on and after 2 September. The ripple data (Figure 8b) also indicate a distinct change in their meridional (but not zonal) components of motion prior to and after this date, with a clear preference for southward wave progression during the first interval followed by a reversal to northward progression (in all but two cases) during the second interval.

### 3.4. Wavelength-Period Trends

Prior to considering possible trends involving spatial scales and observed periods, it is important to distinguish between the measured and the derived quantities and to mention analysis procedures. For nightglow imaging studies, the measurements yield directly ($\lambda_h$, $v_h$) pairs. The measured $\lambda_h$ (typical measurement uncertainty of ±3%) is an intrinsic wave parameter, whereas $v_h$ (typical error bars of ±5%) is an observed phase velocity, which usually differs from its intrinsic counterpart because of background winds. These parameters are used to derive $\tau_{ob}$ (typical error bars of ±6%) from the ratio ($\lambda_h/v_h$). Since values of $\tau_{ob}$ are derived from this ratio, it is important to examine first the distribution of ($\lambda_h$, $v_h$) pairs for the band and ripple events before considering possible trends in their horizontal and vertical scales with observed period. Figure 9 shows a ($\lambda_h$, $v_h$) scatter diagram for all of the wave events listed in Tables 2 and 3. Each point is associated with a $\tau_{ob}$ which is the same as the intrinsic period when Doppler-shifting effects are negligible. The ripple events (crosses) exhibit a visually significant positive trend which is expected, based on the sharply peaked distribution of observed periods in the histogram of Figure 6b. However, an interesting feature, not apparent in the histogram plot, is a strong tendency toward a bimodal trend for the ripples, suggesting two preferred peri-
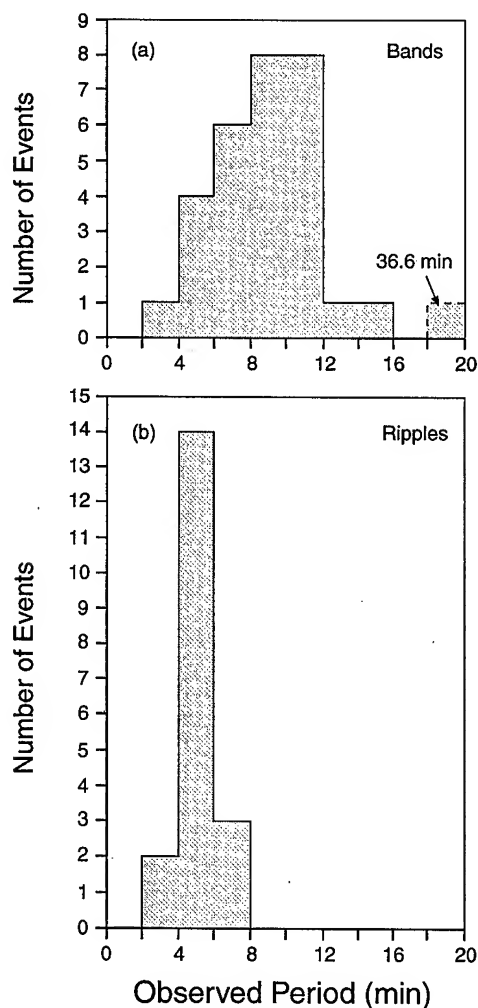


**Figure 5.** Histogram plots showing the distribution of observed horizontal phase speeds for (a) bands and (b) ripples as a function of number of wave events. Note the similar range of phase speeds in each case.
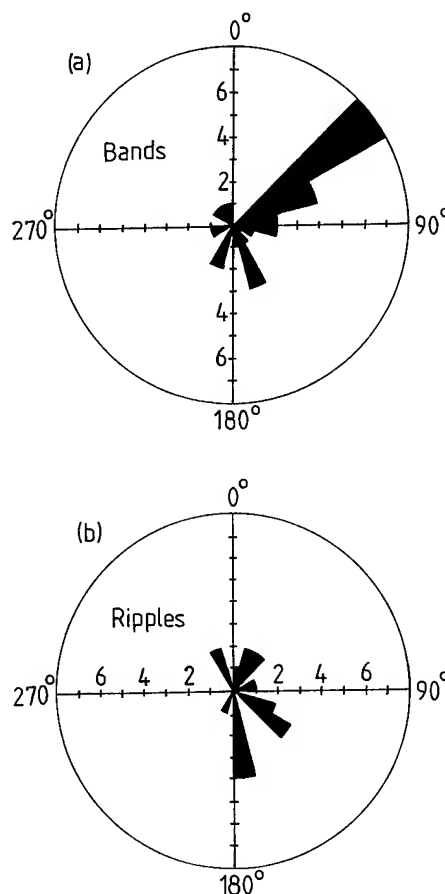
odicities. This feature is also apparent in Figures 10 and 12 (which present $\lambda_h$ and $v_h$ as a function of $\tau_{ob}$) and is discussed in more detail in section 4.4.

Initial inspection of the band events of Figure 9 indicate that they are almost randomly distributed. However, when coded to conform to the division indicated in the velocity distribution data (Figure 8), it is clear that the distribution of ($\lambda_h$, $v_h$) pairs observed prior to 2 September (open circles) is significantly different from that observed after this date (solid circles). The mean $\lambda_h$ values for the two distributions are comparable, at 23 and 26 km, respectively. However, the mean horizontal phase speed of the waves observed $\geq 2$ September is significantly higher ($\sim 57$ ms$^{-1}$) than that observed earlier in the campaign ($\sim 36$ ms$^{-1}$). Furthermore, the spread in the values about each mean is much larger for the waves observed prior to 2 September than after this date (fractional standard deviations of 0.39 and 0.15, respectively). Together, these observations suggest markedly different source and/or propagation conditions during these two observing intervals.

Figure 10 summarizes the Guara image results in a plot of the intrinsic $\lambda_h$ as a function of $\tau_{ob}$. As in the previous figure, the bands are marked by the open and solid circles and the



Figure 7. Plot showing the distribution of wave headings (summed over 15° intervals) for (a) bands and (b) ripples. Note the strong preference for bands to progress toward the $\sim$NE-ENE.



Figure 6. Histogram plots showing the distribution of observed wave period for (a) bands and (b) ripples as a function of number of wave events. Note the prominent peak in the ripple data at $\sim 5$ min.

ripples by the crosses. In this format all of the ripple events are seen to reside in a small cluster bounded by wavelength limits of 5–20 km and periods between 2 and 8 min. In comparison the bands exhibit a clear tendency for larger values of $\lambda_h$ with increasing $\tau_{ob}$. The range of horizontal wavelengths for a given $\tau_{ob}$ also increases significantly as $\tau_{ob}$ increases. To investigate trends in the data, the three wave components identified in Figure 10 (i.e., ripples, bands $\leq 1$ September and bands $\geq 2$ September) are presented in individual scatter diagrams (in log-log format) in Figure 11. Regression analyses were carried out following procedures similar to those described by *Wonnacott and Wonnacott* [1981]. An examination of the deviations associated with $\lambda_h$ and $\tau_{ob}$ revealed similar fractional values which greatly exceed the experimental uncertainties. Hence, for this study, an estimation technique was adopted which accounted for significant stochastic variability in both $\lambda_h$ and $\tau_{ob}$. In Figure 11c the dashed line through the distribution reflects the weighted two-way regression corresponding to a power-law model of the form $\lambda_h = A \tau_{ob}^B$. The power-law model was selected to facilitate comparison with results from other similar-type investigations using radar and lidar data where this model has been widely used [e.g., *Reid*, 1986; *Reid and Vincent*, 1987; *Gardner and Voelz*, 1987]. However, in the present study, the modest ranges in the pertinent variables contributed to very similar confidence levels for both linear and power-law regression analyses.
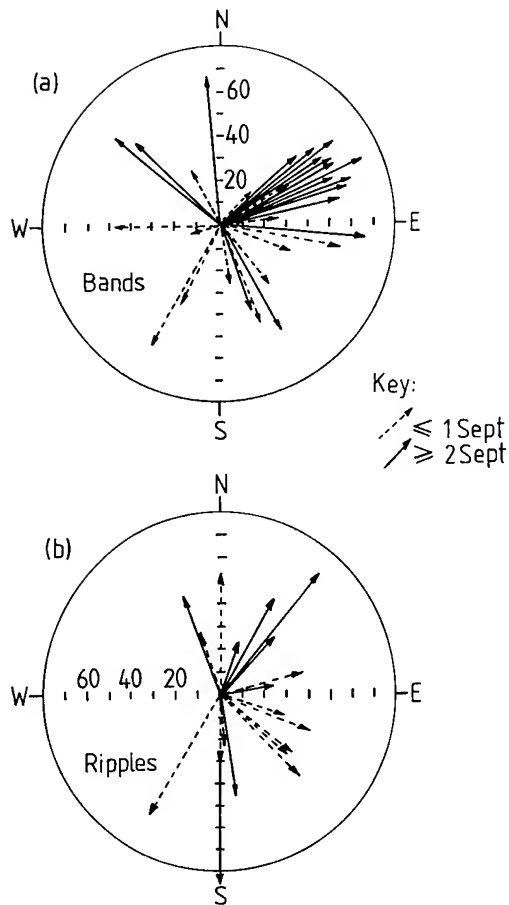
**Figure 8.** Two plots showing the velocity distribution of the waves for (a) bands and (b) ripples. The dashed vectors denote waves recorded prior to 2 September, while the solid arrows show the waves imaged on and after this date. The direction of motion of the waves was usually determined to within an accuracy of typically ±5°. Note the strong preference for band motion toward the ~NE-ENE after 2 September.
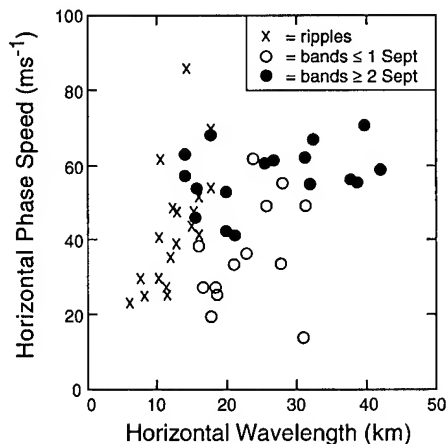


**Figure 9.** Scatter diagram showing the distribution of $(\lambda_h - v_h)$ pairs for the band and ripple data. The bands have been divided into two groups (before and after 2 September) according to the onset of strong directionality in the wave headings.
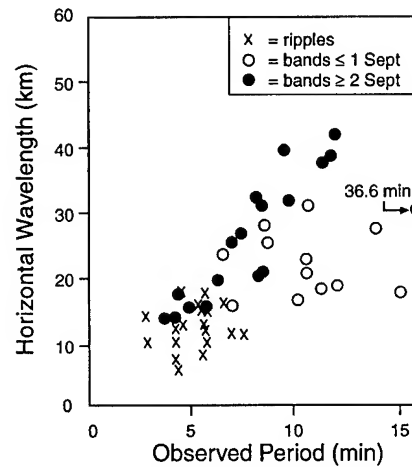


**Figure 10.** Plot of horizontal wavelength as a function of observed wave period for the band (and ripple data). Note the clear tendency for the bands to increase in wavelength with larger observed period and the bimodal clustering of the ripples around ~5 min period.

The ripple data in Figure 11a exhibit a very weak positive trend with a squared correlation coefficient $(r^2)$ of $\sim 10^{-2}$. In this case, the trend is insignificant since the probability of obtaining this value of $r^2$ by chance, with $N = 19$ pairs of
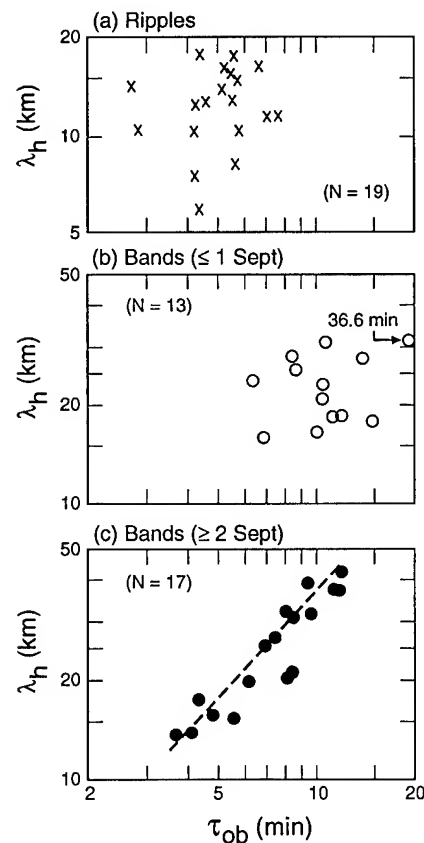


**Figure 11.** Log-log plots showing the data of Figure 10 divided into three groups: (a) ripples, (b) bands ≤1 September, and (c) bands ≥2 September. The dashed line in Figure 11c indicates the best fit power law model $\lambda_h = (3.1 \pm 0.5)\tau_{ob}^{1.06 \pm 0.10}$.

**Table 4.** Results of Correlation Analysis of Figure 11 for Band and Ripple Events

| Type of Wave Motion | Power Law Coefficient, $A$ | Power Law Exponent, $B$ | Square of Correlation Coefficient, $r^2$ | Total Data Pairs, $N$ | Measurement Probability, $P^*$ | Standard Deviation $\sigma_A$ | $\sigma_B$ |
|---|---|---|---|---|---|---|---|
| All bands | 3.9 | 0.86 | 0.29 | 29 | $<3 \times 10^{-3}$ | 1.0 | 0.40 |
| Bands ≥ 2 Sept. | 3.1 | 1.06 | 0.85 | 17 | $<10^{-4}$ | 0.5 | 0.10 |
| Bands ≤1 Sept. | ... | ... | $\sim 10^{-3}$ | 12 | $\sim 1$ | ... | ... |
| Ripples | ... | ... | $\sim 10^{-2}$ | 19 | $\sim 0.5$ | ... | ... |

Parameters $A$ and $B$ were calculated using a weighted two-way regression analysis of the form $\lambda_h = A\tau_{ob}^B$. Note that the data point at (36.6 min, 30.8 km) was not used in the analysis since its parameters did not satisfy Chauvent's criterion.
*Indicates the probability of obtaining the given values of $r^2$ by chance.

observations, is ~0.5. Similarly, the data points in Figure 11b, which represent the band data for the period ≤ 1 September, exhibit no significant trend. In sharp contrast, the data in "Figure 11c" (bands ≥2 September) are characterized by a highly significant ($r^2 = 0.85$ with $N = 17$) positive trend ($B = 1.06 \pm 0.10$). The Student's $t$-test for this case is consistent with a very small probability ($<10^{-4}$) that this level of correlation resulted purely by chance. We have also performed a correlation analysis for the full set of band data which, as expected, is also highly significant (measurement probability of $<3 \times 10^{-3}$). The resultant power-law coefficient in this case ($B = 0.86 \pm 0.4$) was found to be the same as that determined from the band data of Figure 11c given the analysis uncertainties. This trend in the band data is essentially linear for the short-period gravity waves under consideration here. The scaling factor (coefficient $A$) relating $\lambda_h$ to $\tau_{ob}$ was found to lie in the range ~3–4. Thus a wave with a $\tau_{ob}$ close to the local Brunt-Vaisala period of ~5 min would be expected to exhibit a horizontal wavelength of ~15–20 km, whereas a ~20-min period band pattern will have a $\lambda_h$ of typically ~50–70 km. For, convenience, the results of the correlation analyses ($A$, $B$, $r^2$) are summarized in Table 4, where the standard deviations for the parameters $A$ and $B$ are given only for the highly significant correlations.

Figure 12 plots the observed horizontal phase speeds $v_h$ as a
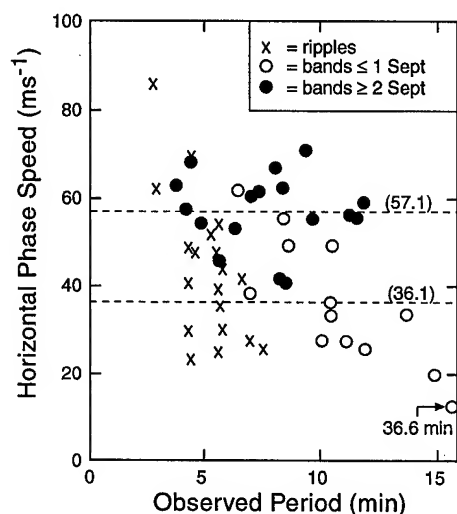
function of $\tau_{ob}$. The previously noted tendency (Figure 9) for the ripple events to be associated with two distinct observed periods, one slightly above and the other just below the mean value of ~5 min, is most apparent (with 14 of the 19 events forming two vertical columns). The difference in the average speed of the bands observed prior to and after 2 September (indicated by the dashed lines) is a key feature of Figure 12. All of the events recorded ≥2 September are characterized by relatively high and similar values of $v_h$ (range 41.0–70.6 ms$^{-1}$), whereas those events observed prior to this date are characterized by significantly lower values of $v_h$ and a somewhat larger spread (range 14.0–61.7 ms$^{-1}$). The implications of this difference are considered in more detail (section 4.2) when the results for the inferred vertical wavelengths are discussed.

## 4. Discussion

Bands were the most prevalent type of wave structure imaged in each of the three nightglow emissions (OI, OH, and Na) investigated. Many of these wave displays were extensive and are considered to be the signature of freely propagating, short-period gravity waves [e.g., *Taylor et al.*, 1987]. However, recent joint radar and imaging studies performed at low latitudes (~20°N) have revealed a tendency for this type of wave motion to be Doppler ducted by the background winds at mesospheric heights (J. R. Isler, private communication, 1996). Depending upon the prevailing wind conditions during the Guara campaign, a significant percentage of the short-period wave events imaged may also have encountered mesospheric ducting thereby increasing their horizontal range of propagation from the source. In general, the range of values ($\lambda_h$, $v_h$, $\tau_{ob}$) present in the Guara equatorial data (bands and ripples) compare favorably with the ensemble of observations recorded at higher latitudes using similar-type instrumentation. However, a tendency toward larger mean values for the horizontal wavelength ($\approx$40 km) and longer observed periods is apparent in some midlatitude band-type data [e.g., *Armstrong*, 1982; *Moreels and Herse*, 1977; *Herse et al.*, 1989; *Swenson and Mende*, 1994; *Fagundes et al.*, 1995; *Taylor et al.*, 1995b]. Significantly, the mean band wavelength during the Guara campaign was 24.3 km and only one event exhibited a $\lambda_h > 40$ km. Furthermore, all but one of the Guara displays manifested observed periods <16 min which are substantially lower than many previous reports from midlatitudes. These results may herald some potentially significant differences in the dominant characteristics of short-period equatorial gravity waves compared with those regularly seen at higher latitudes, possibly associated with variations in their most copious sources.
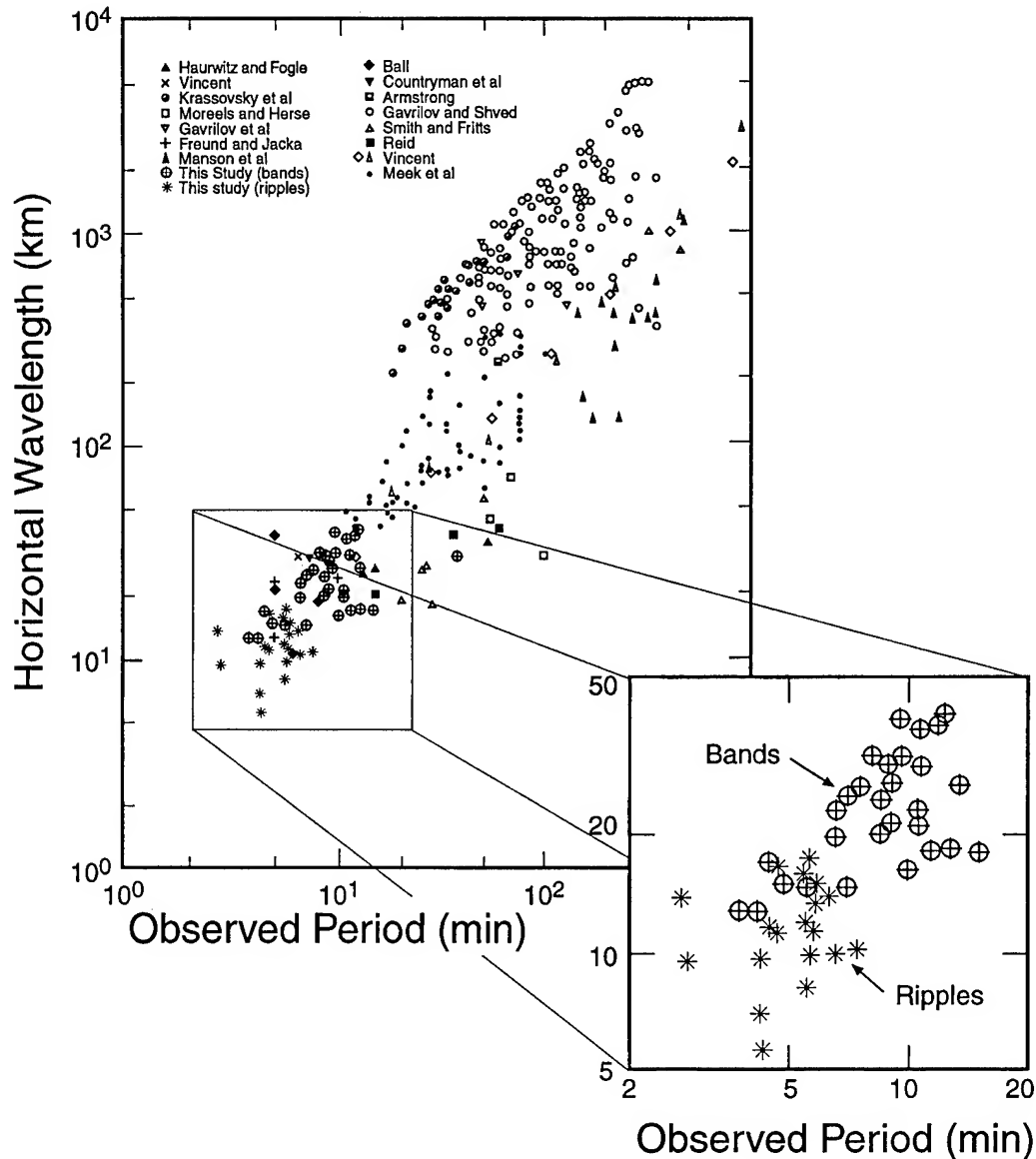


**Figure 12.** Plot showing the distribution of horizontal phase speed as a function of observed period. The two dashed lines indicate the mean phase speeds for the bands imaged prior to 2 September (36.1 ms$^{-1}$) and after this date (57.1 ms$^{-1}$).

**Figure 13.** Comparison of the image measurements recorded during the Guara campaign with the collation of radar and optical measurements of horizontal wavelength versus observed period reported by *Reid* [1986]. The exploded view shows the Guara image component.

## 4.1. Comparison With Radar and Lidar Measurements

Figure 13 compares the results of our imaging study (49 events) with the collation of measurements of horizontal scale versus observed period reported by *Reid* [1986]. This data ensemble consists of a diverse set of 408 measurements 59% of which were derived from radar data and 41% from optical observations. The data are plotted on a log-log scale and span several decades in $\tau_{ob}$ and $\lambda_h$ but are restricted significantly at short scales by the temporal and spatial resolution of the instrumentation and the observing configurations employed. The principal result of this study was the determination of a distinct trend toward longer horizontal wavelengths as the observed period of the waves increased. This data collation has subsequently been expanded greatly by the inclusion of MF Doppler radar measurements [*Reid and Vincent*, 1987] and MF triple bistatic (Gravnet) radar observations [*Manson and Meek*, 1988; *Manson*, 1990]. However, for simplicity we have chosen to

compare our results with Reid's original collation which is in excellent agreement with the more recent radar results, as noted by *Manson* [1990].

With one exception ($\tau_{ob}$ = 36.6 min), all of our data fall within the square area outlined on the figure (which also includes several points from Reid's collation). The trends evident in the image data compare very favorably with those present in the ensemble of measurements (as shown in the exploded view which includes only the "Guara component"). It is clear that the imaging results provide an important addition to this collation of wave events in the region of short observed periods ($\tau_{ob}$ < 20 min) and short horizontal wavelengths ($\lambda_h$ < 50 km). This statement is also pertinent to the more extensive wave measurements reported by *Reid and Vincent* [1987], *Manson and Meek* [1988], and *Manson* [1990] which are characterized by observed periods $\geq$10 min and, in the latter two studies, by $\lambda_h$ $\geq$40 km. Since 22 of the band events in our study

exhibited observed periods ≤10 min and all had horizontal wavelengths ≤40 km, they complement substantially the larger data sets from the MF radar investigations.

In addition to comparison with the optical and radar collation of *Reid* [1986] the results of this study have also been compared with those from previous optical [*Krassovsky et al.*, 1977; *Gavrilov and Shved*, 1982; *Jacob and Jacka*, 1985], radar [*Meek et al.*, 1985], and lidar [*Gardner and Voelz*, 1987; *Beatty et al.*, 1992] studies. Figure 14 summarizes the $(\lambda_h - \tau_{ob})$ trends derived from these investigations. The early optical measurements (lines 1 and 2) yielded trends associated with relatively large horizontal wavelength waves ($\lambda_h > 200$ km) that are outside the nominal limits of detection for the image data. However, more recent radar and optical measurements (lines 3, 4, and 5) extend to much shorter horizontal scales (<50 km wavelength) and indicate comparable trends to that determined from our image data. In particular, the trend (line 6) associated with the image measurements ≥2 September ($\lambda_h = 3.1\tau_{ob}^{1.06}$) is in remarkable agreement with that deduced by *Reid* [1986] from his "global fit" ($\lambda_h = 3.62\tau_{ob}^{1.06}$) to a diverse set of measurements. In contrast, the $(\lambda_h - \tau_{ob})$ trends inferred from the lidar measurements [*Gardner and Voelz*, 1987; *Beatty et al.*, 1992] differ markedly from the radar/optical results, particularly in the small-$\tau_{ob}$ domain. For example, a wave exhibiting a $\tau_{ob}$ of ~10 min would be expected to have a horizontal wavelength ~30 km according to the image measurements, whereas its predicted $\lambda_h$ would be over an order of magnitude smaller (~2 km) when based on the lidar results. Only at very long wave periods (several hours) and large horizontal scales (≥1000 km) do the values predicted by the radar and lidar trends become similar [e.g., *Nakamura et al.*, 1993; *Namboothiri et al.*, 1996]. The difference between radar and lidar measurements of gravity wave scales has been discussed in some detail by *Manson* [1990] and more recently by *Beatty et al.* [1992], but as indicated by both groups, a satisfactory explanation has yet to emerge.

For the short-period data under discussion here, one possible explanation for the disparity between the imager and lidar trends may have its basis in the fact that these two instruments tend to sample different parts of the gravity wave spectrum. It is important to reemphasize that an imager provides direct measurements of $\lambda_h$ and $v_h$ for short-period, quasi-monochromatic waves. In contrast, a lidar samples directly the vertical wave field from which the horizontal scales are inferred using the internal gravity wave (IGW) dispersion relationship [e.g., *Gardner and Voelz*, 1987]. Recently, *Taylor et al.* [1995c] have compared wave data recorded simultaneously by the University of Illinois wind-temperature lidar system and by the all-sky imager used for these studies. Distinct gravity wave signatures were observed simultaneously by both instruments on several occasions, yet comparison of a (limited) data set indicates that the waves detected by each system were quite different. The lidar measured short vertical wavelength waves (few kilometers) corresponding to large apparent horizontal wavelengths (~200 km), while the imager showed directly much shorter horizontal wavelength (~20 km) waves. The primary reason for this was determined to be the differing capabilities of the two instruments for sensing waves of different vertical scales. The lidar is most sensitive to short vertical wavelength waves ($\lambda_z \leq 10$ km) due to the finite width of the Na layer. In contrast, the imager is most responsive to wave events with vertical wavelengths greater than the width of the airglow layers (typically 6–10 km full width at half maximum (FWHM)).
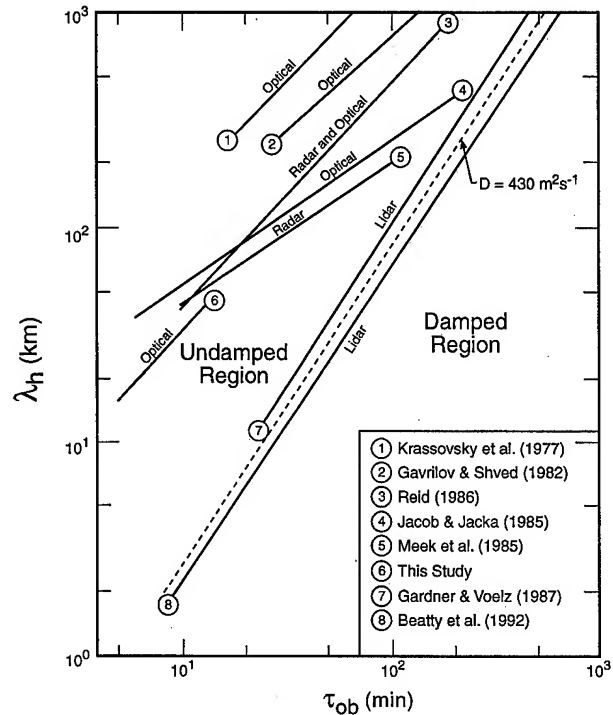


**Figure 14.** Summary plot showing the $(\lambda_h - v_h)$ trends derived from previous optical, radar, and lidar investigations. Trend 6 indicates the results of this imaging study. Note the dashed line indicates the diffusive damping limit determined from the scale independent diffusive filtering theory [*Gardner*, 1994] for a value of $D = 430$ m$^2$ s$^{-1}$.

Examination of the image data of Figure 15 (which presents values for the vertical wavelengths and intrinsic periods calculated using model winds discussed in seciton 4.2) support this conclusion as many of the waves imaged during the Guara campaign exhibited apparent vertical scales significantly larger than 10 km which would make them difficult to detect by lidar techniques. Thus as these two instruments tend to sample different parts of the gravity wave spectrum, it is not surprising that the data indicate different trends. The consequences of these differences require further investigation, but they are clearly important and should be borne in mind when comparing such data sets.

It has been suggested by *Collins et al.* [1996] that the Na lidars preferentially reveal waves which are very near the strong-diffusive-damping limit defined by *Gardner* [1994] in his scale-independent diffusive-filtering theory (SIDFT) for atmospheric gravity waves. In this theory the transition from undamped to damped wave motions is defined by the condition $\omega = m^2 D$, where $\omega$ = the intrinsic angular frequency; $m$ is the vertical wave number ($2\pi/\lambda_z$), and $D$ is the total effective diffusivity of the atmosphere. This condition results when the effective vertical diffusion velocity ($mD$) of particles in the wave-carrying medium equals the vertical phase velocity, $v_z = \omega/m$, of the wave. Wave motions satisfying the inequality $mD > v_z$ are assumed to be severely damped, whereas those with $v_z$ significantly larger than $mD$ are considered undamped.

When the condition $\omega = m^2 D$ is used in the IGW dispersion relationship, the approximate expression $\lambda_h \cong (\sqrt{2\pi D/\tau_b})\tau_i^{1.5}$ follows provided the condition $(\tau_i/\tau_b)^2 \gg 1$ is satisfied. Here, $\tau_i$ denotes the intrinsic wave period ($2\pi/\omega$),
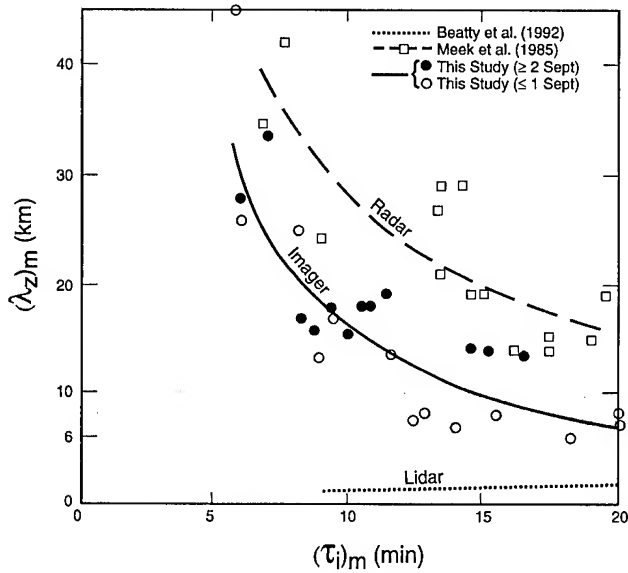
**Figure 15.** Plot showing the estimated vertical wavelength $(\lambda_z)_m$ for 26 band events as a function of their intrinsic period $(\tau_i)_m$ (solid curve) obtained using model wind data. For comparison the $(\lambda_h - \tau_i)$ radar data of *Meek et al.*, [1985] (long-dashed curve) and the $(\lambda_h - \tau_{ob})$ lidar data of *Beatty et al.* [1992] (dotted curve) are shown. The shaded area represents uncertainties in the depths of the emission layers (ranging from ~6 to 10 km full width at half maximum).

and $\tau_b$ is the Brunt-Vaisala period (see section 4.2). In Figure 14 the dashed line between the two lidar trends (7 and 8) represents the $(\lambda_h - \tau_{ob})$ relationship assuming $\tau_i = \tau_{ob}$ and using values of $D = 430$ m$^2$ s$^{-1}$ and $\tau_b = 5.0$ min. This line of demarcation between the undamped (left of line) and damped (right of line) wave motions in the SIDF theory was chosen arbitrarily to lie approximately midway between the two lidar trends for clarity of presentation. (The values of $D$ required to match lines 7 and 8 are ~550 m$^2$ s$^{-1}$ and 350 m$^2$ s$^{-1}$, respectively.) The region to the left of the dashed line (undamped waves) contains all of the trend lines derived from optical and/or radar data. However, as noted by *Manson* [1990], a small but significant number of the radar-deduced wave events also occurred in the strong-damping region even when intrinsic parameters were used in their analysis. Concerning the optical measurements, nearly all of the reported wave events appear to lie well within the undamped region.

The SIDF theory provides a credible physical explanation for the highly significant trends ($r^2 \sim 0.97$) in the lidar results of *Gardner and Voelz* [1987] and *Beatty et al.* [1992] provided these systems preferentially select wave events at or very near the saturation limit for wave growth (i.e., large-amplitude waves). In comparison, the physical basis for the less significant but clearly apparent trends in the optical and radar results is not so evident. However, system and sampling limitations are expected to influence the trend analyses. We are currently investigating trends in the imager data using a larger ensemble of wave events resulting from measurements during other campaigns. Preliminary analysis of these data sets support the general $(\lambda_h - \tau_{ob})$ behavior deduced from the limited number of band events observed during the Guara campaign suggesting an inherent trend in the imager data. A possible "driver" for this trend in the $(\lambda_h, \tau_{ob})$ image results is the finite thick-

ness of the airglow layers. In particular, cancellation effects within the layer are expected to limit the readily observable wave events to those which satisfy the condition $(\lambda_z/d) > 1$, where $d$ represents the effective layer thickness [*Gavrilov and Shved*, 1982; *Schubert et al.*, 1991]. Thus waves with $\lambda_z < 6$–10 km (the typical FWHM of the emission layers) may be strongly damped, whereas waves of longer vertical wavelength would be essentially unaffected. A lower limit for $\lambda_z$ implies a corresponding lower limit for $\lambda_h$, based on the dispersion relationship [*Hines*, 1960], and the lower limit for $\lambda_h$ should increase with increasing intrinsic period. This hypothetical source for the trending in the imager results appears promising, but further analyses are needed to clarify this possibility.

### 4.2. Vertical Wavelength and Background Winds

In the presence of a background wind the observed wave period may differ significantly from its intrinsic period $(\tau_i)$ as a result of Doppler shifting by the background winds. The intrinsic period of the wave, measured in a frame of reference moving with the background wind, is related to the observed period through

$$\tau_i = \tau_{ob}(v_h)/(v_h - \bar{U}), \tag{1}$$

where $\bar{U}$ is the component of the background wind in the direction of horizontal motion of the wave. Once $\tau_i$ is known for each event, the vertical wavelengths $(\lambda_z)$ can then be investigated using the approximate dispersion relationship

$$\lambda_z \simeq (\lambda_h/\sqrt{(\tau_i/\tau_b)^2 - 1}). \tag{2}$$

This relationship is valid for an isothermal, stationary atmosphere when both $\lambda_h$ and $\lambda_z$ are small compared to $C\tau_b$ (typically $C\tau_b \sim 100$ km), where $C$ is the speed of sound and $\tau_b$ the Brunt-Vaisala period (or buoyancy period) of the atmosphere. For this study we have computed height-averaged values (~85–95 km) of $\tau_b$ based on the mean nocturnal rotational temperatures derived from the OH M (6, 2) and O$_2$ atmospheric (0, 1) emissions. These temperature measurements were obtained using a narrow field, tilting-filter photometer [*Takahashi et al.*, 1986] operated in close proximity to the all-sky imager at Alcantara by INPE personnel. The precise values of $\tau_b$ are not critical for this study in view of our use of model winds for the vertical wavelength calculations.

Unfortunately, coincident wind data are not available for the observation period of the imaging measurements. However, in situ rocket soundings of the stratospheric and mesospheric winds were made over a ~10-day period during the first part of the campaign (16–25 August) using the falling-sphere technique (F. Schmidlin, private communication, 1996). These measurements were made close to full moon when almost no image data were recorded and reveal relatively constant eastward (zonal) winds around 0–20 ms$^{-1}$ at 85 km and a variable (~0–40 ms$^{-1}$) northward (meridional) wind component. (Data available at 90 km are less reliable and are not considered here.) To investigate the expected "mean" wind conditions during the primary data-taking interval, we have therefore used model results based on the MSIS model [*Hedin et al.*, 1993a, b] for this site and time of year. Estimates of the meridional and zonal wind components were obtained for three heights, 85, 90, and 95 km (corresponding closely to the centroids of the OH, Na, and OI emission layers) for each night by averaging over a 3-hour period centered on local midnight (M. Hagan, private communication, 1996). The model results at 95

km (where most of the waves were measured) indicate steadily increasing eastward winds rising from ~13 to 19 ms$^{-1}$ during the campaign period. In comparison the meridional winds are <2 ms$^{-1}$ southward during the first period but reverse to northward shortly before the second period and reach ~5 ms$^{-1}$. At 90 km the model predicts similar values for the zonal wind at ~15 ms$^{-1}$, but the meridional wind is northward decreasing steadily from ~15 to 5 ms$^{-1}$ during the campaign period. Thus the model estimates relatively low wind speeds throughout the campaign in reasonable accord with the rocket measurements obtained earlier.

Because of the paucity of equatorial wind measurements from which this empirical model was formulated, these winds can, at best, only be considered as indicative of the true mean wind conditions. The computed estimates of $\tau_b$ and the derived parameters of $(\tau_i)_m$ and $(\lambda_z)_m$ using the model winds (as denoted by the subscript $m$) are listed in Table 2 together with the measured wave parameters. Despite the uncertainties these computations represent our best estimates of the vertical scales of the waves imaged during the Guara campaign. Examination of Table 2 indicates that the background winds had a significantly larger impact on the estimates of intrinsic periods for the waves imaged prior to 2 September, when the observed phase speeds were relatively low (mean value = 36.1 ms$^{-1}$), as compared with the second period when the wave phase speeds were much higher (mean value = 57.1 ms$^{-1}$) (see Figure 12). Assuming a well-defined trend in the intrinsic wavelength-period relationship for the image data, these results suggest that the effect of the background winds is to mask its appearance in the ($\lambda_h$, $\tau_{ob}$) diagram. For example, during the first interval (≤1 September) the intrinsic wave periods differed significantly (up to about 80%) from the observed periods, and no obvious trend was discerned (see Figure 11b). However, for the second observing interval the difference between $\tau_i$ and $\tau_{ob}$ was often small (typically in the range −15% to 30%) due to the higher wave phase speeds, and a clear trend was found (Figure 11c). The overall trend for the campaign was very similar but less well defined and reflected a range of observing conditions. If this is the case, then ($\lambda_h$, $\tau_{ob}$) trends should be most apparent under either very low wind conditions (i.e., around the equinox) or when $v_h \gg \bar{U}$ at the azimuth of wave progression.

This phenomenon has been noted by *Reid and Vincent* [1987] who investigated ($\lambda_h$ − $\tau_{ob}$) trends using radar data obtained during various seasons. The individual plots clearly show a higher degree of correlation around the equinox periods, compared with those of other months, that was attributed to reduced winds. The trend associated with our ($\tau_{ob}$, $\lambda_h$) pairs measured on and after 2 September ($\lambda_h = 3.14\tau_{ob}^{1.06}$) may therefore be more representative of the intrinsic period versus horizontal wavelength relationship. The remarkable agreement with the trend deduced by *Reid* [1986] from his global fit ($\lambda_h = 3.62\tau_{ob}^{1.06}$) is at first glance surprising. However, as Reid's collation reflects a wide variety of local times and seasonal conditions, the average power-law fit to this diverse set of measurements may therefore be more suggestive of an intrinsic trend.

Figure 15 presents our estimates of the vertical wavelengths associated with 26 of the band events versus ($\tau_i)_m$ on a linear scale. The same coding of events as used in previous figures is repeated here. These estimates are compared with a set of 14 intrinsic values deduced by *Meek et al.* [1985] (open squares) using simultaneous observations of mesospheric waves and

wind velocities recorded by the Gravnet MF radar system at Saskatoon (52°N). In addition, the measured ($\lambda_z$ − $\tau_{ob}$) relationship (maximum likelihood power-law fit) obtained by *Beatty et al.* [1992] using Na lidar observations of 62 quasi-monochromatic gravity wave events observed in the vicinity of the mesopause over Arecibo, Puerto Rico (~18°N), is plotted (dotted line). A detailed comparison of trends associated with these three data sets is complicated by the differences in the system limits and in the case of the lidar measurements, by Doppler-shifting effects (as no estimates of the intrinsic periods were made). The Gravnet system limits are $\tau_{ob} \geq 10$ min and $\lambda_z \geq 20$ km at $\tau_i = 10$ min, decreasing to $\lambda_z \geq 10$ km at $\tau_i = 20$ min. The limits for the lidar measurements of interest are $\tau_{ob} \geq 4$ min and $\lambda_z \leq 20$ km [*Beatty et al.*, 1992]. In comparison, the limits associated with the imaging measurements are $\tau_{ob} \geq 2$-3 min and $\lambda_z \geq 6$-10 km, due to layer-thickness limitations (as discussed earlier).

The trend associated with the Gravnet results (long-dashed curve) exhibits a similar shape to that obtained in the present imaging study but is displaced toward longer vertical wavelengths. Both sets of measurements suggest significant vertical scales, ~15 km (imager) and ~25 km (radar) for an intrinsic wave period of 10 min. Furthermore, both curves indicate significantly larger vertical wavelengths near the Brunt-Vaisala period (~5 min), in accord with the expectation of near vertical energy propagation as this limit is approached. In sharp contrast, the lidar results (short-dashed curve) suggest a $\lambda_z$ of only about 1 km at 10 min, with a decreasing trend continuing to near $\tau_b$ [*Beatty et al.*, 1992]. (Note that the shallow gradient of the lidar curve indicates that this conclusion is valid even under significant Doppler-shifting conditions.) Thus both the measured horizontal scale trends and the inferred vertical scale trends highlight a significant difference between the imager and the lidar data at short observed periods. The figure also shows that all of the wave events measured on and after 2 September (solid circles) exhibit values of ($\lambda_z)_m$ which are significantly greater than the nominal airglow layer thickness (indicated by the shaded band). In comparison, several events imaged earlier in the campaign (open circles) exhibit vertical scale sizes less than or similar to the nominal depth of the airglow layer where cancellation effects are expected to be significant [*Gavrilov and Shved*, 1982; *Schubert et al.*, 1991]. These wave events are characterized by relatively low phase speeds (mean value = 36.1 ms$^{-1}$) and are thus more susceptible to an increased uncertainty relating to the impact of background wind corrections for the $\lambda_z$ calculations. The implications are that the model has most probably underestimated the actual mean wind conditions during this period. This suggestion is in good accord with the lack of a significant ($\lambda_h$, $\tau_{ob}$) trend prior to 2 September.

### 4.3. Wave Sources

On the basis of the detection of a major change in the azimuthal distribution of the waves (Figure 8) the image data were divided into two sets covering the periods 6 August to 1 September (prior to the equinox) and 2 September to 16 October (around the equinox). One likely possibility for the apparent predominance for wave propagation toward ~NE-ENE is that seasonal changes in the stratospheric and mesospheric wind fields occurred during this time resulting in large changes in the filtering of the gravity wave spectrum. A second possibility is that a powerful wave source may have developed to the ~SW-WSW of Alcantara (over the South American continent)
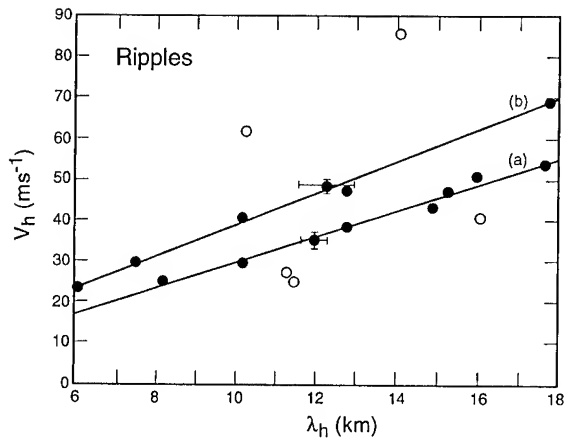
**Figure 16.** Plot of the ripple data of Figure 9 showing the bimodal distribution of the data: Line a indicates a wave period of 5.18 ± 0.26 min close to the Brunt-Vaisala period while line b has a period of 4.32 ± 0.15 min close to the acoustic cutoff period. An example error bar is given for each line to emphasize the distinction between the two trends. Note that only the points which comprised the central peak of the histogram distribution of Figure 6 were used in the trend analysis.

around 2 September. Wind filtering has been shown to play an important role in governing the azimuthal flux of wave energy penetrating into the upper atmosphere through the formation of critical layers [e.g., Ebel et al., 1987; Taylor et al., 1993]. For the Guara campaign a reduction in amplitude of the prevailing winds in the stratosphere and lower mesosphere associated with seasonal changes around the equinox could have opened a "window" permitting wave propagation into the upper mesosphere from sources located over the South American continent. This hypothesis supports the appearance of strong directionality in the wave headings around the equinox period. Alternatively, it is possible that the marked anisotropy in the wave motions may reflect changes in the prevailing flux of gravity waves into the mesosphere from, for example, an ensemble of freely propagating and/or ducted waves that could have originated from a variety of sources to a predominance for waves generated by a "local" tropospheric source located over the South American continent. In either case, the frequent recurrence of wave progression toward the equator on an ~NE-ENE heading indicates that the source region was active for a considerable period of time (persisting throughout September and early October). One possible candidate for the wave source is the Andes mountain range. This is favorably located to the W and SW of Alcantara but at a very large distance of ≥3000 km. In the absence of background winds, short-period (<1 hour) gravity waves generated near the Earth's surface would not be expected to propagate large horizontal distances (a few hundred kilometers) before they

reached the airglow layers [Hines, 1967]. However, if the prevailing stratospheric and mesospheric winds acted to increase the intrinsic periods of the waves progressing toward the ~NE-ENE during this interval, then the horizontal distance traveled by these waves, prior to reaching the airglow layers, could have increased significantly [e.g., Taylor and Edwards, 1991]. Another possibility is that upon reaching airglow altitudes, the waves may have become ducted by the mesospheric background winds further increasing their range of propagation from the source region. Thus although the Andes mountains are at an extreme range, they are a potentially good candidate. An alternative potential source is strong tropospheric convection over central Brazil. The dominant source (or sources) of these waves remains unknown at the present time but is under investigation.

### 4.4. Ripple Periodicities

The sharp distribution in observed periodicities of the ripple events (Figure 6b) (average $\tau_{ob}$ = 5.1 min, range 2.7–6.9 min) is a characteristic property that has not been reported previously. As expected, the ripples exhibited shorter horizontal wavelengths (range typically 5–15 km) than bands. However, they were also found to exhibit a significantly different distribution than the bands when plotted in the ($\lambda_h - \tau_{ob}$) format. This is illustrated in Figure 10 which shows the ripples clustered around the mean observed period of ~5 min and exhibiting no obvious ($\lambda_h - \tau_{ob}$) trend. These properties set ripples apart from most band displays. In particular, the bimodal form of the ($\lambda_h - v_h$) distribution evident in the ripple data of Figure 9 is most unusual. Figure 16 replots the ripple data of Figure 9 on an expanded scale to investigate this phenomenon. In Figure 16 no attempt has been made to distinguish between ripples observed prior to or after 2 September (as no association was found). Out of a total of 19 events, 14 were found to be associated with two well-defined trend lines. The distinct nature of these two trends is emphasized by the example error bars in each case.

A regression analysis was carried out following procedures similar to those described by Wonnacott and Wonnacott [1981]. The results of this analysis (which uses only the 14 events associated with the central peak in Figure 6) are summarized in Table 5, where the parameters $A$ and $B$ for linear fits of the form $v_h = A + B\lambda_h$ are given together with confidence limits and the squared correlation coefficients ($r^2$). The table shows that "$A$" appears to be zero to within $1\sigma$ for both trend lines, suggesting a more simplified relation $v_h = B\lambda_h$. These linear relationships correspond to highly significant trends ($r^2 = 0.990$). Thus despite the relatively small number of events associated with each trend ($N$ = 6 and 8), the relationships are significant at a confidence level of about 0.01%. The apparent frequencies associated with these two trend lines are 3.22 ± 0.16 mHz and 3.86 ± 0.13 mHz which correspond to observed periods of 5.18 ± 0.26 min and 4.32 ± 0.15 min.

**Table 5.** Results of Trend Analysis for Ripple Data of Figure 16 (Using 14 Points Associated With the Central Peak of Figure 6)

| Ripples | Coefficient, $A$ | Frequency, $B$, mHz | Correlation Coefficient Squared, $r^2$ | Total Data Pairs, $N$ | $\tau_{ob}$, min |
|---------|------------------|----------------------|-----------------------------------------|------------------------|---------|
| Line a | −2.34 ± 2.25 | 3.22 ± 0.16 | 0.986 | 8 | 5.18 ± 0.26 |
| Line b | 0.44 ± 1.54 | 3.86 ± 0.13 | 0.996 | 6 | 4.32 ± 0.15 |

Parameters $A$ and $B$ were determined by fitting to the linear equation $v_h = A + B\lambda_h$.

It is interesting to note that these values for $\tau_{ob}$ are very close to those identified with the limits for the gravity wave (Brunt-Vaisala) and acoustic wave regimes in the IGW dispersion relationship. For an isothermal, stationary atmosphere, IGW theory predicts that there is a gap between the acoustic regime and the gravity wave regime (defined by these two limits) where no wave propagation occurs. Examination of Figure 16 reveals a distinct "gap" between the two trend lines where no data points are found. The uncertainties in the measurements (indicated by the example error bars) are insufficient to bridge this gap. Thus one possible interpretation consistent with the determination of two distinct trends is that the ripple patterns imaged during the Guara campaign comprised wave motions generated within the acoustic branch as well as the gravitational branch of the IGW spectrum. However, this interpretation appears to be in conflict with the expectation of much higher phase speeds at acoustic wave periods [Hines, 1960]. As the effect of background winds on the wave motions (assuming they are generated in situ) would be to fill in this gap, and because many of the ripple events exhibited relatively high phase speeds ($>40$ ms$^{-1}$), it is unlikely that Doppler shifting effects can account for the observed bimodal distribution. No obvious differences in morphology of the wave motions comprising this bimodal distribution were found, and it remains to be seen if it is also evident in other more substantial midlatitude ripple measurements that are currently under analysis.

Ripples are similar in morphology and dynamics to the billow-type waves seen in noctilucent clouds many of which are thought to be generated in situ by short-lived velocity shears ($\geq 40$ ms$^{-1}$ km$^{-1}$) in the background winds [Taylor and Hapgood, 1990]. Waves generated by this mechanism (Kelvin-Helmholtz instability) would be expected to exhibit observed periods close to the local Brunt-Vaisala period and would have variable and limited lifetimes (depending on the duration of the shear). Alternatively, it is possible that ripples are generated in situ by the breakdown of a larger-scale wave (possibly of tidal origin) either through parametric excitation [Tuan et al., 1979] or by the onset of a three-dimensional convective-type instability [e.g., Fritts et al., 1993]. In the latter case, the orientation of the ripples would be expected to be near perpendicular to the large-scale perturbing wave. Isolated ripple-type patterns oriented almost orthogonal to large-scale band patterns were observed on several occasions during the Guara campaign, suggesting a causal relationship. However, Fritts et al. [1996] have recently modeled the generation of ripple-type waves using data obtained during the CORN campaign and have determined that the scale size of the perturbing (breaking) wave should be much larger than that of the bands. In general, ripples of scale-sizes ($\lambda_h > 5$ km) and lifetimes ($>$several minutes), which typify most events, are currently not thought to be compatible with the convective instability theory. Without further information it is not possible to distinguish between these potential mechanisms.

Finally, Witt [1962] suggested that if NLC billows are generated in situ, they will tend to move with the background wind. NLC bands, on the other hand, may be expected to progress in any direction provided their horizontal phase speed exceeds the background wind speed [Ebel et al., 1987; Taylor et al., 1993]. Assuming ripples are generated in situ, then their average motions may provide some information on the prevailing wind conditions in the 80–100 km region. As already mentioned, wind measurements were not performed during the period when most of the image data were obtained. However, the dominance of eastward propagating components for the ripples observed throughout the campaign (Figure 8) is remarkably consistent with zonal flow predicted by the MSIS model. Furthermore, the observed reversal in the meridional wave progression from southward to northward during the campaign is also consistent with the modeled winds at the 95 km level. The magnitudes of the predicted winds are, however, generally smaller than the observed wave speeds, and it remains to be seen whether ripples are strongly influenced by the background wind. Indeed, several of the ripple events recorded during the second observing interval progressed in approximately the same direction ($\sim$NE-ENE) as the band displays, suggesting a common origin.

## 5. Summary

Statistical measurements of short-period gravity waves are few and this data set, comprising over 50 events, represents a major first step in quantifying the occurrence frequency and properties of small-scale gravity waves present at equatorial latitudes. Analysis of these data indicates two apparently separable wave sets, termed bands and ripples, and a marked anisotropy in the distribution of wave headings around the equinox with a large fraction ($>65\%$) of the band-type wave motions progressing toward the equator on an $\sim$NE-ENE heading.

Comparison of these wave data with more extensive measurements obtained by radar and lidar techniques in recent years indicates a similar tendency for the observed period of the waves to increase with increasing horizontal wavelength. In particular, the ($\tau_{ob} - \lambda_h$) trend determined from the band data recorded around the equinox period agrees very well with that deduced by Reid [1986] using a diverse collation of radar and optical measurements. As the imaging system is most sensitive to waves of a smaller horizontal scale than those readily detected by radar, these measurement techniques are highly complementary. However, a similar comparison with the lidar data indicates considerable differences that exceed an order of magnitude at short $\tau_{ob}$. The reasons for this discrepancy are thought to be related to the differing sensitivities of the two instruments to waves of different vertical scale sizes, but further joint research is necessary to investigate this effect.

It is conjectured that the high degree of correlation in the measurements obtained around the equinox may have resulted from a reduction in the stratospheric and mesospheric winds associated with seasonal changes. However, it remains to be seen how the trends observed in this data set (limited to $\sim 2$ months) compare with results of other more substantial image measurements obtained during different seasons. The onset of a series of highly directional wave motions during this period also appears to be associated with equinox conditions. One potential source for the large flux of waves observed on an $\sim$NE-ENE heading may be associated with strong winds blowing over the Andes mountain range. However, an investigation of the penetration of wave energy into the mesosphere at equatorial latitudes and of potential tropospheric sources for these waves will be the subject of a separate report.

Short-period mesospheric wave motions have now been observed from a number of middle and low-latitude sites around the world. The data presented here, using a high-resolution CCD imager, contribute significantly to the "global picture" by revealing a wealth of wave structure at equatorial latitudes.

The band displays were usually (but not always) observed in all three of the nightglow emissions imaged (OI, Na, and OH), indicating freely propagating or ducted wave behavior. In comparison, the ripples were often present in only one of the three emissions, consistent with the hypothesis of in situ generation over a limited height range. However, the Guara data indicate a considerable region of overlap in the spatial and temporal scales of the bands and ripples, and the additional information provided by the imager (e.g., geographic extent and pattern lifetimes) was often necessary to distinguish accurately between these two groups. This distinction between waves generated in situ at airglow altitudes and those whose sources reside naturally in the lower atmosphere is an essential first step toward estimating the flux of quasi-monochromatic gravity waves into the mesosphere and lower thermosphere and their associated momentum deposition.

# References

Armstrong, E. B., The association of visible airglow features with a gravity wave, *J. Atmos. Terr. Phys.*, 44(4), 325, 1982.

Armstrong, E. B., Irregularities in the 80–100 km region: A photographic approach, *Radio Sci.*, 21(3), 313, 1986.

Baker, D. J., and A. T. Stair Jr., Rocket measurements of the altitude distributions of the hydroxyl airglow, *Phys. Scr.*, 37, 611, 1988.

Beatty, T. J., C. A. Hostetler, and C. S. Gardner, Lidar observations of gravity waves and their spectra near the mesopause and stratopause at Arecibo, *J. Atmos. Sci.*, 49(6), 477, 1992.

Clairemidi, J., M. Herse, and G. Moreels, Bi-dimensional observations of waves near the mesopause at auroral latitudes, *Planet. Space Sci.*, 33(9), 1013, 1985.

Collins, R. L., X. Tao, and C. S. Gardner, Gravity wave activity in the upper mesosphere over Urbana, Illinois: Lidar observations and analysis of gravity wave propagation models, *J. Atmos. Terr. Phys.*, 58, 1905, 1996.

Ebel, A., A. H. Manson, and C. E. Meek, Short period fluctuations of the horizontal wind measured in the upper atmosphere and possible relationships to internal gravity waves, *J. Atmos. Terr. Phys.*, 49, 385, 1987.

Fagundes, P. R., H. Takahashi, Y. Sahai., and D. Gobbi, Observations of gravity waves from multispectral mesospheric nightglow emissions observed at 23°S, *J. Atmos. Terr. Phys.*, 57(4), 395, 1995.

Fritts, D. C., and R. A. Vincent, Mesospheric momentum flux studies at Adelaide, Australia: Observations and gravity wave-tidal interaction model, *J. Atmos. Sci.*, 44, 605, 1987.

Fritts, D. C., J. R. Isler, G. E. Thomas, and Ø. Andreassen, Wave breaking signatures in noctilucent clouds, *Geophys. Res. Lett.*, 20(19), 2039, 1993.

Fritts, D. C., J. R. Isler, J. H. Hecht, R. L. Walterscheid, and Øyvind Andreassen, Wave breaking signatures in sodium densities and OH nightglow, 2, Simulation of wave and instability structures, *J. Geophys. Res.*, in press, 1996.

Gardner, C. S., Diffusive filtering theory of gravity wave spectra in the atmosphere, *J. Geophys. Res.*, 99, 20,601, 1994.

Gardner, C. S., and D. G. Voelz, Lidar studies of the nighttime sodium layer over Urbana, Illinois. 2, Gravity waves, *J. Geophys. Res.*, 92, 4673, 1987.

Gavrilov, N. M., and G. M. Shved, Study of internal gravity waves in the lower thermosphere from observations of the nocturnal sky airglow [OI] 5577 Å in Ashkhabad, *Ann. Geophys.*, 38(6), 789, 1982.

Goldberg, R. A., M. Friedrich, G. A. Lehmacher, F. J. Schmidlin, C. L. Croskey, J. D. Mitchell, D. C. Fritts, and W. E. Swartz, MALTED: A rocket/radar study of dynamics and turbulence in the equatorial mesopause region, in *Proceedings of the 12th ESA Symposium on Rocket and Balloon Programs and Related Research*, ESA SP-370, p. 113, Eur. Space Agency, Neuilly, France, 1995.

Hapgood, M. A., and M. J. Taylor, Analysis of airglow image data, *Ann. Geophys.*, 38(6), 805, 1982.

Haurwitz, B., and B. Fogle, Wave forms in noctilucent clouds, *Deep Sea Res.*, 16, 85, 1969.

Hedin, A. E., E. L. Fleming, A. H. Manson, F. J. Schmidlin, S. K. Avery, and S. J. Franke, Empirical wind model for the middle and lower atmosphere, 1, Local time average, *NASA Tech. Memo. 104581*, 1993a.

Hedin, A. E., et al., Empirical wind model for the middle and lower atmosphere, 2, Local time variations, *NASA Tech. Memo. 104592*, 1993b.

Herse, M., G. Thuillier, G. Camman, J.-L. Chevassut, and M. Fehrenbach, Ground based instrument for observing near IR nightglow inhomogeneities at zenith and throughout the sky, *Appl. Opt.*, 28, 3944, 1989.

Hines, C. O., Internal atmospheric gravity waves at ionospheric heights, *Can. J. Phys.*, 38, 1441, 1960.

Hines, C. O., On the nature of traveling ionospheric disturbances launched by low-altitude nuclear explosions, *J. Geophys. Res.*, 72, 1877, 1967.

Jacob, P. G., and F. Jacka, Gravity wave vertical energy flux at 95 km, in *Proc. MAP Handb.*, 18, 248, 1985.

Krassovsky, V. I., B. P. Potapov, A. I. Semenov, M. V. Shagaev, N. N. Shefov, V. G. Sobolev, and T. I. Toroshelidze, Internal gravity waves near the mesopause and the hydroxyl emission, *Ann. Geophys.*, 33(3), 347, 1977.

Manson, A. H., Gravity wave horizontal and vertical wavelengths: An update of measurements in the mesopause region (~80–100 km), *J. Atmos. Sci.*, 47(23), 2765, 1990.

Manson, A. H., and C. E. Meek, Gravity wave propagation characteristics (60–120 km) as determined by the Saskatoon MF radar (Gravnet) system: 1983–85 at 52°N, 107°W, *J. Atmos. Sci.*, 45, 932, 1988.

Meek, C. E., I. M. Reid, and A. H. Manson, Observations of mesospheric wind velocities, 1. Gravity wave horizontal scales and phase velocities determined by spaced wind observations, *Radio Sci.*, 20, 1363, 1985.

Moreels, G., and M. Herse, Photographic evidence of waves around the 85 km level, *Planet. Space Sci.*, 25, 265, 1977.

Nakamura, T., T. Tsuda, M. Yamamoto, S. Fukao, and S. Kato, Characteristics of gravity waves in the mesosphere observed with the middle and upper atmosphere radar, 2, Propagation direction, *J. Geophys. Res.*, 98, 9811, 1993.

Namboothiri, S. P., T. Tsuda, M. Tsutsumi, T. Nakamura, C. Nagasawa, and M. Abo, Simultaneous observations of mesospheric gravity waves with the MU radar and sodium lidar, *J. Geophys. Res.*, 101, 4057, 1996.

Peterson, A. W., Airglow events visible to the naked eye, *App. Opt.*, 18, 3390, 1979.

Peterson, A. W., and G. W. Adams, OH airglow phenomena during the 5–6 July 1982 total lunar eclipse, *App. Opt.*, 22, 2682, 1983.

Reid, I. M., Gravity wave motions in the upper middle atmosphere (60–110 km), *J. Atmos. Terr. Phys.*, 48(11–12), 1057, 1986.

Reid, I. M., and R. A. Vincent, Measurements of the horizontal scales and phase velocities of short period mesospheric gravity waves at Adelaide, Australia, *J. Atmos. Terr. Phys.*, 49, 1033, 1987.

Schubert, G., R. L. Walterscheid, and M. P. Hickey, Gravity wave-driven fluctuations in OH nightglow from an extended, dissipative emission region, *J. Geophys. Res.*, 96, 13,869, 1991.

Swenson, G. R., and S. B. Mende, OH emission and gravity waves (including a breaking wave) in all-sky imagery from Bear Lake, UT., *Geophys. Res. Lett.*, 21, 2239, 1994.

Swenson, G. R., M. J. Taylor, P. J. Espy, C. Gardner, and X. Tao, ALOHA-93 measurements of intrinsic AGW characteristics using

airborne airglow imager and ground-based Na wind/temperature lidar, *Geophys. Res. Lett., 22*, 2841, 1995.

Takahashi, H., Y. Sahai, and P. P. Batista, Airglow $O_2(^1\Sigma)$ atmospheric band at 8645Å and the rotational temperature observed at 23°S, *Planet. Space Sci., 34*, 301, 1986.

Taylor, M. J., TV observations of mesospheric wave structure, *in Collection of Works of the International Workshop of Noctilucent Clouds*, 153, Valgus, Tallinn, 1986.

Taylor, M. J., and R. Edwards, Observations of short period mesospheric wave patterns: In situ or tropospheric wave generation?, *Geophys. Res. Lett., 18*(7), 1337, 1991.

Taylor, M. J., and F. J. Garcia, A two-dimensional spectral analysis of short period gravity waves imaged in the OI(557.7 nm) and near infrared OH nightglow emissions over Arecibo, Puerto Rico, *Geophys. Res. Lett., 22*(18), 2473, 1995.

Taylor, M. J., and M. A. Hapgood, Identification of a thunderstorm as a source of short period gravity waves in the upper atmospheric nightglow emissions, *Planet. Space Sci., 36*(10), 975, 1988.

Taylor, M. J., and M. A. Hapgood, On the origin of ripple-type wave structure in the OH nightglow emission, *Planet. Space Sci., 38*(11), 1421, 1990.

Taylor, M. J., and M. J. Hill, Near infrared imaging of hydroxyl wave structure over an ocean site at low latitudes, *Geophys. Res. Lett., 18*(7), 1333, 1991.

Taylor, M. J., M. A. Hapgood, and P. Rothwell, Observations of gravity wave propagation in the OI(557.7 nm), Na(589.2 nm) and the near infra-red OH nightglow emissions, *Planet. Space Sci., 35*(4), 413, 1987.

Taylor, M. J., E. H. Ryan, T. F. Tuan, and R. Edwards, Evidence of preferential directions for gravity wave propagation due to wind filtering in the middle atmosphere, *J. Geophys. Res., 98*(A4), 6047, 1993.

Taylor, M. J., M. B. Bishop and V. Taylor, All-sky measurements of short period waves imaged in the OI(557.7 nm), Na (589.2 nm) and near infrared OH and $O_2(0, 1)$ nightglow emissions during the ALOHA-93 campaign, *Geophys. Res. Lett., 22*(20), 2833, 1995a.

Taylor, M. J., V. Taylor, and R. Edwards, An investigation of thunderstorms as a source of short period mesospheric gravity waves, *in The Upper Mesosphere and Lower Thermosphere: A Review of Experiment and Theory, Geophys. Monogr., Ser.*, vol. 87, edited by R. M. Johnson and T. L. Killeeu, p. 177, AGU, Washington, D. C., 1995b.

Taylor, M. J., Y. Y. Gu, X, Tao, C. S. Gardner, and M. B. Bishop, An investigation of intrinsic gravity wave signatures using coordinated lidar and nightglow image measurements, *Geophys. Res. Lett., 22*(20), 2853, 1995c.

Tuan, T. F., R. Hedinger, S. M. Silverman, and M. Okuda, On gravity wave induced Brunt-Vaisala oscillations, *J. Geophys. Res., 84*, 393, 1979.

Witt, G., Height, structure and displacements of noctilucent clouds, *Tellus, 24*, 1, 1962.

Wonnacott, T. H., and R. J. Wonnacott, Regression: A second course in statistics, John Wiley, New York, 1981.

World Meteorological Organization (WMO), *International Noctilucent Cloud Observation Manual, WMO-250.TP.138*, Geneva, 1970.

S. Clark, W. R. Pendleton Jr., and M. J. Taylor, Space Dynamics Laboratory and Physics Department, Engineering Building, Room 241, Utah State University, Logan, UT 84322. (e-mail: taylor@psi.sci.SDL.usu.edu)

D. Gobbi and H. Takahashi, Instituto Nacional de Pesquisas Espaciais, INPE, C.P. 515, 12201-970, São José dos Campos, São Paulo, Brazil.

R. A. Goldberg, Laboratory for Extraterrestrial Physics, NASA Goddard Space Flight Center, MD 20771.

# Two-dimensional spectral analysis
# of mesospheric airglow image data

F. J. Garcia, M. J. Taylor, and M. C. Kelley

A technique to analyze short-period (<1 hour) gravity wave structure in all-sky images of the airglow emissions is described. The technique involves spatial calibration, star removal, geographic projection, regridding, and flat fielding of the data prior to the determination of the horizontal wave parameters (wavelength, velocity, and period), by use of standard two-dimensional Fourier analysis techniques. The method was developed to exploit the information that is now available with wide-field solid state imaging systems. This technique permits interactive and quantitative investigations of large, complex data sets. Such studies are important for investigating gravity wave characteristics, their interaction with the airglow emissions, and their geographic and seasonal variability. We study one event of this type here and present possible evidence of a nonlinear wave–wave interaction in the upper atmosphere. © 1997 Optical Society of America

*Key words:* Gravity waves, airglow, geographic projection, spectral estimation.

## 1. Introduction

It is now known that there are several airglow emission layers that result from chemiluminescent reactions of atomic and molecular species in the upper mesosphere. Table 1 lists the most prominent of these emissions in the 80–100-km height range. These emissions exhibit considerable spatial and temporal fluctuations that have been attributed to the passage of atmospheric gravity waves through the airglow layers.[1-11] Gravity waves are known to be important drivers of mesoscale fluctuations throughout the atmosphere.[12] At mesospheric heights, the waves can saturate and deposit their energy and momentum into the mean flow, a process that has been found to be an important factor that contributes to the global-scale circulation of the upper atmosphere.[13] Small-scale waves of the type readily detected by airglow imaging (exhibiting horizontal wavelengths ranging from a few to several tens of kilometers and periods of <1 hour) have been shown to contribute significantly (~70%) to the momentum budget.[14,15] Many of these waves are

thought to be generated by localized disturbances within the troposphere, such as thunderstorms, deep convective regions, and fronts, and by orographic forcing resulting from winds flowing over mountains. As these waves propagate through the airglow layers, they induce significant density and temperature perturbations that affect the local chemistry and that are readily detected at ground level as line-of-sight (column) variations in the emission intensity. Various instruments, including photometers, interferometers, spectrometers and imagers, have been used to investigate this phenomenon. In particular, high resolution, solid-state (CCD) imagers are now regularly used to provide detailed information of the occurrence frequency of the waves, their horizontal wavelengths, and their apparent phase velocities.[11,16-19]

In the past most airglow imaging has been performed with relatively narrow-angle optics (typically 30°–40°).[5,8,20-24] This image format has the advantage of limited optical distortion, but it provides information on only a very restricted part of the gravity wave field. Monochromatic all-sky imaging systems have been developed for auroral and thermospheric (630.0 nm) airglow studies that provide information over a much larger field of view (180°). With improvements in CCD detectors, these systems are now capable of viewing wave structure in the mesospheric airglow emissions over a very large geographic area (up to 1,000,000 km$^2$ at 96-km altitude).

To investigate the morphology of these wave motions, Hapgood and Taylor[25] developed a method to

F. J. Garcia and M. C. Kelley are with the Department of Electrical Engineering, Cornell University, Ithaca, New York 14850. M. J. Taylor is with the Space Dynamics Laboratory and the Physics Department, Utah State University, Logan, Utah 84322.

Table 1. Filter Information and Mean Heights for Airglow Emissions in Upper Mesosphere

| Filter | Filter Wavelength (nm) | Filter Bandwidth (nm) | Mean Layer Height (km) |
|--------|------------------------|-----------------------|------------------------|
| OI | 557.7 | 2.67 | ~96 |
| Na | 589.2 | 2.37 | ~90 |
| NIR OH | 715–930[a] | 215 | ~87 |
| $O_2(0,1)$ | 865.5 | 12.0 | ~94 |
| Background | 572.5 | 2.65 | – |

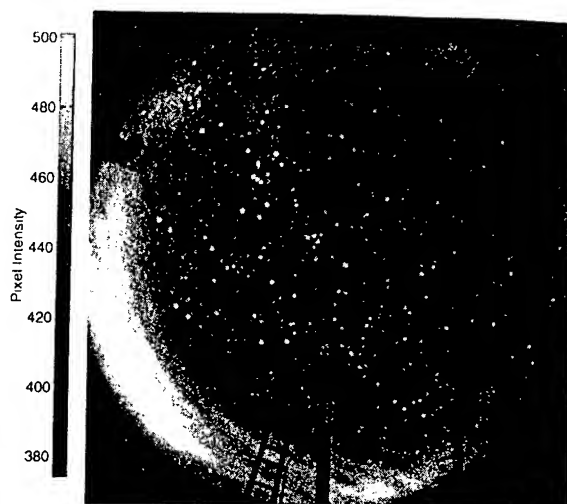[a]With a notch at 865 nm to suppress the $O_2$ (0,−1) emission.



Fig. 1. 512 × 512-pixel resolution all-sky CCD image showing short-period gravity wave structure in the OI (557.7 nm) airglow emission. Data were recorded from Haleakala, Hawaii, on 22 October 1993 at 12:27 UT with a 90-s exposure.

determine horizontal wave parameters from narrow-angle image data. Lanchester[26] subsequently generalized their analysis to the all-sky image format for auroral studies. In both cases, the analysis methods relied heavily on the identification of relatively high-contrast wave patterns (or features) by the observer. Although this method has proven to be extremely useful, it does not take full advantage of the range of information that is now obtainable with solid-state imaging systems, nor does it take advantage of modern signal and image-processing tools.

All-sky monochromatic imaging systems provide high spectral sensitivity and maximum field of view for ground-based measurements, but the image format is not immediately suitable for standard two-dimensional (2-D) spectral analysis techniques. We summarize methods for processing the all-sky image data to allow these techniques to be applied. The effects of geographic projection and regridding of the data are presented together with a discussion of the limits of gravity wave parameter estimation with these data. A report that makes use of some of the techniques described here for the investigation of simultaneous wave signatures in the near-infrared OH and OI (557.7 nm) emissions has been given by Taylor and Garcia.[11]

## 2. Image Processing

### A. Characteristics of All-Sky Images

The CCD imager we used to obtain our example images consists of a large area (6.45 cm²), high resolution, 1024 × 1024 back-illuminated array with a pixel depth of 14 bits. The high quantum efficiency (~80% at visible wavelengths), low dark current [0.5 (electrons/pixel)/s] low readout noise (15 electrons rms), and high linearity (0.05%) of this device provide an excellent capability for quantitative measurements of the airglow emissions.[18] The camera makes use of a fast ($f/4$) all-sky telecentric lens that enables high signal-to-noise ratio (20:1) images of wave structure to be obtained with integration times of typically 15 s for the near-infrared OH emission (715–930 nm passband) and 90 s for the OI (557.7 nm) line emission. Figure 1 shows an example of gravity wave data recorded in the OI (557.7 nm) emission during the Airborne Lidar and Observations of the Hawaiian Airglow in October 1993 (ALOHA-93)

campaign from Haleakala, Hawaii.[18] The image has been binned on-chip down to 512 × 512 resolution to enhance the signal-to-noise ratio.

Two linear wave patterns are evident: one large-scale wave pattern that encompasses the whole field of view while the other smaller-scale wave pattern appears in localized areas of the image (most prominently near the zenith) and is almost orthogonal to the larger-scale waves. The large-scale wave pattern illustrates the problems associated with the use of all-sky optics for airglow studies, namely that linear wave patterns appear curved and compressed at low elevation angles. This occurs because the lens projects an image onto the CCD such that each pixel subtends an equal angle of the sky. As an illustration, Fig. 2 shows the effect of projecting onto a uniform geographic grid an array of 18 × 18 super pixels that represent 10° × 10° elements of the all-sky image. The sizes of the projected pixels vary considerably with elevation, and the shapes are dependent on the viewing azimuth. Further implications of mapping the images onto a uniform geographic grid are discussed in detail in Section 2.E.

The immediate effect of this projection on the resolution is illustrated in Fig. 3(a), in which the range $r$ along the airglow layer is shown as a function of observed elevation angle $el$ for an OI emission layer at 96 km. The function is essentially linear for elevation angles larger than 40° (range up to 400 km), but at lower elevations the distance along the airglow layer increases rapidly, exceeding 1000 km at the horizon. Figure 3(b) shows the resulting radial (solid) and tangential (dashed) resolutions as a function of elevation angle for a 512 × 512 all-sky image. The radial resolution is the interpixel spacing that extends radially from zenith, and the tangential resolution is the interpixel spacing in the orthogonal direction. The two show similar trends at high elevations, but at low elevations the tangential resolu-
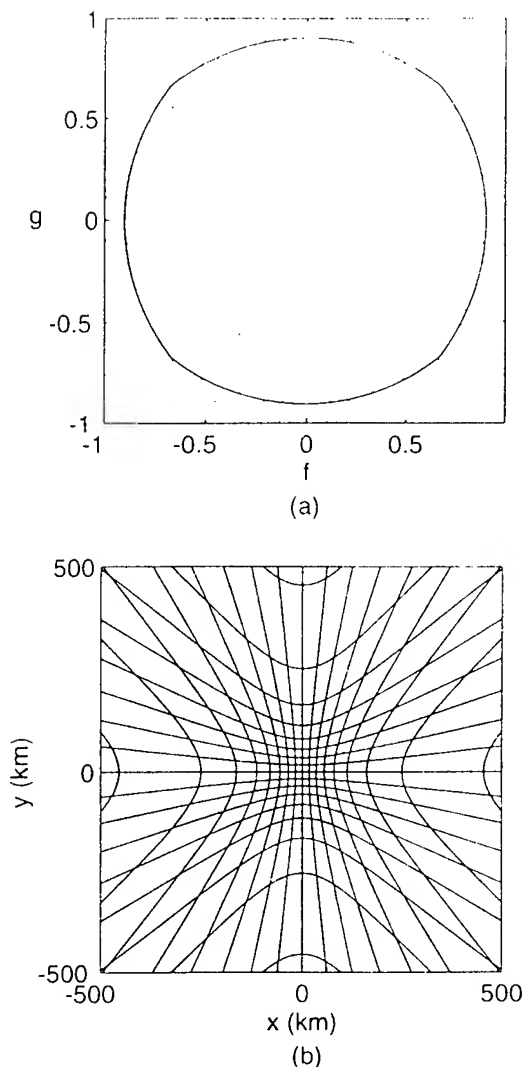
(a)



(b)

Fig. 2. Plots showing effect of projecting a pixel in the all-sky image onto a geographic coordinate system, assuming an emission height of 96 km: (a) all-sky image into 18 × 18 elements corresponding to 10° superpixels; (b) corresponding footprint of each of these superpixels is shown on a 1000 km × 1000 km area. Note the significant increase in size of the footprints at lower elevations. The solid border in (a) indicates the mapped area.
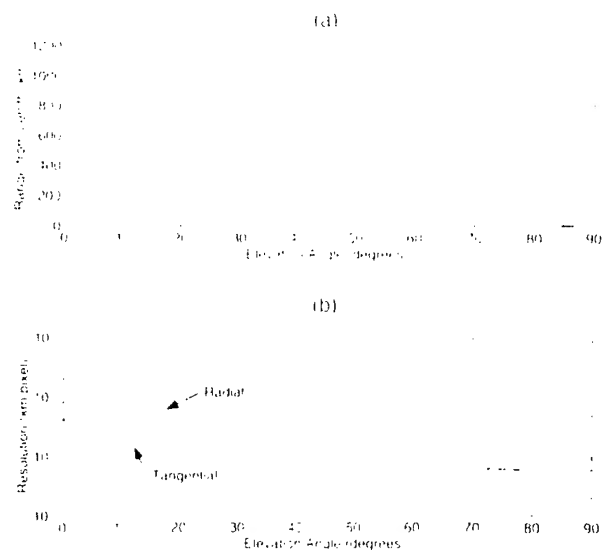


Fig. 3. Plots showing (a) variation in range from zenith along the airglow layer as a function of elevation angle for an emission height of 96 km, and (b) corresponding tangential and radial pixel resolution as a function of elevation angle for an all-sky image of 512 × 512 pixels.

tion is significantly better. The radial resolution is therefore the limiting factor for determining what portion of an image to analyze. For example, for measuring waves of horizontal wavelengths ≤20 km, the waves should be located within ~450 km of the observer (i.e., occur at >10° elevation) because at that point the radial resolution is 10 km/pixel. However, as can be seen in Fig. 11, shorter wavelengths can be observed at lower elevation angles if the waves are oriented tangentially.

Standard 2-D fast Fourier transform (FFT) analysis techniques require that the spatial resolution across the image be constant. For the example plotted in Fig. 3, the zenith resolution is 0.6 km/pixel, reducing to 1 km/pixel at ~50° elevation. Thus without additional processing, this would limit the useful area of the all-sky image to ≤30°–40° of ze-

nith. As the data show, however, there is a considerable amount of wave information outside this range. To maximize the potential of these data, it is necessary to map the images onto a uniformly spaced grid prior to spectral analysis.

B. Coordinate Mapping

Before we can perform a quantitative analysis of the image data, it is necessary to use coordinate systems that relate distances between pixels in the image to physical distances in the airglow layer. In this section we describe the coordinate systems we used in our analysis method and show how to transform from one to another.

Figure 4 illustrates the four coordinate systems used. The original image depicts the array of data recorded by the CCD camera. The $(i, j)$ coordinate axes represent indices in the data array. The axes are not assumed to be aligned along a specific geographic orientation. Following the method described by Hapgood and Taylor[25] for narrow-angle optics, we introduce a standard coordinate system that is a linear transformation of the original image coordinates scaled so that the horizon circle that corresponds to 0° elevation is of unit radius. The azimuth-elevation coordinate system is used to facilitate the transformation between standard coordinates and geographic coordinates. The final geographic coordinate system is a 2-D uniformly spaced grid at the height of the airglow layer. The original image is projected onto this grid to create a regularly sampled array for the 2-D FFT analysis. In this format, zenith is located at the origin of the coordinate system and the x and y axes correspond to geographic east and north, respectively. Because the airglow layer is curved (see Fig. 6), representing
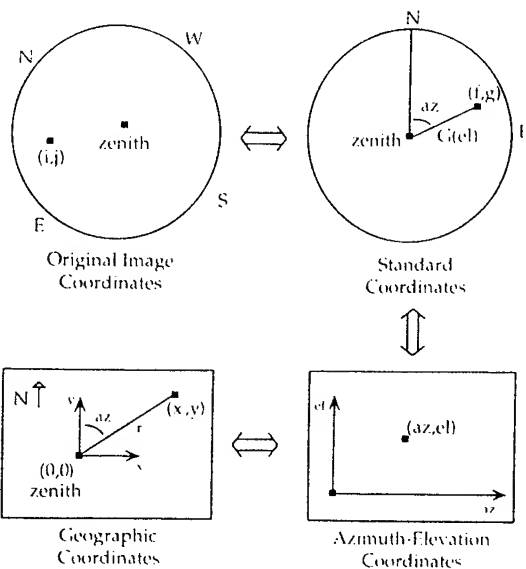
Fig. 4. Illustration showing coordinate mappings used for transforming data from the original all-sky format to geographic coordinates, and vice versa.



Fig. 5. Plot showing variation in the lens function $G$ versus elevation; $G$ is the normalized distance measured from the center of the image.

it on this planar grid will introduce some error; however, since the analysis area is orders of magnitude smaller than the area of the spherical shell at the height of the emission layer, this error is negligible.

Every point $(i, j)$ in the original image corresponds to a point $(f, g)$ in the standard coordinates, which in turn maps to a point $(x, y)$ in geographic coordinates via the azimuth and elevation $(az, el)$ transformation. Because each transformation is invertible, it is possible to map easily between coordinate systems:

$$(i, j) \Leftrightarrow (f, g) \Leftrightarrow (az, el) \Leftrightarrow (x, y). \qquad (1)$$

The original image and the standard coordinates are related by the following linear transformation[25]:

$$\begin{bmatrix} f \\ g \end{bmatrix} = \begin{bmatrix} a_0 & a_1 & a_2 \\ b_0 & b_1 & b_2 \end{bmatrix} \begin{bmatrix} 1 \\ i \\ j \end{bmatrix}, \qquad (2)$$

where the coefficients $a$ and $b$ are determined by spatial calibration of the image with the star background.[27]

Figure 4 illustrates the relationship between $(f, g)$ and $(az, el)$. This can be expressed as

$$\begin{bmatrix} f \\ g \end{bmatrix} = G(el) \begin{bmatrix} \sin (az) \\ \cos (az) \end{bmatrix}, \qquad (3)$$

where $G(el)$ is determined by the format of the all-sky lens and relates elevation angle to distance, measured from the center of the image. A plot of this function for an all-sky lens (of the type used to take the image in Fig. 1) is shown in Fig. 5. We derived the function by fitting a third-order polynomial to the data supplied by the lens manufacturer. If the lens function is unknown, however, the figure shows that to a first approximation this relationship may be assumed to be linear between distance and angle.

Figure 6 illustrates the airglow-observing geometry. The airglow layer is located at a mean height $H$ above the Earth's surface. An observer at $O$ sees structure at a point $P$ on the airglow layer, corresponding to an elevation $el$ above the horizon. The elevation angle is given by

$$el = \cos^{-1}\left( \frac{a \sin \alpha}{c} \right), \qquad (4)$$

where

$$\alpha = (\pi - \psi)/2,$$

$$c = (H^2 + a^2 - 2Ha \cos \alpha)^{1/2},$$

$$a = 2(R + H)\sin \psi/2,$$

$$\psi = r/(R + H),$$

$$r = (x^2 + y^2)^{1/2},$$

$R$ is the mean radius of the Earth (6370 km).

The azimuth of any point $(x, y)$ in the geographic
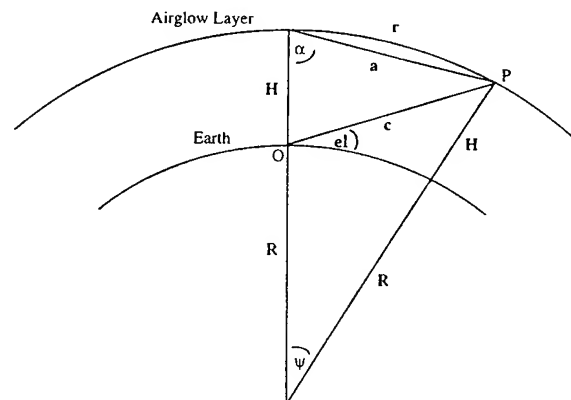


Fig. 6. Illustration showing airglow geometry.
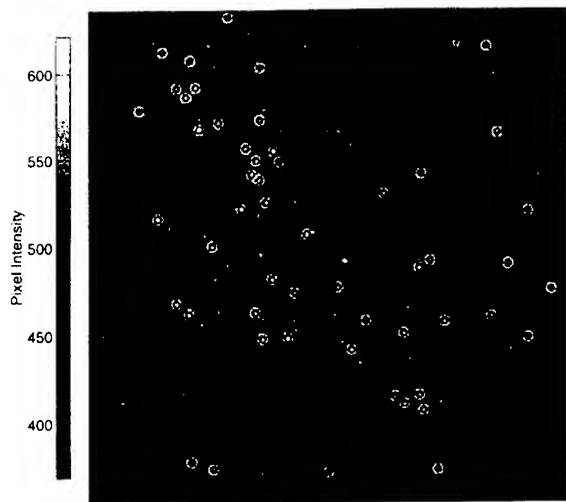
Fig. 7. Example of all-sky star calibration, using the image of Fig. 1; circles indicate the computed positions of all stars of magnitude greater than 1 within the field of view.



Fig. 8. Example illustrating star removal algorithm applied to Fig. 1. A threshold of 20 pixel counts and a maximum star size of 12 pixels were used.

coordinate system is then given by the angle it makes with the y axis, as shown in Fig. 4:

$$az = \tan^{-1}\left(\frac{x}{y}\right). \qquad (5)$$

## C. All-Sky Spatial Calibration

For the large-field information present in the all-sky data, accurate spatial calibration is essential. We can achieve this by using the stars in each image as known reference points in the sky.[28] Spatial calibration provides the necessary $a$ and $b$ coefficients in Eq. (2) for mapping the original image to standard coordinates. We determine the coefficients by performing a least-squares fit using the measured position of the stars in the original image and their positions in standard coordinates (derived from the right ascensions and declinations of the stars, the image time, and the site latitude and longitude).

Figure 7 illustrates the results of spatial calibration applied to the all-sky image of Fig. 1. Using Eq. (2), we calculated the image coordinates for all stars of magnitude 1 or brighter with positive elevation angles at the time the image was recorded. To demonstrate the accuracy of this calibration, we drew circles centered around the position calculated for these stars. Examination of the figure shows that all the bright stars within the image are encompassed by these circles. The mean distance of the calculated position of each star from its true location in the image was found to be less than 1 pixel. When the $a$ and $b$ coefficients are determined from any one image in a data set, they can be applied to all the images in the data set provided that the camera is not moved.

## D. Star Removal

When an image has been calibrated, it is beneficial to remove the stars because they can cause streaking

when an image is projected onto geographic coordinates and when images are averaged for flat fielding (see Section 2.F). We have developed a simple yet effective algorithm for removing stars while leaving the remainder of the image data essentially untouched. The basic premise behind the algorithm is that stars exhibit sharp, localized changes in intensity, the width of which are determined by the point-spread function of the system, while airglow features exhibit much more gradual changes. The key, however, is that the changes must occur in both the $i$ and the $j$ directions of the array. This algorithm seeks out such changes and replaces the stars with interpolated values from the surrounding pixels.

The algorithm scans an image line by line, looking for intensity changes of greater than a certain threshold. When such a change is detected, it continues to scan until the intensity value returns to within a threshold of the background. If, however, the intensity does not return to the background airglow level within a certain number of pixels (corresponding to the largest reasonable size of the stars in the image), the feature is considered too large to be a star and is disregarded. Because stars may not fall exactly on an integral number of pixels, there will be some leakage into the neighboring pixels. To account for this, the pixels immediately before and after a star is detected are also considered to be influenced by the star. When a star has been found, its corresponding intensity values are replaced by a linear fit of the surrounding pixels.

After the algorithm completes scanning the rows, it follows the same procedure with the columns. If a pixel's intensity is modified in both the row and the column scans, the final intensity is the average of the two values. If a pixel was not modified in both scans, it reverts back to its original value. Figure 8 shows the result of this processing as it is applied to the OI (557.7 nm) data in Fig. 1. In this example, the threshold pixel intensity value used to detect

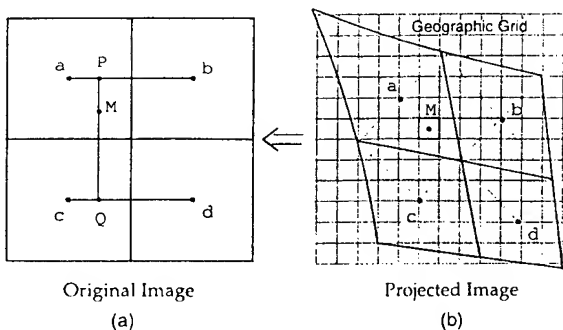Fig. 9. Illustration showing method used to interpolate between the projected image on the geographic grid and the original image pixels; $M$ denotes the grid element for which the intensity is to be estimated.



Fig. 10. Unwarped image showing results of projecting Fig. 8 onto a geographic grid; in this example, an area corresponding to 800 km × 800 km has been mapped with a pixel resolution of 2 km/pixel.

stars was 20 counts, and the maximum star width was assumed to be 12 pixels. The efficacy of this algorithm for removing stars without affecting the airglow data is readily apparent. The algorithm is equally effective in removing pointlike defects (hot pixels) in the CCD chip as well as bright pixels resulting from cosmic ray events. In principle, the removal of objects (such as the antennas and towers) in the low elevation field of view can be accomplished in a similar fashion, but the interpolation becomes much more involved and, as will be shown later, is not usually necessary.

### E. All-Sky Projection onto a Uniformly Spaced Grid

In Section 2.B the transformation from the original image coordinates to the geographic coordinates was described. This transformation, often termed unwarping, is necessary for standard spectral analysis techniques that require uniform sampling of the data. Because the regularly sampled points in the geographic projection will not, in general, map exactly onto the center of the pixels in the image coordinates, some form of interpolation is necessary. This point is illustrated in Fig. 9, which shows the relationship between the original image pixels and their footprints projected onto a geographic grid.

We have experimented with several interpolation techniques, incorporating forward and backward mapping, and have determined that for our purposes a backward mapping followed by bilinear interpolation is most suitable. A short description of the method follows.

A point $M$ (see Fig. 9) in the geographic map is converted to azimuth and elevation using Eqs. (4) and (5). The point is then transformed to standard coordinates with Eq. (3), and its corresponding position in the original image is determined with Eq. (2). Because this point does not lie exactly at the center of an image pixel, adjacent pixels need to be interrogated to estimate its value. A standard bilinear interpolation is performed by first linearly interpolating between points $a$ and $b$ to find the intensity value at $P$ and linearly interpolating between points $c$ and $d$ to find the intensity value at $Q$. An estimate for the pixel value at $M$ is then given by linearly interpolat-

ing between $P$ and $Q$. This procedure is repeated for every point in the geographic grid [see Fig. 9(b)].
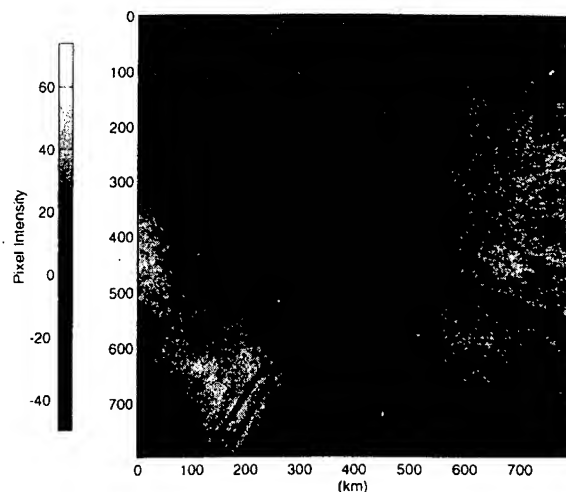
Figures 10 and 11 show two examples of unwarping all-sky images in this manner. In Fig. 10, a large area of the processed image (Fig. 8), corresponding to ~640,000 km$^2$ at the OI airglow layer, is mapped with an assumed emission altitude of 96 km. As expected, the small-scale waves are seen mainly over a limited geographic area within ~200 km radius of zenith. In comparison, the large-scale wave pattern is shown to be much more spatially extensive; however, even it does not appear to occupy the whole projection. This is due to the difference in the tangential and the radial resolution (see Fig. 3). The net effect in this case is that at low elevations the wave crests are visible in the northwest corner of the map (where they are oriented tangentially) but are more difficult to see in the southwest and northeast corners (where they are oriented radially). Never-
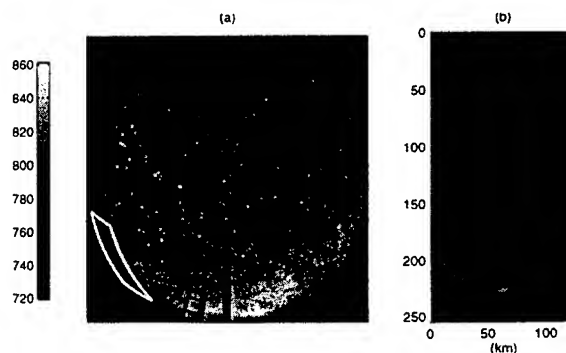


Fig. 11. Example illustrating localized feature unwarping: (a) image taken at 10:19 UT on the same night as Fig. 1, showing small-scale waves to the southeast at extremely low elevation; (b) unwarped image corresponding to the area indicated by the white border.

theless, the unwarping clearly shows the true quasi-linear nature of the wave pattern.

Figure 10 also illustrates that the selection of the area to unwarp is dependent on what type of information is sought. For very short wavelength features (typically 5–15 km), it is better to concentrate the analysis over an area near the center of the image (thus allowing for a higher spatial resolution); longer wavelength features (a few tens of kilometers) can be analyzed with a lower spatial resolution and out to a much greater range from zenith. For significantly longer wavelength features (up to a few hundred kilometers), this method can be used to unwarp out to even larger ranges (approaching the horizon), but the presence in the near field of obstacles such as the antenna and the microwave tower in this example often limit the field.

Figure 11(a) shows a second example of airglow structure recorded on the same night as Fig. 1, when small-scale waves (~20-km horizontal wavelength) were observed close to the horizon. To further illustrate the power of the unwarping technique, we mapped the area that encompasses the structure (indicated by the white border). The resultant image [Fig. 11(b)] clearly shows at least 12 linear wave crests, enabling accurate measurements of their horizontal wavelength. With previous techniques to investigate such a wave pattern this measurement would have been extremely difficult.

### F. Flat Fielding the All-Sky Image

Before we discuss the determination of gravity wave parameters, we consider a practical method for flat fielding the data to investigate relative intensity variations in the airglow (i.e., the ratio of the amplitude of the signal perturbation induced by the waves over the mean airglow signal, $\delta I / \bar{I}$). One common form of flat fielding is the use of a Lambertian-surface image of a white, uniformly illuminated dome for estimating the lens function. This method, however, fails to correct for the Van Rhijn effect (line-of-sight enhancement of the airglow signal resulting from an increase in the optical path length through the emission layer when viewed at low elevations) that is present in the image data. For this reason we describe an alternate method and, although it is not necessary for measurements of horizontal wavelength or phase speed, it is essential for estimating the power in the monochromatic wave components.

For meaningful determinations of $\delta I / \bar{I}$, it is important to make background image measurements alongside the airglow measurements to assess contamination of the data by sources other than the airglow. The OI (557.7 nm) and Na (589.2 nm) line emissions are ideally suited for these studies because the images are taken with an optical filter with a very narrow passband encompassing the emission line (see Table 1). A background image for these narrow-band signals is achieved by the measurement of the sky emissions with a filter of approximately the same bandwidth but centered just off the emission line in a clean part of the sky spectrum. Background images

usually have the same exposure time and are taken in close succession to the signal image. In comparison, accurate background corrections for the broad-band near-infrared OH emission are significantly more difficult to achieve.

The sky signal $S$ is assumed to be composed of a mean airglow signal $\bar{I}$ and the airglow signal perturbation $\delta I$. This signal is contaminated by noise from the stars, $N_{stars}$, and from other sky sources, $N_{sky}$, primarily resulting from continuum emission and aerosol scattering:

$$S = \bar{I} + \delta I + N_{sky} + N_{stars}. \tag{6}$$

To account for the competing effects of optical vignetting (which results in a significant reduction in the light throughput at the edge of the field of view) and Van Rhijn enhancement, we include the operator $H(i,j)$ that modifies the signal incident on the CCD. The effects of electronic noise in the CCD, including readout and thermal noise, are represented by $N_{elec}$. The resultant image $A$ is then given by

$$A = H(i,j)(\bar{I} + \delta I + N_{sky} + N_{stars}) + N_{elec}. \tag{7}$$

The background image can be modeled similarly as follows:

$$B = H(i,j)(N_{sky} + N_{stars}) + N_{elec}. \tag{8}$$

Examinations of dark images (i.e., exposures with the lens cap on) have revealed that most of the power in the readout and thermal noise is in dc, and therefore we make the approximation that $N_{elec}$ is constant for fixed exposure times. Furthermore, we make the assumption that because the data image and its corresponding background image are taken within a short time of each other (usually within 1–2 min), they will effectively have the same sky noise contribution. Owing to the sequential nature of the measurements, however, there occurs a slight displacement in the star positions between the data image and its background; therefore we cannot assume that $N_{stars}$ is the same in both images. To account for this, each data and background image is processed with the algorithm in Section 2.D for removing the stars, resulting in

$$A_{ns} = H(i,j)(\bar{I} + \delta I + N_{sky}) + N_{elec}, \tag{9}$$

$$B_{ns} = H(i,j)(N_{sky}) + n_{elec}, \tag{10}$$

where the subscript $ns$ denotes images with the stars removed. Subtracting $B_{ns}$ from $A_{ns}$ and assuming that $N_{elec}$ is constant and $N_{sky}$ is the same in both images creates a background-corrected image $BC$:

$$BC = A_{ns} - B_{ns} = H(i,j)(\bar{I} + \delta I). \tag{11}$$

Because the airglow perturbation $\delta I$ is not stationary, we may average out the effects of the waves by averaging together a series of background-corrected images, resulting in an average image $AV$:
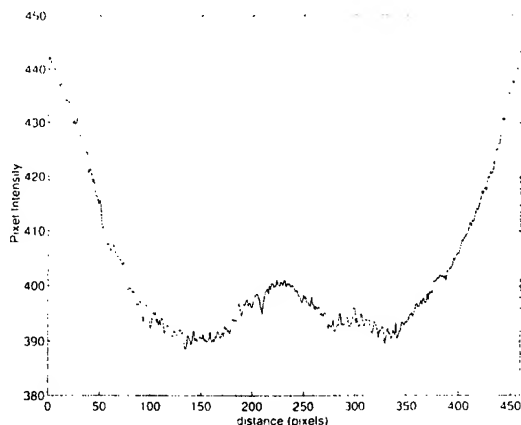
$$AV = \bar{BC} = H(i,j)\bar{I}. \tag{12}$$

Fig. 12.  Scan of averaged image (*AV*) showing the combined effects of lens vignetting and Van Rhijn enhancement on the all-sky image profile.



Fig. 13.  Unwarped $\delta I/\bar{I}$ image corresponding to data from Fig. 1; black features are remnants of near-field antennas and other structures evident along the horizon in Fig. 1.

Figure 12 shows a scan across an example *AV* image we obtained by averaging 15 images spanning approximately 1 h.  The contributions of lens vignetting and Van Rhijn are apparent and must be accounted for when the power in the various signal components are estimated.  To account for gradual changes in the mean airglow signal $\bar{I}$ during a night's observations (due to tides and large-scale gravity waves), a set of *AV* images is usually created.  Because $H(i, j)$ is unity at zenith, we can estimate the mean airglow signal $\bar{I}$ by measuring the zenith intensity of *AV*.  The flat-fielded image *FF* is then given by

$$FF = \bar{I} + \delta I = \frac{BC}{AV} \bar{I}. \qquad (13)$$

However, for estimating the fractional intensity change induced in the airglow emission by the gravity waves $\delta I/\bar{I}$, it is not necessary to determine completely the flat-fielded image because this can be found from the ratio of Eq. (11) and Eq. (12):

$$\frac{\delta I}{\bar{I}} = \frac{BC}{AV} - 1. \qquad (14)$$

Figure 13 shows the results of this processing applied to the original image of Fig. 1.  This $\delta I/\bar{I}$ image is ready for 2-D FFT.  The two areas indicated by the black borders are the subjects of the analysis in Section 3.

### 3.  Determination of Gravity Wave Parameters

Because we have processed the all-sky images, it is now possible to determine the horizontal wave parameters directly with standard 2-D FFT analysis.  The advantage of this method is that measurements of all of the monochromatic features present in the data are now possible.

To create clean, well-defined peaks in the transform, we removed any linear trends associated with gradual variations in $\bar{I}$ across the field of view by fitting a plane to the $\delta I/\bar{I}$ image and then subtracting

it.  A 2-D Welch window is then applied to the data to minimize sidelobes in the frequency spectrum.[29]

We can investigate gravity wave content in any part of the image by isolating the region of interest, taking the 2-D FFT of the selected region, and investigating peaks in the squared magnitude of the frequency spectrum.  Figure 14 shows two examples of this technique applied to the $\delta I/\bar{I}$ image of Fig. 13.  Two regions were selected:  one, indicated by the rectangle, contains the large-scale wave motion; and the second, indicated by the square, isolates most of the smaller-scale waves.  Images (a) and (d) in Fig. 14 reproduce the regions of interest.  The color plot (b) shows the computed squared magnitude of the 2-D FFT of (a).  Owing to the symmetry of the FFT of real data, two mirror-image peaks in the power spectrum are evident at ($\pm 0.021$ km$^{-1}$, $\mp 0.012$ km$^{-1}$), corresponding to the large-scale quasi-monochromatic wave structure present in (a).  We can determine the horizontal wavelength of these waves by computing the inverse of the distance of the peak from the origin, and it was found to be 47 km $\pm 3$ km.  The direction of propagation of the wave is given (with a 180° ambiguity, again owing to the symmetry of the FFT) by the position of the peak in this $k$-space diagram (in this case the wave motion was progressing on a heading of either $-125°$ or $55°$).

To further investigate the spatial frequencies present in this wave motion, we can isolate the peaks in the FFT to reconstruct the image with just those frequencies, corresponding to the quasi-monochromatic wave features.  Figure 14(c) shows the reconstructed image of the large-scale waves shown in Fig. 14(a).  The similarity between the prominent features in both images is clearly evident, indicating we have correctly identified the spatial frequencies associated with this wave.  In comparison, the color plot [Fig. 14(e)] shows the spectral components associated with the waves present in image (d).  Three distinct peaks are evident, one corre-
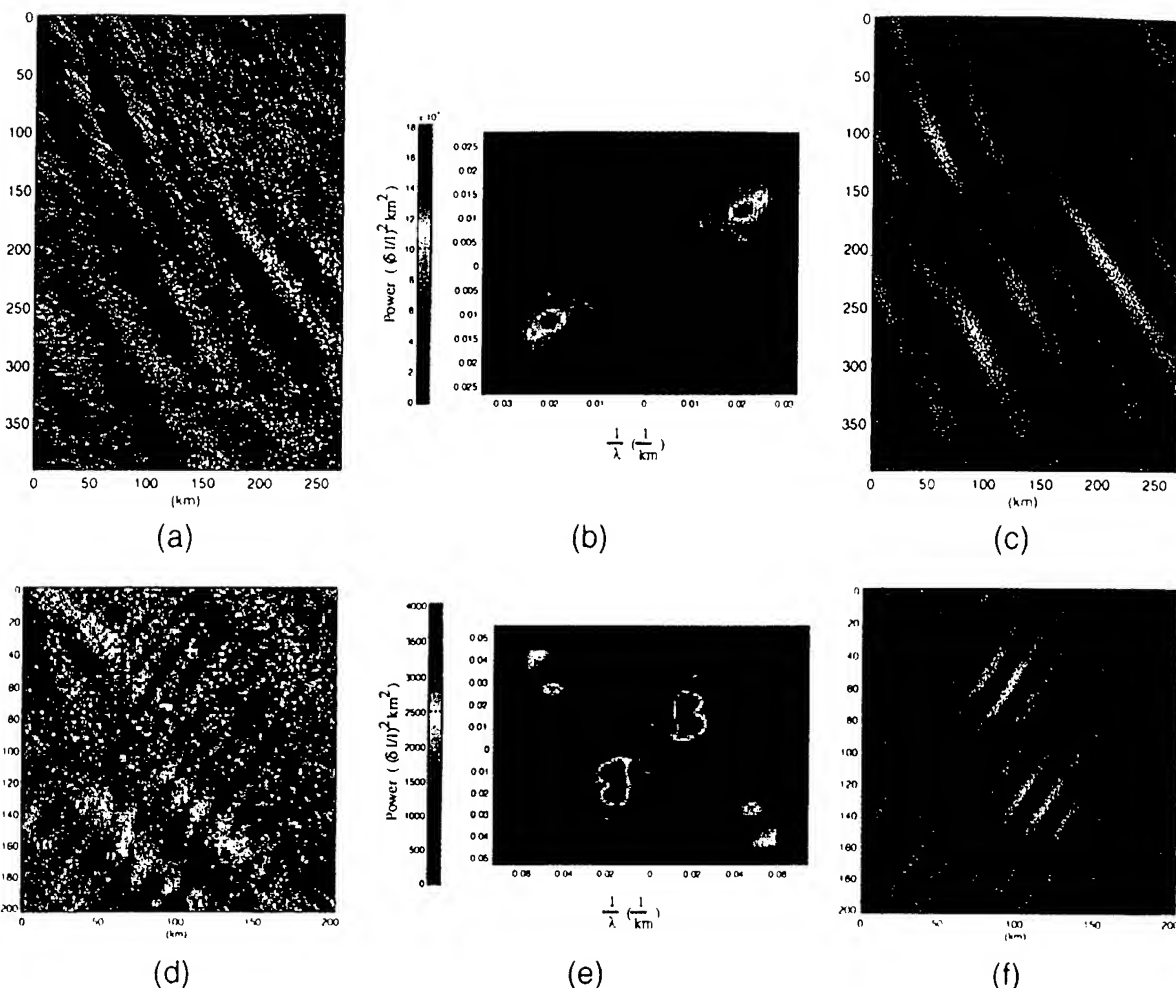
Fig. 14. Two examples illustrating 2-D FFT analysis of airglow data and image reconstruction: (a)–(c) a subsection of Fig. 13 (indicated by the rectangular border) that isolates the large-scale waves along with the 2-D FFT and a reconstruction of the wave pattern, corresponding to just those frequencies in the peak of the FFT; (d)–(f) a similar situation for the analysis of the small-scale waves (indicated by the square border in Fig. 13).

sponding to the larger-scale wave discussed above and two resulting from the smaller-scale waves, both of which are almost orthogonal to the larger-scale wave. Orthogonal wave motions of this type are of considerable interest because they are observed more frequently than would be expected by chance, suggesting a causal relationship.[30] In this case, the apparent splitting of the peaks for the small-scale waves is suggestive of a nonlinear wave interaction (this point is discussed in further detail in Section 4). The reconstruction of the small-scale waves is shown in Fig. 14(f) and was obtained by incorporating only the two small-scale peaks present in the FFT. The effect of this is to remove the large-scale wave from the reconstructed image, which enables clearer examination of the small-scale components.

Two methods are available to determine the periods (and hence phase speeds) of the waves present in these data. Using a sequence of images, we can plot the phase at each peak as a function of time. Figure 15(a) illustrates this method for the large-scale peak. The trend is very nearly linear, indicating uniform
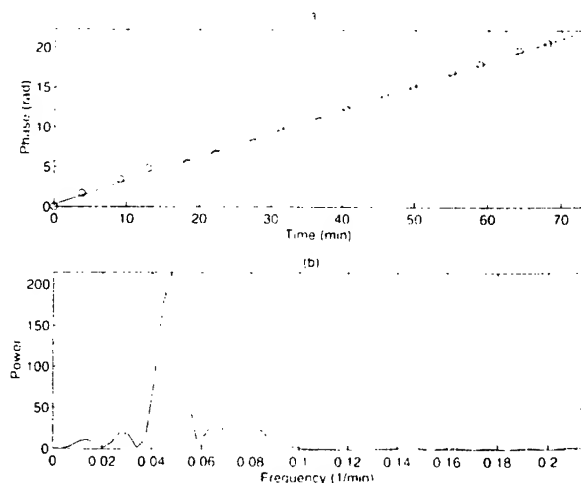


Fig. 15. Plots showing (a) the variation of phase of the spectral peak of the large-scale wave component with time: the slope of the linear least-squares fit to the data gives the period of 21.0 min, and (b) illustrates an alternative method for determining the period from the same data: a 1-D FFT is taken of the complex-valued data at the peak of the 2-D FFT. The peak indicates the wave frequency.

Table 2. Gravity Wave Parameters Derived from 2-D FFT Analysis

| Wave Feature | $\lambda_H$ (km) | $az$ (deg) | $\tau$ (min) | $c_H$ (m/s) | $\delta I/\bar{I}$ (%) |
|---|---|---|---|---|---|
| Large-scale | 47 ± 3 | −125 ± 2 | 21.0 ± 0.2 | 37 ± 2 | 8.9 |
| Small-scale$_a$ | 20 ± 1 | 124 ± 2 | 9.1 ± 0.2 | 37 ± 1 | 2.7 |
| Small-scale$_b$ | 15.1 ± 0.5 | 130 ± 3 | —$^a$ | —$^a$ | 3.9 |

$^a$Owing to the temporary nature of the small-scale$_b$ waves, there were insufficient data to determine their wave period and phase velocity.

phase motion of 37 ± 1 m/s. The slope of this line yields the wave period, which we have determined, using a linear least-squares fit to the data (solid line), to be 21.0 ± 0.2 min. The sign of the slope resolves the ambiguity in the direction of motion, indicating in this case wave progression toward the southwest (i.e., −125°).

The second method of estimating the wave period involves taking the one-dimensional (1-D) FFT in time of the complex 2-D FFT in space. The peaks in the squared magnitude of the 1-D FFT then correspond to the wave frequencies present in the data. Figure 15(b) shows the 1-D FFT for the large-scale wave. A single, well-defined peak is clearly evident at 0.048 min$^{-1}$, corresponding to a wave period of 20.9 min. Because this is a FFT of complex data, there is no symmetry between negative and positive frequencies, and the sign of the frequency of the peak (positive in this case) again resolves the ambiguity in the direction of motion. Table 2 lists the wave parameters we have computed for the waves present in this data set.

## 4. Discussion and Summary

To date, almost all of the short-period gravity wave measurements reported in the literature have been made by the measurement of the spatial separations and motion of the most prominent wave forms present in the original data sequence. This requires accurate visual identification of the wave motions by the operator and has consequently been applied only to high contrast, prominent wave forms.

The analysis techniques we have developed here have proved to be well suited to investigating the types of quasi-monochromatic wave events that are often recorded in airglow image data, including complex data containing more than one wave event. Our algorithms have been incorporated into a Matlab-based graphical user interface, providing a powerful interactive capability for investigating all-sky image data. By accurately unwarping the image, we have now made the analysis of very small scale waves (<20 km horizontal wavelength) practical over a significant portion of the sky (~480,000 km$^2$), and larger-scale waves can be analyzed out to much larger radii (limited by the presence of near-field objects in the image). By regridding the data, we are able to perform a 2-D FFT analysis on localized wave features that occur almost anywhere in the all-sky field of view. In contrast, previous Fourier investigations have focused on near-zenith measurements and have thus failed to take advantage of a large part of the airglow information.[11] The capability to navigate around the ground map in our analysis technique frees us from this constraint and permits maximum use of the all-sky information.

Comparison measurements with the classical spatial analysis technique outlined by Hapgood and Taylor[25] indicate that the errors in determination of the horizontal wavelength are comparable and are typically low (~1-2 km). Measurements of the apparent wave phase speed and direction of motion with the spectral analysis yield uncertainties somewhat lower than those typically achieved with spatial analysis methods (especially for less contrasted wave motions). The main reasons for this are probably the difficulties encountered by the operator in tracing accurately the motion of the wave pattern during analysis. The Fourier technique mitigates this problem through not requiring operator identification of specific wave features for the determination of wave period. This method provides for consistency and repeatability, which has not previously been available, in the wave parameter determination.

In a recent paper Taylor et al. suggested a mechanism whereby two large-scale waves that are progressing on similar azimuths may interfere and generate small-scale wave patterns that would appear almost orthogonal to the larger-scale waves.[30] If this were the case for the data presented here, we would expect to see two peaks in the power spectrum associated with the larger-scale waves and no smaller-scale components because they are simply the manifestation of the interference of the two larger waves. The occurrence of the smaller-scale peaks for this data set suggests that an alternative explanation is needed. The splitting of the peaks that correspond to the small-scale waves is suggestive of a nonlinear wave–wave interaction. If the airglow disturbance had been produced by the product of two waves (one low frequency and one high frequency, both propagating at similar azimuths), this is precisely the type of spectrum we would expect to see. Fritts et al. have investigated the properties of convective instabilities associated with the breakdown of large-scale waves.[31] Their model indicates that short-lived, small-scale waves oriented approximately orthogonal to the large-scale wave can be produced by gravity wave breakdown. This mechanism could possibly explain these data; however the model predicts scale sizes that are significantly smaller (~5 km) than those observed on this night (see Table 2).

A natural extension of the all-sky analysis capability discussed here is the investigation of power law trends in the horizontal spectra of the image data. Several theories have been proposed to account for wave saturation and dissipation in the upper mesospheric and the lower thermospheric regions, which predict the form of the power law trends.[32][34] Quasi-monochromatic waves evident in the airglow emissions may simply be superposed on this turbulent background or may form part of the nonlinear actions that create the power law dependence of wave properties on the horizontal wave number $k$. Using a narrow-field airglow imager (60° field of view) centered on the zenith, Hecht et al. have estimated the spectral slope and found it to be between -2.5 and -3 (Ref. 8). However, the limited field of view restricted the spectral range of these measurements to wavelengths less than 110 km. For all-sky image data, the available spectral range is significantly larger, and we are currently investigating methods to use these large-field data for accurate spectral slope estimates.

In summary, this paper describes how to use the full potential of digital all-sky airglow data for quantitative spectral investigations of quasi-monochromatic gravity waves (periods $\leq 1$ h). By automating most of the processing associated with the wave parameter determination (wavelength, velocity, period, $\delta I/\bar{I}$, we have developed an efficient analysis technique that can now be used for in-depth studies of complex image data. Furthermore, this analysis facilitates long-term studies that promise to provide a wealth of information on seasonal and geographic variability important for improving current atmospheric models.

## References

1. V. I. Krassovsky and M. V. Shagayev, "On the nature of internal gravity waves observed from hydroxyl emission," Planet. Space Sci. 25, 200–201 (1977).
2. N. M. Gavrilov and G. M. Shved, "Study of internal gravity waves in the lower thermosphere from observations of the nocturnal sky airglow [OI] 5577 Å in Ashkhabad," Ann. Geophys. 38, 789–803 (1982).
3. H. Takahashi, P. P. Batista, Y. Sahai, and B. R. Clemesha, "Atmospheric wave propagations in the mesopause region observed by the OH (8,3) band, NaD, $O_2$ (8645 Å) band and OI 5577 Å nightglow emissions," Planet. Space Sci. 43, 381–384 (1985).
4. H. K. Myrabo, C. S. Deehr, R. A. Viereck, and K. Henriksen, "Polar mesopause gravity waves in the sodium and hydroxyl night airglow," J. Geophys. Res. 92, 2527–2534 (1987).
5. M. J. Taylor, M. A. Hapgood, and P. Rothwell, "Observations of gravity wave propagation in the OI (557.7 nm), Na (589.2 nm) and the near-infrared OH nightglow emissions," Planet. Space Sci. 35, 413–427 (1987).
6. R. P. Lowe, K. L. Gilbert, and D. N. Turnbull, "High latitude summer observations of the hydroxyl airglow," Planet. Space Sci. 39, 1263–1270 (1991).
7. S. P. Zhang, R. H. Wiens, and G. G. Shepard, "Gravity waves from $O_2$ nightglow during the AIDA'89 campaign. II. Numerical modeling of the emission rate/temperature ratio, η," J. Atmos. Terr. Phys. 54, 377–395 (1992).
8. J. H. Hecht, R. L. Walterscheid, and M. N. Ross, "First measurements of the two-dimensional horizontal wave number spectrum from CCD images of the nightglow," J. Geophys. Res. 99, 11,449–11,460 (1984).
9. G. R. Swenson and S. B. Mende, "OH emissions and gravity waves (including a breaking wave) in all-sky imagery from Bear Lake, Utah," Geophys. Res. Lett. 21, 2239–2242 (1994).
10. P. R. Fagundes, H. Takahashi, Y. Sahai, and D. Gobbi, "Observations of gravity waves from multispectral mesospheric nightglow emissions observed at 23 °S," J. Atmos. Terr. Phys. 57, 359–405 (1995).
11. M. J. Taylor and F. J. Garcia, "A two-dimensional spectral analysis of short period gravity waves imaged in the OI (557.7 nm) and near-infrared OH nightglow emissions over Arecibo, Puerto Rico," Geophys. Res. Lett. 22, 2473–2476 (1995).
12. J. R. Holton, An Introduction to Dynamic Meteorology, Vol. 23 of International Geophysical Series (Academic, San Diego, Calif., 1979).
13. R. R. Garcia and S. Solomon, "The effects of breaking gravity waves on the dynamics and chemical composition of the mesosphere and lower thermosphere," J. Geophys. Res. 90, 3850–3868 (1985).
14. I. M. Reid and R. A. Vincent, "Measurements of the horizontal scales and phase velocities of short period mesospheric gravity waves at Adelaide, Australia," J. Atmos. Terr. Phys. 49, 1033–1048 (1987).
15. D. C. Fritts and T. E. VanZandt, "Spectral estimates of gravity wave energy and momentum fluxes, I: Energy dissipation, acceleration, and constraints," J. Atmos. Sci. 50, 3685–3694 (1993).
16. M. J. Taylor and M. J. Hill, "Near-infrared imaging of hydroxyl wave structure over an ocean site at low latitudes," Geophys. Res. Lett. 18, 1333–1336 (1991).
17. G. R. Swenson, M. J. Taylor, P. J. Espy, C. Gardner, and X. Tao, "ALOHA-93 measurements of intrinsic AGW characteristics using airborne airglow imager and groundbased Na Wind/Temperature lidar," Geophys. Res. Lett. 22, 2841–2844 (1995).
18. M. J. Taylor, M. B. Bishop, and V. Taylor, "All-sky measurements of short period waves imaged in the OI (557.7 nm), Na (589.2 nm), and near infrared OH and $O_2$ (0,1) nightglow emissions during the ALOHA-93 campaign," Geophys. Res. Lett. 22, 2833–2836 (1995).
19. Q. Wu and T. L. Killeen, "Seasonal dependence of mesospheric gravity waves (<100 km) at Peach Mountain Observatory, Michigan," Geophys. Res. Lett. 23, 2211–2214 (1996).
20. A. W. Peterson and L. M. Kieffaber, "Infrared photography of OH airglow structures," Nature 242, 321–322 (1973).
21. G. Moreels and M. Herse, "Photographic evidence of waves around the 85-km level," Planet. Space Sci. 25, 265–273 (1977).
22. J. Crawford, P. Rothwell and M. J. Taylor, "Airglow TV" sidebar in "ASSESS 2: a simulated mission of Spacelab (Review Article)," Nature 275, 17 (1978).

23. E. B. Armstrong, "The association of visible airglow features with a gravity wave," J. Atmos. Terr. Phys. **44,** 325–336 (1982).

24. M. J. Taylor, P. J. Espy, D. J. Baker, R. J. Sica, P. C. Neal, and W. R. Pendleton Jr., "Simultaneous intensity, temperature, and imaging measurements of short period structure in the OH nightglow emission," Planet. Space Sci. **39,** 1171–1188 (1991).

25. M. A. Hapgood and M. J. Taylor, "Analysis of airglow image data," Ann. Geophys. **38,** 805–813 (1982).

26. B. S. Lanchester, "Relation between discrete auroral forms and magnetic field disturbances," Ph.D. dissertation (Department of Physics, University of Southampton, Southampton, UK, 1985).

27. K. H. Lloyd, "Concise method for photogrammetry of objects in the sky," Weapons Research Establishment Technical Note 72, 1971 (Australian Defence Scientific Service, Canberra, Australia).

28. W. Smart, *Spherical Astronomy*, 5th ed. (Cambridge U. Press, Cambridge, UK, 1965).

29. W. H. Press, S. A. Teukolsy, W. T. Vetterling, and B. P. Flannery, *Numerical Recipes in C* (Cambridge U. Press, Cambridge, UK, 1992).

30. M. J. Taylor, D. C. Fritts, and J. R. Isler, "Determination of horizontal and vertical structure of an unusual pattern of short period gravity waves imaged during ALOHA-93," Geophys. Res. Lett. **22,** 2837–2840 (1995).

31. D. C. Fritts, J. R. Isler, G. Thomas, and O. Andreassen, "Wave breaking signatures in noctilucent clouds," Geophys. Res. Lett. **20,** 2039–2042 (1993).

32. E. M. Dewan and R. E. Good, "Saturation and the 'universal' spectrum for vertical profiles of horizontal scalar winds in the atmosphere," J. Geophys. Res. **91,** 2742–2748 (1986).

33. C. O. Hines, "The saturation of gravity waves in the middle atmosphere, II, Development of Doppler-spread theory," J. Atmos. Sci. **48,** 1360–1379 (1991).

34. C. S. Gardner, "Diffusive filtering theory of gravity wave spectra in the atmosphere," J. Geophys. Res. **99,** 20,601–20,622 (1994).

# Observational evidence of wave ducting and evanescence in the mesosphere

Joseph R. Isler[1]

Laboratory for Atmospheric and Space Physics, University of Colorado, Boulder

Michael J. Taylor

Space Dynamics Laboratory and Physics Department, Utah State University, Logan

David C. Fritts

Colorado Research Associates, Boulder

**Abstract.** A collaborative radar and imaging study of gravity waves over the Hawaiian Islands was performed during October 1993 as part of the Airborne Lidar and Observations of Hawaiian Airglow 1993/Coupling and Dynamics of Regions Equatorial (ALOHA-93/CADRE) campaign to investigate the propagation characteristics of short-period (<1 hour) waves at nightglow altitudes. The horizontal wavelengths and apparent phase speeds of quasi-monochromatic wave events were measured in four separate nightglow emissions using data obtained by a high-resolution CCD imager. This information was correlated with simultaneous MF radar wind measurements over the same height interval (~80–100 km) to infer intrinsic wave parameters in each case. Correlating the two data sets allowed the determination of the local vertical wavenumber for each event, in particular whether it be real (indicative of freely propagating waves) or imaginary (indicative of ducted or evanescent waves). The results of this study indicate a preponderance of ducted or evanescent waves at 80–100 km during the time of the observations, with up to ~75% of the events recorded exhibiting ducted or evanescent behavior. Also noted was a tendency for ducted behavior to be more prevalent among waves with shorter horizontal wavelengths, in agreement with Doppler ducting theory. These results suggest that ducted waves are relatively common in the upper mesosphere and lower thermosphere region, at least over the mid-Pacific Ocean. As small-scale waves which are ducted have the potential to travel much longer horizontal distances than freely propagating waves, the frequency of their occurrence should be taken into account in efforts to quantify gravity wave effects at these altitudes.

## 1. Introduction

Previous optical and radar studies have revealed a wealth and diversity of waves in the middle and upper atmosphere. Resonant sodium lidars, for example, have proven to be most responsive to wave motions with vertical wavelengths less than the depth of the sodium layer (~10 km). For periodicities >1 hour, which are often reported, the small vertical wavelengths imply waves with horizontal scales of ~$10^2$–$10^3$ km. The distinct downward phase progression that often accompanies these wave-like variations provides strong evidence that they are due to freely propagating internal gravity waves of lower atmospheric origin. In comparison, image measurements of the nightglow emissions (primarily image measurements of the near-infrared (NIR) OH emission at ~87 km and $O_2(0,1)$ emission layers) have demonstrated a high sensitivity to smaller horizontal scale (<100 km), shorter-period (<1 hour) waves [e.g., *Taylor and Hill*, 1991; *Hecht et al.*, 1994; *Swenson et*

al., 1995]. Such nightglow observations typically involve line-of-sight summation over an entire vertical (possibly oblique) viewing column, yielding information on horizontal wave parameters only. For this reason, when observations involve only a single emission layer, information on the vertical wave parameters can only be inferred using the horizontal wave parameters and the gravity wave dispersion relationship [*Hines*, 1960]. However, without a knowledge of the background winds (which allows determination of intrinsic wave parameters), this technique entails large uncertainties in the inferred vertical wavelengths. As a consequence, most previous investigations of small-scale gravity waves have simply assumed that the wave motions were of a freely propagating nature. In this paper we describe a new capability for investigating the propagation characteristics of these waves. The method utilizes image measurements from four nightglow emission layers (spanning the height range ~80–100 km) which when combined with simultaneous wind measurements provides a powerful technique for assessing the true propagation characteristics of the wave motions.

While there has been considerable theoretical research on wave ducting mechanisms in the upper atmosphere [*Francis*, 1974; *Tuan and Tadic*, 1982; *Chimonas and Hines*, 1986; *Wang and Tuan*, 1988; *Fritts and Yuan*, 1989], the interpretation of

[1]Now at Physics Department, Wagner College, Staten Island, New York.

**Table 1.** Summary of Filter Characteristics and Operational Parameters

| Filter[a] | Emission, nm | Assumed Height, km | Band-width, nm | Trans-mission, % | Exposure Time, s |
|---|---|---|---|---|---|
| 1 | OI (557.7) | 96 | 2.67 | 81 | 90 |
| 2 | $O_2$(0, 1) | 94 | 12.0 | 85 | 90 |
| 3 | NIR OH[b] | 87 | 715–930 | 87 | 20 |
| 4 | Na (589.2) | 90 | 2–37 | 81 | 120 |
| 5 | Bg (572.5) | $\cdots$ | 2–65 | 83 | 90 |

[a]Filter sequence 1, 5, 4, 1, 3, 2.

[b]With a 20-nm notch at 865 nm to suppress the $O_2$(0, 1) emission.

wave spectra and the inferences for wave fluxes based upon available observational data have usually assumed freely propagating waves [e.g., *Smith et al.*, 1987]. This assumption is particularly critical for small-scale waves for the following reasons: (1) freely propagating small-scale waves have been shown to be the most important waves contributing to wave mean flow forcing and momentum deposition in the mesosphere and lower thermosphere [*Fritts*, 1984], and (2) small-scale waves are highly susceptible to thermal and Doppler ducting in the mesopause region and hence they can travel considerable distances horizontally before contributing irreversible changes to the environment.

Optical measurements of the nightglow emissions provide an important tool for determining the occurrence and horizontal characteristics of small-scale, short-period waves at the emission altitudes [*Taylor et al.*, 1987; *Taylor and Hapgood*, 1990]. While the measured horizontal wavelength is an intrinsic parameter, the measured phase speed (and hence the observed wave period) may differ significantly from the intrinsic phase speed (and intrinsic wave period) due to the presence of background winds. However, when multilayer nightglow data are combined with simultaneous wind measurements, intrinsic wave parameters can be investigated over a range of heights, permitting an in-depth study of the propagation characteristics of the wave motions and a more precise comparison with theoretical predictions. In particular, these can help to quantify the importance of small-scale wave ducting in the mesosphere and lower thermosphere for the first time. In this paper, we use novel all-sky imaging data and radar wind data obtained during the Airborne Lidar and Observations of Hawaiian Airglow 1993/Coupling and Dynamics of Regions Equatorial (ALOHA-93/CADRE) campaign to assess the characteristics and frequency of occurrence of ducted versus freely propagating small-scale wave motions over the mid-Pacific Ocean. Joint measurements were made over the new moon period October 6–22, 1993.

## 2. Measurement Techniques and Data Analysis

### 2.1. Imaging Gravity Waves

The imaging data involved optical observations of four nightglow emissions using a large field (180°), monochromatic imaging system located at the Department of Energy DOE building near the summit (2970 m) of Haleakala Crater, Maui (156°W, 21°N). The imager was designed to investigate gravity wave structures over the 80–100 km range by sequentially recording wave signatures in four nightglow emissions: the NIR OH and $O_2$ band emissions and the OI (557.7 nm) and Na (589.2 nm) line emissions. A brief description of the system is given by *Taylor et al.* [1995a]. The camera consists of a thermoelectrically cooled, bare (1024 × 1024 pixel), charge-coupled device (CCD) of high quantum efficiency, ~80% at visible and ~50% at NIR wavelengths. The large dynamic range and low noise characteristics of this device (dark current $<0.5\,e$ $pixel^{-1}\,s^{-1}$) provide an exceptional capability for quantitative measurements of faint, low contrast (<5%) gravity waves. The imager was fitted with a fast (f/4) all-sky (180°) telecentric lens system and a temperature stabilized filter wheel. The OH measurements were made using a broad band filter of bandwidth 715–930 nm incorporating a notch at ~865 nm to suppress contributions from the $O_2$(0, 1) band. The $O_2$(0, 1) band was isolated using a 12-nm bandwidth filter centered at 865.5 nm. Each line emission was selected using high transmission (typically 60–80%) interference filters of ~2.5 nm half bandwidth. In addition to these observations a background sky measurement was made at 572.5 nm (half width 2.7 nm) to aid the interpretation of the visible wavelength data. Integration times determined for these measurements ranged from 15 s for the bright OH emission to 90 s for the OI (557.7 nm) and $O_2$ emissions and 120 s for the faint NaD lines. A summary of the filter characteristics and operational parameters for this campaign is given in Table 1. Sequential measurements were made every ~9 min except for the OI (557.7 nm) emission which was sampled twice per cycle.

Quasi-monochromatic events in the all-sky data were identified, and their times of occurrence were noted. These events were then measured to determine the horizontal parameters of the wave motions: horizontal wavelengths, phase speeds, and directions of motion. The images were calibrated first using the star background to determine the elevation and azimuth of any point in the image field. (The typical accuracy of this calibration is to within 1 pixel, equivalent to ~20 arc min.) A description of this procedure, as applied to narrow angle data, is given by *Hapgood and Taylor* [1982]. To correct for geometrical distortion arising from nonparallel lines of sight in the image itself, the outline of prominent wave crests in each image was traced and mapped onto the ground, assuming a centroid emission altitude of 87 km for the OH emission [*Baker and Stair*, 1988], 90 km for the Na emission [*Greer and Best*, 1967], and 94 km for the $O_2$ and 96 km for the OI (557.7 nm) emissions [*Offermann and Drescher*, 1973]. For each wave event, measurements from a time series of images and maps were used to determine the mean horizontal wavelength, observed phase speed, and predominant direction of motion (usually determined to within an accuracy of ±5°). On some occasions the direction of motion was observed to rotate by as much as ~20–30° over a period of several hours and with altitude. In these cases we have used the wave direction at the central time of observation for the intrinsic wave calculations.

The nominal full width at half maximum (FWHM) of the emission layers (~5–10 km) and the horizontal field of view of the all-sky imager at nightglow altitudes (~500 km radius) provide natural limits for these measurements. Because of destructive interference within the layer for smaller-scale motions, the FWHM of an emission layer sets an approximate lower limit to the vertical wavelengths of the motions that can be detected. Similarly, the horizontal field of view sets an upper limit of ~250 km on the horizontal wavelengths to which the imaging technique is sensitive [*Taylor et al.*, 1995c]. (Larger-scale waves have been detected using a time series of image measurements, but their two-dimensional morphology is not easily determined.) However, as will be shown later, all of the

waves imaged during this campaign exhibited significantly shorter horizontal wavelengths.

## 2.2. MF Radar Winds

The wind data used for this study were collected by a medium frequency (MF) radar system located at the Pacific Missile Range Facility (PMRF) at Barking Sands, Kauai, Hawaii (160°E, 22°N). The mode of operation and data processing algorithms for this system are described in detail by *Fritts and Isler* [1994]. Nominal wind estimates were obtained at 2-min intervals and 2-km vertical spacing from 60 to 100 km during daytime and from 70 to 100 km during nighttime. As nighttime data tend to be somewhat sparse below 82 km, and since the airglow imager only operated at nighttime, the effective altitude range of the radar for this study is ~82–98 km.

The MF wind data were used to approximate the mean wind environment over Maui, where the CCD imager was located, ~375 km to the southeast of Kauai (Figure 1). Because of the spatial separation of the ground stations, temporal averages of the winds over Kauai were used to represent mean winds over Maui. We have used 3-hour averages of the winds over Kauai for this purpose. Since Doppler ducts arise due to structures in the lower-frequency winds which trap higher-frequency wave motions (see section 3), an estimate of the horizontal scale of a Doppler duct can be made by assuming it to be due to a motion with a period ~6 hours or longer. From the gravity wave dispersion relationship one can infer that motions with periods greater than 6 hours will have a ratio of horizontal to vertical scales of greater than 60 to one. Thus waves with vertical scales representative of typical wind variations (≥10 km) will have horizontal scales ≥600 km, so using 3-hour mean winds should provide sensitivity to ducts that have a horizontal extent comparable to or larger than the distance between the ground stations.

## 3. Wave Ducting Theory

Linear gravity wave theory was first developed for the simplified but illustrative case of an atmosphere which is stratified in density and pressure but assumed to be windless, isothermal, irrotational, and inviscid. The resulting governing equations were shown to admit traveling acoustic and gravity wave solutions [*Hines*, 1960]. The dispersion characteristics and intrinsic properties of these waves, as well as their observed amplitudes and scales, led to the first understanding of their importance for momentum and energy transports, particularly in the upper atmosphere (see *Fritts* [1984] for a review of the historical development). Given that the atmosphere has a variable thermal profile, ubiquitous mean winds, and increasing kinematic viscosity with altitude, it was natural that the theory would be advanced further by the relaxation of the simplifying constraints imposed on the background atmosphere. For our purpose here, we note that for wave propagation in general in any medium, inhomogeneities in the medium will give rise to wave refraction and possible wave reflection. In the atmosphere, the inhomogeneities of importance to gravity wave propagation are gradients in background temperature (or more precisely in the stability) and in the wind field. When such gradients give rise to wave reflection, wave ducts (or waveguides, as they are sometimes called) may also occur. The importance of these wave ducts in the atmosphere arises from the fact that waves trapped in well-defined ducts can propagate large horizontal distances with little attenuation.
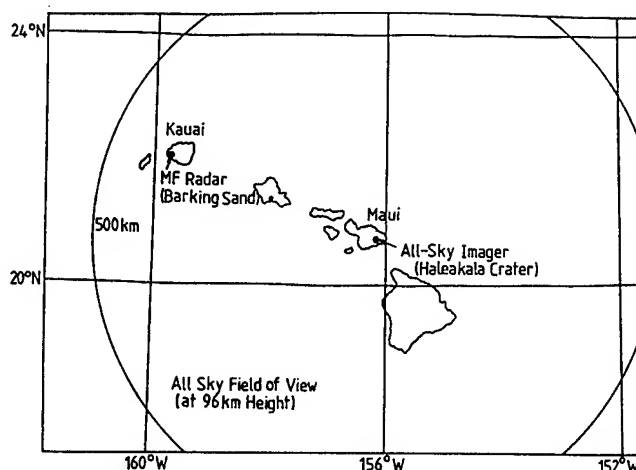


**Figure 1.** Map of observing geometry. Note the field of view of the all-sky camera encompasses the Kauai MF radar site at a range of 375 km.

A good starting point from which to understand wave ducting mechanisms comes from an examination of the Taylor-Goldstein equation, which is the second-order linear, inviscid equation for the vertical velocity field. The Taylor-Goldstein equation can be derived from the linear, inviscid equations of motion after neglecting compressibility effects (acoustic motions) and assuming solutions periodic in time and in the horizontal direction. The Taylor-Goldstein equation is

$$w'_{zz} + \left[ \frac{N^2}{(\bar{u} - c)^2} - \frac{\bar{u}_{zz}}{(\bar{u} - c)} - k^2 \right] w' = 0 \qquad (1)$$

where the subscripts denote partial derivatives, $w'$ is the vertical velocity, $N$ is the buoyancy frequency, $\bar{u}$ is the horizontal wind in the direction of wave propagation, and $c$ and $k$ are the horizontal phase speed and wavenumber, respectively. The most general form of this equation contains additional shear and constant terms associated with compressibility effects; we have neglected these terms because in all the cases studied, the wave phase speeds were much less than the speed of sound. To validate our use of the simplified expression (1), we included the terms associated with compressibility and found our results to be no different than when those terms were neglected.

In equation (1), both $N$ and $\bar{u}$ are functions of altitude. If these are slowly varying functions, WKB solutions can be obtained. Of course, for very narrow velocity jets or steep shears (i.e., $\bar{u}$ varying rapidly), the use of WKB solutions may not be justified. The wind profiles used in this study did not exhibit such rapid variations in $\bar{u}$, though in some cases the WKB approximation may be only marginally justified. However, in order to make quantitative use of Doppler ducting theory, we take WKB solutions to equation (1), with vertical wavenumber $m$ given approximately by

$$m^2 \approx \frac{N^2}{(\bar{u} - c)^2} - \frac{\bar{u}_{zz}}{(\bar{u} - c)} - k^2 \qquad (2)$$

It is now easy to see how wave reflection occurs: if $N^2$ or $\bar{u}$ or both together vary with altitude so as to make $m^2 < 0$, a region of evanescence exists in which the wave cannot freely propagate, causing reflection of wave energy.

Earlier work focused on wave ducting due to mean temperature gradients in the atmosphere and deliberately assumed a
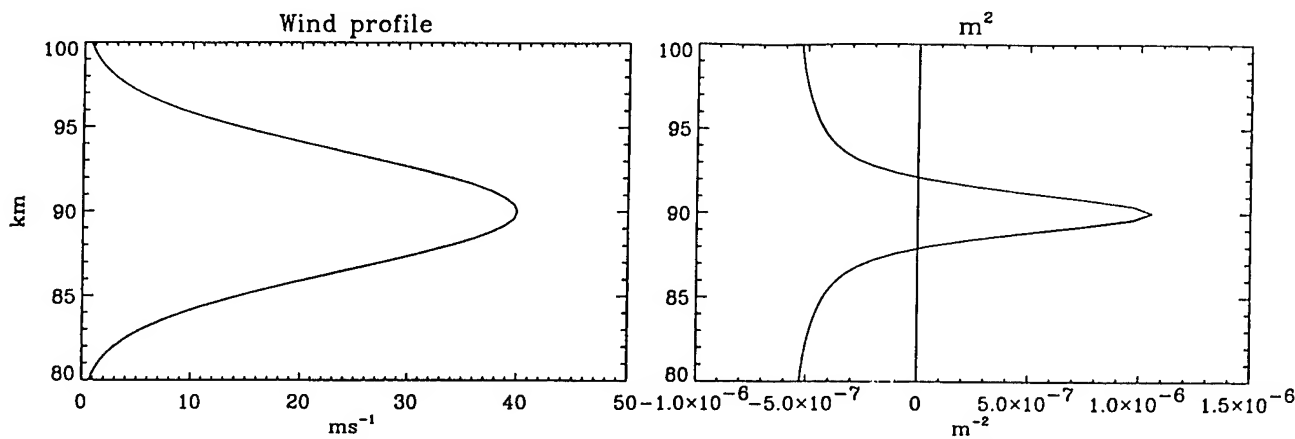
Figure 2.- Sketch of a theoretical Doppler duct due to mean wind fields.

zero mean wind. The ducts due to temperature gradients are called thermal ducts, and a good summary of their dominant wave modes is given by *Francis* [1974]. These are relatively stable, long-lived ducts, which tend to support waves with high horizontal phase speeds and large vertical scales. However, it is smaller-scale waves which play the more important role in wave-mean flow interactions, because of their larger fluxes of wave energy and momentum [*Fritts*, 1989]. Because these motions are typically slower, it is essential to account for wind variations in describing their responses to varying atmospheric conditions.

A theory of wave ducting due to variation in the mean wind has been formulated [*Chimonas and Hines*, 1986]. These ducts are called Doppler ducts. As mean winds are highly variable both spatially and temporally, they give rise to ducted modes having a wide range of phase speeds and vertical scales. Thus, although they may be shorter-lived than thermal ducts, Doppler ducts are potentially more important for the atmospheric circulation because of their potential to trap smaller-scale waves. Such smaller-scale, guided waves could then travel large horizontal distances before their transports of energy and momentum interact with the mean flow.

Theoretically, Doppler ducts can occur whenever the mean wind profile has a local maximum (or minimum) slightly less (or more) than the observed wave phase speed. The increase of $(\bar{u} - c)^2$ away from the local wind maximum or minimum can lead to regions of evanescence on either side of a region of vertical propagation (see equation (2)). To illustrate this situation, a sketch of an idealized Doppler duct is presented in Figure 2.

In the present study we consider only the effects of Doppler ducting. For this purpose, we have evaluated $m^2$ in equation (2) using the airglow observations to provide estimates of $c$ and $k$ and the Hawaii radar data to provide estimates of $\bar{u}$ and have taken $N^2$ to be constant $(0.0002 \ s^{-2})$. Considering only the effects of Doppler ducting should not be too severe a restriction since the observations reported here occurred near the winter mesopause, where $N^2$ is slowly varying in the mean. For lower-frequency motions which might give rise to Doppler ducts, $N^2$ is more variable, but as will be seen, $\bar{u}$ was highly variable over this region, and variations in $\bar{u}$ appear quadratically in equation (2), so it is expected that variations in $\bar{u}$ would be more important than variations in $N^2$. In any case, we have no choice but to take $N^2$ to be constant, as coincident temperature measurements were not made.

Since the observations reported here occurred over a limited altitude range, as will be seen, it was not always possible to identify both edges of a suspected Doppler duct.

Finally, we note that in the following analysis we have evaluated the second term on the right-hand side of equation (2) numerically using a three-point algorithm applied to the radar data. Sensitivity tests showed that this term could not simply be neglected. For example, consider the case of a Doppler duct associated with a velocity jet. Near the jet maximum, $\bar{u}_{zz}$ is negative, so that the second term in (2) is negative (since $c > \bar{u}$), while near the edge of the jet, $\bar{u}_{zz}$ is positive, so that the second term in (2) positive. Thus the overall effect of this term is to decrease $m^2$ in the center of the duct and to increase $m^2$ near the edge of the duct. However, there is unavoidable uncertainty in evaluating a second derivative numerically from a wind profile with nine or fewer data points. So we have evaluated $m^2$ both with and without the curvature term and compared the results for each event. In all of the cases studied, its effect was negligible or in the case of a ducted motion its effect was to lower the value of $m^2$ inside the duct, and somewhat broaden the width of the duct, but not to fundamentally alter its character. In the results which follow, the curvature term has been included.

## 4. Results and Discussion

### 4.1. Analysis of the Images

Table 2 lists the results of an ensemble of wave measurements using the CCD image data during the ALOHA-93 campaign. These results represent a significant fraction of the total data set analyzed to date. For convenience, we have listed the events in chronological order and have assigned each event a number to simplify its identification. Table 2 lists the day of year and mean time (UT) of observation for each wave event, the emissions in which the wave event was most readily observed, the observed phase speed $c$, the mean wind in the direction of wave propagation $\bar{u}$ as measured by the MF radar, and the horizontal wavelength $\lambda_h$. (The rest of Table 2 is described in section 4.2.) Several events exhibited exceptionally clear wave structure in some but not all of the nightglow emissions: for example, events 2, 11, 15, 22, and 33. In comparison, some events, such as events 10, 13, 26, and 36, were prominent in all four nightglow emissions. One of these, event 13, exhibited an unusual reversal in contrast between the OH and OI structures and has already been reported on elsewhere

**Table 2.** Gravity Wave Events Used for This Study, With Corresponding Wave Parameters as Determined, or Inferred, From the Image and Radar Data

| Wave Event | Day of Year | Time, UT | Emission | $c$ | $\bar{u}$ | $\lambda_h$ | $\lambda_z$ | Propagating | Ducted | Evanescent | Evanescent or Ducted |
|---|---|---|---|---|---|---|---|---|---|---|---|
| 1 | 280 | 1045 | OI, Na, OH | 37 | 9 | 20 | 10–50 | X | | | |
| 2 | 281 | 0720 | OI | 58 | −8 | 16 | | | X | | |
| 3 | 281 | 0900 | OI, O$_2$, Na, OH | 42 | −15 | 36 | 15–50 | X | | | |
| 4 | 281 | 1030 | OI, Na, OH | 34 | 2 | 21 | 12–30 | X | | | |
| 5 | 282 | 0700 | OI, O$_2$, Na | 69 | 15 | 12 | | | | X | |
| 6 | 282 | 1025 | OI | 60 | −12 | 27 | | | | | X |
| 7 | 282 | 1030 | OI, O$_2$, Na, OH | 54 | 10 | 25 | | | | | X |
| 8 | 282 | 1110 | OI, O$_2$, Na, OH | 61 | 9 | 10 | | | | X | |
| 9 | 282 | 1240 | OI, O$_2$, Na, OH | 54 | −9 | 22 | | | | X | |
| 10 | 282 | 1330 | OI, O$_2$, Na, OH | 39 | −13 | 23 | | | | X | |
| 11 | 283 | 0930 | OI, Na | 48 | 28 | 13 | | | | | X |
| 12 | 283 | 0940 | OI, O$_2$, Na, OH | 38 | 0 | 19 | | | X | | |
| 13 | 283 | 1100 | OI, O$_2$, Na, OH | 76 | −15 | 19 | | | | X | |
| 14 | 283 | 1100 | OI, O$_2$ | 56 | 9 | 16 | | | | X | |
| 15 | 284 | 1240 | OI, O$_2$ | 36 | −23 | 19 | | | | X | |
| 16 | 285 | 1410 | OI, O$_2$, Na | 41 | −55 | 27 | | | | X | |
| 17 | 286 | 1200 | OI, O$_2$, Na, OH | 60 | −21 | 32 | | | | X | |
| 18 | 286 | 1330 | OI, O$_2$, Na, OH | 50 | 30 | 18 | | | | | X |
| 19 | 286 | 1330 | OI, O$_2$, Na | 89 | −24 | 17 | | | | X | |
| 20 | 286 | 1411 | OI, O$_2$, Na | 70 | −35 | 12 | | | | X | |
| 21 | 286 | 1500 | OI, O$_2$, Na | 61 | 20 | 14 | | | X | | |
| 22 | 287 | 1100 | OI, O$_2$ | 61 | 18 | 30 | | | X | | |
| 23 | 288 | 0950 | OI, O$_2$, Na | 76 | 9 | 53 | | | | | X |
| 24 | 291 | 0730 | OI, O$_2$, Na, OH | 59 | −11 | 16 | | | | X | |
| 25 | 291 | 1400 | OI, O$_2$, Na, OH | 35 | 11 | 14 | | | | | X |
| 26 | 292 | 0930 | OI, O$_2$, Na, OH | 57 | 24 | 14 | | | | | X |
| 27 | 292 | 1235 | OI, Na, OH | 97 | −8 | 19 | | | | X | |
| 28 | 292 | 1430 | OI, O$_2$, Na, OH | 45 | 15 | 15 | | | X | | |
| 29 | 293 | 1030 | OI, O$_2$, Na, OH | 39 | 6 | 21 | 10–20 | X | | | |
| 30 | 293 | 1325 | OI, O$_2$ | 50 | 0 | 29 | 40–80 | X | | | |
| 31 | 293 | 1340 | OI, O$_2$, Na, OH | 37 | −22 | 20 | | | | | X |
| 32 | 293 | 1350 | OI, O$_2$, Na, OH | 38 | −11 | 22 | | | | | X |
| 33 | 294 | 1140 | OI, O$_2$ | 33 | 8 | 20 | 7–14 | X | | | |
| 34 | 294 | 1310 | OI, O$_2$, Na, OH | 53 | −3 | 30 | 10–40 | X | | | |
| 35 | 295 | 0930 | OI, O$_2$, Na, OH | 40 | −24 | 19 | | | | | X |
| 36 | 295 | 1230 | OI, O$_2$, Na, OH | 34 | −20 | 38 | 15–55 | X | | | |

Units for velocities are m s$^{-1}$; units for wavelengths are km.

[*Taylor et al.*, 1995b]. Table 2 shows that on average only about 50% of the wave events were detected in all four nightglow emissions. In general, the OI emission provided images with the greatest contrast, followed by OH, O$_2$, and Na, in that order. The wave structure was usually most prominent in one or two emissions (e.g., OH and Na or OI and O$_2$) and of significantly lower contrast (or absent) in the other emissions. This fact suggests that Doppler ducting may have played an important role during this campaign, but by itself does not provide evidence to that effect, since other processes such as wave breaking or critical level encounters could easily account for localized altitude responses as well.

Figure 3 shows an example of wave structure imaged in all four emissions. This display, event 26, was observed on October 19 and its progression over the Hawaiian Islands was also recorded by a second imager located on Mauna Loa, Hawaii [*Swenson et al.*, 1995], ~450 km to the southeast of Maui (see Figure 1). This display was unusual in that it exhibited a limited number of wave crests (three to four) that moved rapidly southward at ~60 m s$^{-1}$, indicating a wave period of ~5 min, close to the local buoyancy period. The leading edge and the following wave crests are easily identifiable in each emission permitting a good estimation of the relative positions of the phase fronts (discussed later) and have yielded an accurate

measurement of the wave structure in the OI emission indicating a mean height of 95 ± 2 km [*Taylor et al.*, 1995d]. As this pattern was evident in all four emissions extending over the height range ~80–100 km, it may be expected that it is the signature of a freely propagating wave. However, the MF radar data (presented in section 4.2) suggest that it was evanescent in nature. Further evidence in support of this result is given later (Figure 7) when the phase relationship of these waves are examined for different emission altitudes.

Examples of wave data recorded on other nights during the campaign are shown in Figure 4, corresponding to events 2, 10, 13, 25, 24, and 36 (Figure 4a–4f). Prominent wave structures are obvious features of each of these images, representing a variety of wave motions. As will be seen, the waves shown here were inferred to have a range of propagation characteristics, from ducted or evanescent to freely propagating. However, as can be seen, no obvious characteristics of the individual images were found to distinguish ducted or evanescent waves from freely propagating waves.

When images of the same waveforms are clearly identifiable in data from more than one emission, it is possible to estimate whether or not the waves are vertically propagating, since the four nightglow emissions are centered at separate heights. The images from different emissions were made at slightly different
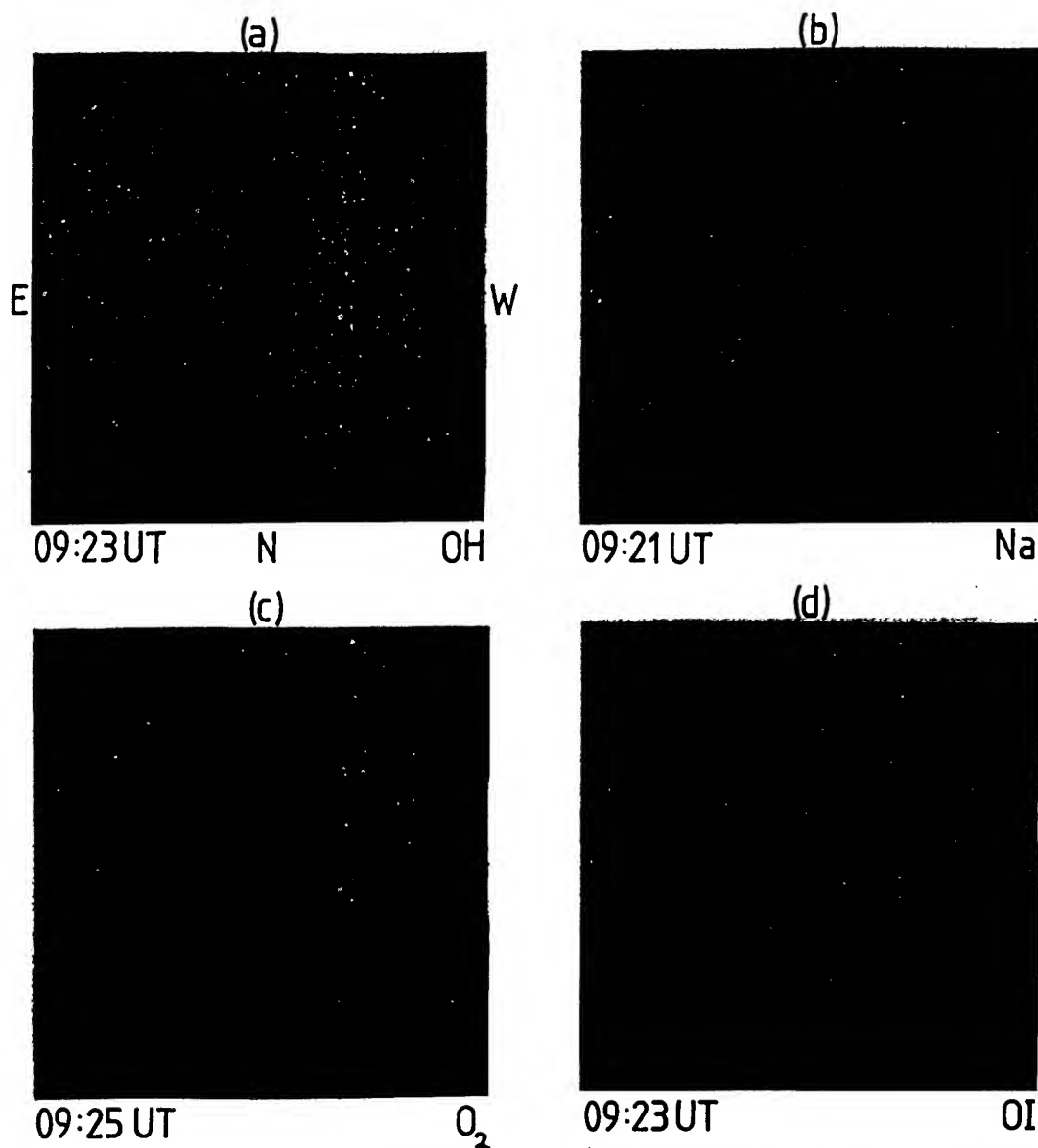
**Figure 3.** Event 26, as imaged by the CCD camera in the (a) OH, (b) Na, (c) $O_2$, and (d) OI emissions. South is to the top in the images.

times because of the finite integration time needed for each exposure (15–120 s). After correcting for this time difference using the measured horizontal phase speed, however, one can obtain approximately simultaneous maps from two (or more) different emissions. Ground maps can then be compared, and the spatial locations of several wave crests can be used to determine the magnitude of the mean phase shift between different emission layers. An alternative approach is more suitable when a single wave crest is much brighter in the images than other wave crests within the same wave pattern. In this case, the motion of the prominent waveform is followed as a function of time in two (or more) different emissions, after once again correcting for the time difference due to finite imaging time. In either case, no apparent spatial shift between the waveforms at different heights suggests that the waves are vertically evanescent or ducted, while a spatial shift between the waveforms is considered suggestive of vertical phase pro-

gression. The lack of a phase shift between images of different airglow layers is only suggestive of ducting because the phase of the intensity response of airglow depends in general on details of the airglow photochemistry, so that the exact phase relationship between the intensity and the perturbing wave depends on which airglow is being imaged.

It is important to note that this technique is most effective when the gravity waves are imaged near the zenith (±40°). Observations at larger zenith angles can be complicated by line-of-sight effects and by difficulties in identifying and mapping accurately the geographic location of a waveform at a large range in the all-sky image format (this limitation does not adversely affect horizontal wavelength measurements which depend on a relative measure of crest separations rather than absolute positions). This analysis has been applied to several of
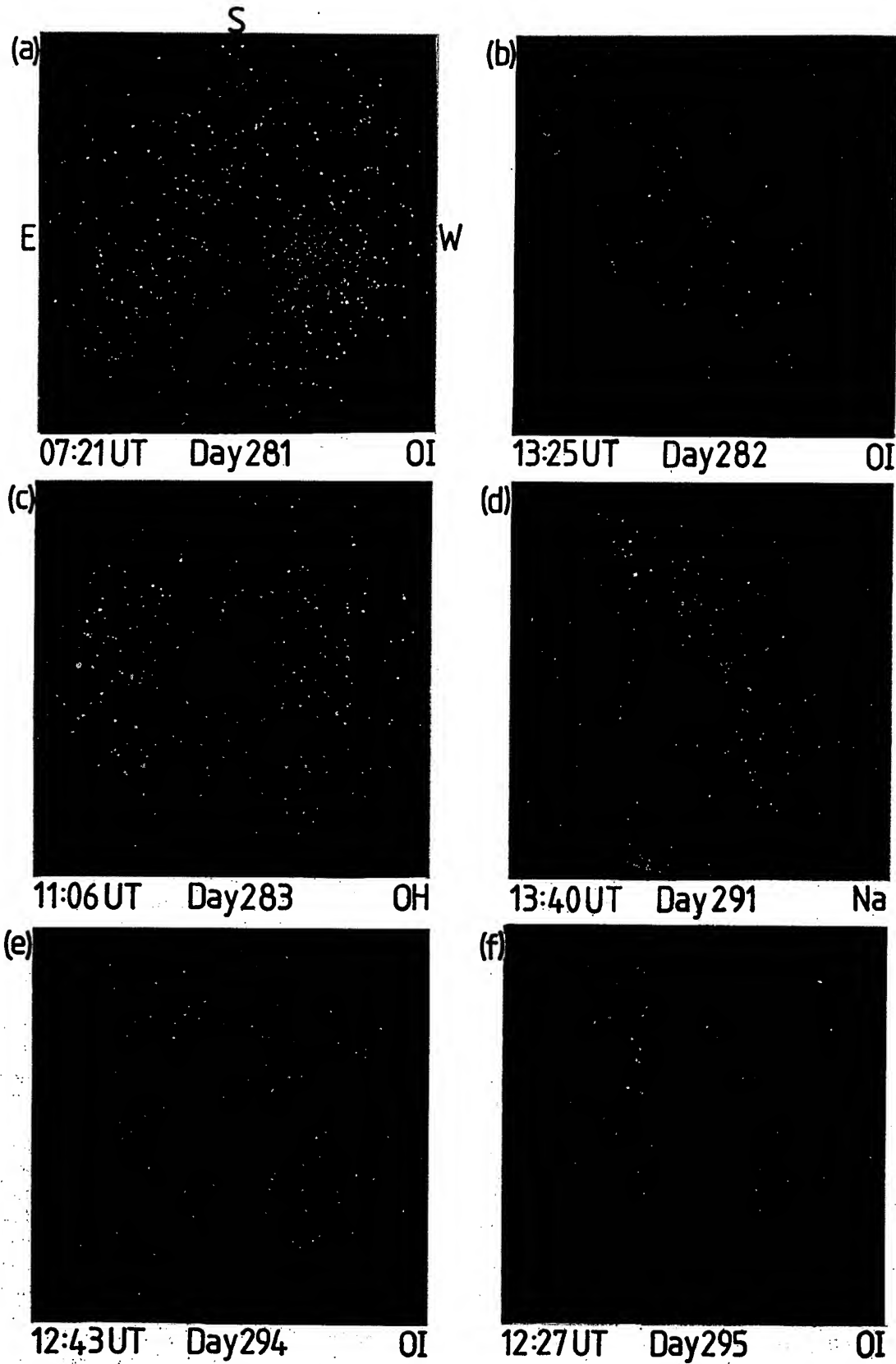
**Figure 4.** As in Figure 3, but for (a) event 2 imaged in the OI emission, (b) event 10 imaged in OI, (c) event 13 imaged in OH, (d) event 25 imaged in Na, (e) event 34 imaged in OI, and (f) event 36 imaged in OI.
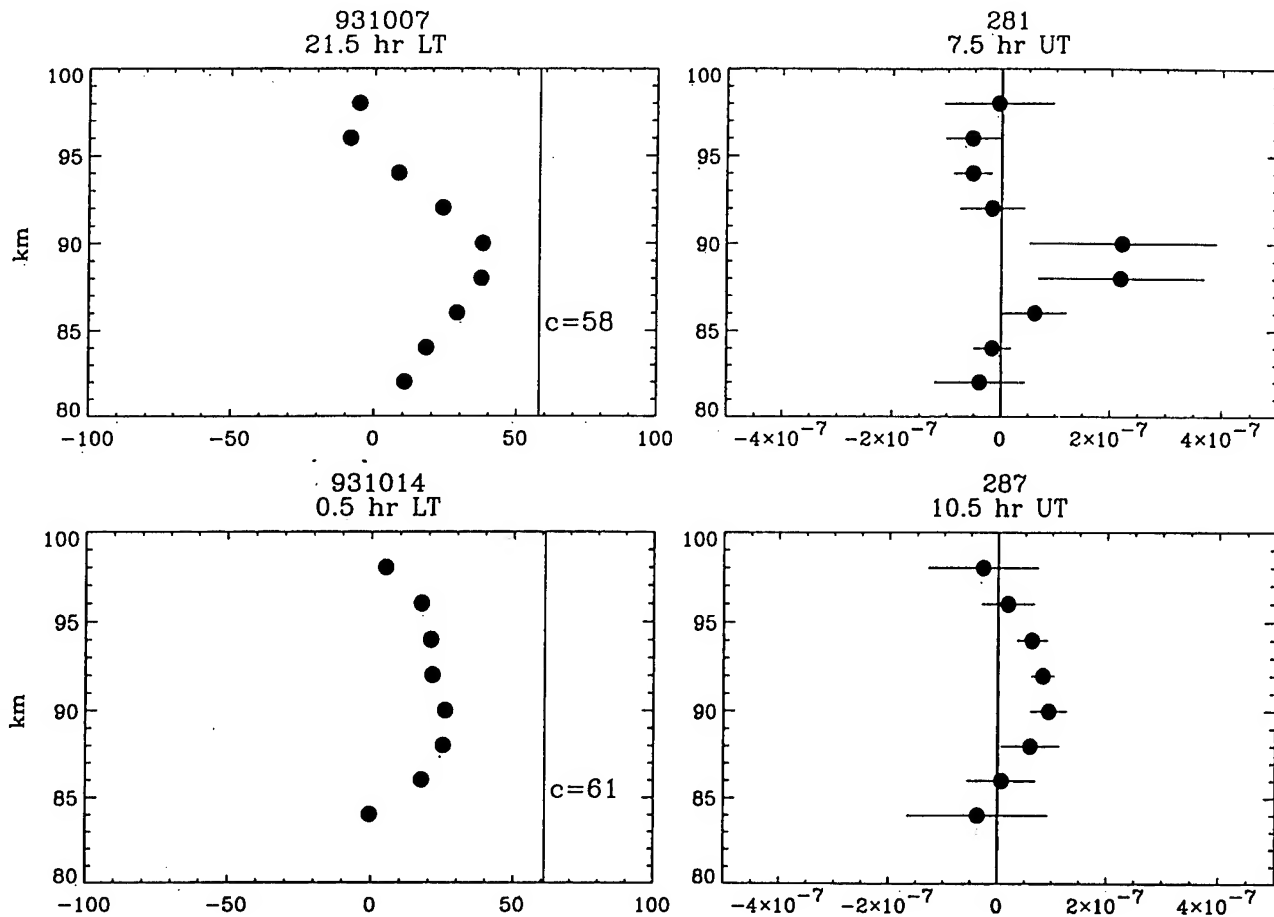
**Figure 5.** (left) Measured wind profiles along the direction of wave propagation for events (top) 2 and (bottom) 22, (right) together with inferred values of $m^2$ in each case.

the wave events listed in Table 2 (whenever possible) to investigate their nature. However, before presenting these results we first examine the characteristics of the waves as determined by the radar measurements of the prevailing mean wind field during each event.

### 4.2. Inferred Wave Parameters

For each wave event, 3-hour mean winds determined from the MF radar data were used to generate profiles of $\bar{u}$, the projection of the mean wind vector onto the wave azimuth. These values of $\bar{u}$ were then inserted into equation (2) together with measurements of $\lambda_h$ and $c$ to calculate profiles of $m^2$ in each case. In each case the error was estimated assuming mean uncertainties for $c$ and $\lambda_x$ (as determined from the image data analysis) of $\delta c/c = 0.05$ and $\delta\lambda_x/\lambda_x = 0.03$. The error in the 3-hour mean wind was determined spectrally and was found to be less than 1 m s$^{-1}$, consistent with error bars of 7–10 m s$^{-1}$ for the 2-min wind data [*Fritts and Isler*, 1994]. An uncertainty in the estimated height from the radar data of ~2 km was used in determining the uncertainty in $\bar{u}_{zz}$. Some recent work suggests that during the time of this study the Hawaii radar may have somewhat underestimated winds at the uppermost heights due to receiver saturation. This implies an additional source of error at the uppermost heights which is difficult to quantify. Finally, as mentioned in section 2, we have chosen 3-hour mean winds in order to address inherent limitations to

the analysis associated with the spatial separation of the imager and the radar.

The results of this analysis are summarized in Table 2. Unless $m^2 > 0$ throughout the wind profile, the $\lambda_z$ column has been left empty. Since $\lambda_z$ varies with $\bar{u}$, a range of $\lambda_z$ is given rather than a single value for those cases where $m^2$ was positive everywhere.

For each event, the values for $\bar{u}$ given in Table 2 were determined as near as possible to the assumed mean altitude of the dominant nightglow emission. Intrinsic wave periods determined for these values of $\bar{u}$ were in most cases less than 10 min, providing further justification for our choice of 3-hour means to represent as closely as possible the background wind environment. Table 2 also shows the propagating or nonpropagating character over the entire height range of the wind profile. In several cases, examples were found that showed a region of positive $m^2$ bounded by regions where $m^2$ was negative, indicative of a Doppler duct. Event 2 is a particularly good example of a Doppler duct. This wave motion was detected only in the OI emission (Figure 4a) and is discussed in more detail later. Many other cases exhibited $m^2$ either positive or negative over the entire altitude range of the wind profile, implying that the wave was vertically propagating or evanescent, respectively. Other cases were less clear and showed a single change in sign of $m^2$ over the altitude range of the wind profile. In light of these possibilities, individual wave
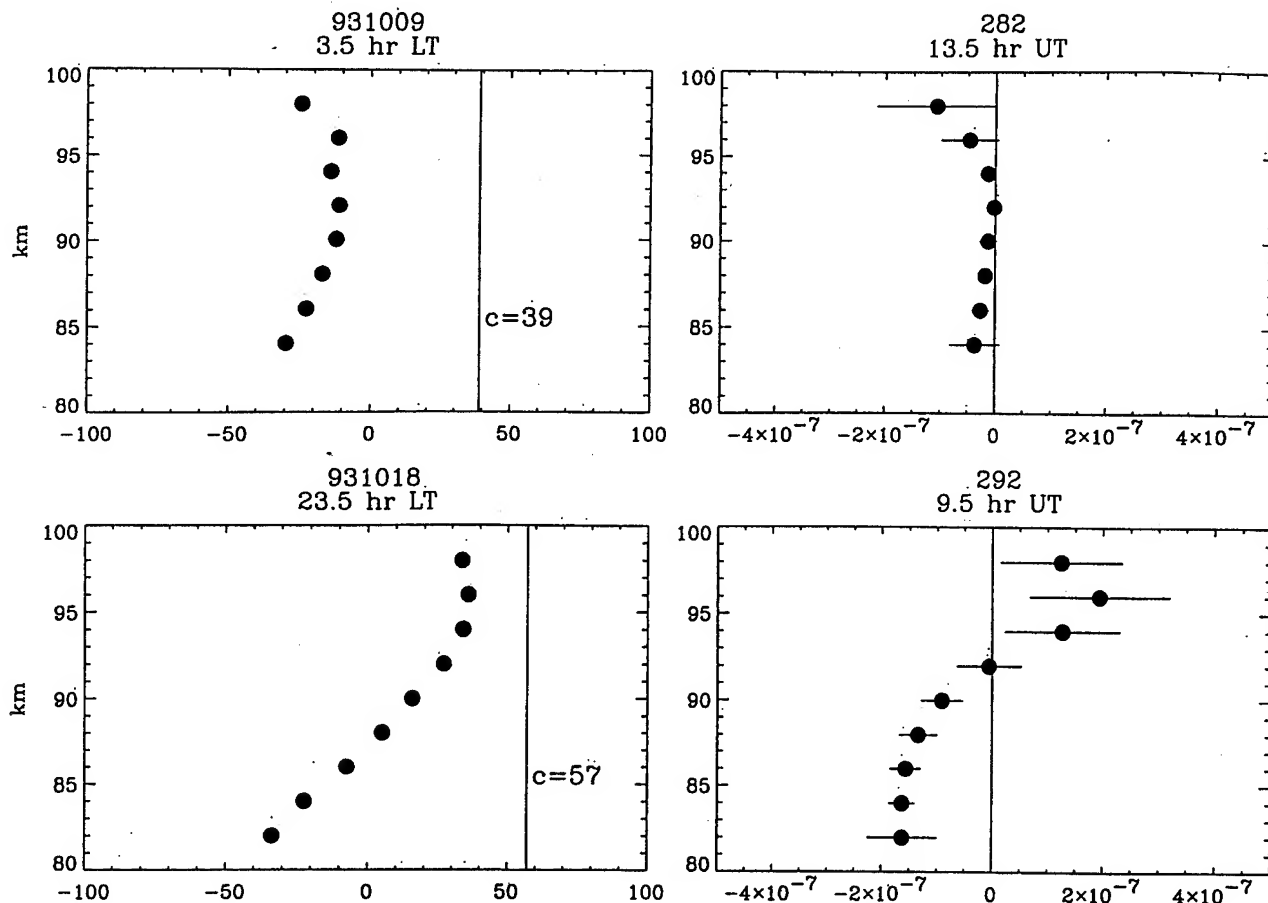
**Figure 6.** As in Figure 5, but for events (top) 10 and (bottom) 26.

events are characterized in Table 2 as propagating ($m^2 > 0$ everywhere), ducted (Doppler duct, with an $m^2 > 0$ region bounded by $m^2 < 0$ regions), evanescent ($m^2 < 0$ everywhere), and evanescent or ducted (a single change of sign of $m^2$ within the height interval). Considering the relatively narrow altitude range of the available wind profiles, it is not surprising that it is not always possible to resolve the full vertical extent of the duct. Cases categorized as "evanescent or ducted" in Table 2 may represent situations when only one edge of a Doppler duct was clearly resolved by the limited altitude range of the wind data. Similarly, the purely evanescent cases may be instances where the duct itself was beyond the altitude range of the wind data, and only an evanescent region outside the duct was resolved. Thus all of the events listed as ducted, evanescent, or both in Table 2 can be considered to be suggestive of ducted behavior. Of the total of 36 events presented here, 28 fall under ducted, evanescent, or both and only 8 occur in the freely propagating column. This indicates that a significant fraction, up to ~75% of the cases studied, were evanescent or ducted waves.

### 4.3. Illustrative Examples

Examples of wave events inferred to be vertically ducted or evanescent are shown in Figures 5 and 6. In each case, the left side shows the measured profile of $\bar{u}$, while the value of $c$ for the event is indicated by a vertical line. The right sides depict the inferred profiles of $m^2$. Plots for events 2 and 22 are shown in Figure 5 (an image corresponding to event 2 was shown in

Figure 4a). These are examples of Doppler ducts, illustrating how the wind Doppler shifts $|c - \bar{u}|$ so that a region of positive $m^2$ is bounded by regions of negative $m^2$. Note that $m^2$ maxima occur where $|c - \bar{u}|$ is a minimum. As mentioned before, event 2 was only detected in the OI emission and, perhaps surprisingly, was not detected in the emissions which originate closer to the wind-inferred ducted region (in this case, ~85–92 km). This sometimes occurs in other cases and could be due to a variety of reasons. First, as mentioned previously, the OI images generally had the greatest contrast, and so waves were most easily detected in them. Second, in general, there is no reason to expect to see ducted waves only in the ducted (i.e., $m^2 > 0$) region. In the evanescent region outside a Doppler duct, wave amplitudes fall off exponentially; how rapid this falloff is depends on the wind and stability profiles responsible for each duct. In some cases, such as event 2 (Figure 5), this falloff is not steep. Third, other waves and/or turbulence may be present which obscure the signature of the ducted wave at one height but not at another. For example, a wave propagating upward from below may have reached the OH layer but not the OI layer.

Plots for events 10 and 26 are shown in Figure 6 (images corresponding to these events were shown in Figures 4b and 3, respectively). Event 10 is an example of an evanescent region throughout the range of the wind profile, while event 26 is an instance where $m^2$ undergoes a single change in sign. In the latter case, this may represent the lower side of a Doppler duct, which may extend beyond the maximum height of the wind
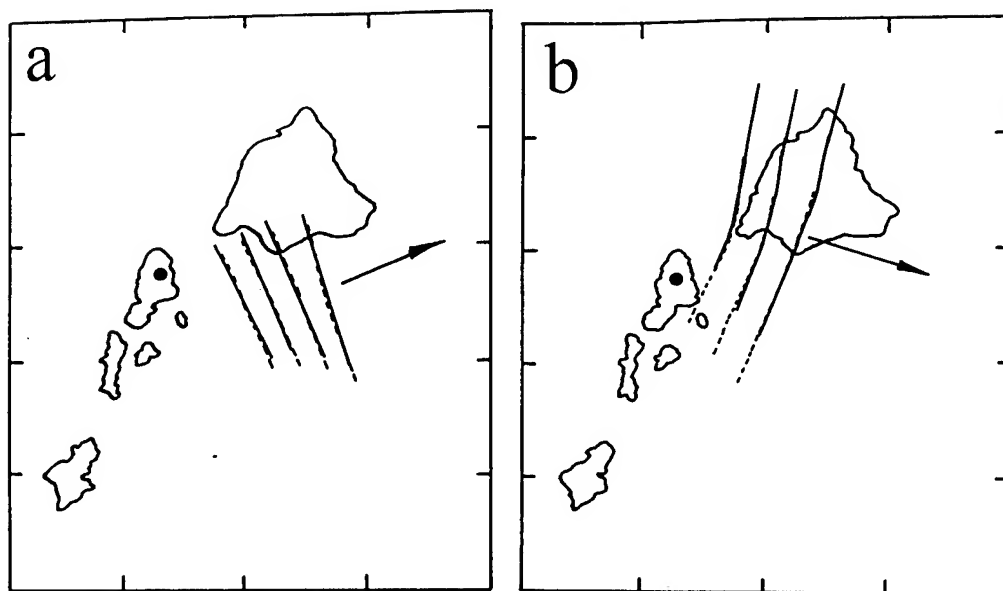
**Figure 7.** Superimposed maps from images of the OH emission (~87 km) and the OI emission (~96 km) corresponding to the events in Figure 6 for (a) event 10 and (b) event 26.

profile. Assuming this to be the case, then both of these events imply waves which were not freely propagating vertically.

For comparison with these inferences, superimposed maps of the OH and OI nightglow waveforms for events 10 and 26 are shown in Figure 7. These emissions were chosen as they are the farthest apart (~10 km) and therefore should be the most sensitive for detecting significant phase shifts associated with the tilt of the wave phase surfaces. As indicated earlier, it was
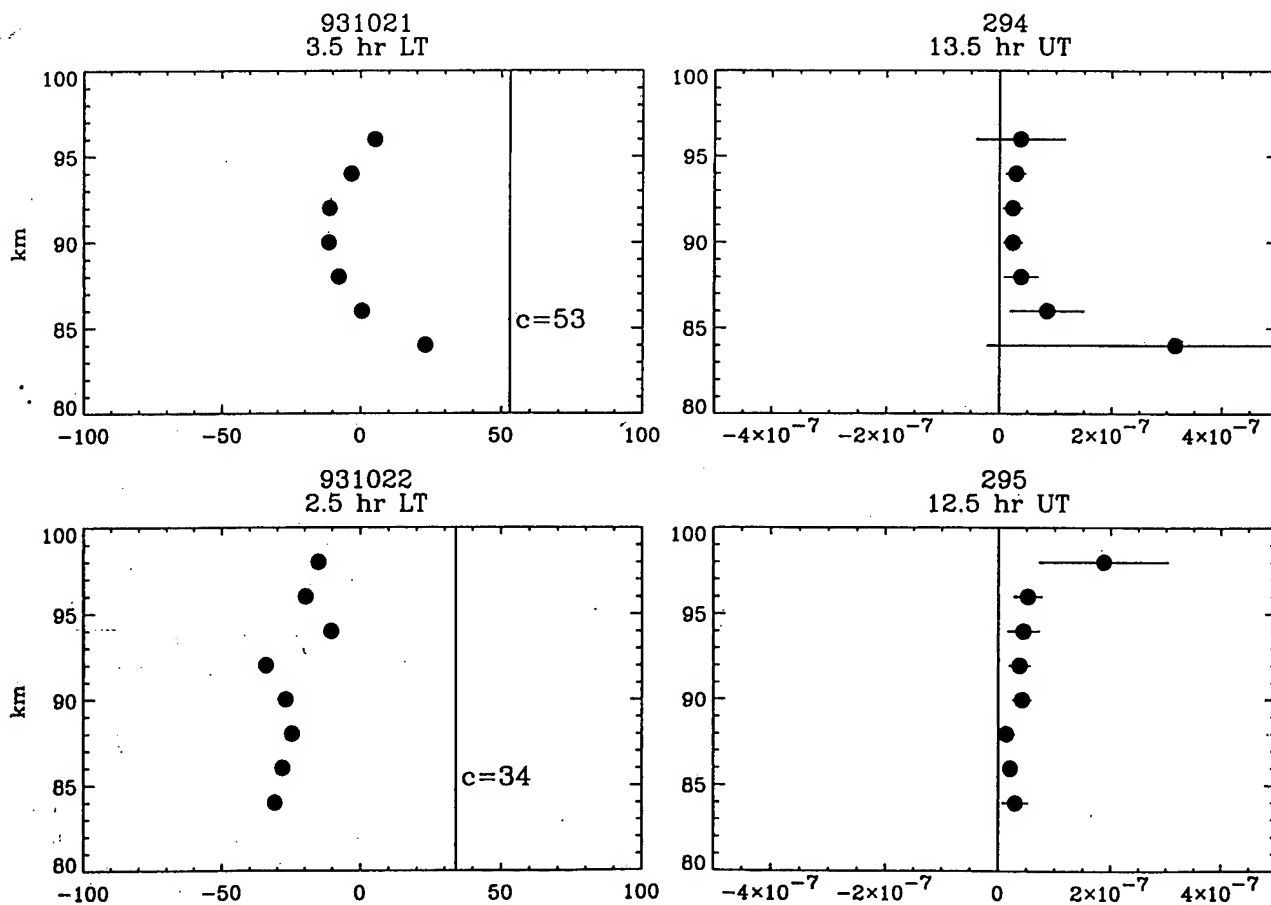


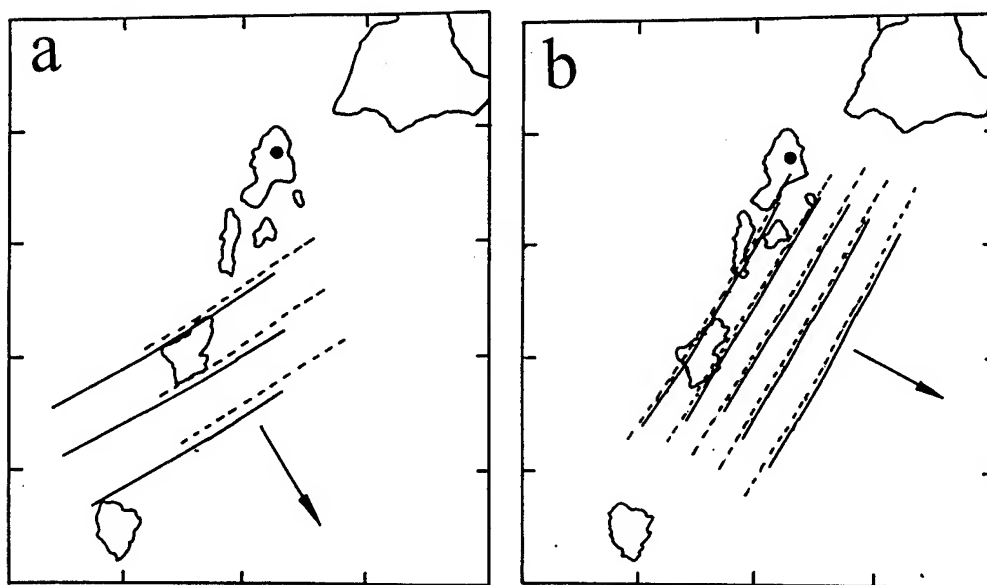**Figure 8.** As in Figure 5, but for events (top) 34 and (bottom) 36.

**Figure 9.** As in Figure 7, but corresponding to the events shown in Figure 8 for (a) event 34 and (b) event 36.

usually not possible to make such ground maps in the cases where Doppler ducts were fully resolved as the wave structure was often only detectable in one (or sometimes two close by) emissions. The map for event 10 was made using several adjacent crests in the wave train imaged at one time, while the map for event 26 was made for the prominent leading waveform and plots its motion as a function of time in the OH and OI emissions. In both cases, a single line has been drawn to mark the location of the center of each bright band measured; the OI features are depicted by the solid lines and the OH features are depicted by the dashed lines. This was done so that the lines would represent the same wave phase, independent of

the width of the band, which can depend on the horizontal displacement of the wave during the differing exposure times, or on factors related to airglow photochemistry. Figure 7 shows that in both cases the phase shifts between the OH and OI wave crests are small, indicating that within the limits of the measurement accuracy these two events exhibited no vertical component of phase progression. This agrees with the non-propagating character inferred from the radar for these events.

In contrast to the previous examples, two examples of waves (events 34 and 36) that were inferred to be vertically propagating are shown in Figure 8 (images corresponding to these events are shown in Figures 4e and 4f). In these two cases, $m^2 > 0$ throughout the height range of the wind profile. For event 34, the inferred vertical wavelength ranged from ~10 to 40 km, while for event 36 it ranged from ~15 to 55 km. Ground maps showing the locations of superimposed OH and OI wave crests for these two events are shown in Figure 9. For consistency the same format is used as in Figure 7, and once again one map illustrates the motion of a single prominent OH/OI waveform as a function of time (event 34), while the other depicts several crests at the same time in both emissions (event 36). In both maps a significant phase shift is evident between the OH and OI waveforms, in good agreement with the inferred propagation character determined from the radar data. Accurate determination of the magnitude of the phase shift from the image data depends critically on the separation of the two emission layers, which was not measured during this campaign. However, a larger phase shift was determined for event 34 than for event 36, which is consistent with the shorter vertical wavelength for event 34 relative to that for event 36 deduced from the radar data comparison.

### 4.4. Scale Dependence

To summarize the measurements and results presented in Table 2, a histogram plot of all 36 events is given in Figure 10, where the number of events of each type have been binned by horizontal wavelength. Events classified in the last three columns of Table 2 are considered to be nonpropagating in Figure
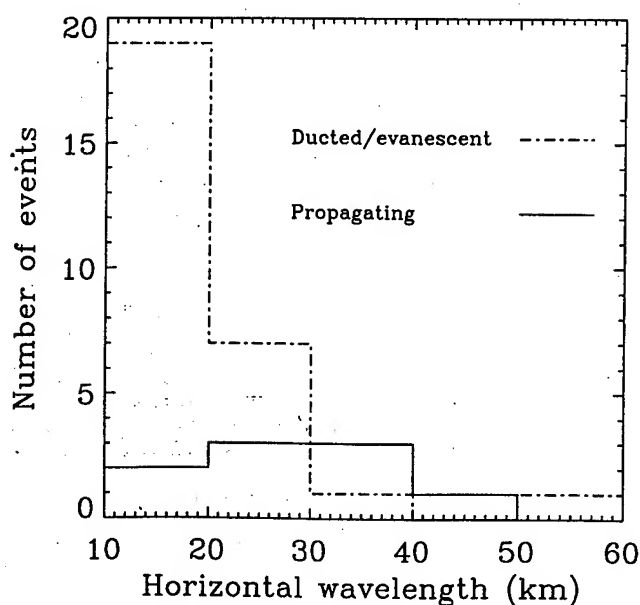


**Figure 10.** Histogram comparing the number of propagating waves to the number of nonpropagating waves per horizontal wavelength bin.

10; a similar histogram plot is shown for the waves which were inferred to be freely propagating. As can be seen, there is an overall tendency for ducted or evanescent behavior to occur more frequently for waves which have smaller horizontal scales. This result is consistent with Doppler ducting theory as small-scale waves have larger horizontal wavenumbers ($k$ in equation (2)) and thus more easily encounter variations in $c - \bar{u}$ leading to $m^2 < 0$.

## 5. Potential Wave Sources

One impact of this study is the investigation of potential wave sources. In the absence of ducting, short-period waves generated in the troposphere would be expected to propagate relatively short horizontal distances (typically a few hundred kilometers) from the source region before penetrating into the upper mesosphere. This is because the elevation angle at which the gravity wave energy is directed depends on the wave period, and short-period waves tend to propagate much more steeply than longer-period waves. For source studies, a first estimate of the horizontal range of propagation can be estimated from the dispersion relation. However, background winds in the intervening stratosphere and lower mesosphere can act either to impede the upward motion of these waves by absorption at critical levels or to extend their horizontal range of propagation by Doppler shifting their motions to longer intrinsic periods. Similarly, ducting in the mesosphere and lower thermosphere can significantly increase the distance over which waves can progress horizontally before dissipating or penetrating to higher altitudes.

For waves observed at mesopause altitudes, investigations of their sources are notoriously difficult for the above reasons and only on rare occasions have isolated sources been positively identified [e.g., *Taylor and Hapgood*, 1988]. One source that is thought to be important for generating extensive wave motions are tropospheric fronts. On numerous occasions during the ALOHA-93 campaign (March–April 1990) extensive, short-period waves were observed to progress towards the SE [*Taylor and Hill*, 1991]. An initial investigation of the sources of these events revealed a series of frontal systems progressing toward the Hawaiian Islands from the NW. However, they were all at a significantly larger range than would be expected assuming the waves were freely propagating in nature, suggesting either wave ducting was occurring or other sources were responsible for their generation [*Taylor and Edwards*, 1991]. More recently, during the ALOHA-93 campaign one of the primary flights of the airborne instrumentation was toward a "storm front" to investigate wave generation by such systems. The airborne all-sky imager recorded considerable wave activity as the aircraft approached within a few hundred kilometers to the NW of Maui [*Swenson and Espy*, 1995]. Wave motions exhibiting a similar horizontal phase speed (39 m s$^{-1}$) and orientation (150°) were recorded several hours later by our all-sky imager located on Haleakala [*Taylor et al.*, 1995a]. An example image of this wave pattern in the OI emission was given in Figure 4b (event 10) which shows the waves as they appeared at low elevations toward the SE sometime after passing through the zenith. Of considerable interest here is the fact that this particular wave pattern was determined to be evanescent using the MF wind data. Thus it appears that Doppler ducting played a major role in extending the horizontal range over which the wave was able to propagate on this occasion.

The similarity of this wave motion to those observed frequently during the ALOHA-93 campaign suggests that these disturbances may also have been signatures of Doppler ducted waves. Assuming this to be so leads us to speculate that Doppler ducting may well be commonplace. This result may also help account for the relatively high occurrence frequency of wave structure that has now been observed during both ALOHA campaigns in the absence of major orographic forcing or nearby tropospheric disturbances such as storm fronts and jet streams [*Taylor and Hill*, 1991; *Swenson and Espy*, 1995; *Taylor et al.*, 1995a].

## 6. Summary and Conclusions

Simultaneous MF radar and high-resolution imaging measurements were made from two low-latitude, oceanic sites located on the islands of Kauai and Maui shortly after the fall equinox (October 6–23) 1993 during the ALOHA-93 campaign. A study of 36 discrete quasi-monochromatic wave events has revealed a significant fraction of them to be occurrences of wave ducting, with ducted or evanescent behavior inferred for up to ~75% of the wave events. Independent evidence for ducted or evanescent versus propagating behavior was obtained using measurements of the same wave structures in different nightglow emissions spanning ~80–100 km. In each instance, where accurate ground maps from the different emissions could be compared, there was good accord between the observed propagating character of the waves and the propagating character inferred from the radar wind data. Furthermore, smaller-scale waves were found more likely to be ducted than larger-scale waves, in agreement with Doppler ducting theory which predicts that smaller-scale waves are more likely to be ducted than larger-scale waves because $k^2$ is large.

Owing to natural limitations of the imaging technique, only waves with horizontal scales less than ~250 km and vertical scales greater than ~8–10 km could be studied. Waves at these scales tend to have short periods; whether our finding of ducted behavior in up to ~75% of the cases is representative of short-period wave behavior for other geographical regions (e.g., mountainous sites) and/or other times of the year is an important question that has yet to be addressed. However, the predominance of ducted waves over vertically propagating waves revealed by this study has important implications for future observational and/or modeling studies which assume small-scale waves to be vertically propagating, since their transports of energy and momentum may occur over a much larger geographic area than would normally be achieved by vertical propagation.

## References

Baker, D. J., Jr., and A. T. Stair, Rocket measurements of the altitude distributions of the hydroxyl airglow, *Phys. Scri.*, 37, 611–622, 1988.

Chimonas, G., and C. O. Hines, Doppler ducting of atmospheric gravity waves, *J. Geophys. Res.*, *91*, 1219–1230, 1986.

Francis, S. H., Global propagation of atmospheric gravity waves: A review, *J. Atmos. Terr. Phys.*, *37*, 1011–1054, 1974.

Fritts, D. C., Gravity wave saturation in the middle atmosphere: A review of theory and observations, *Rev. Geophys.*, *2*, 275–307, 1984.

Fritts, D. C., A review of gravity wave saturation processes, effects, and variability in the middle atmosphere, *Pure Appl. Geophys.*, *130*, 343–371, 1989.

Fritts, D. C., and J. R. Isler, Mean motions and tidal and two-day structure and variability in the mesosphere and lower thermosphere over Hawaii, *J. Atmos. Sci.*, *51*, 2145–2164, 1994.

Fritts, D. C., and L. Yuan, An analysis of gravity wave ducting in the atmosphere: Eckart's resonances in thermal and Doppler ducts, *J. Geophys. Res.*, *94*, 18,455–18,466, 1989.

Greer, R. G. H., and G. T. Best, A rocket-borne photometric investigation of the oxygen lines at 5577-A and 6300-A, the sodium D-lines and continuum at 5300-A in the night airglow, *Planet. Space Sci.*, *15*, 1857–1866, 1967.

Hapgood, M. A., and M. J. Taylor, Analysis of airglow image data, *Ann. Geophys.*, *38*, 805–813, 1982.

Hecht, J. H., R. L. Walterscheid, and M. N. Ross, First measurements of the two-dimensional horizontal wave number spectrum from CCD images of the nightglow, *J. Geophys. Res.*, *99*, 11,449–11,460, 1994.

Hines, C. O., Internal gravity waves at ionospheric heights, *Can. J. Phys.*, *38*, 1441–1481, 1960.

Offermann, D., and A. Drescher, Atomic oxygen densities in the lower thermosphere as derived from in situ 5577-A night airglow and mass spectrometer measurements, *J. Geophys. Res.*, *78*, 6690–6702, 1973.

Smith, S. A., D. C. Fritts, and T. E. VanZandt, Evidence for a saturated spectrum of atmospheric gravity waves, *J. Atmos. Sci.*, *44*, 1404–1410, 1987.

Swenson, G. R., and P. J. Espy, Observations of 2-dimensional airglow structure and Na density from the ALOHA, October 9, 1993 'storm flight,' *Geophys. Res. Lett.*, *22*, 2845–2848, 1995.

Swenson, G. R., M. J. Taylor, P. J. Espy, C. Garndner, and X. Tao, ALOHA-93 measurements of intrinsic AGW characteristics using airborne airglow imager and groundbased Na wind temperature lidar, *Geophys. Res. Lett.*, *22*, 2841–2844, 1995.

Taylor, M. J., and R. Edwards, Observations of short-period mesospheric wave patterns: In situ or tropospheric wave generation?, *Geophys. Res. Lett.*, *18*, 1337–1340, 1991.

Taylor, M. J., M. B. Bishop, and V. Taylor, All-sky measurements of short-period waves imaged in the OI (557.7 nm), and Na (589.2 nm) and near infrared OH and $O_2(0, 1)$ nightglow emissions during the ALOHA-93 campaign, *Geophys. Res. Lett.*, *22*, 2833–2836, 1995a.

Taylor, M. J., D. C. Fritts, and J. R. Isler, Determination of horizontal and vertical structure of an unusual pattern of short period gravity waves imaged during ALOHA-93, *Geophys. Res. Lett.*, *22*, 2837–2840, 1995b.

Taylor, M. J., Y. Y. Gu, X. Tao, C. S. Gardner, and M. B. Bishop, An investigation of intrinsic gravity wave signatures using coordinated lidar and nightglow image measurements, *Geophys. Res. Lett.*, *22*, 2853–2856, 1995c.

Taylor, M. J., and M. A. Hapgood, Identification of a thunderstorm as a source of short period gravity waves in the upper atmospheric nightglow emissions, *Planet. Space Sci.*, *36*, 975–985, 1988.

Taylor, M. J., and M. A. Hapgood, On the origin of ripple-type wave structure in the OH nightglow emission, *Planet. Space Sci.*, *38*, 1421–1430, 1990.

Taylor, M. J., M. A. Hapgood, and P. Rothwell, Observations of gravity wave propagation in the OI (557.7 nm), Na (589.2 nm) and the near infrared OH nightglow emissions, *Planet. Space Sci.*, *35*, 413–427, 1987.

Taylor, M. J., and M. J. Hill, Near infrared imaging of hydroxyl wave structure over an ocean site at low latitudes, *Geophys. Res. Lett.*, *18*, 1333–1336, 1991.

Taylor, M. J., G. R. Swenson, and V. Taylor, Height measurements of OI (557.7 nm) gravity wave structure over the Hawaiian Islands during ALOHA-93, *Geophys. Res. Lett.*, *22*, 2881–2884, 1995d.

Tuan, T. F., and D. Tadic, A dispersion formula for analyzing 'model interference' among guided and free gravity wave modes and other phenomena in a realistic atmosphere, *J. Geophys. Res.*, *87*, 1648–1668, 1982.

Wang, D. Y., and T. F. Tuan, Brunt-Doppler ducting of small-period gravity waves, *J. Geophys. Res.*, *93*, 9916–9926, 1988.

D. C. Fritts, Colorado Research Associates, 3380 Mitchell Lane, Boulder, CO 80301.

J. R. Isler, Physics Department, Wagner College, Staten Island, NY 10301.

M. J. Taylor, Space Dynamics Laboratory, Utah State University, Logan, UT 84322.

# Numerical simulations of gravity waves imaged over Arecibo during the 10-day January 1993 campaign

Michael P. Hickey,[1] Richard L. Walterscheid,[2] Michael. J. Taylor,[3] William Ward,[4] Gerald Schubert,[5] Qihou Zhou,[6] Francisco Garcia,[7] Michael C. Kelly,[7] and G. G. Shepherd,[4]

**Abstract.** Recently, measurements were made of mesospheric gravity waves in the OI (5577 Å) nightglow observed from Arecibo, Puerto Rico, during January 1993 as part of a special 10-day campaign. Clear, monochromatic gravity waves were observed on several nights. By using a full-wave model that realistically includes the major physical processes in this region, we have simulated the propagation of two waves through the mesopause region and calculated the O($^1S$) nightglow response to the waves. Mean winds derived from both UARS wind imaging interferometer (WINDII) and Arecibo incoherent scatter radar observations were employed in the computations as were the climatological zonal winds defined by COSPAR *International Reference Atmosphere 1990 (CIRA)*. For both sets of measured winds the observed waves encounter critical levels within the O($^1S$) emission layer, and wave amplitudes, derived from the requirement that the simulated and observed amplitudes of the O($^1S$) fluctuations be equal, are too large for the waves to be gravitationally stable below the emission layer. Some of the model coefficients were adjusted in order to improve the agreement with the measurements, including the eddy diffusion coefficients and the height of the atomic oxygen layer. The effect of changing the chemical kinetic parameters was investigated but was found to be unimportant. Eddy diffusion coefficients that are 10 to 100 times larger than presently accepted values are required to explain most of the observations in the cases that include the measured background winds, whereas the observations can be modeled using the nominal eddy diffusion coefficients and the *CIRA* climatological winds. Lowering the height of the atomic oxygen layer improved the simulations slightly for one of the simulated waves but caused a less favorable simulation for the other wave. For one of the waves propagating through the WINDII winds the simulated amplitude was too large below 82 km for the wave to be gravitationally stable, in spite of the adjustments made to the model parameters. This study demonstrates that an accurate description of the mean winds is an essential requirement for a complete interpretation of observed wave-driven airglow fluctuations.

## 1. Introduction

In January 1993 the incoherent scatter radar community undertook an unprecedented observational campaign extending over 10 consecutive days that provided a unique opportunity to explore ionospheric and thermospheric variations.

[1]Center for Space Plasma, Aeronomy, and Astrophysics Research, University of Alabama, Huntsville.
[2]Space and Environment Technology Center, The Aerospace Corporation, Los Angeles, California.
[3]Space Dynamics Laboratory, Utah State University, Logan, Utah.
[4]Institute of Space and Terrestrial Science, York University, North York, Canada.
[5]Department of Earth and Space Sciences, Institute of Geophysics and Planetary Physics, University of California, Los Angeles, California.
[6]Arecibo Observatory, Cornell University, Arecibo, Puerto Rico.
[7]Department of Electrical Engineering, Cornell University, Ithaca, NY.

These global observations, combined with detailed information obtained from instrument clusters at selected sites, provide a unique data set to explore atmospheric physics and dynamics and to test global and theoretical models. Atmospheric gravity waves, which comprise the shorter period variations in the atmosphere, are the subject of the present study.

The coupling between the lower and upper atmosphere through atmospheric gravity waves is now recognized as being of fundamental importance to the dynamics and energetics of the mesopause region [e.g., *Hines*, 1960; *Lindzen*, 1981; *Fritts*, 1984; *Garcia and Solomon*, 1985]. Most of our present understanding concerning the energetics of these waves in the mesopause region has derived from either radar [e.g., *Vincent and Reid*, 1983] or nighttime sodium lidar observations [e.g., *Bills et al.*, 1991; *Tao and Gardner*, 1995], because wave amplitude, a key parameter required for the calculation of wave energy, is quite easily derived from these observations. However, while passive optical techniques have been used to measure the fluctuations occurring in various natural mesospheric and lower thermospheric nightglow emissions and often provide useful measurements of gravity wave parameters such as horizontal wavelengths, periods, and azimuths of propagation [*Taylor et al.*, 1995; *Swenson et al.*,

1995], they are unable to provide a direct measure of wave amplitude (or wave energy) for two principal reasons. First, the nightglow emissions behave as a chemical tracer of gravity wave motions through the fluctuations in the concentrations of the minor species involved in the airglow chemistry (and not, for example, fluctuations of the major gas). Second, the nightglow measurements constitute a height integral of the emissions over the entire vertical extent of the emission layer (usually ~ 10 km) rather than providing a measurement at a discrete altitude (as in the case of the radars and lidars).

·In recent years much attention has focused on the calculation of Krassovsky's ratio based on either optical measurements of airglow fluctuations [*Hecht et al.*, 1987; *Sivjee et al.*, 1987; *Viereck and Deehr*, 1989; *Zhang et al.*, 1992a; *Oznovich et al.*, 1995] or theoretical models of these fluctuations [*Hines and Tarasick*, 1987; *Tarasick and Hines*, 1990; *Tarasick and Shepherd*, 1992a, b; *Walterscheid et al.*, 1987, 1994; *Walterscheid and Schubert*, 1987; *Schubert and Walterscheid*, 1988; *Schubert et al.*, 1991; *Hickey*, 1988a, b; *Hickey et al.* 1992, 1993a; *Zhang et al.*, 1992b; *Isler et al.*, 1991; *Makhlouf et al.*, 1995]. While these investigations have provided much impetus to study the interaction of gravity waves with chemically active minor species and the concomitant nightglow fluctuations, no definitive tests of the models have ever been performed. Furthermore, Krassovsky's ratio is a parameter that is independent of wave amplitude and so provides no information concerning the wave energetics.

The main objectives of the present paper are to determine whether acceptable values of wave amplitude can be indirectly determined from these optical measurements and to determine which are the most sensitive parameters affecting the derived wave amplitude. This novel approach, which has not been attempted before, involves combining the optical (nightglow) measurements of gravity wave fluctuations with numerical simulations of these nightglow fluctuations. We perform a detailed investigation employing a realistic full-wave model describing wave propagation in the mesosphere that includes dissipation due to both eddy and molecular diffusion processes and the effects of mean background winds [*Hickey et al.*, 1994, 1995] and which can also calculate the response of a particular nightglow emission to a gravity wave. The wave amplitude is then inferred by requiring that the modeled and measured airglow fluctuations be equal. The present study provides an opportunity to qualitatively and quantitatively assess the viability of this new approach.

The gravity waves were measured in the $O(^1S)$ nightglow over Arecibo at mesopause altitudes using a two-dimensional (2-D) all-sky CCD imaging system [*Taylor and Garcia*, 1995]. These observations provide the wave parameters and the nightglow intensity fluctuations needed for our model calculations. The other measurements required for the modeling are the mean winds at the height of the $O(^1S)$ nightglow emission (~ 97 km altitude), and these were provided for the approximate times of the nightglow observations by the incoherent scatter radar at Arecibo [*Zhou et al.*, 1997] and by the wind imaging interferometer (WINDII) instrument aboard the upper atmosphere research satellite (UARS) [*Shepherd et al.*, 1993]. Additionally, we investigated using the *COSPAR International Reference Atmosphere 1990* (*CIRA*) . climatological monthly mean, zonal-mean winds to define the mean winds for our model calculations. The waves studied here have small phase speeds, making them susceptible to critical level effects associated with the mean winds.

The layout of this paper is as follows. In section 2 the pertinent observations from the January 1993 10-day campaign are described. The full-wave model and the $O(^1S)$ nightglow fluctuation model are briefly described in section 3. This is followed by the results section, which comprises a detailed numerical analysis for each of the observed waves. Following this we conclude by discussing the limitations of the approach and suggest some possible improvements for future wave measurement campaigns.

## 2. January 1993 10-Day Campaign Observations

The January 1993 campaign provided an opportunity to study wave motions in the atmosphere and in particular gravity waves in the mesosphere. The waves were observed in the $O(^1S)$ nightglow emission, as described in section 2.1.2. The modeling of these waves also requires knowledge of the winds at the altitude of the observations, which are described in sections 2.2.1 and 2.2.2. The observations described here were all obtained at Arecibo, Puerto Rico (18.35°N, 66.75°W) on the night of January 20/21, 1993.

### 2.1. All-Sky Image Measurements and Gravity Wave Parameters

**2.1.1. Instrumentation.** The image measurements were made using a digital camera fitted with a Kodak KAF-4200 CCD array (area 3.4 cm$^2$) comprising 2048 x 2048 pixels. The detector was operated at -40°C (dark current to ~0.12 $e^-$ /pixels/$s$) and data were binned to 512 x 507 pixels, resulting in a spatial resolution of ~0.6 km in the zenith at mesospheric heights. The camera was fitted with an all-sky (180°) telecentric lens system enabling monochromatic measurements of small-scale gravity waves to be recorded over a large area of sky (>750,000 km$^2$) within a ~500 km radius of Arecibo. Observations of two nightglow emissions were made: the near infrared (NIR) OH emission which originates from a well-defined layer (~8 km halfwidth) centered at ~87 km altitude, and the OI(557.7 nm) emission which arises from a similar-type layer centered at a higher altitude of ~96 km. The OI (557.7 nm) measurements were made using a narrow band (2.4 nm halfwidth) interference filter and an exposure time of 120 s. Observations of the NIR OH emission were obtained using a broad band filter (715-930 nm halfwidth with a notch to suppress signal from the $O_2$ (0,1) band), and a significantly shorter exposure time of 15 s. The filters were changed manually at intervals during the night and images of the selected emission were recorded once every 3 min. Data were digitized to 12-bit resolution and stored onto optical disk following the subtraction of an electronic "dark noise" image.

**2.1.2. Observations and Analysis.** The camera was located at the Optical Site, Arecibo Observatory, Puerto Rico (18.35°N, 66.75°W). Image measurements commenced on January 16 and continued until January 29, 1993, encompassing the incoherent scatter radar "10 Day Run" measurement period. The observing conditions were good considering the low altitude of the site (~350 m), and a variety of small-scale wave data were recorded on nine nights during this period. For this study, image data from a complex wave display imaged on January 21 have been used. The display imaged on this night consisted of two intersecting quasi-monochromatic gravity waves progressing on approximately

S



W

E

N
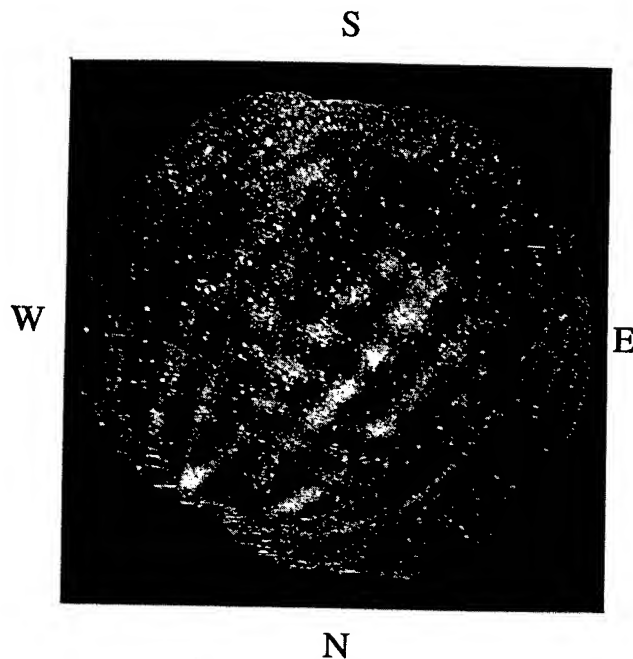
**Figure 1.** A complex wave pattern resulting from the intersection of two gravity waves progressing on approximately orthogonal headings over Arecibo on January 21, 1993. The image has been flat-fielded to enhance the wave structure and to determine the quantity $I'$. Wave A was observed to progress towards the SW (top left of image) while wave B moved towards the ~NNW (~bottom left of image).

orthogonal headings and creating a distinctive cross-hatch pattern. Figure 1 illustrates this situation for the OI (557.7 nm) emission at 07:50 UT. Both wave patterns were extensive and highly coherent but exhibited quite dissimilar spatial and temporal characteristics (see Table 1). Prior to midnight the data were characterized by a single well defined wave train (termed wave A), progressing towards the SW that was evident for over 5 hours. During the course of these observations a second wave train entered the field of view progressing towards the NNW. Both displays were detected in the OI and OH emissions, suggesting that they were caused by freely propagating waves. However, the visibility of the second wave in the OI emission decreased considerably after ~1 hour (but images of this second wave were recorded for an additional ~70 min). Table 1 lists the results of a spectral analysis of these data. Further information on the determination of the spectral components of this display is given by *Taylor and Garcia* [1995].

In addition to measurements of the horizontal wave parameters (horizontal wavelength, $\lambda$; horizontal phase speed,

$v_h$; and observed period, $T_{ob}$), this study requires information on the intensity perturbations induced by the two gravity waves. In particular, the quantity $\langle I' \rangle / \langle \bar{I} \rangle$ is needed for modeling of the wave propagation. Here, $\langle \bar{I} \rangle$ represents the average intensity of the image, $\langle I' \rangle$ is a measure of the amplitude of the wave-induced intensity fluctuation, and the brackets denote that the observables represent an integral over the height of the emission region. To determine this quantity, a series of 21 images encompassing the images to be measured were averaged together to form a "background" image. To a first approximation this process removes from the data the effects due to lens vignetting and line-of-sight (van Rhijn) enhancements at low elevations. This image was then used to flat-field the data, an example of which is shown in Figure 1. Intensity values at the peaks ($\langle I \rangle_{max}$) and troughs ($\langle I \rangle_{min}$) for waves A and B were then measured at various points within the flat-fielded image to determine a mean peak-to-trough variation ($\langle I \rangle_{max} - \langle I \rangle_{min}$) from which an average value of ($\langle I \rangle_{max} - \langle I \rangle_{min}$)/2 was determined. The value $\langle \bar{I} \rangle$ was then estimated from the mean intensity of the background image. This procedure was performed for the wave structures imaged in Figure 1 and several adjacent images over a time period of approximately 30 min to obtain estimates of the induced wave contrast ($\langle I \rangle_{max} - \langle I \rangle_{min}$)/$\langle \bar{I} \rangle$ and hence the intensity amplitude ratio, the results of which are included in Table 1. The mean values for $\langle I' \rangle / \langle \bar{I} \rangle$ were found to be 3.9% $\pm$ 0.7% for wave A and 2.9% $\pm$ 0.5% for wave B, indicating that wave A had a higher contrast than wave B.

## 2.2. Observed Winds

Daytime winds were measured by the incoherent scatter radar at Arecibo, as described in the next section (2.2.1), while nighttime winds were measured by WINDII on UARS, as described in section 2.2.2. These measured winds were provided for altitudes down to about 90 km. Below 90 km we linearly interpolated the winds to zero at 80 km. We investigated interpolating the winds to zero at lower altitudes (e.g., 70 km), but this caused the simulations to be less favorable (see discussion section). We also investigated the effects on our simulations of interpolating the measured zonal winds at 90 km to the *CIRA* climatological zonal-mean winds near 70 km, but again this caused the simulations to be less favorable.

The measured winds were represented analytically using the equation [*Lindzen*, 1970]

$$\bar{u}(z) = \frac{a_1}{2} z + \sum_i^N \frac{\delta_i}{2} (a_{i+1} - a_i) \ln\left( \frac{\cosh(z - z_i)/\delta_i}{\cosh z_i/\delta_i} \right) \quad (1)$$

The values of $a_i$, $\delta_i$, $z_i$ and $N$ for the measured wind profiles are listed in Tables 2 and 3. Note that the last entry of the gradient ($a_i$) in these tables (equal to zero) produces a zero

**Table 1.** Horizontal Wave Parameters Derived From a Spectral Analysis of the OI (557.7 nm) Image Data and Estimates of the Wave Amplitude Ratios Around 0750 UT

|  | $\lambda_h$, km | Period, min | Azimuth, deg | $V_{ph}$, m s$^{-1}$ | $\langle \delta I \rangle / \langle \bar{I} \rangle$, % | Contrast, % |
|---|---|---|---|---|---|---|
| Wave A | 39 | 25 | 236 | 26 | 3.9±0.7 | 7.8±0.7 |
| Wave B | 27 | 12 | 346 | 37.5 | 2.9±0.5 | 5.8±0.5 |

Image data adapted from *Taylor and Garcia* [1995].

gradient (i.e., constant wind) at heights above the last entry of altitude $(z_i)$ in the tables. The actual wind profiles used in our modeling are displayed and discussed in the results section.

**2.2.1. Incoherent scatter radar observations and winds.** In principle, an incoherent scatter radar (ISR) measures the motion of ionized particles. The motions of neutral particles generally differ from those of the ionized particles in the presence of electric and magnetic fields. The degree of the difference depends on the relative magnitude of the collisional force and the electric and geomagnetic forces. Using a set of reasonable assumptions, neutral winds are derived using the electric field measured by the ISR and the ion-neutral collision frequency derived from the MSIS model [*Hedin*, 1991]. A detailed discussion on neutral wind derivation is given by *Harper et al.* [1976].

Neutral winds derived for the January 1993 10-day campaign at Arecibo are given by *Zhou et al.* [1997]. Briefly, the reduced $E$ region wind had a 17-min time resolution and a 3.5-km height resolution. The radar was operated in a sweeping line-feed mode, with the beam directed $15°$ off zenith and completing a single sweep in ~17 min. The error in the meridional wind component was typically 15 m s$^{-1}$ for the altitude range 95 - 145 km. The error in the zonal wind component is generally comparable to that of the meridional wind below 130 km, but it increases exponentially above this altitude. Owing to the lack of sufficient ionization, neutral winds are generally not obtainable during the nighttime in the $E$ region. Therefore the daytime winds for January 20 and 21 were Fourier decomposed into mean, 48-hour, 24-hour, and 12-hour components, and the derived amplitudes and phases were then used to extrapolate the daytime winds into the nighttime. We realize that this approach can, at times, be problematic. We use it here in order to provide us with another wind data set that otherwise would be unavailable.

**2.2.2. UARS WINDII observations and winds.** The WINDII on UARS is a wide-angle Michelson interferometer which measures winds using the Doppler shifts of selected airglow emissions (see work by *Shepherd et al.* [1993] for an instrument description and by *Gault et al.* [1996] for a description of the validation of the green line winds). Line-of-sight winds and emission rate are measured in two orthogonal directions and then combined to provide an emission rate profile and wind profiles in the meridional and zonal directions. The wind profiles used in this paper are derived using V496 of the WINDII Science Data Processing Production Software. They are chosen to coincide as closely as possible in time and location with the ground-based gravity wave observations at Arecibo.

Exact coincidences are in general not possible because of the sampling associated with the UARS orbit. For a given day, the UARS orbit is essentially fixed relative to the Sun, and the Earth rotates under it [*McLandress et al.*, 1996; *Ward et al.*, 1996]. At a given latitude, the same local time is sampled for a given leg of the orbit. For a given location, each day there are two possibilities for a coincidence, one associated with the upleg, and the other associated with the downleg portion of the orbit. Unfortunately, during the time period of the campaign, for the latitude of Arecibo either the upleg or the downleg observations were close to the terminator so that only one overpass per day was possible.

The WINDII profile selected was at 01:47 UT (21:29 LT) and was located at a latitude of $16.8°$ N and a longitude of $65.8°$ W, slightly northeast of Arecibo. Zonal and meridional winds were provided from 90 to 115 km altitude. The emission observed at this time was the oxygen green line nightglow $O(^1S)$. The volume of atmosphere sampled for each height is about 2 km thick, 400 km along the line-of-sight, and 400 km along the satellite track. The profile shows strong meridional and zonal winds at 92 km height with magnitudes of approximately 100 m s$^{-1}$. Neighboring measurements on the same orbit show similar magnitudes, but the zonal winds on neighboring orbits at the same latitude are about 40 m s$^{-1}$ weaker (the meridional winds on neighboring orbits remain strong). Although there is a strong 2-day wave event taking place at this time [*Ward et al.*, 1996], and the observations are within 3 hours of the calculated local time of maximum amplitude for the zonal diurnal tide at 90 km altitude [*McLandress et al.*, 1996], these components are not strong enough to account for the observed zonal wind. There is, however, a significant wave 1 component to the wind field in this latitude band with an amplitude of ~ 30 m s$^{-1}$ which accounts for some of the difference. In addition, the airglow volume emission rate was very strong at this time with a peak magnitude of almost 200 photons cm$^{-3}$ s$^{-1}$ at 94 km altitude, a value close to double that for the other profiles in the same latitude band as Arecibo on this day. This suggests the pos-

**Table 2.** Coefficients Used in (2) to Represent ISR Winds

| | Meridional ($N$=10) | | | Zonal ($N$=8) | | |
|---|---|---|---|---|---|---|
| | $a_i$, | $\delta_i$, | $z_i$, | $a_i$, | $\delta_i$, | $z_i$, |
| $i$ | s$^{-1}$ | km | km | s$^{-1}$ | km | km |
| 1 | 0 | 1.0 | 80.00 | 0 | 1.0 | 80.00 |
| 2 | -2.07 x 10$^{-3}$ | 1.0 | 94.45 | 7.17 x 10$^{-4}$ | 1.0 | 96.21 |
| 3 | 1.44 x 10$^{-2}$ | 1.0 | 97.95 | 1.18 x 10$^{-3}$ | 1.0 | 101.42 |
| 4 | -2.30 x 10$^{-2}$ | 1.0 | 101.42 | -3.04 x 10$^{-3}$ | 1.0 | 118.81 |
| 5 | 2.73 x 10$^{-2}$ | 1.0 | 104.90 | 9.47 x 10$^{-3}$ | 1.0 | 122.29 |
| 6 | 3.46 x 10$^{-3}$ | 1.0 | 111.86 | 1.09 x 10$^{-2}$ | 1.0 | 125.76 |
| 7 | -1.02 x 10$^{-2}$ | 1.0 | 118.81 | -5.75 x 10$^{-3}$ | 1.0 | 129.24 |
| 8 | -2.56 x 10$^{-3}$ | 1.0 | 122.29 | -9.35 x 10$^{-4}$ | 2.0 | 150.00 |
| 9 | 7.23 x 10$^{-4}$ | 1.0 | 127.50 | 0 | -- | -- |
| 10 | 7.59 x 10$^{-4}$ | 2.0 | 150 | -- | -- | -- |
| 11 | 0 | -- | -- | -- | -- | -- |

**Table 3.** Coefficients Used in (2) to Represent WINDII Winds

| | Meridional ($N=8$) | | | Zonal ($N=5$) | | |
|---|---|---|---|---|---|---|
| | $a_i$, | $\delta_i$, | $z_i$, | $a_i$, | $\delta_i$, | $z_i$, |
| $i$ | $s^{-1}$ | km | km | $s^{-1}$ | km | km |
| 1 | 0 | 1.0 | 80.00 | 0 | 1.0 | 80.00 |
| 2 | $8.93 \times 10^{-3}$ | 1.0 | 92.00 | $-9.58 \times 10^{-3}$ | 1.0 | 92.00 |
| 3 | $8.68 \times 10^{-3}$ | 1.0 | 96.00 | $1.74 \times 10^{-2}$ | 1.0 | 98.00 |
| 4 | $-4.30 \times 10^{-3}$ | 1.0 | 98.00 | $1.62 \times 10^{-3}$ | 1.0 | 108.00 |
| 5 | $-1.20 \times 10^{-2}$ | 1.0 | 102.00 | $-4.50 \times 10^{-4}$ | 2.0 | 120.00 |
| 6 | $-1.89 \times 10^{-2}$ | 1.0 | 106.00 | 0 | -- | -- |
| 7 | $3.32 \times 10^{-3}$ | 1.0 | 116.00 | -- | -- | -- |
| 8 | $-1.07 \times 10^{-2}$ | 2.0 | 120.00 | -- | -- | -- |
| 9 | 0 | -- | -- | -- | -- | -- |

sibility that the dynamics of the region over Arecibo was disturbed locally. Unfortunately, it is impossible to determine from WINDII data whether these anomalous conditions persisted to the time when the gravity wave images were observed. However, the fact that the gravity waves observed were not common features in the imager data suggests that they did.

### 2.3. CIRA Zonal Winds

*CIRA* provides climatological monthly-mean winds as a function of altitude and latitude. Only zonal-mean winds are provided. Therefore the lack of meridional winds in the *CIRA* model means that a wave propagating in an orthogonal direction to the zonal winds will not be influenced by the winds. This restricted the use of the *CIRA* winds to wave A, because wave B propagated predominantly in the meridional plane.

The *CIRA* zonal winds were employed in this study mainly to provide an additional set of wind measurements other than those provided by the observations and also to provide winds throughout the complete altitude range of interest. The *CIRA* zonal winds we used were represented using cubic splines.

## 3. Full-Wave Model

The gravity wave model is a robust, one-dimensional, time-independent full-wave model describing the propagation of non hydrostatic, linear gravity waves from the troposphere up to a maximum altitude of 500 km [*Hickey et al.*, 1994, 1995]. It includes dissipation due to eddy processes in the lower atmosphere and molecular processes (viscosity, thermal conduction and ion drag) in the upper atmosphere. Height variations of the mean temperature and horizontal winds, as well as Coriolis force are all included. The model therefore accurately describes the propagation of gravity waves in an inhomogeneous atmosphere. Instabilities and accompanying wave saturation are not explicitly considered here, although they are important processes affecting some of the waves propagating through the middle atmosphere [e.g., *Fritts*, 1984]. However, wave saturation is sometimes implicitly included using *Lindzen's* [1981] WKB approach to calculate diffusion coefficients, which are then used as input to the full-wave model.

The equations that we solve are the continuity equation (2), the Navier-Stokes equations (3), the energy equation (4), and

the ideal gas equation (5). These equations are used to describe fully compressible wave motions. In our coordinate system, $x$ is positive due south, $y$ is positive due east, and $z$ is positive upwards. The equations are

$$D\rho/Dt + \rho \underline{\nabla} \cdot \underline{v} = 0 \tag{2}$$

$$\rho \frac{D\underline{v}}{Dt} + \underline{\nabla} p - \rho \underline{g} + 2\rho \underline{\Omega} \times \underline{v} + \underline{\nabla} \cdot \underline{\underline{\sigma}}_m + \underline{\nabla} \cdot (\rho \eta_e \underline{\nabla} \underline{v})$$
$$+ \rho \nu_{ni}(\underline{v} - \underline{v}_i) = \underline{0} \tag{3}$$

$$c_v \rho \frac{DT}{Dt} + p \underline{\nabla} \cdot \underline{v} + \underline{\underline{\sigma}}_m : \underline{\nabla} \underline{v} - \underline{\nabla} \cdot (\lambda_m \underline{\nabla} T)$$
$$- \frac{c_v \overline{T}}{\theta} \underline{\nabla} \cdot [\overline{\rho} \kappa_e \underline{\nabla} \theta] + \rho \nu_{ni}(\underline{v} - \underline{v}_i)^2 = 0 \tag{4}$$

$$p = \rho RT/M \tag{5}$$

where $\underline{v}$ is the velocity with $x$, $y$, $z$ components $u$, $v$, and $w$, respectively; $\rho$ is the neutral mass density; $p$ is atmospheric pressure; $g$ is the gravitational acceleration; $\underline{\Omega}$ is the Earth's angular velocity; $\underline{\underline{\sigma}}_m$ is the molecular viscous stress tensor; $\eta_e$ is the eddy momentum diffusivity; $\nu_{ni}$ is the neutral-ion collision frequency; $\underline{v}_i$ is the ion velocity; $c_v$ is the specific heat at constant volume; $T$ is temperature; $\lambda_m$ is the molecular thermal conductivity; $\theta$ is the potential temperature ($\theta = T(p_0/p)^{R/c_p}$, where $p_0 = 1000$ mbar, $c_p$ is the specific heat at constant pressure, and $R$ is the gas constant); $\kappa_e$ is the eddy thermal diffusivity; and $M$ is the mean molecular weight. The operator $D/Dt$ is the substantial derivative and is equal to $\partial/\partial t + \underline{v}_0 \cdot \underline{\nabla}$, where $\underline{v}_0$ is the background wind velocity. In the above equations all of the coefficients vary with altitude, except for $\underline{\Omega}$.

The linear wave solutions to these equations are assumed to vary as $\exp i(\omega t - kx - ly)$, where $\omega$ is the wave frequency, and $k$ and $l$ are the horizontal wavenumbers in the $x$ (meridional) and $y$ (zonal) directions, respectively. Note that $k$, $l$, and $\omega$ are not functions of altitude. The form of these solutions assumes that the mean state varies neither in time nor in the horizontal direction. The six linearized equations are reduced to five by eliminating the density perturbation using the linearized ideal

gas equation. The remaining five equations are second-order, ordinary differential equations in the vertical coordinate $z$. This coupled system of equations is solved subject to boundary conditions for the wave variables $u'$, $v'$, $w'$ (the meridional, zonal, and vertical velocity perturbations, respectively), $T'$, and $p'$ (the temperature and pressure perturbations, respectively). First, these variables ($\Psi$) are transformed to new variables ($\Psi^*$) by dividing by the square root of the mean atmospheric density, $\overline{\rho}$ (i.e., $\psi^* = \psi/\sqrt{\overline{\rho}}$). We solve for the transformed variables by expressing vertical derivatives as centered finite differences and then using the tridiagonal algorithm [Bruce et al., 1953] to solve the resulting set of difference equations subject to boundary conditions. The untransformed lower boundary condition is $w' = 0$, and vertical gradients in $u'$, $v'$, $T'$, and $p'$ are defined on the basis of the equations for an adiabatic and isothermal atmosphere. At the upper boundary the radiation condition is applied, using the WKB solution described by Hickey and Cole [1987]. The upper boundary is chosen to be high enough so that wave reflection from the upper boundary will not influence results at lower altitudes in the model (this was implemented by adjusting the upper boundary height until a WKB wave experiences severe damping within a time-scale of one wave period). A vertical profile of wave forcing (in $w'$) is assumed to be Gaussian. The half-width of the profile is about 1.5 km, while its height depends on the wave parameters and is near the tropopause for most of our studies. The final wave variables are obtained by a simple inverse transformation. The finite difference equations in the region between the lower boundary (ground) and the upper boundary (the latter lying between 200 and 500 km) are represented on a grid of 10,000 points with a vertical resolution of 20 to 50 m.

The model outputs the wave variables $u'$, $v'$, $w'$, $T'$, and $p'$ given the wave frequency ($\omega$), the horizontal wavelength ($\lambda$) and the azimuth of propagation ($\varphi$). Mean state quantities required for the full-wave computations are nominally provided by the MSIS-90 model [Hedin, 1991]. The molecular coefficients of viscosity and thermal conductivity are taken from Rees [1989]. The eddy momentum diffusivity increases exponentially from 0.1 m$^2$ s$^{-1}$ at the ground to a maximum value of about 300 m$^2$ s$^{-1}$ at 80 km altitude and decreases exponentially above that to an insignificant value near 140 km altitude. This eddy diffusion profile approximates that given by Strobel [1989]. The eddy thermal diffusivity is calculated from the eddy momentum diffusivity by assuming a Prandtl number of 3 [see Strobel, 1989].

### 3.1. O($^1S$) Airglow Fluctuation Model

The response of nightglow emissions to gravity wave forcing has been described before (see introduction). For each of the minor species involved in a particular emission chemistry the linearized continuity equation can be written as

$$i\omega n' = \delta P - \delta L + w'\frac{\partial \overline{n}}{\partial z} - \overline{n}\underline{\nabla}\cdot\underline{v}' \qquad (6)$$

where $\delta P$ and $\delta L$ are the perturbations in the chemical production and loss, respectively; $n'$ is the minor species number density perturbation about its mean value, $\overline{n}$; $w'$ is the gravity wave vertical velocity component; and $\underline{\nabla}\cdot\underline{v}'$ is the gravity wave velocity divergence. The perturbations in chemical production and loss ($\delta P$ and $\delta L$) are due to perturbations in temperature (for temperature-dependent

reactions), perturbations in the major gas density (for 3-body recombination reactions), and are also due to chemical coupling between reacting minor species. Prior to this study, the gravity wave perturbations in the vertical velocity, velocity divergence, temperature, and major gas density, were calculated using our WKB models [e.g., Schubert and Walterscheid, 1988; Schubert et al., 1991; Hickey et al., 1993a, b], but here we use the full-wave model described in section 3 and by Hickey et al. [1994, 1995].

The fact that the nightglow emission intensity $I$ is proportional to the density $n$ of the emitting species allows us to write $\delta I/\overline{I} = \delta n/\overline{n}$. The imager collects photons that originate from all altitudes within the nightglow emission layer. Therefore, in order to simulate the airglow images, the airglow response to the gravity wave was integrated over the complete vertical extent of the airglow layer. The integration covered the altitude interval between 75 and 130 km. The amplitude of the modeled gravity wave is then adjusted so that the modeled relative intensity fluctuation, $\langle\delta I\rangle/\langle\overline{I}\rangle$, compares with the measured value, thus providing an estimate of the wave amplitude (here the angle brackets denote an altitude integral). The chemical scheme that we employ to describe the production of the O($^1S$) emission in the mesopause region as well as the pertinent reaction rates and efficiencies are given in the Appendix.

The gravity wave forcing on the minor species concentrations is specified by the perturbation variables $T'/\overline{T}, \underline{\nabla}\cdot\underline{v}', w'$ and $n'(M)/\overline{n}(M)$ output by the full-wave model. A set of complex dynamical factors derived from these perturbation variables and defined by (A6) to (A8) are then substituted into algebraic expressions describing the minor species fluctuations (equations (A3) to (A5)). The mean state densities of O$_2$($c^1\Sigma_u^-$) and O($^1S$) are calculated using (A1) and (A2). The only other parameters required to solve for $n'$ in (1) are those defining the undisturbed state of the atomic oxygen ($\overline{n}(O)$ and its vertical derivative). We employ the
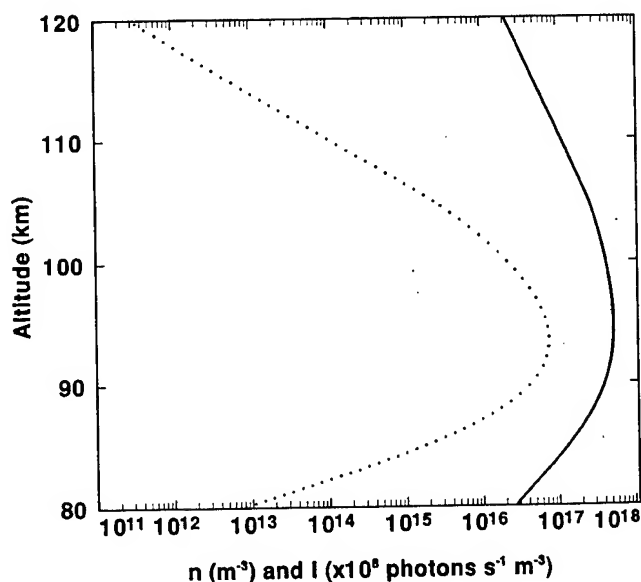


**Figure 2.** Atomic oxygen density taken from the model of Garcia and Solomon [1985] for January 18°N (solid line) and derived O($^1S$) emission profile (dashed line) employing the chemistry given in the appendix.
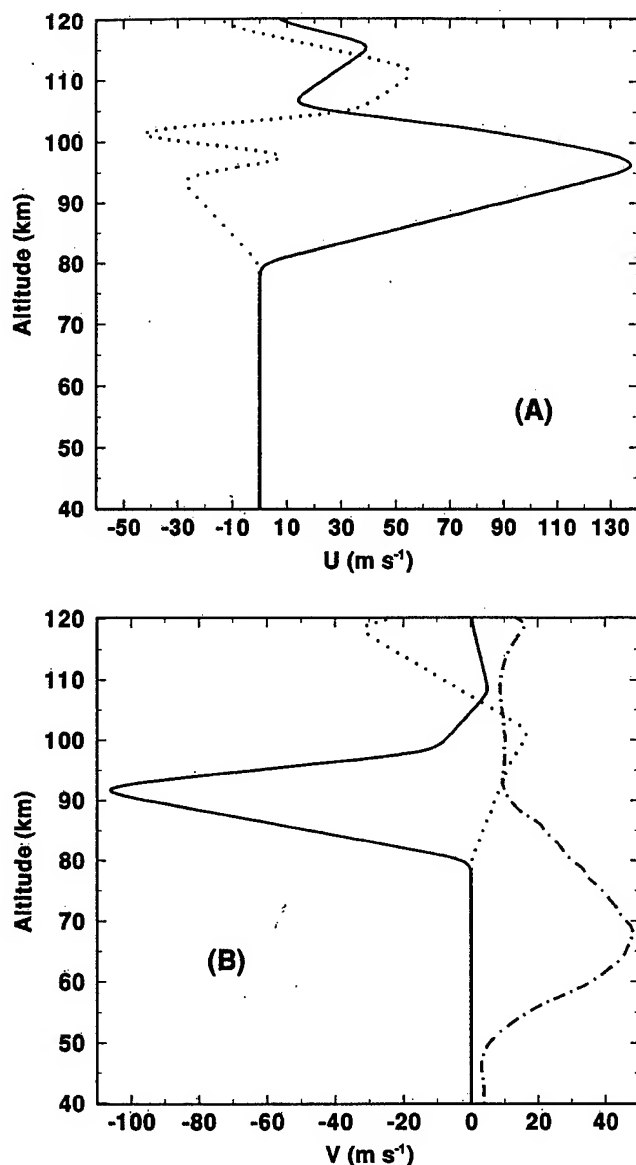
**Figure 3.** Mean (a) meridional (U), and (b) zonal (V), wind profiles used in the computations, derived from the WINDII observations (solid line), ISR observations (dotted line), and for the CIRA model (dashed-dotted line for zonal winds only). The positive direction corresponds to due south in Figure 3a and due east in Figure 3b.

undisturbed atomic oxygen density profile derived from the model of *Garcia and Solomon* [1985] for January at 18°N. The atomic oxygen concentration and the $O(^1S)$ emission intensity resulting from the chemical scheme described in the Appendix are shown in Figure 2. The $O(^1S)$ emission layer peaks near 93.5 km with a full-width half-maximum of about 5 km. This is close to the value of the peak height measured by WINDII (94 km) at 01:47 UT, discussed in section 2.2.2.

## 4. Results

The waves studied here have small phase speeds, making them susceptible to critical level effects associated with the mean winds. Our simulations were performed using either WINDII winds, the ISR background winds, or the monthly

mean zonal winds at 18°N as prescribed by CIRA. The CIRA zonal winds were not employed for wave B because that wave propagates predominantly in the meridional direction (see Table 1) and the wind component in the direction of wave propagation is about 10 m s$^{-1}$ (or about one quarter of the phase speed). Therefore wave B would be relatively unaffected by the CIRA zonal winds. A similar argument also holds for wave B propagating in the ISR zonal winds (although the ISR meridional winds are obviously important). However, wave B will be affected by the WINDII zonal winds because they have a maximum speed of about 100 m s$^{-1}$, with the wind component in the direction of wave propagation reaching values as large as about 25 m s$^{-1}$ (or about two thirds of the phase speed).

The resulting wind profiles employed in this study are shown in Figure 3a for the meridional winds and in Figure 3b for the zonal winds. The WINDII winds are much larger than those derived from the ISR measurements. Also, the WINDII zonal wind between 90 and 100 km altitude is westward, in contrast to the ISR and CIRA zonal winds, which are eastward. The WINDII meridional winds are directed southward between 80 and 120 km altitude, but the ISR winds are directed northward between about 80 and 105 km altitude and southward between 105 and 115 km altitude.

The behavior of the waves propagating in the various wind systems can be anticipated by comparing the wave phase velocities with the mean wind velocities. The observed phase speeds and directions of propagation of waves A and B are 26 m s$^{-1}$ due SW and 37.5 m s$^{-1}$ due NNW, respectively. Therefore wave A will encounter critical levels near 82 and 98 km altitude when propagating through the WINDII wind system. When propagating through the ISR wind system, wave A will encounter a critical level near 105 km altitude, that is, above most of the $O(^1S)$ emission layer. Wave B will encounter a critical level near 100 km altitude when propagating through the ISR wind system. In the WINDII wind system, wave B will be Doppler shifted to increasingly higher frequencies as it approaches the 82 km level whereupon it will become evanescent. Significant wave reflection should then occur. We do not expect wave B to be affected by the CIRA zonal winds because this wave has an insignificant component of zonal propagation. As wave A propagates up through the CIRA zonal winds it is Doppler shifted to higher frequencies, but the wind component in the direction of wave propagation is not large enough to cause wave reflection.

In order to match the observed nightglow perturbation amplitudes provided in Table 1, the resulting wave amplitudes that we obtain using our dynamics-nightglow perturbation model can be large depending on the wind system through which the wave propagates. Sometimes these wave amplitudes may be large enough to render the wave unstable on the basis of standard gravitational instability criteria. The criterion for wave instability is that the wave velocity amplitude exceed the wave phase speed [*Orlanski and Bryan*, 1969; *Lindzen*, 1981; *Fritts*, 1984; *Walterscheid and Schubert*, 1990]. Alternatively, a wave becomes convectively unstable when the vertical derivative of the total (mean plus wave) potential temperature (θ) becomes sufficiently negative. Note that the numerical simulations of *Walterscheid and Schubert* [1990] and *Andreassen et al.* [1994] suggest that some overshoot is possible, whereby wave amplitudes may become somewhat larger than those implied from simple stability analysis. In the results that follow we plot the wave

temperature amplitude as a function of altitude that gives a relative intensity perturbation equal to the observed value. We also plot in the same figure the maximum permitted stable temperature amplitude based on the second instability criterion described above (this definition of wave stability is adopted for the rest of the paper). Results are presented separately for waves A and B.

### 4.1. Wave A

The temperature amplitude for wave A propagating in the WINDII wind system for the nominal model parameters is shown in Figure 4. The wave amplitude increases with increasing altitude below 80 km because the eddy diffusion is not sufficient in this region to offset the adiabatic growth of the wave that occurs in a dissipationless atmosphere [*Hines*, 1960]. Near 82 km altitude the wave encounters a critical level (where the Doppler-shifted, i.e., intrinsic, wave frequency is zero). As the wave approaches the critical level from below, its frequency decreases, and a strong reduction in wave amplitude associated with severe dissipation occurs. Above this altitude the wave begins to be Doppler shifted to higher frequencies, decreasing the dissipation and allowing the wave to again grow with increasing altitude. Another critical level is encountered near 105 km altitude, with a further reduction in wave amplitude. Above this altitude the effects of molecular dissipation eventually dissipate the wave.

The maximum stable temperature amplitude, shown as a dotted line in Figure 4, indicates that the wave is unstable below about 80 km altitude. In order that the wave cause a significant nightglow perturbation, the wave amplitude in the $O(^1S)$ nightglow layer (between about 90 and 105 km) must be several K. Because the critical level exists below the nightglow layer, this forces the wave amplitudes to be extremely large below the critical level.

The temperature amplitude for wave A propagating in the ISR wind system for the nominal model parameters is shown
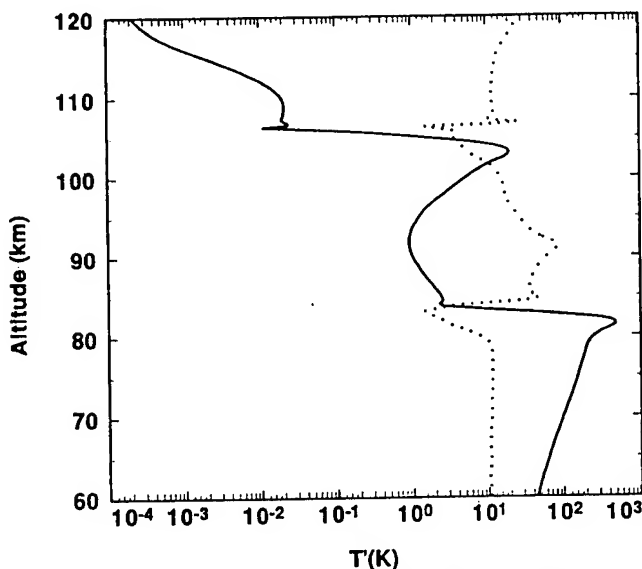


**Figure 5.** As in Figure 4 except for the ISR winds.

in Figure 5. The wave amplitude increases with increasing altitude up to the critical level near 105 km altitude. Above this altitude the wave is strongly attenuated. Comparison with the maximum stable temperature amplitude shows that this wave is stable below ~103 km altitude, and that the wave is only slightly unstable over a narrow height range of a couple of kilometers above 103 km.

The temperature amplitude for wave A propagating in the *CIRA* zonal wind system for the nominal model parameters is shown in Figure 6. The wave amplitude increases with increasing altitude up to about 120 km altitude, above which molecular dissipation becomes severe and wave amplitude diminishes. The wave becomes unstable above about 107 km altitude, which is essentially above the $O(^1S)$ emission layer.

The wave observations described in section 2.1.2 show that wave A was a well-defined, monochromatic wave lasting for a period of at least several hours. Therefore the observations strongly suggest that wave A was stable and linear. In the case of wave A propagating through the ISR and *CIRA* zonal winds, our simulations produced the observed nightglow fluctuations with reasonable, stable wave amplitudes within the bulk of the $O(^1S)$ emission layer. However, in the case of the WINDII winds, large unstable wave amplitudes are required to explain the magnitude of the nightglow fluctuations. In the case of the WINDII winds, we attempt to explain the nightglow observations by adjusting model parameters in order to determine if our model can produce the observed magnitude of the relative nightglow fluctuation with stable wave amplitudes. We have found very little sensitivity of our results to the chemical kinetic parameters listed in Table A1 (optional parameters are provided in parentheses there) and to the assumed Prandtl number (nominally equal to 3, and set to unity for Lindzen's parameterization). Therefore these parameters are not varied in the simulations that follow. The parameters that we adjust are the height of the atomic oxygen profile and the magnitude of the eddy diffusion. In the case of the height of the O layer, we lower the whole layer by 2 km, which increases the nightglow response to the wave by "immersing" more of the nightglow layer into regions of significant wave amplitude. In the case of the eddy diffusion, we either in-



**Figure 4.** Wave A temperature perturbation amplitude ($T'$) required to produce the observed relative intensity perturbation for nominal conditions and WINDII winds. The dotted line represents the limiting temperature perturbation amplitude based on linear stability theory.
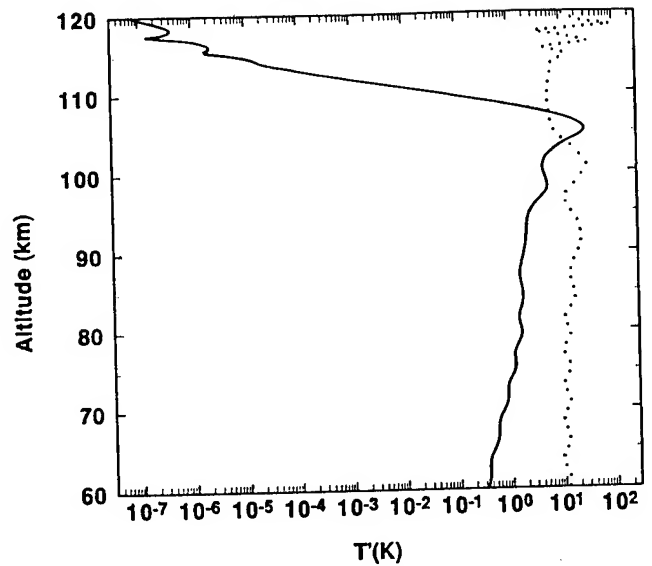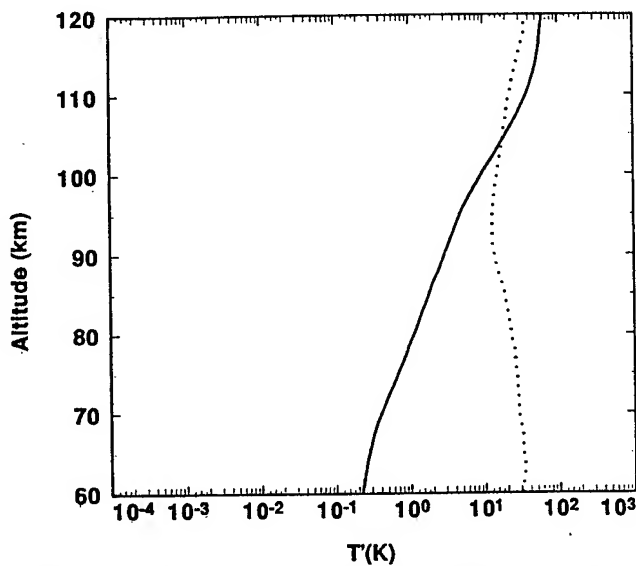
**Figure 6.** As in Figure 4 except for the *CIRA* zonal winds.

crease the nominal eddy diffusion in the model by a simple scaling factor (10 or 100), or else we employ the parameterization scheme of *Lindzen* [1981]. It is expected that increasing the dissipation will increase the vertical wavelength, thereby decreasing the destructive interference that occurs between different phases of the intensity perturbation, and increase the nightglow response. Eddy diffusion is apt to be quite variable in the mesopause region. Our motivation for increasing the nominal eddy diffusion by factors of 10 to 100 are solely to determine the sensitivity of our wave simulations to the values of eddy diffusion in the model and are not intended to imply the existence of such large eddy diffusion coefficients over large height ranges in the mesosphere. We note, however, that large diffusion coefficients probably do exist over limited height ranges during times of wave breakdown and overturning [*Walterscheid and Schubert*, 1990], but these considerations are beyond the scope of the present study.

The temperature amplitude for the wave propagating in the WINDII winds with the eddy diffusion increased by a factor of 100 is shown in Figure 7. It is immediately evident that the increased eddy diffusion has not improved the simulated amplitudes (Figure 7a). The phases of the temperature fluctuations displayed in Figure 7b for both the nominal and 100 times nominal eddy diffusion cases show that the vertical wavelength has not been significantly altered (as anticipated, see above) within the O($^1$S) emission layer by the increased eddy diffusion. Instead, we believe that vertical variations of phase will depend more on altitude variations of intrinsic wave frequency when the intrinsic wave frequency changes significantly over a narrow height range. Because wave A is significantly Doppler shifted by the WINDII winds in the vicinity of the O($^1$S) nightglow layer and the mean winds change significantly over a narrow height range, this argument appears to be justified.

We also examined the result of propagating wave A in the WINDII winds using the saturation equations of *Lindzen* [1981]. In this case we chose breaking altitudes of both 60 and 80 km. In both instances no significant improvement was achieved, for the same reasons discussed in the preceding paragraph.

A decrease in the altitude of the atomic oxygen layer by 2 km decreased the simulated amplitude of wave A required to match the nightglow perturbation. The resulting temperature perturbation amplitudes are everywhere 62% of the nominal amplitudes shown in Figure 4. However, while the required amplitudes have been decreased by lowering the atomic oxygen layer, they still exceed their stability limits below about 80 km altitude.

## 4.2. Wave B

Wave B propagates with an azimuth of 346°, which is almost in the meridional plane. For this reason wave B is relatively unaffected by the almost orthogonal zonal winds, provided the zonal winds are not significantly greater than the phase speed of the wave. Therefore we do not investigate the
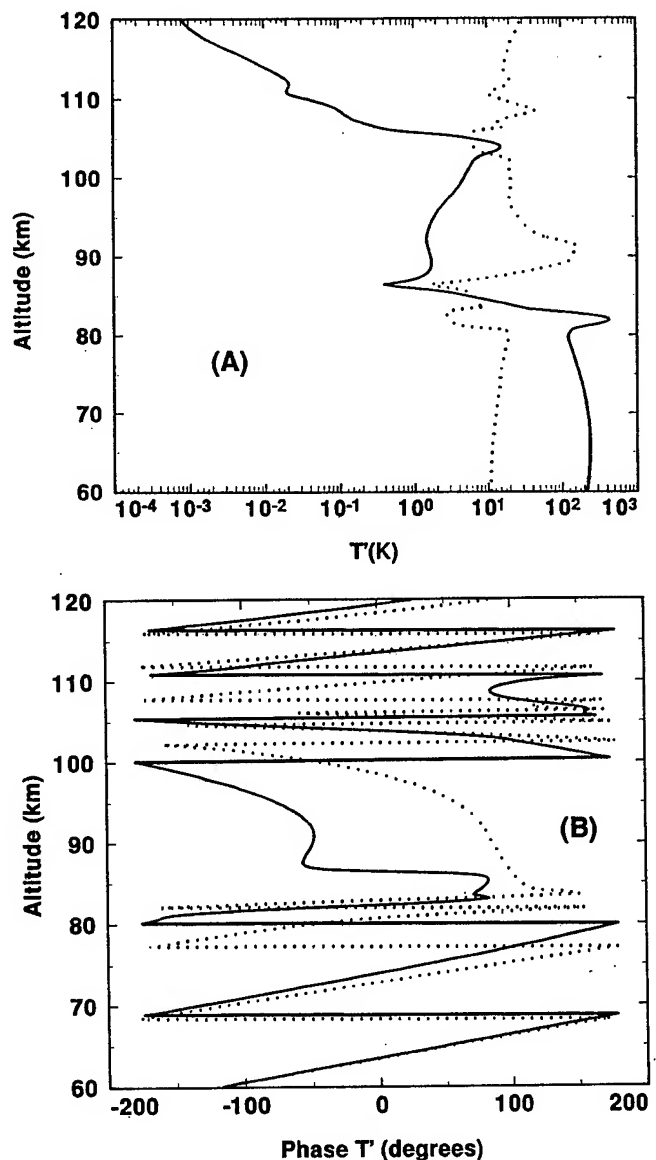
**Figure 7.** Wave A temperature perturbation (a) amplitude and (b) phase required to produce the observed relative intensity perturbation for the WINDII winds and the nominal eddy diffusion increased by a factor of 100. The dotted line in Figure 7a represents the limiting temperature perturbation amplitude based on linear stability theory. The dashed line in Figure 7b represents the phase of $T'$ obtained for nominal conditions.
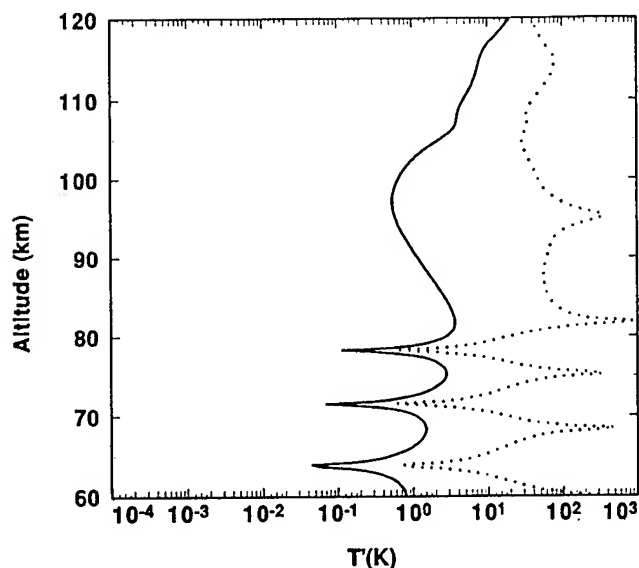
**Figure 8.** Wave B temperature perturbation amplitude ($T'$) required to produce the observed relative intensity perturbation for nominal conditions and WINDII winds. The dashed line represents the limiting temperature perturbation amplitude based on linear stability theory.



**Figure 10.** Wave B temperature perturbation amplitude required to produce the observed relative intensity perturbation for the ISR winds and the nominal eddy diffusion increased by a factor of 30. The dashed line represents the limiting temperature perturbation amplitude based on linear stability theory.

propagation of wave B through the *CIRA* zonal winds, and we note that this wave is mainly affected by the ISR and WINDII meridional winds. At some altitudes, however, the ISR and WINDII zonal wind components are of an appreciable magnitude and must be considered along with the meridional wind components.

The temperature amplitude for wave B propagating in the WINDII wind system for the nominal model parameters is shown in Figure 8. This wave is reflected from about the 82-km level owing to its wave frequency being Doppler shifted to the Brunt-Väisälä frequency there. However, partial transmission of this wave enables it to perturb the $O(^1S)$ nightglow with a relative intensity amplitude of 2.9%. The temperature amplitudes required to do so appear to be
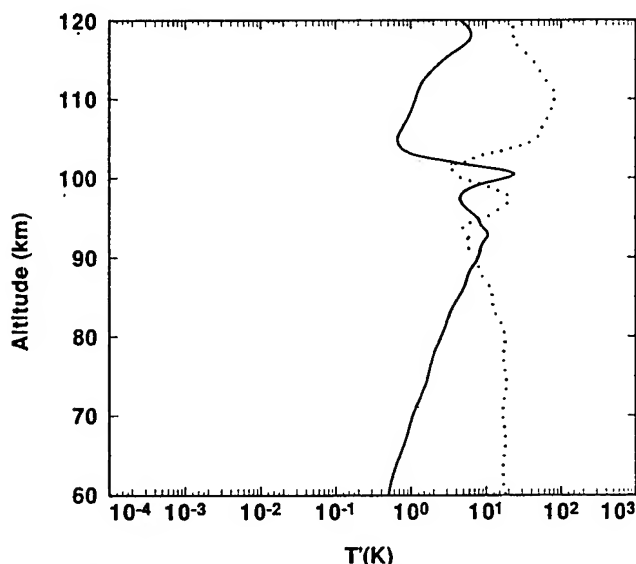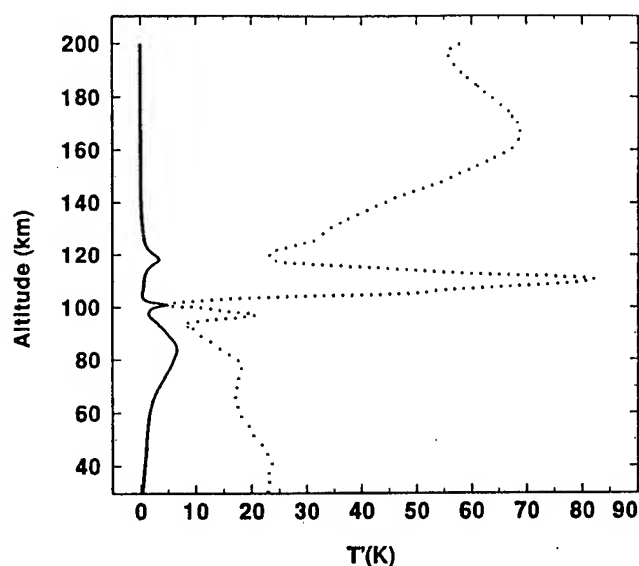


**Figure 9.** As in Figure 8 except for the ISR winds.

everywhere stable, and the maximum temperature perturbation amplitude is about 10 K near 120 km altitude. Note that the stability criterion we used previously will break down when wave reflection is strong, as the dashed curve in Figure 8 shows.

Wave B temperature amplitudes for the wave propagating in the ISR winds (Figure 9) are unstable only over limited height ranges near 90 and 100 km altitude. This wave encounters two critical levels near 100 km altitude in the ISR wind system, and its amplitude decays in their vicinity. Above this, the mean meridional wind reverses direction, the wave is Doppler shifted to higher frequencies, the vertical wavelength is increased, dissipation is decreased, and wave amplitude increases with increasing altitude up to about 120 km altitude. Above this height the mean meridional wind is small, Doppler shifting is minimal, and the wave amplitude decays due to molecular dissipation.

We tested the sensitivity of the results for wave B propagating in the ISR wind system by increasing the nominal eddy diffusion by a factor of 10, by using *Lindzen*'s [1981] saturation parameterization, and by lowering the O profile by 2 km. An increase of the nominal eddy diffusion by a factor of 10 did not significantly improve the simulations. However, an increase of the nominal eddy diffusion by a factor of about 30 reduced the wave amplitudes below their stability limits between 85 and 100 km altitude (see Figure 10). Employment of the saturation parameterization also decreased wave amplitudes, but they still exceeded their stability limits between about 90 and 100 km altitude. Lowering of the O profile by 2 km increased the wave amplitudes, thus worsening our simulations.

### 4.3. Results Summary

The results of our simulations and sensitivity tests are summarized in Table 4. Given the uncertainties in some of the

**Table 4.** Summary of Wave Simulations

| Wind | Wave A | Wave B |
|------|--------|--------|
| CIRA | unstable above 105 km altitude | not studied (see main text) |
| WINDII | always unstable below 82 km altitude, for nominal and nonstandard diffusion | always stable; wave reflected near 82 km altitude |
| ISR | unstable only above about 105 km altitude for nominal diffusion; nonstandard diffusion eliminates instability | unstable between 90 and 100 km altitude, except for very large non-standard diffusion (> 10 times nominal values) |

model parameters and some of the measurements, the *CIRA* winds allowed us to simulate the observed airglow fluctuations quite well for both waves A and B. Wave A was always unstable below the emission layer for the WINDII winds, even when large adjustments were made to some of the model parameters. In the case of the ISR winds any large amplitudes were eliminated in the simulations by increasing the eddy diffusion in the model. Wave A was unstable only above about 105 km altitude in the ISR winds, which is well above the peak of the $O(^1S)$ nightglow emission.

The results obtained for wave A propagating in the different wind systems have been combined in Figure 11 and displayed over a limited altitude range near the peak of the $O(^1S)$ nightglow. Although the wave amplitudes (as indicated by the magnitude of $T'$ in Figure 11a) required to produce the observed nightglow fluctuations are very similar for the different wind conditions, they vary by a factor of at least 2 over much of the nightglow region. The phase of $T'$ (shown in Figure 11b) reveals that within the $O(^1S)$ emission layer the vertical wavelength of wave A exceeds 17 km in the WINDII winds and is about 15 and 10 km in the ISR and *CIRA* winds, respectively. Due to the effects of cancellation in the height-integrated intensity fluctuations, waves of shorter vertical wavelength require correspondingly larger wave amplitudes in order to simulate the observed intensity fluctuation.

Comparison of the vertical wavelengths inferred from Figure 11b with the wave amplitudes near 95 km (Figure 11a) support this reasoning.

A similar summary of the results obtained for wave B propagating in the WINDII and ISR winds are shown in Figure 12. The wave amplitudes required to simulate the observed nightglow intensity fluctuations are significantly larger for the case of the ISR winds than for the WINDII winds (Figure 12a). The almost-constant phase of $T'$ for the case of the WINDII winds (shown in Figure 12b) implies that the vertical wavelength is extremely large and the wave displays evanescent behavior (as expected on the basis of our discussion in the third paragraph of section 4). The vertical wavelength in the case of the ISR winds (~ 7 km) is small by comparison, requiring greater wave amplitudes in order to simulate the observed intensity fluctuation.

## 5. Discussion

The three wind profiles employed in this study are very different. At $O(^1S)$ emission altitudes (~90 to 105 km) the ISR zonal winds are comparable to the CIRA zonal winds and are generally positive (eastward), but the WINDII zonal winds are large and negative (westward) over the same height range. The meridional winds derived from the WINDII observations
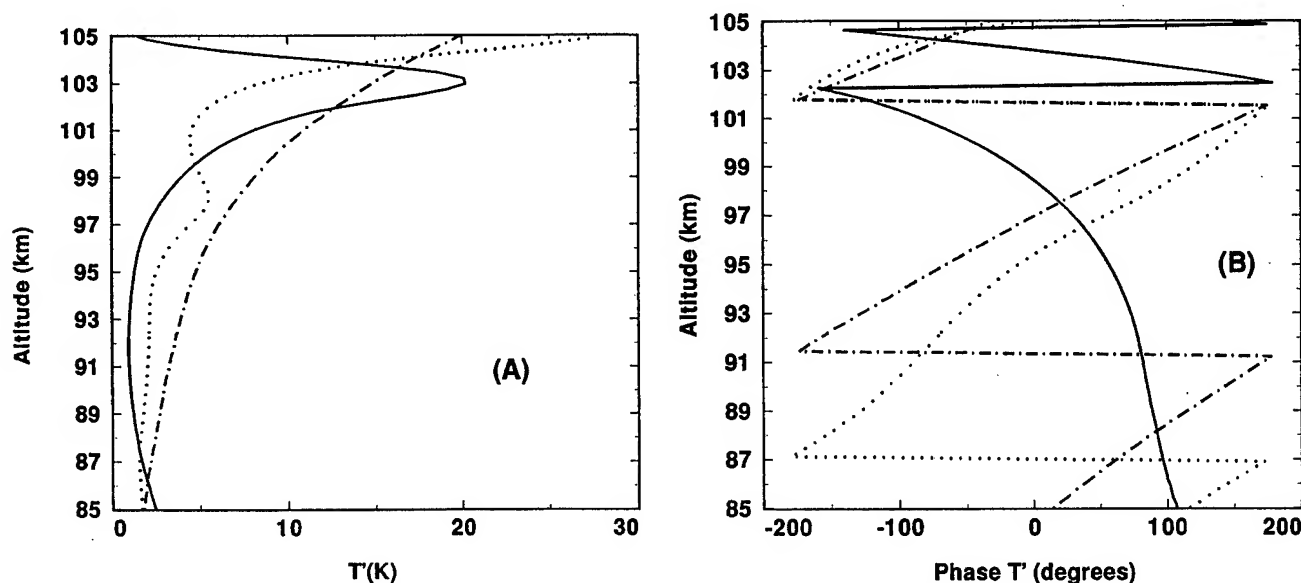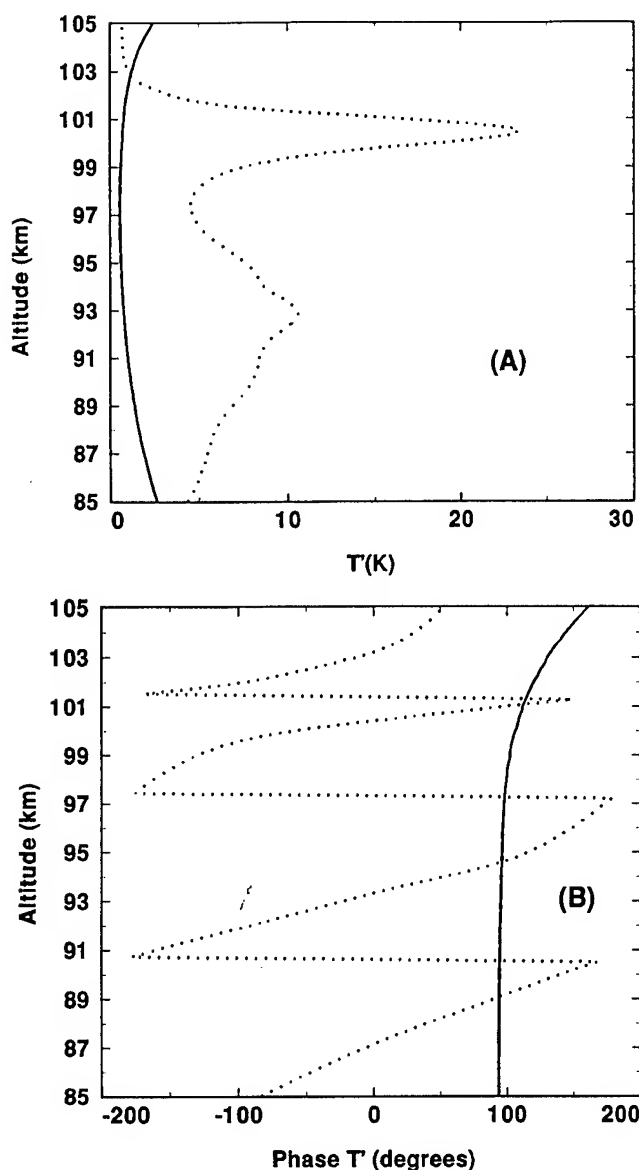


**Figure 11.** Wave A temperature perturbation (a) amplitude and (b) phase, required to produce the observed relative intensity perturbation for the WINDII winds (solid curve), ISR winds (dotted curve) and *CIRA* winds (dashed-dotted curve) for nominal model conditions.

**Figure 12.** Wave B temperature perturbation (a) amplitude and (b) phase, required to produce the observed relative intensity perturbation for the WINDII winds (solid curve) and ISR winds (dotted curve) for nominal model conditions.

zonal winds at 90 km to the CIRA climatological winds near 70 km. Again, this caused our simulations to be less favorable.

The Fourier decomposition of the daytime ISR winds into a mean and tidal components necessarily removes the high-frequency gravity wave components from the derived (interpolated) nighttime winds. Similarly, the spatial averaging inherent in the WINDII measurements also removes the small-scale, high-frequency gravity wave components from the derived winds. The neglected "irregular" wind component cannot be accounted for in our analysis because we do not consider the effects of wave-wave interactions. The slowly varying background components are also removed from the derived mean winds. Nontidal variations that are slow enough to be counted as background could affect the validity of our results if they were of sufficiently large amplitude compared to the background wind and the phase velocities of the waves that we consider. The effect of unmodeled background variations is an unknown but probably secondary effect.

The waves observed in the $O(^1S)$ nightglow emission appeared to be linear and remained coherent over a time span of several hours and over a large region of the sky. Adjustment of some of the model parameters allowed us to simulate the observed nightglow fluctuations assuming that the gravity waves were linear. However, the fact that the use of the measured winds combined with the nominal model parameters required nonlinear wave amplitudes to exist in certain regions suggests that either the winds or some of the model parameters were not specified correctly for the simulations. The weak wave amplitudes within the emission region compared to those below the emission region suggests that the winds employed in our simulations were blocking the waves [e.g., *Cowling et al.*, 1971; *Taylor et al.*, 1993]. However, the observations suggest otherwise, especially for wave A.

The nominal $O(^1S)$ emission layer employed in this study peaked near 93.5 km, which is significantly lower than the commonly accepted value of about 97 km. The WINDII observations discussed in section 2.2.2 showed that at 01:47 UT the $O(^1S)$ emission layer peaked near 94 km, suggesting that the region over Arecibo was dynamically disturbed. Although we do not know whether these anomalous conditions persisted to the time when the gravity wave images were obtained, it appears that our decreasing the height of the atomic oxygen layer by 2 km from its nominal position is not supported by the WINDII observations.

We have used a time-independent model to simulate the propagation of gravity waves through mean winds that are in reality time-dependent. This is not an unreasonable assumption because for the wave parameters employed in our study the vertical component of group velocity (several meters per second) calculated from WKB theory implies that the waves propagate through the $O(^1S)$ nightglow emission layer in only a couple of hours or less. This is significantly less than the period of the semidiurnal tide, suggesting that errors associated with the use of static winds may not be bad. However, waves tend to spend more time near critical levels, meaning that time-dependent effects may be important under such conditions.

also differ considerably from those derived from the ISR observations. While the ISR meridional and zonal winds are generally no more than a few tens of m s$^{-1}$, the WINDII winds reach magnitudes of over 100 m s$^{-1}$. The ISR-measured winds and the WINDII-measured winds were neither coincident in both position and time with each other nor with the gravity wave observations, and the limitations of each have been discussed in sections 2.2.1 and 2.2.2.

No information was available below about 90 km altitude for the measured winds, which was the region where some of the largest wave amplitudes were simulated. Below about 90 km we linearly interpolated the winds to zero at 80 km. The sensitivity of our wave simulations to this was tested by interpolating the winds to zero at lower altitudes (e.g., 70 km), but this caused the comparison to be less favorable (i.e., larger wave amplitudes were required below the airglow layer in order to simulate the observations). We also investigated the effects on our simulations of interpolating the measured

## 6. Conclusions

Our simulations have demonstrated that perturbations in the $O(^1S)$ nightglow emission are sensitive to the mean winds

in the emission region as well as to the values of some of the parameters employed in the wave-nightglow interaction model, such as the shape of the O profile and the nature of eddy diffusion in the vicinity of the $O(^1S)$ nightglow emission layer.

We have learned from this study that the information inferred from measured airglow fluctuations is greatly enhanced by a complete knowledge of the background winds. In particular, knowledge of the mean winds extending down to altitudes much lower than the height of the airglow layer would allow us to extend our description of the waves down to low altitudes. Future experiments should include observations that allow us to constrain more of our model parameters. Mean winds that are coincident in time and location with the nightglow emission fluctuation measurements should be obtained. The winds should also be measured over a greater altitude range than that employed in the present study and should extend to altitudes well below the nightglow emission layer. A sodium temperature/wind lidar [e.g., *Bills et al.*, 1991] could be used for this purpose to provide accurate winds as a function of altitude extending from below to well above the peak of the $O(^1S)$ emission layer. Doppler lidar systems can provide mean winds in the middle atmosphere, and the Doppler Rayleigh lidar system of *Chanin et al.* [1989] provides these between altitudes of about 25 and 60 km. Other independent measurements of gravity waves should also be employed, allowing a thorough evaluation of any wave-nightglow interaction model. Lidar measurements of waves, for example, could provide perturbations as a function of altitude, a useful diagnostic for our model evaluation.

## Appendix

The $O(^1S)$ chemistry responsible for the green line emission at 557.7 Å is described by the following reactions (see Table A1). Here, we have assumed, in accordance with *Bates* [1988], that the production of $O(^1S)$ is by a two-step process in which the intermediate state is $O_2(c^1\Sigma_u^-)$. The reaction rates employed here are those given by *Torr et al.* [1985].

The assumption that the mean state is a steady state and use of the above reactions allows us to write for the mean state densities of $O_2(c^1\Sigma_u^-)$ and $O(^1S)$:

$$\bar{n}(O_2(c^1\Sigma_u^-)) = \xi k_1 \bar{n}^2(O)\bar{n}(M)$$
$$/(k_2 \bar{n}(O_2) + k_3 \bar{n}(O) + A_1) \qquad \text{(A1)}$$

$$\bar{n}(O(^1S)) = \delta k_3 \bar{n}(O)\bar{n}(O_2(c^1\Sigma_u^-))$$
$$/(k_6 \bar{n}(O_2) + A_3) \qquad \text{(A2)}$$

Gravity wave perturbations in temperature ($T'$), velocity divergence ($\underline{\nabla}\cdot\underline{v}'$) and major gas density ($n'(M)$) produce corresponding perturbations in the chemically reactive minor species. We use the method described by *Walterscheid et al.* [1987] to derive the perturbation number densities of O, $O_2(c^1\Sigma_u^-)$ and $O(^1S)$. The fluctuations in O and $O_2(c^1\Sigma_u^-)$ have been described previously by *Hickey et al.* [1993a], while the fluctuations in $O(^1S)$ have been described by *Hickey et al.* [1993b].

$$\{i\omega + 2\bar{k}_1 \bar{n}(O)\bar{n}(M)\}n'(O)$$
$$= \bar{n}(O)\{(2-f_3)\bar{k}_1 \bar{n}(O)\bar{n}(M) - f_1 + f_2/\bar{H}(O)\}T'/\bar{T} \qquad \text{(A3)}$$

$$\{i\omega + k_2\bar{n}(O_2) + k_3\bar{n}(O) + A_1\}n'(O_2(c^1\Sigma_u^-))$$
$$= \{2\xi\bar{k}_1\bar{n}(O)\bar{n}(M) - k_3\bar{n}(O_2(c^1\Sigma_u^-))\}n'(O)$$
$$+ \left\{\begin{array}{l}\xi\bar{k}_1\bar{n}^2(O)\bar{n}(M)(f_3-2)\\ -\bar{n}(O_2(c^1\Sigma_u^-))[k_2\bar{n}(O_2)f_3 - f_1 + f_2/\bar{H}(O_2(c^1\Sigma_u^-))]\end{array}\right\}\frac{T'}{\bar{T}} \qquad \text{(A4)}$$

$$\{i\omega + \bar{k}_6\bar{n}(O_2) + A\}n'(O(^1S))$$
$$= \delta k_3\{\bar{n}(O)n'(O_2(c^1\Sigma_u^-)) + \bar{n}(O_2(c^1\Sigma_u^-))n'(O)\}$$
$$+ \left\{f_2/\bar{H}(O(^1S)) - f_1 - \bar{k}_6\bar{n}(O_2)\left[\frac{865}{T} + f_3\right]\right\}\bar{n}(O(^1S))\frac{T'}{\bar{T}} \qquad \text{(A5)}$$

We have used $\bar{H}(X)$ to denote the scale height of a species X. The complex dynamical factors $f_1$, $f_2$, and $f_3$ relate the temperature perturbation to the velocity divergence, the vertical velocity, and the major gas density perturbation, respectively, such that

$$\underline{\nabla}\cdot\underline{v}' = f_1 T'/\bar{T} \qquad \text{(A6)}$$

$$w' = f_2 T'/\bar{T} \qquad \text{(A7)}$$

$$n'(M)/\bar{n}(M) = f_3 T'/\bar{T} \qquad \text{(A8)}$$

**Table A1.** Chemical Kinetic Parameters Employed in the $O(^1S)$ Nightglow Model

| Reaction | Rate of Reaction[*] |
|---|---|
| $O + O + M \rightarrow O_2 + M$ | $k_1 = 4.7 \times 10^{-33} (300/T)^2$ |
| $O + O + M \rightarrow O_2(c^1\Sigma_u^-) + M$ | $k = \zeta k_1$, $\zeta = 0.8$ (or $\zeta = 0.03$ & $\delta = 0.2$) |
| $O_2(c^1\Sigma_u^-) + O_2 \rightarrow O_2(b^1\Sigma_g^+) + O_2$ | $k_2 = 5.0 \times 10^{-13}$ |
| $O_2(c^1\Sigma_u^-) + O \rightarrow O_2 + O$ | $k_3 = 3.0 \times 10^{-11}$ (or $6.0 \times 10^{-12}$) |
| $O_2(c^1\Sigma_u^-) + O \rightarrow O_2 + O(^1S)$ | $k = \delta k_3$, $\delta = 0.01$ (or $\delta = 0.2$ & $\zeta = 0.03$) |
| $O_2(c^1\Sigma_u^-) \rightarrow O_2 + h\nu$ | $A_1 = 2.0 \times 10^{-2}$ (or $1.0 \times 10^{-3}$) |
| $O(^1S) + O_2 \rightarrow O(^3P) + O_2$ | $k_6 = 4.0 \times 10^{-12} \exp(-865/T)$ |
| $O(^1S) \rightarrow O + h\nu$ (5577 Å, 2972 Å) | $A_2 = 1.105$ |
| $O(^1S) \rightarrow O + h\nu$ (5577 Å) | $A_{5577} = 1.06$ |

[*] Units are $s^{-1}$, $cm^{-3} s^{-1}$ and $cm^{-6} s^{-1}$ for unimolecular, bimolecular, and termolecular reactions, respectively.

The emission intensity of the $O(^1S)$ is proportional to $A_{5577}n(O(^1S))$ and so it follows that the fractional emission fluctuation at a specific altitude is equal to $n'(O(^1S))/\bar{n}(O(^1S))$. The observed fractional emission fluctuation is obtained by integrating both the numerator and denominator over the vertical extent of the emission, giving

$$\langle \delta I \rangle / \langle \bar{I} \rangle = \int_{-\infty}^{\infty} n'\left(O\left(^1S\right)\right)dz \bigg/ \int_{-\infty}^{\infty} \bar{n}\left(O\left(^1S\right)\right)dz \qquad (A9)$$

In practice, we only needed to integrate between 75 and 130 km altitude to accurately define $\langle \delta I \rangle / \langle \bar{I} \rangle$.

# References

Andreassen, Ø., C. E. Wasberg, D. C. Fritts, and J. R. Isler, Gravity wave breaking in two and three dimensions, I, Model description and comparison of two-dimensional evolutions, *J. Geophys. Res.*, *99*, 8095, 1994.

Bates, D. R., Excitation of 557.7 nm OI line in nightglow, *Planet. Space Sci.*, *36*, 883, 1988.

Bills, R. E., C. S. Gardner, and C. Y. She, Narrowband lidar technique for sodium temperature and Doppler wind observations of the upper atmosphere, *Opt. Eng.*, *30*, 13, 1991.

Bruce, C. H., D. W. Peaceman, H. H. Rachford Jr., and J. P. Rice, Calculations of unsteady-state gas flow through porous media, *Petrol. Trans. AIME*, *198*, 79-92, 1953.

Chanin, M. L., A. Garnier, A. Hauchecorne, and J. Porteneuve, A Doppler lidar system for measuring winds in the middle atmosphere, *Geophys. Res. Lett.*, *16*, 1273, 1989.

Cowling, D. H., H. D. Webb, and K. C. Yeh, Group rays of internal gravity waves in a wind-stratified atmosphere, *J. Geophys. Res.*, *76*, 213, 1971.

Fritts, D. C., Gravity wave saturation in the middle atmosphere: A review of theory and observations, *Rev. Geophys. Space Phys.*, *22*, 275, 1984.

Garcia, R. R., and S. Solomon, The effect of breaking gravity waves on the dynamics and chemical composition of the mesosphere and lower thermosphere, *J. Geophys. Res.*, *90*, 3850, 1985.

Gault, W. A., et al., Validation of $O(^1S)$ wind measurements by WINDII: The wind imaging interferometer on UARS, *J. Geophys. Res.*, *101* (D6), 10,405, 1996.

Harper, R. M., R. H. Wand, C. J. Zamlutti, and D. T. Farley, $E$ region ion drifts and winds from incoherent scatter measurements at Arecibo, *J. Geophys. Res.*, *81*, 25, 1976.

Hecht, J. H., R. L. Walterscheid, G. G. Sivjee, A. B. Christensen, and J. B. Pranke, Observations of wave-driven fluctuations of OH nightglow emission from Sondre Stromfjord, Greenland, *J. Geophys. Res.*, *92*, 6091, 1987.

Hedin, A. E., Extension of the MSIS thermosphere model into the middle and lower atmosphere, *J. Geophys. Res.*, *96*, 1159, 1991.

Hickey, M. P., Effects of eddy viscosity and thermal conduction and Coriolis force in the dynamics of gravity wave driven fluctuations in the OH nightglow, *J. Geophys. Res.*, *93*, 4077, 1988a.

Hickey, M. P., Wavelength dependence of eddy dissipation and Coriolis force in the dynamics of gravity wave driven fluctuations in the OH nightglow, *J. Geophys. Res.*, *93*, 4089, 1988b.

Hickey, M. P. and K. D. Cole, A quartic dispersion equation for internal gravity waves in the thermosphere, *J. Atmos. Terr. Phys.*, *49*, 889, 1987.

Hickey, M.P., G. Schubert, and R. L. Walterscheid, Seasonal and latitudinal variations of gravity wave-driven fluctuations in OH nightglow, *J. Geophys. Res.*, *97*, 14,911-14,922, 1992.

Hickey, M. P., G. Schubert, and R. L. Walterscheid, Gravity wave-driven fluctuations in the $O_2$ Atmospheric (0-1) nightglow from an extended, dissipative emission region, *J. Geophys. Res.*, *98*, 13,717-13,730, 1993a.

Hickey, M. P., R. L. Walterscheid, and G. Schubert, A model of wave-driven fluctuations in the $O(^1S)$ nightglow, *Eos Trans. AGU*, *74* (16), Spring Meet. Suppl., 218, 1993b.

Hickey, M. P., R. L. Walterscheid and G. Schubert, A numerical model of gravity wave propagation in an inhomogeneous atmosphere, *Eos Trans. AGU*, *75* (44), Fall Meet. Suppl., 508, 1994.

Hickey, M. P., R. L. Walterscheid and G. Schubert, The propagation and dissipation of gravity waves in the terrestrial atmosphere: Full-wave versus WKB models, *Eos Trans. AGU*, *76* (46), Fall Meet. Suppl., 436, 1995.

Hines, C. O., Internal atmospheric gravity waves at ionospheric heights, *Can. J. Phys.*, *38*, 1441, 1960.

Hines, C. O., and D. W. Tarasick, On the detection and utilization of gravity waves in airglow studies, *Planet. Space Sci.*, *35*, 851, 1987.

Isler, J. R., T. F. Tuan, R. H. Picard, and U. Makhlouf, On the nonlinear response of airglow to linear gravity waves, *J. Geophys. Res.*, *96*, 14,141, 1991.

Lindzen, R. S., Internal gravity waves in atmospheres with realistic dissipation and temperature, I, Mathematical development and propagation of waves into the thermosphere, *Geophys. Fluid Dyn.*, *1*, 303-355, 1970.

Lindzen, R. S., Turbulence and stress owing to gravity wave and tidal breakdown, *J. Geophys. Res.*, *86*, 9707, 1981.

Makhlouf, U., R. H. Picard, and J. R. Winick, Photochemical-dynamical modeling of the measured response of airglow to gravity waves, I, Basic model, *J. Geophys. Res.*, *100*, 11,289, 1995.

McLandress, C., G. G. Shepherd, and B. H. Solheim, Satellite observations of thermospheric tides: Results from the Wind Imaging Interferometer on UARS, *J. Geophys. Res.*, *101*, 4093-4114, 1996.

Orlanski, I., and K. Bryan, Formation of the thermocline step structure by large-amplitude internal gravity waves, *J. Geophys. Res.*, *74*, 6975, 1969.

Oznovich, I., D. J. McEwen, and G. G. Sivjee, Temperature and airglow brightness oscillations in the polar mesosphere and lower thermosphere, *Planet. Space Sci.*, *43*, 1121, 1995.

Rees, M. H., *Physics and Chemistry of the Upper Atmosphere*, Cambridge Univ. Press, New York, 1989.

Schubert, G., and R. L. Walterscheid, Wave-driven fluctuations in OH nightglow from an extended source region, *J. Geophys. Res.*, *93*, 9903-9915, 1988.

Schubert, G., R. L. Walterscheid, and M. P. Hickey, Gravity wave-driven fluctuations in OH nightglow from an extended, dissipative emission region, *J. Geophys. Res.*, *96*, 13,869-13,880, 1991.

Shepherd, G. G., et al., WINDII, the Wind Imaging Interferometer on the Upper Atmosphere Research Satellite, *J. Geophys. Res.*, *98*, 10,725-10,750, 1993.

Sivjee, G. G., R. L. Walterscheid, J. H. Hecht, R. M. Hamwey, G. Schubert, and A. B. Christensen, Effects of atmospheric disturbances on polar mesopause airglow OH emissions, *J. Geophys. Res.*, *92*, 7651, 1987.

Strobel, D. F., Constraints on gravity wave induced diffusion in the middle atmosphere, *Pure Appl. Geophys.*, *130*, 533, 1989.

Swenson, G. R., M. J. Taylor, P. J. Espy, C. S. Gardner, and X. Tao, ALOHA-93 measurements of intrinsic AGW characteristics using airborne airglow imager and ground-based Na wind/temperature lidar, *Geophys. Res. Lett.*, *22*, 2841, 1995.

Tao, X., and C. S. Gardner, Heat flux observations in the mesopause region above Haleakala, *Geophys. Res. Lett., 22*, 2829, 1995.

Tarasick, D. W., and C. O. Hines, The observable effects of gravity waves on airglow emissions, *Planet. Space Sci., 38*, 1105, 1990.

Tarasick, D. W., and G. G. Shepherd, The effects of gravity waves on complex airglow chemistries, 1, $O_2(b^1\Sigma_g^+)$ emission, *J. Geophys. Res., 97*, 3185, 1992a.

Tarasick, D. W., and G. G. Shepherd, The effects of gravity waves on complex airglow chemistries, 2, OH emission, *J. Geophys. Res., 97*, 3195, 1992b.

Taylor, M. J., and F. J. Garcia, A two-dimensional spectral analysis of short period gravity waves imaged in the OI(557.7 nm) and near infrared OH nightglow emissions over Arecibo, Puerto Rico, *Geophys. Res. Lett., 22*, 2473, 1995.

Taylor, M. J., E. H. Ryan, T. F. Tuan, and R. Edwards, Evidence of preferential directions for gravity wave propagation due to wind filtering in the middle atmosphere, *J. Geophys. Res., 98*, 6047, 1993.

Taylor, M. J., Y. Y. Gu, X. Tao, C. S. Gardner, and M. B. Bishop, An investigation of intrinsic gravity wave signatures using coordinated lidar and nightglow imaging measurements, *Geophys. Res. Lett., 22*, 2853, 1995.

Torr, M. R., D. G. Torr, and R. R. Laher, The $O_2$ Atmospheric 0-0 band and related emissions at night from Spacelab 1, *J. Geophys. Res., 90*, 8525, 1985.

Viereck, R. A., and C. S. Deehr, On the interaction between gravity waves and the OH Meinel (6-2) and the $O_2$ Atmospheric (0-1) bands in the polar night airglow, *J. Geophys. Res., 94*, 5397, 1989.

Vincent, R. A., and I. M. Reid, HF Doppler measurements of mesosphere gravity wave momentum fluxes, *J. Atmos. Sci., 40*, 1321, 1983.

Walterscheid, R. L., and G. Schubert, A dynamical-chemical model of tidally driven fluctuations in the OH nightglow, *J. Geophys. Res., 92*, 8775-8780, 1987.

Walterscheid, R. L., and G. Schubert, Nonlinear evolution of an upward propagating gravity wave: Overturning, convection, transience and turbulence, *J. Atmos. Sci., 47*, 101-125, 1990.

Walterscheid, R. L., G. Schubert, and J. M. Straus, A dynamical-chemical model of wave-driven fluctuations in the OH nightglow, *J. Geophys. Res., 92*, 1241-1254, 1987.

Walterscheid, R. L., G. Schubert, and M. P. Hickey, A comparison of theories for gravity wave induced fluctuations in airglow emissions, *J. Geophys. Res., 99*, 3935, 1994.

Ward, W. E., D. Y. Wang, B. H. Solheim, and G. G. Shepherd, Observations of the two-day wave in WINDII data during January 1993, *Geophys. Res. Lett., 23 (21)*, 2923, 1996.

Zhang, S., R. N. Peterson, R. H. Wiens, and G. G. Shepherd, Gravity waves from $O_2$ nightglow during the AIDA '89 Campaign, I, Emission rate/temperature observations, *J. Atmos. Terr. Phys.*, 355, 1992a.

Zhang, S., R. H. Wiens, and G. G. Shepherd, Gravity waves from $O_2$ nightglow during the AIDA '89 Campaign, II, Numerical modeling of the emission rate/temperature ratio, $\eta$, *J. Atmos. Terr. Phys.*, 377, 1992b.

Zhou, Q. H., M. P. Sulzer, C. A. Tepley, C. G. Fesen, R. G. Roble, and M. C. Kelly, Neutral winds and temperature at Arecibo $E$ region heights during January 1993: Observation and comparison with TIME-GCM results, *J. Geophys. Res., this issue*, 1996.

F. Garcia and M. C. Kelley, Department of Electrical Engineering, Cornell University, Ithaca, NY. (email: fgarcia@protono.ee.cornell.edu; mikek@ee.cornell.edu)

M. P. Hickey, Center for Space Plasma, Aeronomy, and Astrophysics Research, University of Alabama, OB 344, Huntsville, AL 35899. (e-mail: hickeym@cspar.uah.edu)

G. Schubert, Department of Earth and Space Sciences, Institute of Geophysics and Planetary Physics, University of California, Los Angeles, CA. (e-mail: gschubert@mgnvax.ess.ucla.edu)

G. G. Shepherd and W. Ward, Institute of Space and Terrestrial Science, York University, North York, Canada. (e-mail: william@stpl.ists.ca)

M. J. Taylor, Space Dynamics Laboratory, Utah State University, Logan, UT. (e-mail: taylor@psi.sci.sdl.usu.edu)

R. L. Walterscheid, Space and Environment Technology Center, The Aerospace Corporation, Los Angeles, CA. (e-mail: richard_walterscheid@qmail2.aero.org)

Q. Zhou, Arecibo Observatory, Cornell University, Arecibo, Puerto Rico. (e-mail: zhou@naic.edu)

# High resolution OI (630 nm) image measurements of F-region depletion drifts during the Guará campaign

M. J. Taylor

Space Dynamics Laboratory and Physics Department, Utah State University, Logan, UT

J. V. Eccles

Space Environment Corporation, Logan, UT

J. LaBelle

Department of Physics and Astronomy, Dartmouth College, Hanover, NH

J. H. A. Sobral

Instituto Nacional de Pesquisas Espaciais, São José dos Campos, Brazil

**Abstract.**
A high performance, all-sky, imaging system has provided data on the evolution and drift motions of F-region depletions above the magnetic dip equator at Alcântara, Brazil, (2.3° S, 44.5° W). Monochromatic images of depletions in the OI(630 nm) nightglow were recorded on eight nights during 1-16 October, 1994, as part of the Guará campaign. The drift motions of the depletions were typically 80-100 m/s eastward prior to local midnight and reduced to a minimum of ~30-50 m/s in the morning hours, in accord with previous observations. However, on October 2–3 and 12–13 the depletions were observed to reverse direction for ~60–90 min, achieving westward speeds of ~30 m/s before the motion reverted to eastward around 0100 LT and accelerated to 35-45 m/s near dawn. Magnetic activity and other evidence suggests that these reversals in the motion of the airglow depletions probably result from reversals in the F-region dynamo rather than from shifts in the altitude of the shear in the nighttime F-region plasma drift.

## Introduction

For about thirty years, it has been known that the high altitude (250–300 km) equatorial OI(630 nm) nightglow emission often exhibits irregularities associated with spread-F. Weber et al. [1978] recorded the first images of magnetically N-S aligned bands of diminished 630 nm intensity (termed depletions) coincident with ionosonde measurements of spread-F. Since then, several groups have reported measurements of depletions at low magnetic latitudes [e.g Mendillo and Baumgard-ner, 1982; Tinsley et al., 1995]. These observations establish that depletions are the bottomside signatures of flux-tube aligned plasma bubbles and provide measurements of their horizontal sizes, shapes, and drift speeds.

Almost without exception, previous observers have reported eastward drifts during nighttime hours, consistent with the downward electric field which predominates in the nighttime equatorial F-region. Relatively high eastward velocities (100-200 m/s) are usually observed in the early evening hours, but during the post-midnight period the depletion drift speeds reduce significantly to 20-100 m/s, reflecting the well known diurnal dependence of the vertical electric field. Weber et al. [1978] report a single observation (26 March 1978) at ~16° N in which the eastward drift of the depletions reversed and turned westward. There are two possible interpretations for such a reversal in the zonal velocity of the depletions: the F-region dynamo itself may reverse; or the natural shear in the zonal drift (which in the evening sector creates a boundary between westward drift at low altitudes dominated by the E-region dynamo and eastward drift at higher altitudes) may shift to higher altitudes, placing the airglow layer in the influence of the E-region dynamo. Electric field studies show that at 200-600 km altitude, the drift is usually eastward throughout the night, reversing to westward near 0600 LT [Fejer et al., 1991], although the reversal time depends on season, geomagnetic activity and phase of the solar cycle. The drift reversal observed near midnight by Weber et al. [1978], though unusual, is not inconsistent with this pattern as airglow features at 16°N map up to ~500 km altitude above the equator where the onset of drift reversal from eastward to westward has been observed as early as local midnight in some electric field measurements [e.g., Coley and Heelis, 1989]. Nighttime reversals in the motion of depletions at low latitudes, where the field lines map to lower altitudes above the equator, have not been previously reported.

## Data Presentation

During October 1–16, 1994, high resolution (512 x 512 pixel) all-sky, monochromatic image measurements of F-region depletions in the 630 nm nightglow emission were made using a high quantum efficiency CCD detector ~80% at visible wavelengths. The camera was fitted with an all-sky telecentric lens system and a narrow-band interference filter (bandwidth ~2.4 nm) permitting high signal-to-noise ratio (SNR≈ 20 − 50) images of the depletions to be obtained using an exposure time of 180s. These measurements were incorporated into a 5–9 minute sequence of observations that also included OI(557.7 nm), which also exhibited signatures of the depletions.

The imager was operated from the INPE Satellite Tracking Station at Alcântara, Brazil, (2.33°S, 44.5°W). Assuming a peak emission altitude of 280 km for the OI emission the useful field of view of the instrument was 1000 km radius.

Depletions were evident on 8 out of 15 nights during period 1-16 October but, due to variable cloud conditions the duration of the measurement was often restricted. A clear preference for sightings prior to local midnight consistent with previous measurements from higher latitude sites was found. Depletions were sighted most frequently to the west and appeared generally brighter in this direction. However, high contrast events extending over an area significantly greater than the all-sky field-of-view of several million km² were common.

Figure 1 shows four examples of OI(630 nm) depletions recorded during the campaign. Due to the fa-
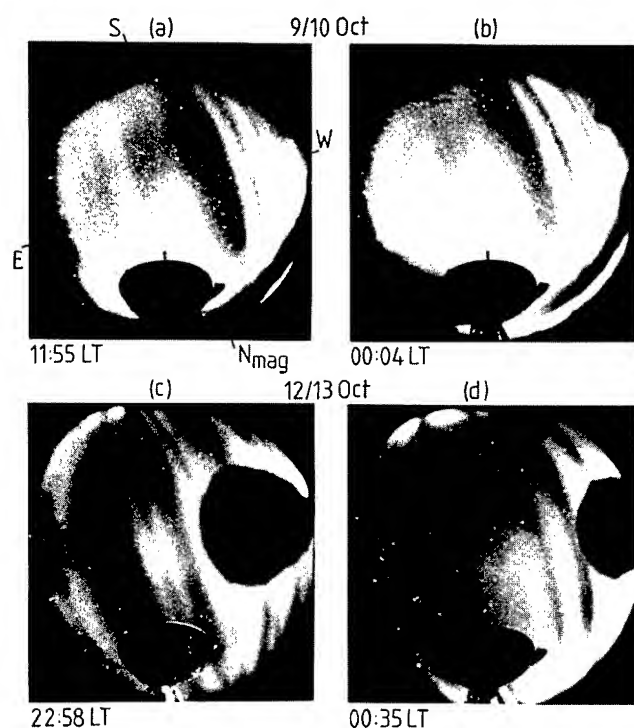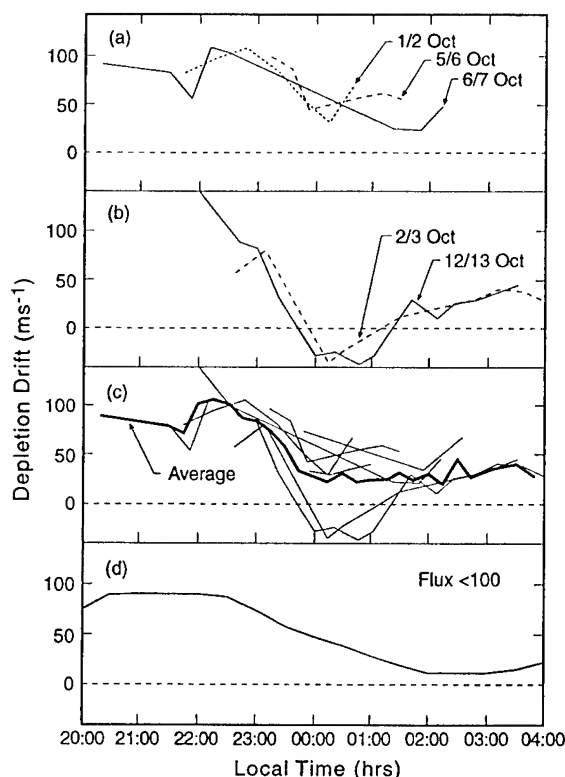


**Figure 2.** Summary of depletion drift measurements indicating (a) typical nighttime behavior, (b) westward motions, (c) average zonal behavior, and (d) comparison with Jicamarca average zonal drifts for low solar f10.7 fluxes (after Fejer et al. [1991]).

vorable location of the imager on the magnetic equator the depletions exhibit marked magnetic N-S symmetry. The first two images (a,b) were recorded at 2355 and 0004 LT on October 9–10 and show several high contrast depletions to the west of Alcântara. Before 2300 LT and after 0100 LT cloud obscured these observations. Analysis of this display indicates motion towards the east with an average speed of 40 m/s during this period. The narrow striations and the enhanced 630 nm intensity towards the north were typical of several of the depletion events observed during this campaign.

Figure 1c-d shows a sequence of two 630 nm images recorded near local midnight on October 12–13, 1994, when reversal to westward motion was observed. Depletions were imaged continuously for more than eight hours (1951–0439 LT) on this night. Initially, the observations were limited by the high elevation moon which was masked out in later images by the large dark spot evident in the figures. Figure 1c shows several well-defined, narrow depletions imaged at 22:58 LT during the period of rapid eastward motion. Figure 1d shows the depletion pattern at 00:35 LT which is equally extensive but has now reversed its direction of motion to westwards. Towards dawn the separation between depletions increased considerably and only three depletions were evident (not shown).

By comparing successive images like those shown in Figure 1, the speed and direction of the airglow features were measured as a function of local time. Figure 2a



**Figure 1.** Four all-sky CCD images showing OI(630 nm) depletions from Alcântara, Brazil.

shows three typical drift profiles for which the eastward drift in the evening sector (2000–2300 LT) is ~100 m/s, and thereafter the drift speed decreases steadily reaching ~50 m/s in the post-midnight hours. Figure 2b shows the drift profile for the two "anomalous nights". On October 12–13, initial measurements around 2200 LT indicate eastward drifts of ~150 m/s which decrease steadily until 2345 LT, when the drift reverses to westward. The reversal is quite prompt, occurring within the 9-minute sample interval, and the westward drift is relatively low (~30 m/s) but lasts for about 90 min. At 0115 LT the motion reverts back to eastward for the remainder of the night and accelerates up to 45 m/s. Measurements on October 2–3 indicate a somewhat lower eastward drift (80 m/s) in the pre-midnight period prior to the westward reversal, which again occurs near local midnight. The westward drift again reaches a similar maximum value of ~30 m/s shortly after midnight but reverts to eastward at 0100 LT. In both cases the drift motion at the end of the observations (0300–0400 LT) was 35-45 m/s eastward, comparable to the drifts measured at the same local time on other nights.

Figure 2c shows a superposition of all seven drift profiles. The dark trace indicates the average drift speed as a function of local time as determined from this data set. For comparison, Figure 2d shows the average zonal drift extracted from the Jicamarca incoherent scatter radar (ISR) data base for solar 10.7 radio flux index < 100 [Fejer et al., 1991]. This index was generally in the range 70-90 during the 15 day campaign. The average airglow drift profile agrees remarkably well with the Jicamarca average profile in both magnitude and shape, given the small number of samples comprising the airglow data set. In both profiles a distinct downward trend in eastward drift speed is evident in the evening hours followed by a broad post-midnight minimum. This minimum occurs a slightly earlier local times in the airglow profile (near 0100 LT compared with 0230 LT in the Jicamarca data). The phase of the minimum in the averaged airglow profile was clearly affected during the two anomalous nights.

To investigate the ionospheric conditions during the two anomalous nights, Figure 3 shows the virtual height bottomside of the F-layer (h′F) scaled from the INPE digital ionsoundings measured from Sao Luis (located ~40 km from the camera site). The virtual height of the F-peak was obscured by spread F during most of the time, but h′F was observed continuously. Changes in this parameter provide a measure of vertical motions of the ionosphere over the altitude range 225- 325 km, roughly coincident with the height of the airglow layer (~280 km). In each panel, the time of the reversal from eastward to westward drift, as inferred from the image data, is indicated by a vertical line. On both nights, this reversal in the zonal motion of the depletions occurs when the vertical motion of the F-layer inferred from h′F reduces to nearly zero and also appears to reverse. This observation is reminiscent of spaced receiver scintillation drift measurements, which show that reversals in the zonal drift of F-region irregularities, near the
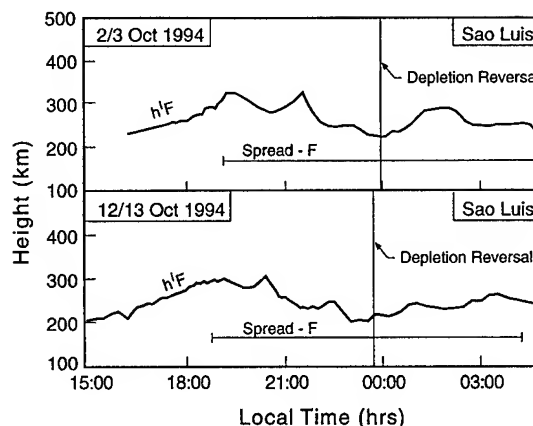


**Figure 3.** Plots of h′F for 2/3 and 12/13 October, 1994. The vertical line in each plot indicates the time of drift reversal determined from the image data. The horizontal bars show when spread-F occurred.

peak of the F-layer are associated with times when the vertical drift nearly vanishes [Abdu et al., 1985]. The coupling between the zonal and vertical plasma drifts, whereby the zonal drift decelerates as h′F decreases (e.g., during 2200-0000 on October 2) and accelerates as h′F increases (e.g., during 0000-0300 on October 3), has been demonstrated in a model of the low-latitude electric fields [Eccles, 1996]. Curl free requirements on the electric field cause the vertical plasma drift to respond in proportion to the rate of change of the zonal drift, which is strongly coupled to the zonal neutral wind dynamo.

## Discussion

There are two possible mechanisms for reversing the zonal velocity of the airglow depletions: First, the nighttime F region plasma drift may have reversed direction; second, the boundary between eastward drift in the F-region and westward drift below the F-region may have shifted to higher altitude, placing the airglow layer in westward-drifting region.

The zonal F region wind dynamo drives Pedersen currents and creates a vertical polarization electric field, which forces the plasma to drift at nearly the neutral wind velocity [Rishbeth, 1971]. The reversal of the nighttime plasma drift to the west may suggest an unusual reversal in the F region dynamo. High-latitude magnetic activity can alter low-latitude drifts [Fejer, 1993] though high latitude electric field penetration and thermospheric wind disturbances. Though October 1-16 had only moderate magnetic activity, the Kp index increased significantly several hours before the drift reversal on October 2–3 (from ≤ 1.7 preceding 1200 LT to ≥ 5.3 after 1800 LT on October 2.) The significant magnetic activity may have altered the neutral wind dynamo. Due to the delay between the increased Kp and the drift reversal, field penetration is not a likely cause. The reversal of October 12–13 is not accompanied by the same level of Kp activity as October 2–3. However, a significant change in Kp, from 1.7 to 4.0, occurs at

1800 LT on October 12. No other nights during October 1–16 have comparable increases in Kp in the early evening when a magnetic disturbance could contribute to the observed reversal.

The second possibility for the drift reversal is the shear in the nighttime zonal plasma drift. The altitude profile of the zonal drift has a strong eastward flow at F region altitudes and weaker westward flow below the F-ledge. The shear is created by the competing E and F region dynamo winds which are directed oppositely near sunset [Haerendel et al., 1992]. At altitudes equal to or above the F-peak, the field-line-integrated Pedersen conductivity is dominated by the F region, so the F region dynamo controls the drifts. Below the F-peak peak the E region dynamo dominates. The altitude of the shear rises and falls with the F region ionosphere. The 630 nm airglow region of 260–300 km might generally lie above the shear so that the depletions drift eastward. One might suggest that the shear may have moved above the airglow region causing depletions to move westward during the anomalous westward drifts near midnight.

The dominant E region winds below the shear altitude are represented well by atmospheric tidal modes with the dominate mode being the [-1,2] diurnal mode [Tarpley, 1970]. The near-equator zonal winds move westward in the evening with speeds of ~20 m/s near sunset and decreasing to zero near 0200LT. The resulting westward plasma drift below the shear near local midnight would be much smaller than the observed 30 m/s in the airglow irregularity drift. There are other E region wind modulations upon the [-1,2] diurnal tide that could produce the observed westward drifts below the shear. However, since the shear height rises and falls with the F region ledge, it is difficult to see why the anomalous zonal drifts occur near midnight when h'F is near its minimum (Figure 3). When h'F is near its minimum the shear is most likely to be below the airglow region, which would suggest eastward flows. Additionally, during 2200–2300LT the h'F is much higher than at local midnight, yet the depletions show no hint of a westward drift. Together these arguments suggest that the anomalous westward drifts near local midnight on Oct 2/3 and Oct 12/13 are actual reversals in the F region dynamo winds, possibly due to impulsive magnetic activity earlier in the evenings.

# References

Abdu, M.A., I.S. Batista, J.H.A. Sobral, E.R. de Paula, and I.J. Kantor, Equatorial ionospheric plasma bubble irregularity occurrence and zonal velocities under quiet and disturbed conditions from polarimeter observations, *J. Geophys. Res. 90*, 9921, 1985.

Coley, W.R., and R.A. Heelis, Low-latitude zonal and vertical ion drifts seen by DE-2, *J. Geophys. Res. 94*, 6751, 1989.

Eccles. J.V., A simple model for low-latitude global scale electric fields, *Eos Trans. AGU*, Fall, 1996.

Fejer, B.G., E.R. de Paula, S.A. Gonzales, and R.F. Woodman, Average vertical and zonal F-region plasma drifts over Jicamarca, *J. Geophys. Res. 96*, 13901, 1991.

Fejer, B.G., F region plasma drift over Arecibo. Solar cycle, seasonal, and magnetic activity effect, *J. Geophys. Res. 98*, 13,645-13,652, 1993.

Haerendel, G., J.V. Eccles, and S. Cakir, Theory for modeling the equatorial evening ionosphere and the origin of the shear in the horizontal plasma flow, *J. Geophys. Res. 97*, 1209-1223, 1992.

Mendillo, M., and J. Baumgardner, Airglow characteristics of equatorial plasma depletions, *J. Geophys. Res. 87*, 7641, 1982.

Rishbeth, H., Polarization fields produced by winds in the equatorial F-region, *Planet. Space Sci. 19*, 357-369, 1971.

J.D. Tarpley, The ionospheric wind dynamo II: Solar Tides, Planet. Space Sci., 18, 1091-1103, 1970.

Tinsley, B.A., R.P. Rohrbaugh, W.B. Hanson, and A.L. Broadfoot, Images of transequatorial F-region bubbles in 630- and 777-nm emission compared with satellite measurements, submitted *J. Geophys. Res.*, 1995.

Weber, E.J., J. Buchau, R.H. Eather, and S.B. Mende, North-south field aligned equatorial airglow depletions, *J. Geophys. Res. 83*, 712, 1978.

J. LaBelle. Department of Physics and Astronomy, Dartmouth College, Hanover, NH 03755

J. V. Eccles, Space Environment Corporation, 399 North Main, Logan, UT 84321

M. J. Taylor, Space Dynamics Laboratory, Utah State University, Logan, UT 84322

J. H. A. Sobral, Instituto Nacional de Pesquisas Espaciais, Av. de los Astronautas 1758, São José dos Campos, Brazil

Pergamon

# GRAVITY WAVES AND VERTICAL DIFFUSION IN THE LOWER THERMOSPHERE FROM 557.7NM AIRGLOW

U. B. Makhlouf*, R. H. Picard**, M. J. Taylor*** and
J. R. Winick**

* Stewart Radiance Laboratory, Utah State University, 139 The Great Road,
Bedford MA 01730, USA
** Phillips Laboratory, Geophysics Directorate, 29 Randolph Road, Hanscom
AFB, Bedford MA 01731, USA
*** Space Dynamics Laboratory, Utah State University, Logan UT 84322,
USA

## ABSTRACT

The 557.7 nm oxygen airglow is emitted in the 90-100 km region. This is the region where a large part of the gravity-wave (GW) spectrum saturates and where nonlinear effects and wave breaking become important to limit the amplitude growth of the waves through the generation of turbulence, which enhances the mixing in the region. Mixing leads to diffusion, especially of O, which diffuses downward from its rich source above 95 km. Studying the 557.7 nm airglow enables one to characterize both the gravity waves and the enhanced vertical diffusion. Model predictions of fluctuations due to gravity waves in the atomic-oxygen green line emission are calculated and used in conjunction with ground-based data from a CCD all-sky camera to predict the density fluctuations and estimate the GW enhanced vertical diffusivity $D_{zz}$ as derived by Weinstock [1976]. Three wave events were used for this study, and an average $D_{zz}$ of $3.6 \times 10^4$ m$^2$/sec was calculated.

© 1997 COSPAR. Published by Elsevier Science Ltd.

## INTRODUCTION

Photochemical-dynamical models are one of the basic tools in theoretical studies that are used to simulate and quantitatively predict the global distribution of important chemically active constituents. Each species in the atmosphere has its own sources and sinks, in addition to being advected and transported by the global-scale circulation or by dynamical processes of various spatial and temporal scales, such as gravity waves and turbulence. Thus, it is crucial that these models correctly include a quantitative parametrization of consistent transport processes.

In the mesosphere and lower thermosphere, the effect of wave and turbulence processes on constituent transport is often parametrized in terms of an eddy diffusivity, which is a freely adjustable parameter, without explicit reference to the underlying physical processes. In the current study we attempt to obtain eddy diffusivity from one physical process namely GW nonlinear interactions, using GW parameters from actual observations.

The main emphasis will be on the vertical eddy diffusivity $D_{zz}$ due to GW nonlinearity which should be considered as a lower limit of the general case [Reed and German 1965; Ebel 1980].

Using a coupled photochemical-dynamical model for the OI(557.7 nm) green airglow emission in conjunction with a relative brightness fluctuation as measured by a CCD all sky imager, the relative fluctuation in the atmospheric density will be estimated. The relative density fluctuation will then be used to infer $D_{zz}$ from Weinstock nonlinear theory of acoustic gravity waves [Weinstock,1976].

## OBSERVATIONS AND ANALYSIS
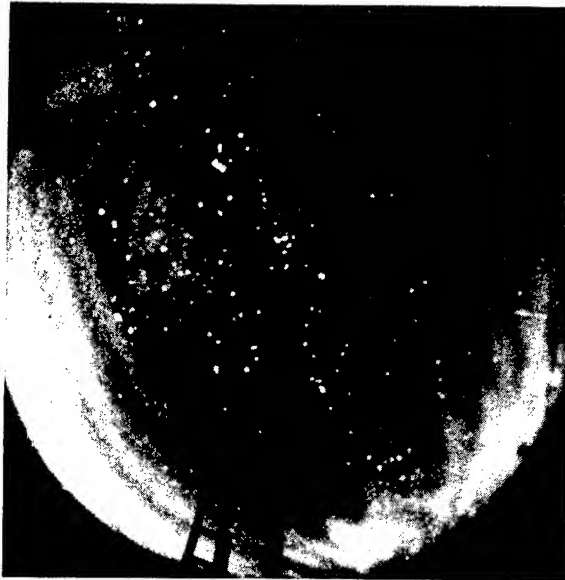


**Figure 1.** *An all sky image of OI(557.7 nm) recorded during the ALOHA-93 campaign, day 295 at 12:55 UT.*
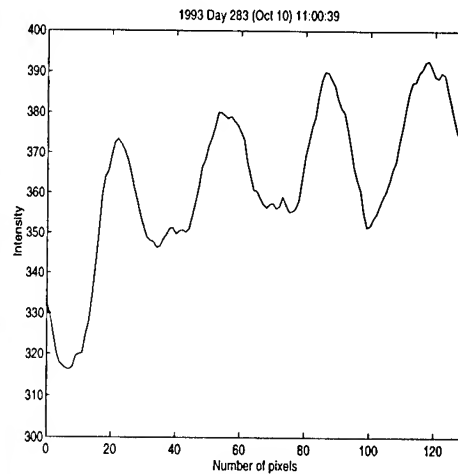


**Figure 2.** *A scan across a flat-fielded image for day 283, during the ALOHA-93 campaign. The scan shows the fluctuation in the OI (557.7 nm) brightness.*

The data used in this study are GW images recorded in October 1993 during the ALOHA-93 campaign [Gardener,1995] from Maui (20.8°N, 156.2°W) using an all-sky CCD imaging system [Taylor et al. 1995]. Structure in the OI(557.7 nm) emission was recorded as shown in Figure 1. In Figure 1, a quasi monochromatic wave is the dominant feature in the image. The image was corrected by removing the contribution of lens vignetting and the off-zenith (Van Rhijn) enhancement. For more details, see Taylor and Garcia, [1995]. A relative intensity scan across the flat-fielded image, normal to the wave crests, is taken as shown in Figure 2. From the intensity scan, the average brightness $B_0$ and the brightness fluctuation, $\Delta B = B - B_0$, are measured, and the relative brightness $\Delta B/B_0$ is calculated. The parameters of the wave motion; horizontal wavelength $\lambda_h$, apparent phase speed $v_{phx}$ and direction of motion are also measured and used to calculate the apparent wave period, $\tau_{obs} = \lambda_h/v_{phx}$. The Doppler shift of the phase speed is calculated from the wind speed u along the direction of the wave propagation and used to calculate the intrinsic period $T_{int}$. The wind data used for this study were obtained using a medium frequency (MF) radar system located ~ 375 km to the NW of Maui at the Pacific Missile Range Facility at Barking Sands, Kauai, Hawaii. For more information about the mode of operation and data processing, see Fritts and Isler, [1994].

## Table 1:

| Wave event | UT Day | UT hr:min | Apparent phase speed (m/s) | Wind speed along wave direction u (m/s) | Horizontal wavelength $\lambda_h$ (km) | Apparent period $T_{obs}$ (min) | Intrinsic period $T_{int}$ (min) | $\Delta B/B_0$ |
|---|---|---|---|---|---|---|---|---|
| 1 | 283 | 11:00 | 77.0 | 17.0 | 20.1 | 4.4 | 5.6 | 9.8% |
| 2 | 292 | 09:23 | 60.9 | 30.0 | 14.6 | 4.0 | 7.9 | 7.2% |
| 3 | 295 | 12:55 | 34.0 | -22.2 | 38.0 | 18.6 | 11.3 | 5.5% |

This procedure is followed for those data sets showing strong quasi-monochromatic wave events, as Table 1 shows the wave parameters for the three nights selected.

MODEL AND VERTICAL DIFFUSION

A chemical kinetic model for the OI(557.7 nm) airglow was developed by Makhlouf et al. [1996], using up to date chemical rates. The model assumes a two step Barth type mechanism to produce the $O(^1S)$ excited state, included in the model is the collisional quenching by $O_2$, $N_2$, and atomic oxygen O.

The chemical model is coupled to a realistic gravity wave model through the continuity equation in a similar fashion to what was done in Makhlouf et al. [1995] paper. The coupled chemical-dynamical model is used to calculate the transfer function $\tau$, which is the ratio of the relative brightness fluctuations to the relative density fluctuations:

$$\tau = \frac{\Delta B / B_o}{\Delta \rho / \rho_o} \qquad (1)$$

$\tau$ is calculated from equation (1) in a similar fashion as the Krassovsky eta, which is the ratio of the relative brightness fluctuations to the relative temperature fluctuations, was calculated in Makhlouf et al. [1995] paper. The transfer function is a complex number and is plotted in both amplitude and phase as a function of wave period for a gravity wave of horizontal phase speed of 30.9 m/sec, see Figure (3).

As described in the previous section, $\Delta B/B_0$ is estimated from the all sky image, and $\tau$ is calculated from the coupled photochemical-dynamical model, so using equation (1), one can estimate the relative density fluctuations $\Delta \rho / \rho_0$.

Weinstock [1976] using a nonlinear theory of acoustic gravity waves derived a formula for the enhanced eddy diffusion in terms of the Fourier components of the perturbation wave velocity. Using the same approximations as Battaner and Molina [1980], one derives an expression for the enhanced vertical diffusion $D_{zz}$ in terms the periods and wavelengths of gravity waves and the amplitude of the density fluctuations:



**Figure 3.** The amplitude and phase of the transfer function for a constant intrinsic horizontal phase speed of 60.9 m/s.

$$D_{zz} = A \left[ \frac{\lambda_h P (4\pi^2 P^2 \lambda_h^2 + (\nu - 1)^2 g^2 T^4 B^2)}{T^3 (P^2 B^2 \lambda_h^2 + 4\pi^2 T^4 H^2)} \right] \left| \frac{\Delta \rho}{\rho_o} \right|^2 (2)$$

where
$A = HB^3/16(\gamma-1)^2 \pi^2$ and $P = (T^2-B^2)^{1/2}$
T is wave period; B is Brunt period; H is atmospheric scale height; $\gamma$ = specific heat ratio and $\lambda_h$ is the horizontal wavelength.

Using the derived density fluctuations from the model with the measured wave parameters, one can estimate the vertical eddy diffusivity from the gravity wave using equation 2. The eddy diffusivity for the 3 events are shown in Table
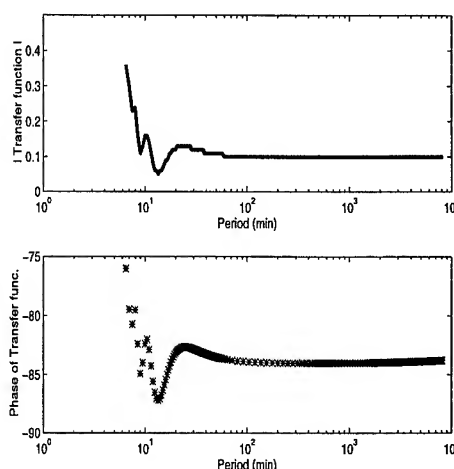
**Table 2:**

| Wave event | 1 | 2 | 3 |
|---|---|---|---|
| Eddy diffusivity (m²/sec) | $2.1 \times 10^3$ | $3.3 \times 10^4$ | $7.3 \times 10^4$ |

## SUMMARY

Ground based all sky images of green line airglow is a useful technique for studying gravity waves in the mesosphere lower thermosphere regions and for estimating the vertical diffusion coefficient ($D_{zz}$) due to gravity waves propagating in the region. This was a preliminary study applied to only few images. More data processing is needed especially with data collected in different seasons to statistically infer the seasonal variability of $D_{zz}$. This method can be applied to other airglow emissions, like hydroxyl and sodium airglow, which produces the altitude dependence of $D_{zz}$.

## ACKNOWLEDGEMENT

## REFERENCES

Battaner E. and A. Molina, "Turbopause Internal Gravity Waves, 557.7 nm airglow, and Eddy Diffusion Coefficient", J. Geophys. Res. 85, No. A12, 6803, (1980).

Ebel A., "Eddy diffusion models for the mesosphere and lower thermosphere", J. Atmos. Terr. Phys. 42, 617, (1980).

Fritts D. C. and J. R. Isler, "Mean motions and tidal and two day structure and variability in the mesosphere and lower thermosphere over Hawaii", J. Atmos. Sci. 51, 2145, (1994).

Gardner C. S., "Introduction to the ALOHA/ANLC-93 campaign", Geophys. Res. Let. 22, No. 20, 2789, (1995).

Makhlouf U. B., R. H. Picard and J. R. Winick, "Photochemical-dynamical modeling of the measured response of airglow to gravity waves 1. Basic model for OH airglow", J. Geophys. Res. 100, No. D6, 11,289, (1995).

Makhlouf U. B., R. H. Picard and J. R. Winick, J. Geophys. Res., to be submitted, (1996).

Reed R. J. and K. E. German, "A Contribution to the problem of stratospheric diffusion by large-scale mixing", M. Weath. Rev. 93, 313, (1965).

Taylor M. J. and F. J. Garcia, "A two-dimensional spectral analysis of short period gravity waves imaged in the OI(557.7 nm) and near infra red OH nightglow emissions over Arecibo, Puerto Rico", Geophys. Res. Let. 22, No. 18, 2473, (1995).

Taylor M. J., G. R. Swenson and V. Taylor, "Height measurements of OI(557.7 nm) gravity wave structure over the Hawaiian Islands during ALOHA-93", Geophys. Res. Let. 22, No. 20, 2881, (1995).

Weinstock J., "Nonlinear Theory of Acoustic-Gravity Waves, 1. Saturation and Enhanced Diffusion", J. Geophys. Res. 81, No. 4, 633, (1976).